Emergent Magnetic Effects in Spintronic Devices with 3D Chiral Geometries

Dissertation

zur Erlangung des
Doktorgrades der Ingenieurwissenschaften
(Dr.-Ing.)

der Naturwissenschaftlichen Fakultät II
Chemie, Physik und Mathematik

der Martin-Luther-Universität
Halle-Wittenberg

vorgelegt von Herrn

André Miguel Alves Farinha

Gutachter:
Prof. Dr. Stuart S. P. Parkin
Dr. Amalio Fernandéz-Pacheco
Prof. Dr. Georg Woltersdorf

Tag der öffentlichen Verteidigung:
26.06.2023

Contents

Zusammenfassung

Es wird erwartet, dass dreidimensionale magneto-elektronische Bauelemente erhebliche Verbesserungen der Speicherdichte [1], einzigartige 3D-geometriegesteuerte magnetische Effekte [2] und die Stabilisierung komplexer magnetischer Strukturen [3] ermöglichen werden. Die Realisierung solcher 3D-Bauteile stellt jedoch viele große Herausforderungen dar, wie die Entwicklung neuer 3D-Fertigungs- und Charakterisierungstechniken [4, 5], neue 3D-Modellierungs-Frameworks [6], die Anpassung der 2D-Fertigungswerkzeuge an 3D und die Integration all dieser Elemente [4, 7].

In dieser Arbeit verfolgen wir einen schrittweisen Ansatz zur experimentellen Demonstration von spintronischen Bauelementen mit komplexen 3D-Geometrien und den neuartigen Effekten, die sie ermöglichen. Zunächst wird ein Multi-Photon Lithography (MPL)-System zur Herstellung von Freiform-3D-Strukturen entwickelt. Zweitens wird ein vereinfachter Arbeitsablauf für die Herstellung von spintronischen 3D-Bauelementen entwickelt. Durch die Ausnutzung von Schatteneffekten zur Herstellung der elektrischen Kontaktflächen wird der Arbeitsablauf auf nur zwei Schritte vereinfacht, nämlich die Herstellung eines Gerüsts und das Sputtern von magnetischen Filmen. Drittens wurden spintronische Bauelemente mit chiralen 3D-Geometrien hergestellt und charakterisiert. Es wurde festgestellt, dass die geometrische Chiralität die magnetischen Eigenschaften der Systeme beeinflusst, so dass Bauelemente mit entgegengesetzter geometrischer Chiralität unterschiedliche magnetische Reaktionen zeigen, d.h., die chirale Symmetrie der Systeme ist gebrochen. Es wurden zwei verschiedene Studien durchgeführt. In einer Studie wird die strominduzierte Domänenwand (DW)-Bewegung über μm breite Bänder mit Torsion charakterisiert. Für verschiedene DW-Konfigurationen und Torsions-Chiralitäten werden unterschiedliche Schwellströme und DW-Geschwindigkeiten gemessen, was die Realisierung eines selektiven DW-Filters ermöglicht. In der anderen Studie zeigen spulenförmige Bauteile asymmetrische Anisotropic Magnetoresistance (AMR). Die AMR-Reaktionen sind für Spulen mit entgegengesetzter Chiralität gespiegelt.

Schließlich wurde ein verbessertes MPL-Verfahren entwickelt, das eine in-situ-Echtzeit-Charakterisierung und Kontrolle des 3D-Strukturherstellungsprozesses sowie die 3D-Rekonstruktion der hergestellten Struktur direkt nach der Herstellung ermöglicht.

Der demonstrierte Arbeitsablauf ermöglicht ein schnelles Prototyping von spintronischen Bauelementen mit dreidimensionalen Strukturen und ist mit einer breiten Palette unterschiedlicher Geometrien kompatibel. Bei der Integration in spintronische Bauelemente führen die neu demonstrierten Geometrien nachweislich zu neuartigen magnetischen Effekten von großem praktischen Interesse. Die Ergebnisse dieser Arbeit motivieren zur weiteren Erforschung des 3D-Nanomagnetismus, während die hier vorgestellten Methoden zur Entwicklung neuer 3D-magneto-elektronischer Bauelemente verwendet werden können und deren vielversprechende Wirkung weiter demonstrieren.

Abstract

Three-dimensional magneto-electronic devices are expected to enable major improvements in memory density [1], uniquely 3D geometry-driven magnetic effects [2], and stabilize complex magnetic textures [3]. However, achieving such 3D devices poses many great challenges, such as the development of new 3D fabrication and characterization techniques [4, 5], new 3D modeling frameworks [6], the adaptation of the 2D fabrication toolset to 3D and the integration of all of the above [4, 7].

In this thesis, we take a stepwise approach to the experimental demonstration of spintronic devices with complex 3D geometries and the novel effects they enable. First, a MPL system is developed to fabricate freeform 3D structures. Second, a simplified workflow for the fabrication of 3D spintronic devices is developed. By taking advantage of shadowing effects to establish the electrical contact pads, the workflow is simplified to comprise only two steps, the MPL fabrication of a scaffold and the magnetic film sputtering. Third, spintronic devices with chiral 3D geometries were fabricated and characterized. The geometrical chirality is seen to influence the magnetic properties of the systems, such that devices of opposite geometrical chirality present different magnetic responses, i.e., the chiral symmetry of the systems is broken. Two different studies were realized. In one study, current-induced Domain Wall (DW) motion is characterized over μm wide ribbons with torsion. Different threshold currents and DW velocities are measured for different DW configurations and torsion chiralities, enabling the realization of a selective DW filter. In the other study, coil-shaped devices display asymmetric AMR. The AMR responses are mirrored for coils of opposite chirality.

Finally, an improved MPL process is developed that enables in-situ real-time characterization and control of the 3D structure fabrication process, as well as the 3D reconstruction of the fabricated structure right after the fabrication.

The demonstrated workflow enables fast prototyping of spintronic devices with three-dimensional structures and is compatible with a wide range of different geometries. When integrated into spintronic devices, the newly demonstrated geometries are shown to lead to novel magnetic effects of substantial practical interest. The results in this thesis motivate further investigation into 3D nanomagnetism, while the methods presented herein can be used to prototype new 3D magneto-electronic devices and further demonstrate their promise.

List of Figures

Listings

List of abbreviations

AFM Atomic Force Microscopy
AMR Anisotropic Magnetoresistance
AOM Acousto-Optical Modulator
APD Avalanche Photo-Detector

CARS Coherent Anti-Stokes Raman Spectroscopy
CIDWM Current Induced Domain Wall Motion
CVD Chemical Vapour Deposition
CW Continuous Wave

DC Direct Current
DETC 7-diethylamino-3-thenoyl-coumarin
DMI Dzyaloshinskii–Moriya interaction
DW Domain Wall

EDX Energy-Dispersive X-ray Spectroscopy

FD-OCT Fourier-Domain Optical Coherence Tomography
FEBID Focused Electron Beam Induced Deposition
FIB Focused Ion Beam
FM Ferromagnetic
FPGA Field Programmable Gate Array
FWHM Full-Width Half Maximum

GLAD Glancing Angle Deposition

ISC Inter-System Crossing

JSON JavaScript Object Notation

LLG Landau-Lifshitz-Gibert

MOKE Magneto-Optical Kerr Effect
MPL Multi-Photon Lithography
MRML Medical Reality Modeling Language

NA Numerical Aperture

PALM Photo Activated Localization Microscopy
PEEM Photoemission Electron Microscopy
PETA Pentaerythritol Triacrylate
PETTA Pentaerythritol Tetraacrylate
PMA Perpendicular Magnetic Anisotropy
PMT Photo-Multiplier Tube
PSF Point Spread Function

PVD Physical Vapour Deposition

RAPID Resolution Augmentation Through Photo-induced Deactivation
REE Red Edge Effects
RF Radio-Frequency
RMS Root Mean Square

SAF Synthetic Anti-Ferromagnet
SEM Scanning Electron Microscopy
SHE Spin Hall Effect
SLM Spatial Light Modulator
SNR Signal-to-Noise Ratio
SOT Spin-Orbit Torque
STED Stimulated Emission Depletion
STORM Stochastic Optical Reconstruction Microscopy
STT Spin-Transfer Torque

TCP Transmission Control Protocol
TEM Tunneling Electron Microscopy
THG Third-Harmonic Generation
TNB Tangential-Normal-Binormal
TPA Two-Photon Absorption
TPEF Two-Photon Excited Fluorescence

VSM Vibrating Sample Magnetometry

XMCD X-Ray Magnetic Circular Dichroism

Chapter 1

Introduction

In 1959 Richard Feynman gave a lecture entitled "There is Plenty of Room at the Bottom" [8] about the immense potential of what would become known as nanotechnology. In it, he argued that the ability to pattern materials at a small scale would enable access to an enormous range of different material properties and possible applications beyond what could be envisioned. Indeed, achievements in nanotechnology have shaped the world very differently today.

The potential of 3D micro- and nano-fabrication has strong parallelism with what was described by Feynman in that lecture[1]. Over the last two decades, the field of 3D micro- and nano-fabrication has progressed enormously [9], consistently surpassing the expectations one could have about it. It is now possible to fabricate inside cells[2] [12], to achieve invisibility cloaks [13], 100-nm-sized coils [14], to do time-resolved characterization of the magnetization in 3D [15], and to operate robots at the micrometer scale [16]. And yet, the tiny fraction of the 3D parameter space that has been explored so far makes me consider that there is, still, plenty of space at the bottom.

Particularly, the 3D fabrication techniques developed so far have been successful in fields such as optics [17], micro-fluidics [18], cell scaffolds [19], robotics [20] and meta-materials [21], among others, but have achieved limited success in relevant and wide-ranging fields such as electronics and magnetism [22, 23]. In the latter, the requirements for homogeneous layers of very high-purity inorganic materials are typically hard to satisfy with existing 3D fabrication workflows.

Still, the effort to pursue 3D magneto-electronic devices at the micron and nanoscale is justified. Recent theoretical studies indicate the possibility of influencing the magnetic properties of a device through its 3D shape [6]. This includes, for example, the ability to modulate magnetic interactions based on 3D geometrical shape alone [2] and to stabilize complex magnetic textures [3]. Furthermore, proposals for prospective 3D devices demonstrate the promise of the field. They establish how the third dimension can be leveraged, for example, to increase the density of bits[3] in a memory by many orders of magnitude [1], or to combine logic and memory in the same device, enabling neuromorphic devices and architectures [4] which are highly sought after [24].

The two main approaches to the fabrication of 3D magneto-electronic devices are direct fabrication and scaffold-based fabrication. In the former, the desired material is patterned directly, corresponding to a 3D directed material growth, e.g., as achieved through Focused Electron Beam Induced Deposition (FEBID) [25]. This approach has been mostly limited by the range of compatible materials and their purity. For scaffold-based fabrication, the desired material can either be deposited onto a 3D structure as a coating or be embedded into the scaffold material. In the latter case, the scaffold core is ideally removed after fabrication, e.g., by thermal processing, leaving behind a structure with high purity but typically heterogeneous features [26]. Scaffold-based approaches are mostly limited by the properties of the scaffold material and the integration with standard techniques in complex workflows.

---

[1]Interestingly, the idea of 3D systems is covered in the lecture but only subtly and never explicitly referred. Particularly, the fabrication, described as the extrusion or pressing of planar features, is closer to the standard 2D fabrication techniques.

[2]"a surgeon we can swallow", as Feynman alluded to, is also now within reach [10, 11].

[3]per surface area

In this thesis, we aim to develop a fabrication workflow for 3D electronic and magneto-electronic devices from micro to nanoscales. As explained in section 2.5, we choose MPL to be the basis of such workflow. We focus on the generality of the workflow by minimizing the extent of its limitations, i.e., it should be compatible with the highest possible number of different designs and the largest possible range of high-quality materials. Thus, we do not aim to inherently improve the chosen 3D fabrication method[4] but rather to maximize the variety and quality of electronic devices we can readily achieve with it.

Beyond establishing a 3D fabrication workflow for magneto-electronic devices, we seek to utilize this workflow to demonstrate novel and inherently 3D improvements to device performance, properties, or even inherently 3D functionalities. As is seen in chapters 5 and 7, this objective is accomplished by showing a coupling between geometrical 3D chirality and the magnetic response of the films deposited onto the chiral 3D structure. This is achieved for two different structural designs, each using a different magnetic film stack. Particularly, in chapter 5, a 3D DW filter is demonstrated.

Outline of this thesis

In chapter 2, I lay out the basic knowledge that is necessary to understand and interpret the concepts and phenomena addressed throughout this thesis. Specifically, the basics of MPL are first laid out in section 2.1, followed by an explanation of Red Edge Effects (REE) in section 2.2 and of the mechanisms behind current induced DW motion and 3D curvilinear ferromagnetism in sections 2.3 and 2.4, respectively. In section 2.5, the state of the art of magnetic and magneto-electronic devices at the micron and nanoscale is reviewed, providing the necessary context for the experimental work that follows. In section 2.6, the aims of this project are presented.

In chapter 3, the experimental methods utilized throughout this thesis are described. Particularly, the developed MPL apparatus, which includes a Stimulated Emission Depletion (STED) module and a confocal detection module, is described in detail.

Chapter 4 presents the description of the software modules developed to implement and control the MPL fabrication process. Furthermore, I also describe the data processing software developed to analyze the Magneto-Optical Kerr Effect (MOKE) microscopy data and to perform the 3D reconstruction of the fabrication results. These data processing software packages are used in chapter 5 and chapter 6, respectively.

In chapter 5, the fabrication of spintronic devices consisting of suspended ribbons with torsion is presented. Herein, the differences in the current-induced DW motion over the twisted ribbons for devices with different torsion chiralities and for DWs with different configurations are shown and interpreted.

In chapter 6, an improved MPL process is presented that enables real-time characterization and control of the fabrication. The underlying mechanism to the real-time characterization is investigated and identified, the practical impacts of this improved process on the fabrication results are presented. Furthermore, the 3D reconstruction of fabricated structures from the acquired characterization data is demonstrated.

In chapter 7, the Anisotropic Magnetoresistance (AMR) response of coil-based devices is analyzed for coils of different chirality. The devices are fabricated with the same workflow utilized in chapter 5 but with smaller critical features. The geometrical chirality of the coils appears to interact with the magnetic response of the film, leading to asymmetric AMR responses for coils of opposite chirality.

In chapter 8, the experimental results pertaining to this thesis are reviewed as a whole. The accomplishment of the project aims, established in section 2.6, is evaluated and the relevance of the achieved experimental results is assessed in the context of the state of the art. The outlook of the project is presented in section 8.3. It addresses the ways in which the achieved results can contribute to future developments and identifies the shortcomings of the presented workflow, along with proposals on how to address them.

Finally, a short conclusion is presented in chapter 9.

---

[4]although this ends up happening, as described in chapter 6.

Chapter 2

Fundamentals

2.1 Multi-Photon Lithography

Multi-Photon Lithography (MPL) is a fabrication technique capable of producing arbitrary 3D polymer structures down to the nanometer scale. A focused laser is scanned along pre-programmed trajectories inside a photoresist[1], modifying the properties of the volume around the focus at each location. For the typical case of a negative photoresist, the exposed volumes become insoluble and remain after solvent washing while the unexposed volumes are removed. In this case, the final resulting structure can be thought of as the assembly of small building blocks, called voxels[2], that form the desired 3D geometry.

In the landscape of 3D fabrication, MPL has a unique set of characteristics. It is able to achieve sub-100 nm features[3], both laterally and axially [27], and to operate over meso-scale ranges [21] at industrially relevant fabrication rates [28], particularly when using multi-foci approaches [28]. Due to the nature of its local modification, MPL is one of the few techniques that enables essentially unrestricted freeform geometries, including intermeshing, hollow and suspended structures, as can be seen in fig. 2.1.

MPL is a digital maskless fabrication method, i.e., it can be digitally configured and controlled. Relying on automation and fast hardware, it enables very fast iteration cycles. This is particularly relevant during fabrication optimization, where a given structure can be automatically replicated under different fabrication conditions without pause. On the other hand, sample preparation time is in the order of a few minutes.

Although mostly limited to the patterning of polymeric materials and hydrogels [9], MPL offers significant flexibility within such material types. Particularly, many significant advances in MPL have been achieved through improvements to the utilized photoresists [12, 19, 29, 30]. However, in some applications, such as electronics, the applications of MPL are hindered by the restriction to the use of polymers [4, p. 3], as further seen in chapters 5 and 7. In the latter case, new post-processing methods [31, 32] and MPL-like fabrication techniques capable of patterning inorganic materials contribute to the progress towards more general 3D fabrication methods [33, 34]. These are reviewed in section 2.5.1.1.

2.1.1 History and Applications

Multi-photon absorption has been theoretically modeled since the 1930's [41]. However, the lack of sufficiently powerful light sources delayed its experimental realization for many years. In practice, MPL appears at the end of the 20th century [42, 43] in the context of nanophotonics research into non-linear light-matter interaction and following the realization of two-photon microscopy [44] and 3D optical data storage [45]. The technique attracted significant attention in the nanophotonics community, prompting fast-paced developments and many new applications [31, 46–51].

As it matured, MPL started being adopted in many other research fields and, over the years, it has had a far-reaching impact, enabling 3D applications in leading fields such as magnetism and electronics [23,

---

[1]Photoresist is a light-sensitive material affected by the lithography process, typically a liquid

[2]A voxel is the smallest volume element that can be modified in an MPL experiment, the 3D equivalent of a pixel

[3]A feature is a structural element generated by the lithography process. The minimum achievable feature is a voxel.
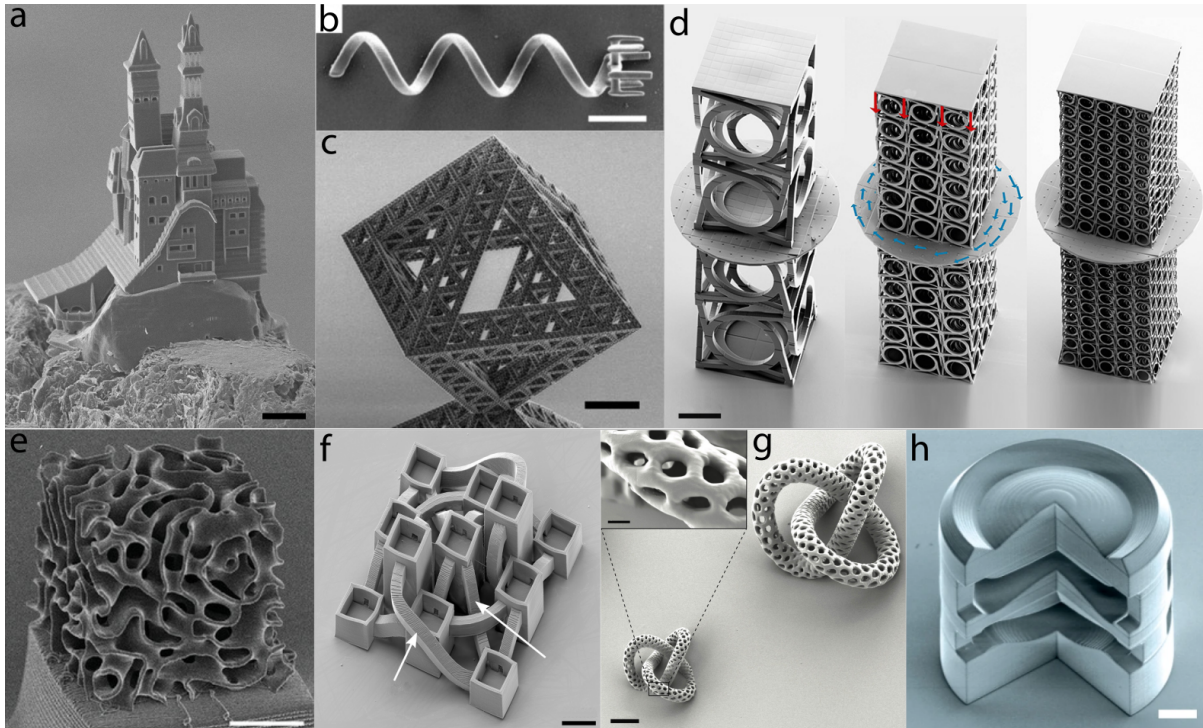
Figure 2.1: Examples of freeform 3D structures fabricated by MPL. (a) Replica of a model inspired by the Sutyagin house, fabricated on the tip of a pencil. Scale bar is 50 μm. Reproduced with permission from [35]. (b) Helical micromachine with microholder coated with a magnetic film for remote actuation. Scale bar is 10 μm. Reproduced with permission from [36]. (c) Third-order hierarchical octahedron nanolattice. Scale bar is 25 μm. Reproduced with permission from [37]. (d) Chiral mechanical metamaterials. Stacking of metamaterials of opposite chirality enable twists without the ends rotating. Scale bar is 200 μm. Reproduced with permission from [21]. (e) Glassy carbon nanospinodals resulting from pyrolysis of a polymer with an inorganic backbone. Scale bar is 5 μm. Reproduced with permission from [38]. (f) Network of hollow towers and channels for directing growth of in-vitro neuronal cultures. Scale bar is 25 μm. Reproduced with permission from [39]. (g) A set of hollow torus knots with open surface. Scale bar is 40 μm and 4 μm for the inset. Reproduced with permission from [40]. (h) Cut-out triplet lens to be used on single optical fiber cores. Scale bar is 20 μm. Reproduced with permission from [17].

52–54], photonics [17, 55], cell scaffolding [19, 56–58], microfluidics [18], robotics [59, 60], mechanical metamaterials [61, 62], and materials science [63, 64], among others.

While, at its core, MPL remains a 3D analogue to standard 2D photolithography, its widespread adoption has motivated continuous improvements in a wide range of functional aspects that took it beyond its 2D counterpart [65–68]. Beyond standard photolithography, MPL is able to match the feature size and resolution of electron-beam lithography [65, 66] and the feature size modulation of grayscale lithography [69, 70] while further achieving freeform 3D structures.

MPL continues to display fast-paced developments in optical systems [28], photoresist chemistry [64, 71, 72] and algorithms [51, 70] and is now a highly diversified research topic at the core of many innovative research endeavors [20, 29, 30, 32, 73]. A comparison of MPL with other 3D fabrication techniques in the context of 3D electronic device development is realized in section 2.5.[4]

2.1.2   Workflow

In its simplest configuration, MPL is realized by focusing a laser source, typically in the near infrared, e.g., 760-800 nm wavelength range, through a glass substrate and into a drop, typically in the μl range, of photoresist. Under sufficient exposure, the laser triggers a modification of the material, locally changing its solubility around the laser focus. For a negative tone photoresist, exposed regions become insoluble,

---

[4]For other introductions to MPL see [74, 75, pp. 13–32].

while for a positive tone photoresist, they become soluble following the post-processing [74]. Scanning the laser along a computer-controlled trajectory while the laser is affecting the sample imparts the scanned trajectory onto the material, as shown in fig. 2.2, converting a digital representation into a physical one. The scan can be realized layer by layer or along a desired 3D path. Once the complete geometry is scanned, the sample is post-processed in order to remove the soluble material, leaving the desired structure behind.
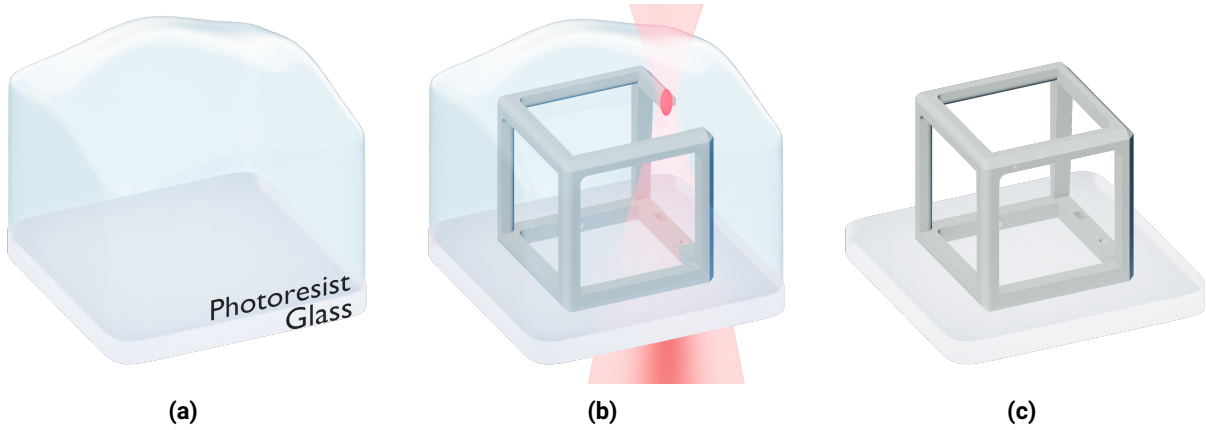
Figure 2.2: Multi-Photon Lithography (MPL) process workflow. (a) A small volume of photoresist is drop casted onto a coverslip glass substrate. (b) The laser is scanned within the photoresist along pre-programmed trajectories, modifying it. (c) After scanning the sample is developed through a solvent wash, with only the modified sections remaining.

2.1.3 Polymerization

The exposure mechanisms and the chemical reactions taking place in an MPL process depend on the photoresist material composition [74]. The photoresists used in this thesis belong to a common class that undergoes radical photopolymerization. In radical photopolymerization, the light exposure triggers a chain-growth-reaction where acrylate monomers agglomerate into chains and networks, forming larger solidified molecules through a liquid to solid phase-transition that renders the material insoluble. Examples of other processes are cationic polymerization, as with the SU-8 photoresist [76], or cationic ring opening reactions in a positive-tone photoresist [77, 78]. Both such processes use photo-acid generators as initiators.

A photoresist formulation can have a different number of functional components. A common case, used in this thesis, is to have a photoresist composed of photoinitiator molecules in an acrylate monomer solution. Having a dedicated photoinitiator, which absorbs the incoming light and generates radicals, enables to greatly improve the quantum yields of the underlying molecular processes and therefore the efficiency of the fabrication process [79]. It decreases the necessary laser intensity and the sensitivity to fluctuations in the fabrication parameters, and improves the fabrication rate and control over the fabrication features [79].

The polymerization process is composed of three stages: photoinitiation, chain-growth-reaction and termination.

The photoinitiation starts with a multi-photon absorption by the photoinitiator molecule, as explained in section 2.1.4. After excitation, some photoinitiator molecules will undergo inter-system crossing into a triplet state and generate radicals through either bond cleavage or electron transfer, as schematized in fig. 2.3 and described by eq. 2.1 [74].

$$I \xrightarrow{2\hbar\nu} I^* \to R\cdot \tag{2.1}$$

The number of generated radicals per excitation energy dose depends on the quantum yields of the underlying processes in the specific molecule. The multi-photon absorption can also be decoupled from the radical generation by having a co-initiator for radical generation, which is typically activated by electron transfer from the photoinitiator.
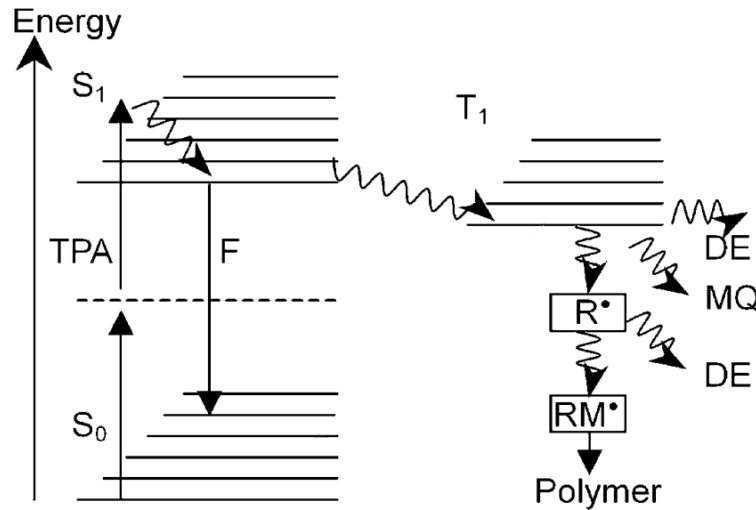
Figure 2.3: Jablonski diagram describing a two-photon lithography process. The process starts with Two-Photon Absorption (TPA), followed by Inter-System Crossing (ISC) of the excited molecule into T_1. It then proceeds with the formation of the radical ($R\cdot$), e.g., by electron transfer, that will start the polymerization chain reaction($RM\cdot$). There are several competing mechanisms which can deactivate the polymerization reaction, such as fluorescence (F) from the excited singlet state S_1, phosphorescence from the triplet state T_1 and monomer (MQ) or radical quenching (DE). Reproduced with permission from [74].

After the photoinitiator generates a radical, the chain-growth-reaction is started. A surrounding monomer attaches to the formed radical, creating a new radical at the monomer end and enabling the acquisition of further monomers, as depicted in eq. 2.2:

$$R \cdot + M \rightarrow RM \cdot \xrightarrow{M} RMM... \cdot \rightarrow RM_n \cdot \tag{2.2}$$

As a single radical can lead to many reactions, the quantum yield of the chain-growth process can be very high, even in the order of 10 000 [80, pp. 103–105]. The monomer properties are mostly responsible for the final polymer properties. For example, the usage of monomers with more functional groups enable monomers to not only form chains but also connect between different chains, forming networks, which are denser, more rigid and less prone to shrink [81, pp. 15–21, 82, 83]. Typical polymerization reaction time constants are on the order of 100 to 400 μs [84].

The chain reaction runs until a termination event occurs[5]. In experimental conditions, the termination of the polymerization chain reaction, described in eq. 2.4, can either occur due to combination with another active radical chain or due to the action of an inhibiting molecule, such as oxygen. Besides spontaneous termination, including photo-activated inhibitors has also been researched in the context of super-resolution MPL, as reviewed in section 2.1.6.

$$RM_n \cdot + RM_m \cdot \rightarrow RM_{m+n} R \tag{2.3}$$

$$RM_n \cdot + RM_m \cdot \rightarrow RM_m + RM_n \tag{2.4}$$

2.1.4   Non-linear Absorption Processes

Non-linear absorption processes refer to the absorption of energy by a material through interaction with more than one photon from a radiation field. In the following I present several descriptions of the absorption process to highlight different aspects of it. Particularly, I present the energy exchange rate (section 2.1.4.1), macroscopic (section 2.1.4.2) and microscopic (section 2.1.4.3) descriptions.

---

[5]For further information on the polymerization process see [74, 85, pp. 1–5, 86, pp. 1–5, 41–117]

2.1.4.1 Three-dimensional Exposure

The energy absorption by the material in an n-photon, or n^{th}-order, absorption process is often described through rate equations:

$$\left(\frac{dE}{dt}\right)_n = \delta_n N I^n. \tag{2.5}$$

where δ_n is the cross section of the absorption event, N the density of energy-absorbing molecules, described in section 2.1.3, and I is the laser intensity.

The non-linear dependence on the radiation intensity for $n > 1$ is the critical aspect for the achievement of three-dimensional lithography features. Let us see why by considering a hypothetical case where a region, labeled region 1, is exposed to 10 times higher intensity than a second region, region 2, but only for one-tenth of the time. The total exposure dose D is given by the product of the energy absorption rate, eq. 2.5, and the total exposure time, i.e., $D \propto I^n T$ for an n-photon process. For a linear, one-photon, absorption case, both regions will have the same exposure dose since the higher intensity in region 1 is fully compensated by the longer exposure in region 2 and therefore both regions will either undergo polymerization or not. Instead, for a 2-photon non-linear absorption case, the exposure dose at region 1 will be 10-times higher than the exposure dose at region 2 and therefore region 1 might undergo polymerization without it occurring at region 2.

This hypothetical case describes one important aspect of the scanning of a focused laser on a sample: assuming a Gaussian beam, the laser intensity is significantly higher at the focal point. However, because the beam focus shape is wider outside the focus region, as depicted in fig. 2.4, the exposure time during the scanning of the laser will be larger there. In non-linear absorption, the increase in intensity is predominant, as an exposure mechanism, over the increase in exposure time, thus enabling complex and long 3D scanning paths to produce selective 3D features mostly by intensity control. For one-photon absorption, on the other hand, the lack of such asymmetry is the main limitation to the achievement of 3D lithography [75, pp. 16–19, 72].

An equivalent relation is also used to describe the attenuation of plane waves along the propagation direction (z) in a medium, namely:

$$\frac{dI}{dz}_n = -\delta_n N I^n(z). \tag{2.6}$$

which, for an $n = 1$ photon absorption event, leads to the Beer-Lambert law. This relation highlights the importance of the transparency of the material to achieve 3D lithography in two ways. First, a significant light absorption at low intensities, e.g., as with one-photon, greatly limits the maximum fabrication depth due to significant cumulative absorption below the focal plane, thus limiting 3D fabrication capabilities. Second, since the cross section of an nth-order event, δ_n, greatly decreases with increasing n, a higher order event can only take place if any lower order events are mostly inexistent, e.g., for two-photon lithography to take place the material should be transparent to the laser wavelength, i.e., not display one-photon absorption of it, otherwise the latter will be dominant.

2.1.4.2 Dipole Enabled Transitions

In further detail, the rate of energy transfer from a radiation field to matter per unit time and volume is given by the Lorentz force. For a dielectric and non-magnetic medium, as is the case for a typical photoresist, it becomes [88, pp. 166–167]:

$$\frac{dW}{dt} = \langle \mathbf{E} \cdot \dot{\mathbf{P}} \rangle \tag{2.7}$$

where $\mathbf{E}$ and $\mathbf{P}$ denote the electric field and material polarization vectors and the $\langle \rangle$ brackets denote the time average. The material polarization, in turn, can be expanded as:

$$P = \chi^{(1)} E + \frac{1}{2}\chi^{(2)} E^2 + \frac{1}{4}\chi^{(3)} E^3 + \dots \tag{2.8}$$
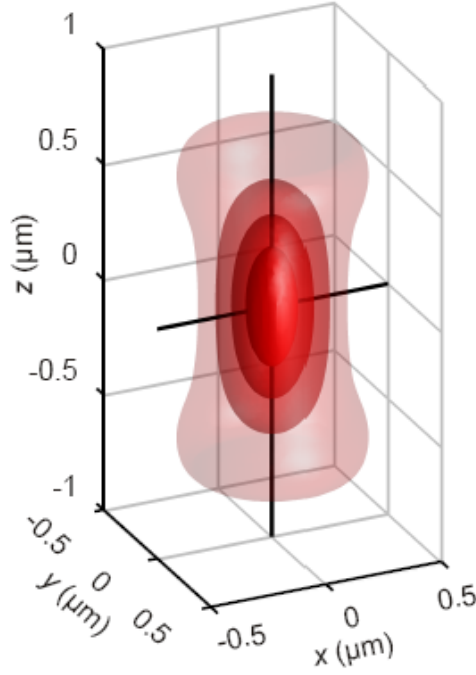
Figure 2.4: Spatial distribution of $|E|^2$ for a typical MPL writing spot. Spatial regions with increasingly stronger shades of red represent iso-surfaces of $|E|^2$ corresponding to $|E|^2 > 0.1, 0.25, 0.5$ and $0.75 \times |E|^2_{peak}$, respectively. The laser beam intensity is proportional to $|E|^2$. By modulating $|E|^2_{peak}$, and therefore I, the polymerized region at each position can be modulated towards the stronger or fainter regions, changing its shape in the process. Because higher-order effects ($n \geq 2$) scale with $|E|^{2n}$, the volumes where $I^n \geq I^n_{threshold}$ become more confined and are therefore smaller than the corresponding $|E|^2$ regions represented here. Reproduced with permission from [87].

where $\chi^{(n)}$ is the nth order susceptibility, which is a $(n+1)^{th}$ order tensor, and P and E the amplitudes of the corresponding vectors. The first order term relates to linear absorption and the third order term relates to two-photon absorption. The second order term plays no role as it becomes zero for centrosymmetric materials and ensembles of randomly oriented molecules, as it is the case of photoresists.

Developing eq. 2.7 for the case where the polarization and electric field are planar waves with the same frequency ω, i.e., the polarization is driven by the electric field, it results that:

$$\frac{dW}{dt} = \frac{\omega}{2} Im(|E| \cdot |P|) \tag{2.9}$$

with $|E|$ and $|P|$ being the modulus of the amplitude of the waves. It is noteworthy that the energy transfer from the radiation field to the matter is related only to the imaginary part of the dot product. Processes involving such energy transfer are called non-parametric as opposed to parametric processes, such as frequency doubling, where no energy is transferred to matter.

The rate of energy transfer for two-photon absorption is obtained by substituting the third order term from eq. 2.8 in eq. 2.9 [88, pp. 166–167]:

$$\frac{dW}{dt} = \frac{3}{8} \omega |E|^4 Im(\chi^{(3)}), \tag{2.10}$$

with n the refractive index of the material. It follows from eq. 2.10 that the energy transfer is actually driven by the radiation electric field. This is due to the involved transitions being dipole enabled transitions, as is further explained in section 2.1.4.3. In this context, the exposure dose is rather given by $D \propto E^{2n} T$ for a n-photon process. Typically, however, the laser intensity I can be described as a function of $|E|^2$, e.g., in non-magnetic media, leading to the more common dependency on I^2:

$$\frac{dW}{dt} = \frac{8\pi^2 \omega}{c^2 n^2} I^2 Im(\chi^{(3)}) \tag{2.11}$$

2.1.4.3 Perturbation Theory

Fundamentally, two-photon absorption, the simplest case of multi-photon absorption, is a quantum mechanical process modeled by second order time dependent perturbation theory [41] through the two-photon tensor. It corresponds to the almost simultaneous absorption, within a few fs, of two photons by an electron in the photoinitiator molecule. Such transition is mediated by a virtual state which, as opposed to real excited states, is an unobservable quantum state.

Different factors can contribute to a virtual state and its lifetime depending on the symmetries of the photoinitiator molecule, i.e., its point group. Specifically, the photoiniator molecule point group will define the allowed transitions between molecular states and each of these allowed states will then contribute to the virtual state in a two-photon process.

For example, in centrosymmetric, or non-polar, photonitiators, only transitions between levels of opposite inversion symmetry, i.e., parity, are allowed, making one and two-photon selection rules complementary [89]. In this case, the contribution of each allowed energy level to the virtual state lifetime is given by the Heisenberg uncertainty principle [90] and is inversely proportional to the energy difference between the virtual state and the contributing real state, as in fig. 2.5.

On the other hand, in polar molecules, excitations to states of the same symmetry are possible if their dipole moments differ, making one and two-photon selection rules no longer complementary [89] and making the virtual states lifetime proportional to the difference in dipole moments between the initial and final states, i.e., the transition dipole moment. In this case, the two-photon absorption cross section is directly proportional to the transition dipole moment. This was confirmed, for example, by comparing the non-linear absorption cross section of polar and non-polar molecules with the same backbone [89, 90].

These different types of two photon absorption are summarized in figure fig. 2.5[6]. As the lifetime of a virtual state is typically on the order of few fs, a laser source must be able to produce a high photon density at such short timescale, driving the requirements for actual laser sources for MPL.

Upon increasing the photoinitiator transition dipole moment, the associated TPA pathway becomes dominant, enabling much higher TPA cross sections. For reference, while two-photon cross sections of up to $10GM$, with $1GM = 1cm^4s$, have been reported for non-polar molecules, cross sections in the order of 100 GM can be achieved by increasing the transition dipole moment of polar molecules [90]. This prompted significant research into polar photoinitiators with large transition dipole, which are now one of the most significant class of photoinitiators [74, 79]. Particularly, π-conjugated systems with electron donors or absorbers substituents, such as D-π-A-π-D, A-π-D-π-A and similar molecular systems, were seen to be efficient initiators [79] where the substantial electron transfer results in extremely large differences between the ground and excited states dipole moments. The transition dipole moment in these systems can be enhanced by extending the π-conjugation length or by increasing the strength of the absorbers or donor substituents [74, 79]. As all photoinitiators used in this thesis belong to this class, further discussions about photoresists will refer to it unless otherwise specified.

2.1.4.4 Excited State Absorptions

A second or higher order process does not always imply an almost simultaneous absorption of several photons via virtual states. Instead, higher order effects can take place through real, rather than virtual states [92, 93], as shown in figs. 2.6a to 2.6b. Such events are called excited-state absorptions and can be rather understood as a series of linear events, i.e., resonant absorptions, rather than one non-linear event. Excited state absorptions display a non-linear dependency on the laser intensity, just as a virtual-state mediated event, and can therefore be easily mistaken with the latter [93]. However, due to the much longer lifetime of the real excited states and the dynamics of the excited state population over such lifetime, the excitation rates of such events vary with the pulse length, introducing a characteristic time dependent response [92, 93]. Such events have recently been shown to enable 3D structuring at the nanoscale [94], as

---

[6]For a deeper analysis into the two photon cross section in the quantum mechanical perturbation theory framework see [41, 89–91]

$$\delta \cong 0.12\, \sigma_{b0}\, \sigma_{ba}\, t_I \qquad\qquad \delta \cong 0.12\, \sigma_{b0}^2\, t_{II}$$

$$t_I \cong \frac{h}{4\pi\, \Delta E_{ib}} \qquad\qquad t_{II} \cong \frac{4\,\pi^2\, \Delta\mu^2}{c\, \sigma_{b0}\, \Delta E_{b0}}$$
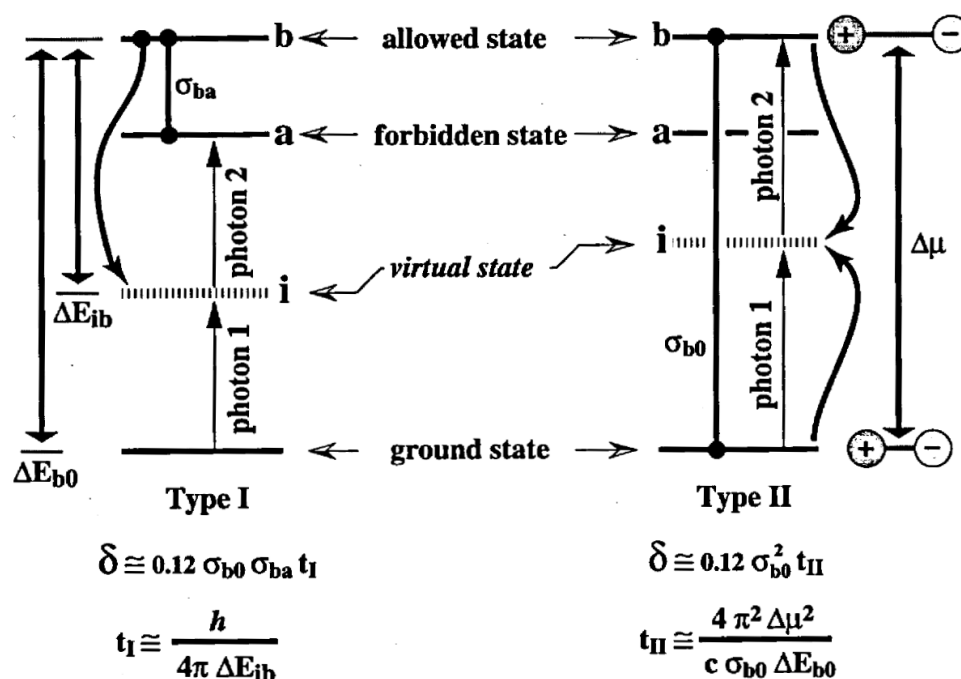
Figure 2.5: Comparison of Two-Photon Absorption (TPA), and the corresponding cross sections δ, in non-polar (type I process, left) and polar (type II process, right) molecules. Qualifications of forbidden and allowed states refer to one-photon absorption into those states. For non-polar molecules the TPA selection rules are complementary to that of one-photon absorption. In this case, only the excited state contributes to the lifetime (t_I) of the virtual state, which is defined by the Heisenberg uncertainty principle ($\Delta E \Delta t \geq h/4\pi$). In polar molecules, the TPA selection rules are no longer complementary to those of one-photon absorption and both the ground and excited state contribute to the virtual state lifetime (t_{II}). Particularly, this lifetime, and thus the TPA cross section, are proportional to the square of the transition dipole moment. Reproduced with permission from [90].

described in fig. 2.6c, although with rather specific material requirements since their linear nature and longer lifetimes makes it typically harder to achieve the desired selectivity and feature size.
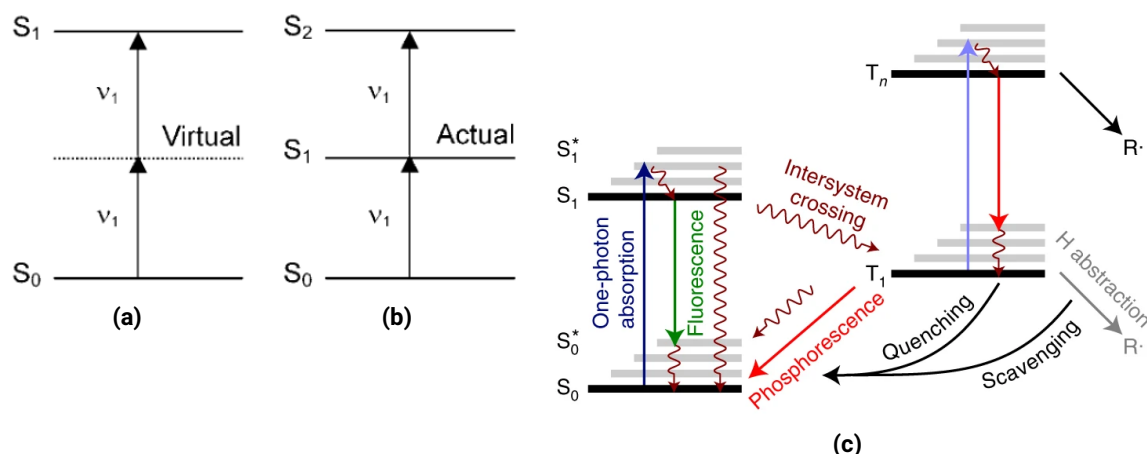
Figure 2.6: Excited state absorption as an alternative mechanism for MPL. (a) Typical TPA through simultaneous absorption with a virtual intermediate state. (b) Simplest case of excited state absorption. It corresponds to TPA through two sequential absorptions with a real intermediate excited state. It would then be followed by intersystem crossing. This approach typically results in coarse, if any, controllable features. Reproduced with permission from [74]. (c) MPL through excited state absorption with the second absorption occurring after intersystem crossing. Only the excited triplet state will proceed to generate withstanding radicals. This approach provides a mechanism to quench unspecific excitations, enabling performances similar to those of standard MPL while using greatly reduced laser powers. Reproduced with permission from [94].

2.1.5 Diffusion Kinetics, Threshold Model and Photoresist Memory

Beyond the complexity of the absorption process [41], some of the other underlying molecular processes, such as diffusion kinetics, are not yet fully understood [85, 95] and lack appropriate models. Furthermore, a single excitation event is unlikely to lead to a voxel formation since most underlying processes have quantum yields below one. Instead, the system behaves as a molecular ensemble [96, 97].

Although lacking an analytical model, a significant functional model of the polymerization process has been abstracted, referred to as threshold model. The threshold model states that a given photoresist volume undergoes polymerization, i.e., sufficient conversion to withstand the development process, if the local energy dose surpasses a given material-specific threshold. The energy dose absorbed by the material through an n-photon process is given by:

$$D \propto I^n T, \qquad (2.12)$$

where I is the laser average intensity and T the exposure time. This can be understood as an intrinsic material non-linearity that discretizes, or digitizes [72], local energy doses into polymerized or non-polymerized regions.

Intrinsic to the threshold model, however, are considerations about how dose accumulates over time, i.e., whether the photoresist keeps memory of past exposures. Under typical MPL conditions, it is a good approximation to consider that the photoresist keeps memory of all past exposures and that these add linearly [75, pp. 30–32, 95]. In this regime, it is the predominant effect of the intensity over the exposure time, see eq. 2.12, in multi-photon absorption that enables its 3D nature, as exemplified in section 2.1.4.1 and further explained in [72].

However, under specific conditions such as long exposures under low absorption regimes, the photoresist appears to forget weak exposures, giving rise to a different type of material non-linearity which enables, for example, to fabricate 3D structures under exposure by Continuous Wave (CW) lasers [98, 99]. Regularly described as a Schwarzschild effect [95], this is likely related to molecular diffusion over longer timescales, with small polymer chains being able to move far from the weakly illuminated regions before growing into appreciable features, resulting as if the past exposures had no effect [85].

2.1.6 Resolution Improvements in Multi-Photon Lithography

The threshold model, presented in section 2.1.5, establishes no limit for the minimum feature size, i.e., a polymerized feature can be made as small as desired, within atomic limits, as long as only the corresponding volume absorbs an energy dose above the threshold. In practice, the feature size is limited by the precision and reliability of the control over experimental parameters such as the laser intensity and the scanning speed.

However, the ability to fabricate two closely packed features and still resolve them as separate is limited, i.e., the fabrication resolution is limited. Modelled by the Sparrow resolution criterion [87], represented in fig. 2.7, two diffraction broadened MPL features are considered resolvable as long as there is a local minimum in the middle of the accumulated signal. As in section 2.1.5, the photoresist memory is once more relevant here, e.g., as a system without dose accumulation would not be limited in its resolution. Assuming typical MPL conditions, the best approximation is to consider that sequential exposures add linearly. Simulating the Sparrow criterion for a 2-photon excitation, the resolution is shown to improve by a factor of $\sqrt{2}$ over one-photon excitation [87].

Besides the resolution, the voxel aspect ratio is also limited to be ≥ 2.5 by the difference in the objective lens ability to resolve different wavevectors components along the optical axis, i.e., z, and along the planar coordinates [75]. This results in significantly larger feature sizes along the optical axis.

2.1.6.1 Resolution Improvement Techniques

Different techniques have been deployed to improve the achievable MPL resolution and feature sizes, and they typically go by the name of super-resolution MPL. The most relevant examples are STED [101],
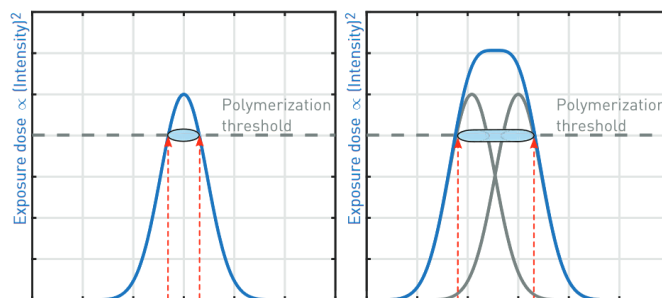
Figure 2.7: Representation of the Sparrow criterion. Two sequential exposures (right) do not generate two resolvable features if their total accumulated dose, the solid blue line, is above the polymerization threshold, the horizontal gray line. Since the size of the polymerized feature, represented by the light blue ellipsoid and the red arrows, is defined by the accumulated dose, the polymerized feature from the sequential exposure can be larger than the sum of the features that would be polymerized by each of the exposures separately, as represented on the right. The MPL resolution is, therefore, intrinsically limited. Reproduced from [100].

Resolution Augmentation Through Photo-induced Deactivation (RAPID) [102] and photo-activated inhibitors [103].

Although the specific mechanisms differ, these methods have a shared functional principle: They modulate the MPL-inducing energy dose at the focus location by shining a second, MPL-inhibiting, laser source at the periphery of the excitation source, as depicted in fig. 2.8a. The Point Spread Function (PSF) of the inhibition source is modified to have zero intensity at the center of the excitation source while achieving maximum intensity at its periphery. This configuration modulates the effective energy dose and concentrates it in a smaller volume around the excitation source focus, improving the feature size, resolution, aspect ratio and robustness to exposure fluctuations.
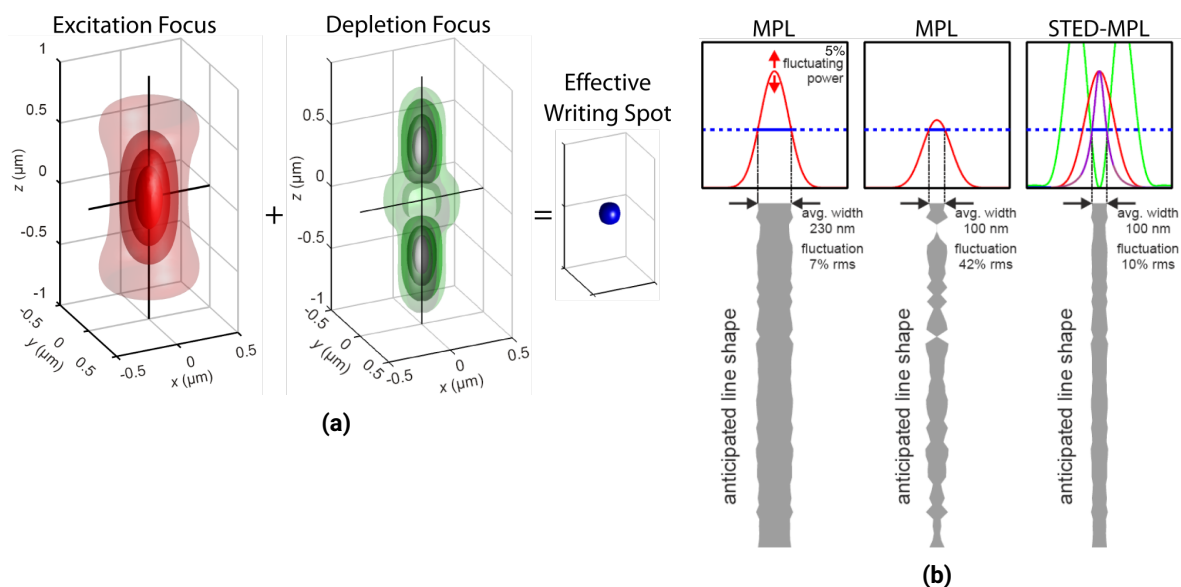
Figure 2.8: Effects of super-resolution MPL. Reproduced from [87]. (a) By combining the excitation beam with a depletion beam having a modified 3D PSF, the effective MPL writing spot is greatly reduced, allowing for smaller features, improved resolution and aspect ratios closer to 1, i.e., spherical voxels. (b) Fluctuations in the excitation laser power influence the size and continuity of the resulting polymerized feature. In MPL, the fluctuations in the size of the polymerized features become more significant when the peak laser power is close to the polymerization threshold (left and center), affecting mechanical stability and feature continuity. Super-resolution techniques such as STED-MPL (right) decrease the width of the effective MPL writing beam without requiring laser powers close to the threshold, and therefore enable both small and stable features.

The compounded effect of the excitation and inhibition beams is equivalent to exposing to an effective

beam with smaller Full-Width Half Maximum (FWHM), as shown in fig. 2.8b. The effective beam width can be decreased by increasing the inhibition laser power, resulting in a more localized energy exposure that leads to smaller feature sizes and resolutions (fig. 2.8b). The effective beam has a smaller width but the same peak intensity as the excitation source, resulting in a steeper intensity distribution that translates into smaller fluctuations in the feature size when the excitation laser intensity fluctuates. As for the aspect ratio, it is improved by having a 3D inhibition PSF that overlaps the excitation PSF differently in the xy plane and in the axial (z) direction.

As represented by the green arrows in fig. 2.9, a significant difference between STED, RAPID and photo-activated inhibitors is the moment in the photopolymerization process at which the deactivation occurs, i.e., whether the deactivation occurs at the excited singlet level [101], at the triplet level [102] or during the polymerization chain reaction by a photo-activated polymerization inhibitor [103], respectively. STED is the fastest mechanism, significantly enabling higher MPL fabrication rates. Furthermore, the first two mechanisms are reversible, i.e., the molecules return to the initial state after deactivation.
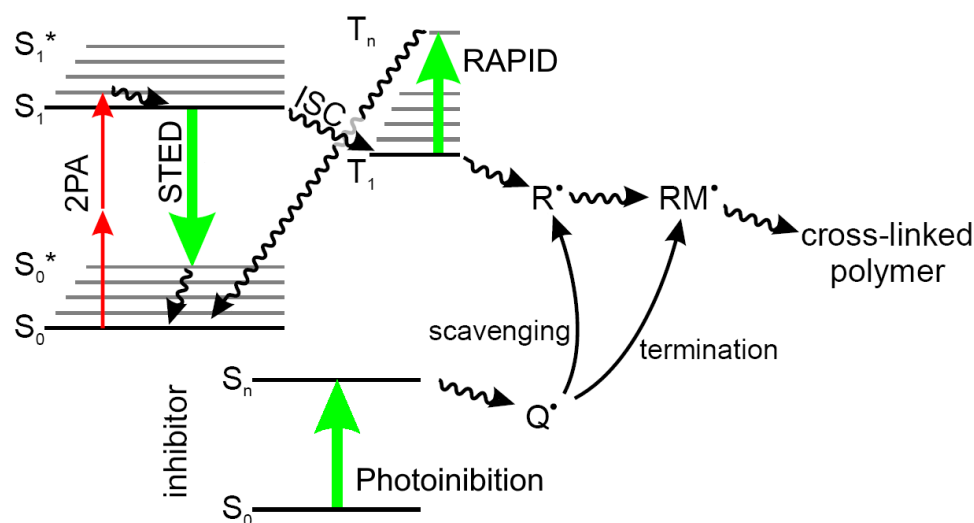
Figure 2.9: Deactivation pathways for super-resolution MPL methods. STED is based on the stimulated emission depletion of the S_1 excited state back to the ground state. RAPID is based on excitation from the T_1 to a higher order excited triplet state followed, for example, by a non-radiative decay. Photoinibition terminates the polymerization chain reaction. Adapted from [87].

2.2   Red Edge Effects

In this section, I will explain how REE result from inhomogeneous broadening and, in turn, from solute-solvent interactions. REE [104] are a wide range of effects where the static and dynamic properties of the emission and/or absorption spectra of a fluorophore[7], the solute, vary significantly as a function of the mechanical and polar properties of their surroundings, the solvent. These effects are essential to explain the observations in chapter 6.

In a typical photoresist, a photoinitiator molecule[8] is surrounded by acrylate monomers. If both are polar molecules, dipole-dipole interactions will be established among them, favouring a particular relative orientation in order to minimize their combined dipole. A closer alignment of the dipoles will result in a more stable, lower energy, state.

However, because the photoresist exists in a disordered state, e.g., due to thermal effects, a range of relative dipole orientations will co-exist, each with slightly different energies. These different solvation, or stabilization, energies, will modify the energies of the ground and excited states of each fluorophore. Thus, at the level of the ensemble of fluorophores, a distribution of energies is formed around the ground- or excited-state level energy, as seen in fig. 2.10 ($\Omega(W_{dd}^{g})$). This is called inhomogeneous broadening of the energy levels, since it affects different molecules differently. Oppositely, homogeneous broadening is the appearance of discrete energy levels due to vibration and affects all molecules in the ensemble equally. Inhomogeneous broadening causes, for example, the appearance of continuous, rather than discrete, absorption and emission spectra [104, 105].

The energy range of the distribution, i.e., its standard deviation, is mostly defined by the rigidity and dipole moment of the solvent and the dipole moment of the solute [105]. A high solvent rigidity, for example, might frustrate, i.e., impede, the rotation of a fluorophore into a lower energy state, resulting in a higher energy state than possible in a less rigid medium. On the other hand, an increase in the solvent polarity increases the strength of the dipole-dipole interaction, increasing the energy shift of fluorophores with aligned and misaligned dipoles.

Let us now consider the excitation of the ensemble, as in fig. 2.10. This is typically the case in experiments, where the excitation source affects a large set of molecules. Upon excitation, the energy distribution will be shifted up by the energy quanta of the photons. The fluorophore, however, changes in the transition. For example, it can rotate, e.g., through twisted intramolecular charge transfer, and its dipole moment can change significantly, both in magnitude and direction. Thus, in the instants after excitation, the molecule and its interaction with the surroundings have changed, but it has not reached a new equilibrium conformation. The new range of stabilization energies might even vary significantly from those at the ground state, significantly affecting the energy distribution of the ensemble ($\Omega(W_{dd}^{e})$ in fig. 2.10).

The first type of REE then ensues: broadening of the absorption spectrum at the red- and blue-edges of the absorption. Considering two samples with the same fluorophore, one with strong and one with weak inhomogeneous broadening, the energy distribution in the former will be wider than in the latter and therefore, it would be possible to excite the former sample with a larger range of wavelengths than in the latter. This is easy to observe by considering two diagrams similar to fig. 2.10, one with large and one with small standard deviations for the energy distributions of both the ground- and excited-state energy levels, respectively. There would be, for example, a range of longer wavelengths [9] that would excite the fluorophore in the former case while not exciting the same fluorophore in the latter. Experimentally, this translates, for example, into solvent-specific absorption spectra and can even manifest in the same solvent if it changes over time, e.g., by vitrification [105].

A second type of REE is intrinsically related with the one just presented: photoselection [106]. If one excites a sample with photons at the long, or short, wavelength limit of the absorption, only a small group of fluorophores in a very specific set of conditions, i.e., a subspecies, will be excited, see $h\nu_a^{edge}$ in fig. 2.10.

---

[7]REE can be observed through other mechanisms, e.g., phosphorescence, but these are not relevant for this thesis

[8]the MPL photoinitiators are typically fluorescent dyes, i.e., fluorophores. In this section, the latter term is preferred to stress the fluorescence nature of REE

[9]the longer wavelength range corresponds to $h\nu_a^{edge}$ in fig. 2.10
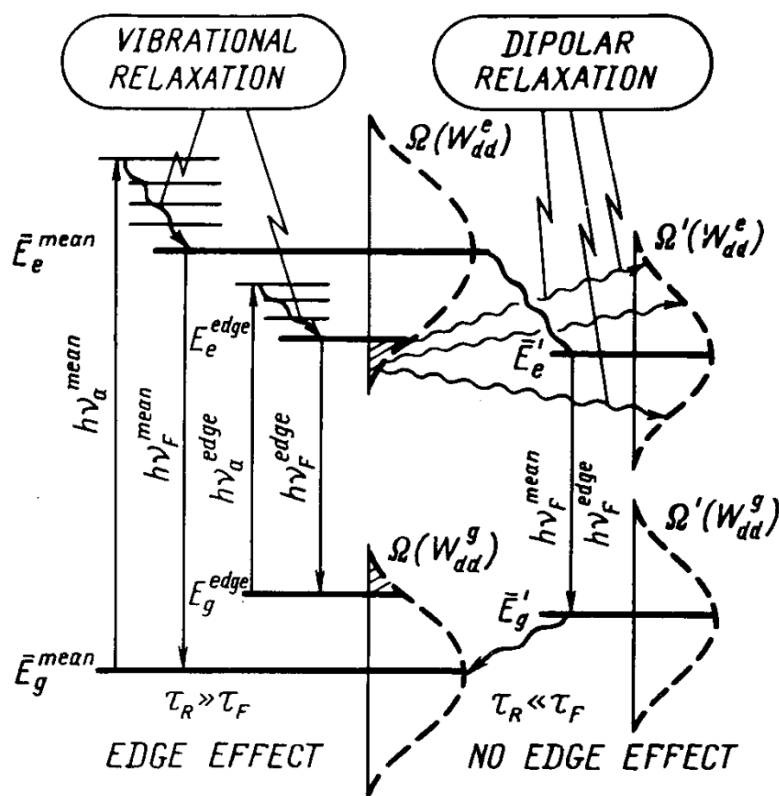
Figure 2.10: Energy diagram of the ground and first excited electronic states, accounting with homogeneous (i.e., vibrational, only shown for excited state) and inhomogeneous broadening of the energy levels. Blue and red-edge effects are particularly noticeable when the fluorescence timeconstant is much smaller than the dipolar (dielectric) relaxation. As shown on the right, dipolar relaxation corresponds to the temporal loss of photo-selection between different subspecies excited at the red-edge of the absorption. Reproduced with permission from [104].

The selectivity of the excitation is much higher at the edges of the spectrum since a larger overlap of the energetic states of different subspecies in the middle of the absorption spectra ($h\nu_a^{mean}$ in fig. 2.10) will lead to a broader excitation. Despite originating from the same molecular species, different subspecies are influenced by their local environment into having significantly different equilibria, e.g., by undergoing excited-state isomerization. The different equilibrium energies enable selective excitation of different subspecies.

While both ground and excited state energy distributions contribute to REE, one is typically dominant. For example, if a fluorophore has a much larger dipole moment in the excited-state than in the ground-state, the corresponding energy distribution will be wider and its contribution to REE more significant.

Let us now recover the picture of the fluorophore in a non-equilibrium state instantly after excitation. Over time, the dipolar relaxation will stabilize the system towards an equilibrium position, which corresponds to the equilibrium emission spectrum. If, however, fluorescence emission occurs significantly before complete relaxation, another REE effect is observed, the transient broadening of the emission spectrum [105, 107].

In this case, the energy distribution assumed immediately after excitation will still significantly influence the energy distribution of the ensemble at the time of the fluorescence emission, contributing to its widening and, consequently, to the broadening of the emission spectrum. The magnitude of this effect is proportional to the ratio τ_R/τ_F between relaxation and fluorescence time constants, and is particularly significant in rigid or viscous solvents and low temperatures, where the relaxation times are longer.

This broadening is a transient effect, thus providing an important tool to characterize the dynamics of the ensemble. Particularly, the relaxation of subspecies at the blue- and red-edge of the emission spectrum involve significantly different mechanisms, giving rise to many interesting phenomena such as the failure of energy transfer in an ensemble [108, 109] or optically induced cooling [104].

2.3   Current Induced Domain Wall Motion

MPL is the common denominator throughout this thesis. Yet, to appreciate the results from chapters 5 and 7, a basic understanding of some fundamental concepts of nanomagnetism is helpful. This section presents a brief overview of the necessary concepts based on [110]. For a more complete and in-depth analysis, see also [111–113].

2.3.1   Angular Momentum and Magnetism

Magnetism arises from the quantum mechanical properties of spin and orbital angular momentum. While the spin angular momentum is an intrinsic property of an elementary particle, the orbital angular momentum is defined by the orbit of an electron around an atom, and it is therefore defined by the electrons' surroundings and the forces it is subject to. Both spin and orbital angular momenta contribute to the appearance of a magnetic moment that defines the interaction with surrounding magnetic fields. The total magnetic moment μ of an atom is related to its total angular momentum $\mathbf{J}$, the sum of the spin and orbital angular momenta, through the gyromagnetic ratio γ and the Landé g-factor:

$$\mu = -|\gamma|\mathbf{J} = -g\frac{\mu_B}{\hbar}\mathbf{J}. \tag{2.13}$$

The Landé g-factor can then be thought of as a material constant describing the proportionality between the total angular momentum and the total magnetic moment, or their ratio, and it is seen to increase with material thickness.

The magnetic moments in a material can assume different types of magnetic ordering, such as ferromagnetism (e.g., parallel alignment), anti-ferromagnetism (e.g., antiparallel alignment), paramagnetism (disordered), etc. In particular, ferromagnetism leads to the effects observed in chapters 5 and 7 and will therefore be the focus of this section. Ferromagnetism is a material property and a type of magnetic ordering where all magnetic moments collectively point along the same direction. At the nanoscale, the ferromagnetic ordering is defined by a set of interactions, and their interplay, which will be reviewed over the following paragraphs. Each of these contribute significantly to the energetic landscape of the systems in chapters 5 and 7 and the effects observed therein.

Heisenberg Exchange

The Heisenberg exchange is a quantum mechanical interaction describing the coupling of magnetic moments through the coupling of electron spins:

$$E_{Heisenberg} = -2J_{ex}^{ij}\mathbf{S}^i \cdot \mathbf{S}^j, \tag{2.14}$$

where J_{ex}^{ij} is the exchange constant describing the coupling strength, and sign, between $\mathbf{S}^i$ and $\mathbf{S}^j$. Under its influence, the spins of neighboring electrons, tend to either have the same orientation, contributing to a ferromagnetic ordering, or opposite orientations, contributing to an antiferromagnetic ordering. The Heisenberg is both symmetric and isotropic.

Magnetic Anisotropy

Unlike Heisenberg exchange, the magnetic anisotropy describes the preferential alignment of the magnetization along a particular direction or axis. The most and least favorable axes, i.e., with lowest and highest energies, for the magnetization to align along are called easy and hard axis, respectively.
The magnetic anisotropy has two sources: magnetocrystalline anisotropy and shape anisotropy. Magnetocrystalline anisotropy appears due to relativistic spin-orbit coupling. The ordered disposition of atoms, as in a crystal, leads to a redistribution of orbitals, and their energies, due to orbital mixing. The coupling of spin angular momentum to such recombined orbitals will then lead to the appearance of axes, related to the crystal axes, along which it is energetically favorable for the magnetization to align.

As for shape anisotropy or demagnetization anisotropy, it arises from dipole-dipole (i.e., magnetostatic) interactions. These interactions act to align the magnetization in the direction, within the sample, that will minimize surface charges. It is, therefore, dependent on the shape of the sample.

Both anisotropy types have distinct bulk and surface components of different magnitude. In the thin film limit, i.e., for thicknesses in the nm-range, the surface effects become more significant due to an increase of the surface to volume ratio. In this context, the surface component of the magnetocrystalline anisotropy, also referred to as surface anisotropy [111, pp. 132–133], is typically the most relevant and the volume component is ignored. For the case of magnetic materials (Co/Ni) studied in chapter 5, the magnetocristalline anisotropy acts to align the magnetization perpendicularly to the sample surface, i.e., along the z direction in fig. 2.11. The energy contribution of the magnetocrystalline anisotropy with anisotropy constant K_{Cryst}^S is then given by

$$G_{Cryst}^S = K_{Cryst}^S sin^2(\theta),$$ (2.15)

for the geometry shown in fig. 2.11, i.e., a planar ribbon-like film with longer, or main, axis along x and thickness along z and with the θ describing the clockwise deviation from the z direction in the xz plane. This geometry is assumed throughout this section.
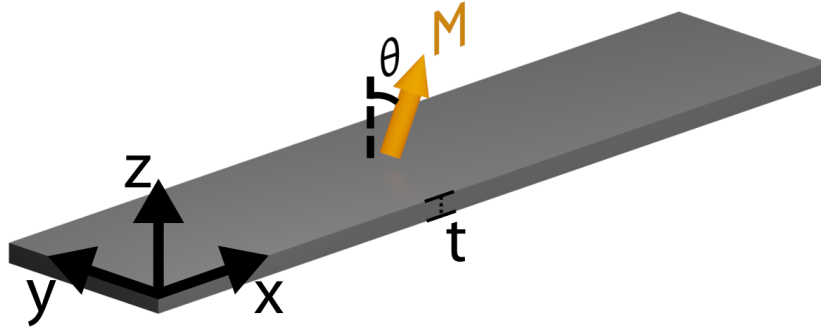
Figure 2.11: Reference frame utilized to model the magnetization of the thin ribbon. The main axis is along x, i.e., regarding dimensions $x \gg y \gg z$.

Similarly, the shape anisotropy energy contribution in this geometry is defined by its the volume component [110, p. 10]:

$$G_{Shape}^V = \frac{\mu_0}{2} M_s^2 cos^2(\theta).$$ (2.16)

As the shape anisotropy is related to a demagnetizing field, it is commonly associated with a negative anisotropy constant $K_{Shape}^V = -\frac{\mu_0}{2} M_s^2$ [110, p. 10, 111, pp. 132–133]. Unlike the magnetocrystalline component in eq. 2.15, the shape anisotropy energy component is minimized when the magnetization lies in the plane, along the main axis of the film. With both anisotropy components having competing effects, the effective anisotropy in multilayer stacks is seen to depend on the thickness of the ferromagnetic layer, t_F:

$$K_{eff} = K_{shape} + 2\frac{K_{cryst}}{t_F}.$$ (2.17)

A negative K_{eff} corresponds to an in-plane magnetization, driven by K_{shape}, while a positive K_{eff} corresponds to an out-of-plane magnetization driven by the K_{cryst}. For each combination of K_{shape} and K_{cryst}, there exists a critical thickness for the ferromagnetic layer, $t_c = \frac{|K_{shape}|}{2K_{cryst}}$ below which the effective anisotropy aligns with z, i.e., below which the film displays Perpendicular Magnetic Anisotropy (PMA). The anisotropy energies are much smaller than the Heisenberg exchange energy given by eq. 2.14.

Dzyaloshinskii–Moriya Interaction

The Dzyaloshinskii–Moriya interaction, on the other hand, is an anti-symmetrical exchange interaction typically resulting from spin-orbit coupling at magnetic interfaces with broken inversion symmetry. The energy term for two coupled spins of nearby electrons is given by:

$$E_{DMI} = \mathbf{D}_{12} \cdot (\mathbf{S}_1 \times \mathbf{S}_2), \tag{2.18}$$

where $\mathbf{D}_{12}$ is a constant vector describing the strength and direction of the DMI interaction. Unlike the Heisenberg exchange (eq. 2.14), the DMI is an indirect exchange interaction, i.e., the exchange between two neighboring spins in the magnetic material is mediated by a third atom of the material with spin-orbit coupling, as represented in fig. 2.12. The DMI vector $\mathbf{D}_{12}$ is perpendicular to the plane defined by the two coupled electrons and the ligand atom.

The DMI can be perceived as following. The interfacial symmetry breaking causes a non-vanishing orbital momentum to occur at the interface, perpendicular to the magnetization of the ferromagnetic layer. Under this momentum, the spin-orbit coupling will act to align the electrons spin perpendicularly to the magnetization, establishing a competing effect between the alignment of the spins along the magnetic or the orbital momentum. The energy is minimized when nearby spins are canted perpendicularly to each other, as noted in eq. 2.18, in such a way that their external product is antiparallel to $\mathbf{D}_{12}$. The direction of vector $\mathbf{D}_{12}$ determines the axis of rotation for the spin while its sign determines the direction of rotation: a negative (positive) $\mathbf{D}_{12}$ corresponds to a clockwise (anti-clockwise) rotation of the neighboring spins.
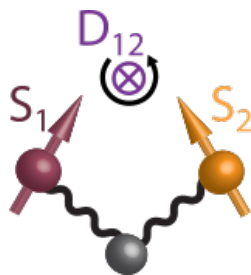
Figure 2.12: Dzyaloshinskii–Moriya interaction (DMI) is an anti-symmetrical exchange interaction that promotes the perpendicular orientation of neighboring spins. The DMI is an indirect exchange that is mediated by a third ligand atom of another species (in gray), e.g., a heavy metal like Pt, and therefore typically occurs at interfaces. DMI also defines a preferential chirality for the rotation of spins, which is established by whether the DMI vector $\mathbf{D}_{12}$ points into- or out-of-plane, as shown. Adapted with permission from [110].

Naturally, the magnetic ordering of a material saturates when all magnetic moments follow that specific ordering. For example, in a ferromagnet with a preferential collinear alignment, the saturation occurs when all magnetic moments are pointing in the same direction. In that case, the ferromagnetic material achieves its maximum magnetization, the saturation magnetization M_s. This is not typically the case because the thermal energy is sufficient to drive some magnetic disorder. Particularly, at the material-specific Curie temperature, the thermal energy is sufficient to promote a disordered paramagnetic phase in the material, with no net magnetization.

2.3.2   Domain Walls

Different regions of a ferromagnetic film might have magnetic moments pointing in opposite directions. Each spatially delimited region with the magnetization pointing in a given direction is called a magnetic domain. In the boundary between two domains, the magnetization rotates laterally from one magnetization direction to the other. This boundary magnetic texture is called a magnetic Domain Wall (DW). A DW is a chiral magnetic texture whose properties are defined by the magnetic interactions previously described, as well as any existing external factors, such as magnetic fields. The size of a DW, for example, is defined by a competition between the Heisenberg exchange interaction and effective anisotropy. The domain walls

are of great interest in nanomagnetism and spintronics [1, 114, 115], and they are relevant to understand the effects presented in chapter 5.

2.3.2.1 One Dimensional Model

In a nanowire, or a ribbon-shaped magnetic thin film, with small enough thickness t_F and width w, where the orientation of the magnetic moments can be considered constant along both width and thickness, the magnetization can be described as a 1D array of magnetic moments. In this case, a DW can be described by a time and position dependent distribution of the magnetization orientation. Let us consider the geometry described in fig. 2.13a: the wire is aligned along x; has PMA, i.e., the magnetization is oriented along $\pm z$ outside a DW; and θ defines the deviation of the orientation from z. Then, a DW is described by

$$\theta(x, t) = 2 \tan^{-1} \left[exp \left(\pm \frac{x - q(t)}{\Delta} \right) \right]. \tag{2.19}$$
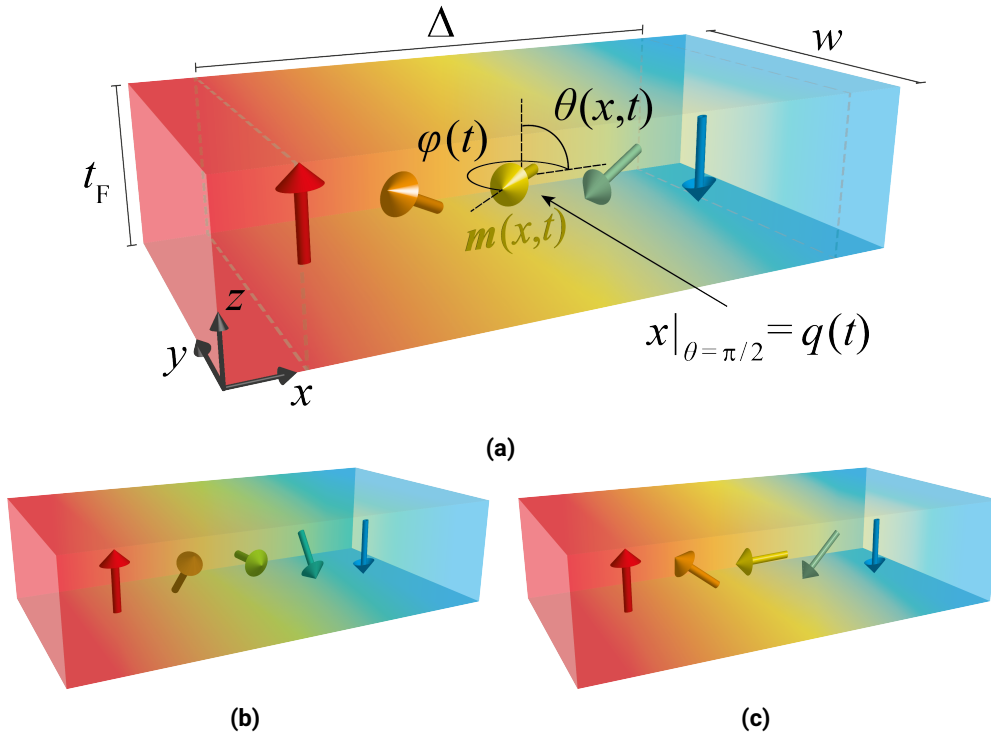
Figure 2.13: DW reference frame, DW describing parameters and DW types. Reproduced with permission from [110]. (a) A DW corresponds to the magnetization rotation between two anti-parallel states. It is described by the ribbon width w and thickness t_f and by the DW width parameter Δ, on the order of 10 nm, i.e., much smaller than the ribbon length. Being a local feature, the DW is modelled by a magnetization rotation around the DW center position q, which is defined by the coordinate x where the magnetization points along $\theta = \pi/2$. The DW motion can be evaluated as the motion of its center position, i.e., q(t). (b) Bloch DW type, described by $\phi = 90; 270$ ° at the point q(t). (c) Néel DW type, described by $\phi = 0; 180$ ° at the point q(t).

As seen from the DW profile in eq. 2.19, the magnetic moment orientation only differs from the anisotropy defined equilibrium (along $\pm z$ or $\theta = 0; \pi$) in a vicinity defined by the domain wall width, Δ, about the position of the center of the DW, q(t). The latter is defined the position along x where the magnetization lies in plane, i.e., $\theta = \frac{\pi}{2}$, as stated by the convention $x|_{\theta=\frac{\pi}{2}}$ shown in fig. 2.13a.
Furthermore, with the magnetization rotation occurring along θ, as described in eq. 2.19, the magnetization orientation angle ϕ is considered fixed throughout the DW. The variables $q(t)$ and ϕ are commonly used for describing the domain wall dynamics, referred to as the $q - \phi$ model [116].

For the ± sign in eq. 2.19 a convention is adopted, as in [110], where the upper sign relates to the case of an ↑↓ DW, as seen in fig. 2.13a, while for the lower sign relates to the case of a ↓↑ DW, i.e., rotating the orientations in fig. 2.13a by π.

The geometry defined in fig. 2.13a will be considered for the remainder of this section. The cartesian components of the magnetization are obtained from its spherical coordinates by:

$$\mathbf{m} = m \begin{bmatrix} \sin(\theta)\cos(\phi) \\ \sin(\theta)\sin(\phi) \\ \cos(\theta) \end{bmatrix}. \tag{2.20}$$

The rotation of the magnetization in a domain wall can occur in two different planes, xz or yz. This corresponds to the magnetization at the DW center, q(t), pointing along x, i.e., $\phi = 0; \pi$, or perpendicular to it, i.e., $\phi = \pi/2; 3\pi/2$, respectively. These two types of DWs are referred to as Néel and Bloch DWs, respectively, and are represented in figs. 2.13b and 2.13c.

The appearance of one type over the other is defined by the equilibrium resulting from the interplay of the interactions reviewed in section 2.3.1 and their corresponding DW energy terms, reviewed in section 2.3.2.2. Since each type of DW reflects a different energetic equilibrium with different predominant interactions, their dynamics can differ, as mentioned in section 2.3.3.

Additionally, for each DW type, the magnetization can rotate either clockwise or anti-clockwise, e.g., corresponding to $\phi = 0$ and $\phi = \pi$ (as in fig. 2.13c) for a Néel DW, respectively.

It is important to note that the 1D model presented here is not relied on to provide a quantitative description of the systems in chapter 5, but rather to provide insight into key physical phenomena underlying the experimental observations therein. For a quantitative description of the observations in chapter 5, see the 3D model in section 5.F.

2.3.2.2   Domain Wall Energy Terms

The properties of a DW, such as DW type and width, are defined by the energetic balance of the interactions presented in section 2.3.1. The influence of each interaction on a complex magnetic texture as a DW is, so far, still unclear. Furthermore, these interactions must be accounted for over the complete multi-layer material stack. For each interaction presented in section 2.3.1, the corresponding energy density term for a DW is presented in this section, along with the interpretation of its influence on the equilibrium properties of the DW. A more complete derivation can be found in [110].

The energy components considered are the intra-layer exchange, the anisotropy energies, and the DMI.

In this section I will focus on a system close to the experimental ones in chapter 5: a stack with a heavy-metal underlayer with spin-orbit-coupling (Pt) topped by ferromagnetic multi-layers (Co and Ni). In the multi-layer, the magnetic moments of the individual Co and Ni layers couple ferromagnetically and the multi-layer can be treated as a single layer with a total net magnetic moment given by the sum of the parts. In this case, the PMA of the stack is also improved.

Let us consider a ferromagnetic layer with thickness t and temperature dependent saturation magnetization $M_S^i(T)$. Its net magnetic moment given by:

$$\mathbf{m} = tM_S(T)\hat{\mathbf{M}}, \tag{2.21}$$

where the notation $\hat{\mathbf{M}}$ designates the unitary vector with the same direction as $\mathbf{M}$.

Within the gradual rotation of the magnetization in a DW, the intra-layer (Heisenberg) exchange energy density will act to favor the parallel alignment of neighboring spins, acting to increase the domain wall width such that $\Delta \to \infty$. The intra-layer exchange energy density ω_A^i of the ferromagnetic layer is then

$$\omega_A = A_{ex}t(\nabla\hat{\mathbf{m}})^2 = \frac{A_{ex}t}{\Delta^2}sin^2\theta. \tag{2.22}$$

which is normalized to the layer thickness and where A_{ex} represents the Heisenberg exchange constant.

Regarding the magnetic anisotropy energies, the ferromagnetic layers used experimentally (chapter 5) favor PMA, i.e., $K_{eff} > 0$. As the magnetic moments in a DW have to go through an in-plane configuration while rotating between $\pm z$ orientations, however, the magnetic anisotropy will act to minimize the DW width so as to minimize the number of magnetic moments pointing in-plane. The DW width is then inversely dependent on K_{eff}. The effective anisotropy energy density is given by

$$\omega_{K_{eff}} = tK_{eff}sin^2\theta. \tag{2.23}$$

The shape anisotropy promotes the magnetization alignment along the y direction, favoring the appearance of a Bloch DW. If only the exchange and anisotropy components were present, the shape anisotropy would be more significant and the DWs would be of Bloch type.

In the systems studied in chapter 5, however, the Dzyaloshinskii–Moriya interaction (DMI), established at the interface between the Pt and the ferromagnetic layers, also significantly contributes to the DW properties.

In section 2.3.2.1, it was noted how a domain wall can rotate with both chiralities. In a system with DMI, however, the rotation of the magnetization with a given chirality is more energetically favorable than with the opposite, as noted from eq. 2.18, since $(\mathbf{e_x} \times \mathbf{e_y}) = -(\mathbf{e_y} \times \mathbf{e_x})$. Therefore, in the presence of DMI, DWs of opposite chiralities have their degeneracy lifted and the DWs with the same chirality as the DMI-induced rotation, defined by the DMI vector $\mathbf{D}$, are stabilized. Furthermore, it results from eq. 2.18 that the same rotation chirality, i.e., clockwise or anti-clockwise, is favored for DWs of opposite configuration, i.e., ↑↓ and ↓↑, since the $\mathbf{D}$ vector is the same in both cases, as shown in fig. 2.14.
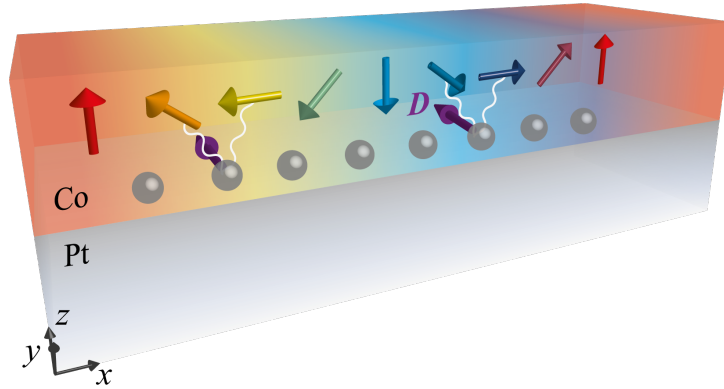
Figure 2.14: In the presence of DMI, two sequential Néel DWs of opposite types will have the same chirality. This is due to the preferential chirality for the rotation of magnetization established by DMI. This occurs because the DMI breaks the chiral symmetry of Néel DWs, energetically favoring one DW chirality over the other. Reproduced with permission from [110].

At a DW, the DMI interaction energy density term is given by

$$\omega_{DMI} = \mathbf{D}_x \cdot \left(\hat{\mathbf{m}} \times \frac{\partial\hat{\mathbf{m}}}{\partial x} \right), \tag{2.24}$$

with the DMI vector $\mathbf{D}_x$ pointing along $\pm y$. This expression is obtained from the general form description of the DMI interaction [117, 118], by taking into account that $\mathbf{m}_y = 0$ and the magnetization is constant along y and z.

In this case, the energy is minimized when $\left(\hat{\mathbf{m}} \times \frac{\partial\hat{\mathbf{m}}}{\partial x} \right)$ is antiparallel to $\mathbf{D}$, which can only be fulfilled in the case of a Néel DW, i.e., when $\phi = 0; \pi$. Thus, the DMI not only stabilizes the DW rotation chirality, it also stabilizes Néel DW type over the Bloch DW type. These aspects have been observed experimentally [119–121] and significantly impact the DW motion in the presence of DMI, as noticed in section 2.3.3.

Having all the energy terms defined, the total energy of the DW is given by integrating the sum of the different energy density components over the whole 1D system:

$$\sigma_{DW} = \int_{-\infty}^{\infty} \omega_{DW}(x)dx, \tag{2.25}$$

from where it is possible to show that the (static) equilibrium DW width, i.e., without any external factors, is given by [110]

$$\Delta = \sqrt{\frac{A_{ex}}{K_{eff}}}, \tag{2.26}$$

with A_{ex} the Heisenberg exchange constant and K_{eff} the effective anisotropy constant.

2.3.3   Domain Walls Dynamics

Modeling and understanding DW motion are essential to interpret the results in chapter 5. To do so, one must consider the energetic balance reviewed on section 2.3.2.2, as well as the different external mechanisms for driving DW motion.

The motion of the magnetization in the presence of a magnetic field **H** is described by the Landau-Lifshitz-Gibert (LLG) equation:

$$\dot{\mathbf{m}} = -\gamma \mathbf{m} \times \mathbf{H} + \frac{\alpha}{m} \mathbf{m} \times \dot{\mathbf{m}}, \tag{2.27}$$

where $\dot{\mathbf{m}}$ denotes the time derivate of **m**, i.e., $\frac{d\mathbf{m}}{dt}$.

Each of the terms in eq. 2.27 describes a torque arising from a particular interaction that influences the magnetization dynamics. The first torque describes the precession of the magnetic moment around the direction of the field **H**, with γ the gyromagnetic ratio defining the frequency of the precession. The second torque describes the damping of the magnetic moment, with damping strength defined by the Gilbert damping parameter α. The latter term is related to the dissipation of energy and is responsible for the progressive alignment of the magnetization with **H** over time.

The different influence of both terms of eq. 2.27 on the magnetization gives rise to the expressions field-like torque and damping-/anti-damping-like torque as being a torque that causes the magnetization to precess or one that modulates the amplitude of a precession, respectively.

The effect of each DW energy term ω (see section 2.3.2.2) in the DW dynamics can be accounted for in eq. 2.27 by adding, for each term, an effective field given by:

$$\begin{aligned}
\mathbf{H}_{eff} &= -\nabla\omega \\
&= -\frac{1}{m}\frac{\partial\omega}{\partial\theta}\hat{\theta} - \frac{1}{m\sin(\theta)}\frac{\partial\omega}{\partial\phi}\hat{\phi}.
\end{aligned} \tag{2.28}$$

In eq. 2.28 the magnetization magnitude is assumed constant ($\dot{m} = 0$) and therefore any term contributing to $\dot{\mathbf{m}}$ in eq. 2.27 can be discarded. The **H** term in eq. 2.27 is then substituted by the term $\mathbf{H}_{eff}$ accounting for the sum of all the energy driven effective fields calculated with eq. 2.28.

The DW equations of motion can then be obtained from solving the LLG equation. It is also common to do so through the Rayleigh-Lagrange equations, as in [110].

Let us now consider the different mechanisms that can be used to drive DW motion.

Previously, it was noted that eq. 2.19 describes a DW as an angular distribution of magnetic moments (i.e., a magnetic texture) around a position in a given linear axis. By taking its derivative, it results

$$\dot{\theta} = \mp\frac{1}{\Delta}\sin(\theta)\dot{q}, \tag{2.29}$$

which relates the linear velocity of a DW to the angular velocity of its moments. In other words, for a DW to move with a linear velocity $\dot{q}$, its magnetic moments have to be made to rotate at a corresponding angular velocity $\dot{\theta}$. Following the remarks in section 2.3.2.1, any DW motion steady state is considered to have $\dot{\phi} = 0; \phi = constant$ and $\dot{q} = constant$.

It also follows from eq. 2.29 that the rotation of magnetic moments only occurs locally, i.e., within the DW, with distant magnetic moments remaining still, as specified by the $\sin(\theta)$ term.

Therefore, to move a DW linearly along a wire, a mechanism must be provided to rotate the magnetic

moments within a DW. These mechanisms are divided into field-driven DW motion and current-driven DW motion. Within current-driven DW motion, the motion can be induced by either Spin-Transfer Torque (STT) and Spin-Orbit Torque (SOT).

As field-driven DW motion and Spin-Transfer Torque (STT)-induced current-driven DW motion do not play significant roles in the experiments in this thesis, particularly those in chapter 5, they are considered out of scope and are not further described.

Spin-Orbit Torque Current Induced DW Motion

Spin-orbit torque is a torque induced by a pure spin-current that results from spin-orbit coupling, e.g., current generated through the SHE. It is the effect used to drive DW motion in chapter 5.

The SHE describes the separation of opposite spins and their accumulation at opposite surfaces of a material, akin to the separation of opposite charges in the Hall effect. The SHE has an extrinsic component, due to spin-dependent scattering of conduction electrons at impurities, and an intrinsic component, due to spin-orbit coupling induced band splitting.

In a material stack, the SHE induced spin separation can be used to create a spin current in interfacing layers, as seen in fig. 2.15a. As they move into other layers, the polarized spins apply a torque on the local magnetic moments, the spin-orbit torque (fig. 2.15a).

The SHE induced spin current **s** is given by

$$\mathbf{s} = \frac{\hbar \theta_{SH}}{2e} (\mathbf{j} \times \hat{\mathbf{z}}) \tag{2.30}$$

where **j** is the **non** spin-polarised current going through the SHE material and **z** is the direction perpendicular to the interface surface and also the direction the polarized current flows in. θ_{SH} is the spin hall angle, given the ratio of the spin polarized current to the current that generates it, and describes the strength of the SHE on a material. In chapter 5, the SHE is present in the Pt underlayer.

In eq. 2.30, the spin polarization is perpendicular to both the direction of current **j** and the direction of its flow ($\hat{\mathbf{z}}$). In the 1D model, assuming a current **j** along x, the spin current is polarized along **y**. This would give rise to an effective field $\mathbf{H}_{SH}$ in the ferromagnetic layer given by

$$\begin{aligned} \mathbf{H}_{SH} &= \frac{1}{m} (\hat{\mathbf{m}} \times \mathbf{s}) \\ &= H_{SH} \left(\cos \phi \hat{\theta} + \cos \theta \sin \phi \hat{\phi} \right), \end{aligned} \tag{2.31}$$

with $H_{SH} = \frac{\hbar \theta_{SH} j}{2em}$. Notice that $\mathbf{H}_{SH}$ is zero for a Bloch DW, since $\hat{\mathbf{m}}$ at $q(t)$ is parallel to **s**. $\mathbf{H}_{SH}$ can be accounted for in the LLG equation through the torque

$$\begin{aligned} \tau_{SH} &= -\gamma \hat{\mathbf{m}} \times \mathbf{H}_{SH} \\ &= -\gamma H_{SH} \left(\cos \theta \sin \phi \hat{\theta} + \cos \phi \hat{\phi} \right) \end{aligned} \tag{2.32}$$

For a Néel DW, this torque causes the magnetic moments to rotate away from $\phi = 0; \pi$, as shown in fig. 2.15b. While this does not result in DW motion, the appearance of a magnetization component along y leads to the appearance of a new term in the DMI energy (eq. 2.24), given by [117, 118]:

$$\omega_{DMI} = \mathbf{D}_y \left(\hat{\mathbf{m}}_\mathbf{y} \times \frac{\delta \hat{\mathbf{m}}_\mathbf{z}}{\delta x} \right) \tag{2.33}$$

with $\mathbf{D}_y$ pointing along x. In other words, the DMI energy of the DW is no longer at equilibrium, and a $\mathbf{H}_{DMI}$ field component appears along x in order to minimize it (see fig. 2.15b). Accounting with both DMI components (eq. 2.33 and eq. 2.24), the total $\mathbf{H}_{DMI}$ field is [118]:

$$\mathbf{H}_{DMI} = -\frac{2D}{\mu_0 M_s} \left[\frac{\partial m_z}{\partial x} \hat{\mathbf{x}} - \frac{\partial m_x}{\partial x} \hat{\mathbf{z}} \right]. \tag{2.34}$$

This field will give rise to the following torque:

$$\tau_{DMI} = -\gamma m_y \hat{\mathbf{y}} \times \mathbf{H}_{DMI}, \qquad (2.35)$$

which points along $\hat{\theta}$. Having the same chirality along the whole DW, this torque will drive the motion of the DW, as shown in figs. 2.15b and 2.15c. It is important to note that the component $m_y\hat{\mathbf{y}}$ results from the SHE torque given by eq. 2.32, i.e., this driving mechanism depends both on SHE and DMI, and therefore it is only present while a non-polarized spin current flows through the Pt underlayer, giving rise to the spin current.

This DW motion mechanism is represented in fig. 2.15 and summarized as follows: First, the SHE will create a spin-polarized current that flows into the ferromagnetic layer (fig. 2.15a). Second, within the ferromagnetic layer the spins will apply a torque that will cant the magnetic moments away from $\phi = 0; \pi$ (fig. 2.15a). Third, an effective DMI field along x will respond to the appearance of a magnetization component along y by rotating the magnetic moments along $\hat{\theta}$ (fig. 2.15b), thus driving DW motion (fig. 2.15c).
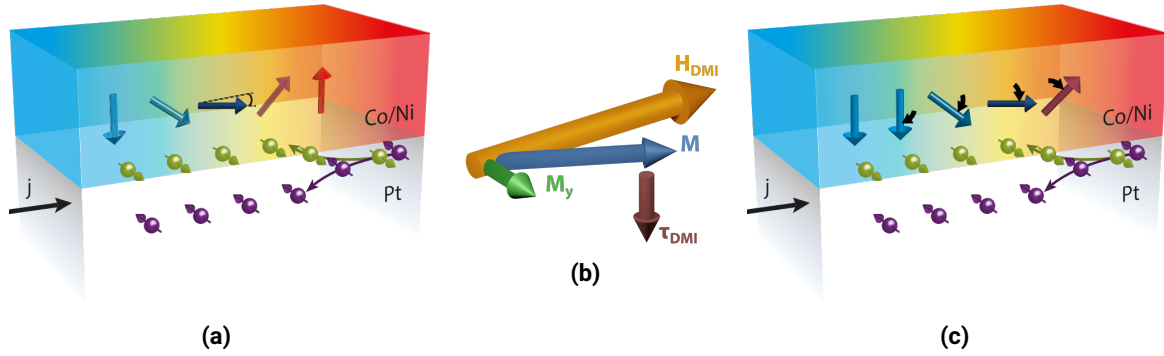
Figure 2.15: Current-induced spin-orbit torque driven DW motion. (a) Current flowing through a heavy metal underlayer such as Pt gives rise to a spin-polarized current at the interface with the ferromagnetic film due to the spin Hall effect. By propagating into the ferromagnetic layer, the SHE-induced spin polarized current will cant the Néel DW magnetization towards $\pm y$. Adapted with permission from [110]. (b) With the magnetization now having a component along $\pm y$, the DMI field component along x will give rise to a torque along θ (see eq. 2.35) that will rotate the moments in the DW. (c) The coherent rotation of the magnetic moments throughout all of the DW drives its motion along $\pm x$ and, due to the DMI, the motion occurs in the same direction for both DW configurations (see fig. 2.14), which is the direction of the current flow. Adapted with permission from [110].

Finally, it can be easily noticed that the application of an external field H_x while driving a DW through this method will add to or subtract from the DMI field, modulating the DW velocity [121].

2.4 3D Curvilinear Ferromagnetism

As mentioned in section 2.3.2.1, the 1D model covered so far is unsuited for describing the intricate behaviors in complex 3D geometries as those allowed by MPL. This became increasingly clear in the light of the latest developments in the field of 3D nano-magnetism [122], discussed in section 2.5. To overcome such limitations, the topic of 3D curvilinear ferromagnetism has been actively and extensively modelled in recent years [2, 6, 7, 123–125]. Here, I will briefly summarize the results therein which are of greatest relevance to this thesis.

The 3D modelling of a nanowire or a ribbon in the context of 3D curvilinear ferromagnetism does not relate to considering a higher magnetic dimensionality, i.e., specifically modelling the magnetization along x, y, z in planar nanowires or ribbons, but rather to considering the same magnetic dimensionality [10] laid out over a 3D space by geometrical transformations such as curvature and torsion. In this context, the interactions affecting the magnetic moments are still the same and described by the same relations as those in section 2.3.1, but they are driven by geometry to manifest differently.

To see how, let us consider a ferromagnetic system with energy defined by the exchange, magnetocristalline anisotropy, magnetostatic and DMI interactions:

$$E = E_{exchange} + E_{anisotropy} + E_{magnetostatic} + E_{DMI}. \tag{2.36}$$

As seen in section 2.3.1, the magnetostatic interaction can be divided into a short-range component, responsible for the shape anisotropy and accounted for in the effective anisotropy term, and a long-range component that couples spins over longer distances. The latter term is more relevant in closed 3D surfaces such as shells [7, 125] while being usually neglectable for nanowires and ribbons [2, 7].

In order to account for the 3D geometry of the magnetic structures, 1D wires are described by their 3D center curve $\gamma(s)$ as a function of s, the position along the curve. s is defined in the range $[0; l]$ with l being the wire length. Equivalently, 2D surfaces such as ribbons are described by a cross sectional surface swept through 3D space by a center curve $\gamma(s)$, defined as in the 1D case. The orientation of the cross section in the plane perpendicular to $\gamma(s)$ is defined by the angle $\alpha(s)$, as shown in fig. 2.16 [2].
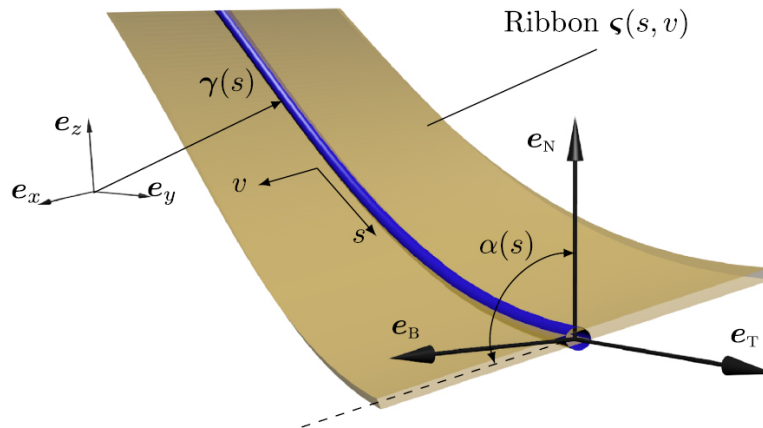
Figure 2.16: Description of 3D ribbon geometry using a center curve $\gamma(s)$ and an angle $\alpha(s)$. A local reference frame is defined in terms of the tangent $\mathbf{e}_T$, normal $\mathbf{e}_N$ and bi-normal $\mathbf{e}_B$ vectors. Coordinates s and v are used on the ribbon surface. Unit vectors $\mathbf{e}_x, \mathbf{e}_y, \mathbf{e}_z$ describe the laboratory reference frame. Reproduced with permission from [2].

The effective anisotropy defines the preferential alignment directions for the magnetization. Such preferential alignment is, however, relative to the sample orientation and follows it as it changes, i.e., the effective anisotropy follows the sample geometry.

For general 3D sample geometries, this means that the anisotropy is no longer constant under translation

---

[10] i.e., the modelling a nanowire as a 1D array of magnetic moments and a ribbon as a 2D surface

in the cartesian reference frame. In order to recover the translation invariance of the effective anisotropy, a local curvilinear reference frame is considered that follows the sample geometry, with the magnetization easy axis along one of the reference axis [7, 126, 127]. This curvilinear reference frame is based Tangential-Normal-Binormal (TNB) frame [128], constructed as

$$\mathbf{e}_T = \gamma' \qquad\qquad \mathbf{e}_N = \frac{\mathbf{e}'_T}{|\mathbf{e}'_T|} \qquad\qquad \mathbf{e}_B = \mathbf{e}_T \times \mathbf{e}_N, \qquad (2.37)$$

with $\mathbf{e}_T$ corresponding to the unitary axis along the direction tangent to γ and γ' corresponding to the partial derivative with regard to s, $\frac{\partial \gamma}{\partial s}$. This reference frame corresponds, for example, to the $\mathbf{e}_T, \mathbf{e}_N, \mathbf{e}_B$ frame in fig. 2.16.

By considering this curvilinear reference frame, the anisotropy influence to align the magnetization relative to the 3D curvilinear geometry is accounted for. The exchange interaction, however, while being isotropic in the cartesian reference frame, unfolds into three different components of different symmetries in the local reference frame:

$$E^{ex} = (m_\alpha \mathbf{e}_\alpha)'(m_\beta \mathbf{e}_\beta)' = E^{ex}_0 + E^{ex}_A + E^{ex}_D \qquad (2.38)$$
$$E^{ex}_0 = A m'_\alpha m'_\alpha$$
$$E^{ex}_A = K^{ex}_{\alpha\beta} m_\alpha m_\beta$$
$$E^{ex}_D = D^{ex}_{\alpha\beta}(m_\alpha m'_\beta - m'_\alpha m_\beta).$$

where α and β correspond to components in the curvilinear frame, i.e., either T, N or B as defined by the TNB frame.

While the term E^{ex}_0 in eq. 2.38 is the common isotropic exchange, equivalent to the exchange in structures with 1D geometries (see eq. 2.14), the terms E^{ex}_A and E^{ex}_D represent two emergent contributions to the anisotropy and DMI, respectively, that are induced by geometry. Particularly, these contributions are determined by the geometric parameters of curvature (κ) and torsion (τ) [7], as defined by the Frenet equations [128]. Unlike their intrinsic counterparts, these emergent contributions to the anisotropy and DMI are solely controlled by the sample geometry and therefore can be manipulated extrinsically to the material properties.

Being defined by geometry, the terms in eq. 2.38 differ significantly for different sample geometries. For the simplest case of a 1D nanowire, the tensors $K^{ex}_{\alpha\beta}$ and $D^{ex}_{\alpha\beta}$ are given by

$$K^{ex}_{\alpha\beta} = \begin{vmatrix} 0 & \kappa & 0 \\ -\kappa & 0 & \tau \\ 0 & \tau & 0 \end{vmatrix} \qquad (2.39)$$

and

$$D^{ex}_{\alpha\beta} = \begin{vmatrix} \kappa^2 & 0 & -\kappa\tau \\ 0 & \kappa^2 + \tau^2 & 0 \\ -\kappa\tau & 0 & \kappa^2 \end{vmatrix} \qquad (2.40)$$

These tensors can be generalized to a mesoscale DMI tensor, including the intrinsic and extrinsic DMI components, as well as a total anisotropy tensor, including the intrinsic and extrinsic anisotropy components [7]. Along with the intrinsic exchange energy, these provide a complete description of the exchange energy of a 1D nanowire with 3D geometry. For the case of a 2D magnetic ribbon, similar to those in chapter 5, the total energy of the ribbon is defined by [2, 7]

$$E_{rib} = hw \int \left(E^{Exchange}_{rib} + E^{Anisotropy}_{rib} + E^{DMI}_{rib} \right) ds. \qquad (2.41)$$

with h and w being the ribbon thickness and width.

The exchange energy term is:

$$E^{ex}_{rib} = A(\Theta - \Gamma_1)^2 + A\left[\sin\Theta(\Phi' - \Omega_1) - \cos\Theta \frac{\partial\Gamma_1}{\partial\Phi} \right]^2 + A\Gamma_2^2 + A\cos^2\Theta\left(\frac{\partial\Gamma_2}{\partial\Phi} \right), \qquad (2.42)$$

where Θ and Φ define the deviation of the magnetization orientation from the binormal and tangential directions, respectively. Parameters Ω, Γ_1 and Γ_2 are defined:

$$\Omega = -\kappa \cos \alpha \mathbf{e}_T \tag{2.43}$$

$$\Gamma_1 = -\kappa \sin \alpha \cos \Phi + (\alpha' + \tau) \sin \Phi \tag{2.44}$$

$$\Gamma_2 = (\alpha' + \tau) \cos \Phi \tag{2.45}$$

The effective anisotropy energy term is:

$$E_{rib}^{ex} = -K_{eff}^1 \sin^2 \Theta \cos^2 \Phi + K_{eff}^3 \cos^2 \Phi \tag{2.46}$$

$$K_{eff}^1 = K_1^{mc} + 2\pi M_s^2 N_2 - A(\alpha') \tag{2.47}$$

$$K_2 = K_3^{mc} + 2\pi M_s^2 - 4\pi M_s^2 N_2 \tag{2.48}$$

$$N_2 = \frac{h}{\pi w} \ln \frac{w}{h} + \frac{3h}{2\pi w}, \tag{2.49}$$

with K_1^{mc} and K_3^{mc} being the magnetocristalline anisotropy

By considering the 3D displacement of 1D and 2D magnetic structures, the intrinsic magnetic interactions are seen to give rise to additional, geometry-driven, components to the anisotropy and DMI, providing a new degree of freedom for tuning the magnetic properties of a system. It is important to note that the anisotropy is the enabler for such geometrical effects, since it is the only interaction that causes the magnetization to follow the geometry [7], as shown in fig. 2.17a. As the magnetization is made to follow the geometry in a local curvilinear frame, however, the exchange interaction leads to the emergent anisotropy and DMI components.

Under different geometries, such as shells, further emergent phenomena is seen to appear due to the magnetostatic interactions [125, 129].
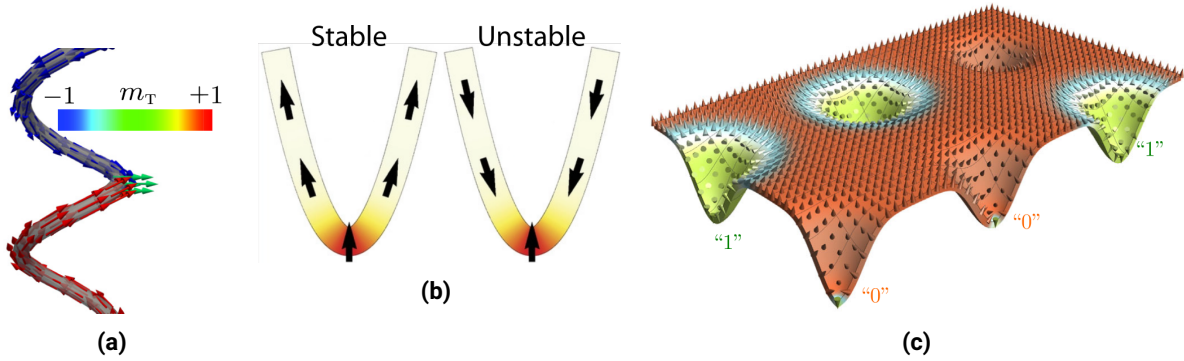
Figure 2.17: Curvilinear ferromagnetism in complex geometries and effects resulting thereof. (a) The magnetic anisotropy influences the magnetization to follow the geometry. Reproduced with permission from [130].
For non-trivial geometries and magnetic textures, e.g., DWs, the additional influence to the geometry leads to novel effects such as non-degenerate DWs, i.e., DW chiral symmetry breaking with stabilization of a geometry-defined DW chirality as in (b). Reproduced with permission from [131]. (c) 3D Shells are also significantly influenced by magnetostatics which can contribute to the stabilization of particularly relevant magnetic textures such as skyrmions. Reproduced with permission from [3].

These geometry-induced components of the magnetic interactions have important practical consequences, both for static and dynamic effects. In magnetostatics, the geometry driven energy components are able to stabilize complex magnetic structures such as skyrmions [3] as well as to break the chiral symmetry of a magnetic system, e.g., by lifting the degeneracy between oppositely magnetized DWs [131], as shown in figs. 2.17b and 2.17c. Regarding dynamical effects, the geometry-related emergent energy components are able to induce and stop DW motion without an external driving source, with DWs of opposite chiralities being driven in opposite directions [122, 132]. Furthermore, it possible to use curvilinear geometries to induce asymmetries in the dispersion relation of spin waves [133, 134]. Geometry induced magneto-dynamic effects will be further discussed in section 2.5.

2.5   3D Micro- and Nano-Magnetic and Electronic Devices

A few years into the exploration of 3D nanomagnetism [4][11], we are still grasping to understand the full potential of the field [5, 129, 135]. Thus my opening adaption of Feynmans' remark: With the emergent artificial control over a new dimension in electronics and magnetism (among other developments) there is, still, plenty of space at the bottom.

Having briefly discussed the basics of 3D curvilinear ferromagnetism in section 2.4, in this section I will review the state-of-the-art of 3D magnetic and electronic devices at the micro- and nano-scale and present my perspective on it, which motivates the experimental work developed through the remainder of this thesis.

The motivation for 3D nanomagnetism is that lower dimensional magnetic systems, such as 1D nanowires or 2D nanoribbons, when oriented along 3D geometries, will leverage the hallmark phenomena of planar nanomagnetism while opening a widely unexplored parameter space, one expected to lead to a large plethora of novel effects with significant practical implications [5].

Experimentally fulfilling such potential, however, involves satisfying demanding requirements on 4 critical aspects: 3D fabrication, material properties, characterization and theoretical modeling, with each aspect often requiring state-of-the-art techniques in its topic. This has often involved, and continues to involve, a concerted effort from groups with different backgrounds in the 3D nanomagnetism community [5, 122, 136, 137]

Despite such complexity, important progress has been made in recent years. On the theoretical side, a framework for modeling of 3D nanomagnetic systems has been established which shows, as introduced in section 2.4, that the geometric and magnetic properties are closely coupled [2, 6, 7, 123, 126, 127, 129, 132]. On the experimental side, significant results have been achieved which include, but are not limited to, 3D field-driven DW motion [22], 3D DW automotion [122], geometry-induced chiral symmetry breaking in magnetic materials [131], asymmetric spin-wave propagation [133], topological magnetic textures in the induction-field **B** [137], improved DW velocities under STT [138], artificial spin-ice [139] and novel magnetoresistive response components [54], showcasing significant progress. Some of these developments are represented in fig. 2.18

Yet, the experimental realization of freeform 3D magnetic systems is still greatly limited [5, 7, 123]. Following several decades of developments focused on planar systems, particular difficulties arise in the fabrication and characterization of 3D magnetic geometries. The adaptation of existing techniques to 3D and the development of new, intrinsically 3D, methods for fabrication and characterization is a challenging and time-consuming endeavour that is still recent and ongoing. For example, when adapting planar technologies to 3D through 3D micromanipulation of the sample [22], it is important that complex automated control mechanisms are set in place to properly reflect the 3D nature of the process and avoid time-consuming and less reliable step-wise manual processes.

As these structures move towards application, it is also important in many cases to consider their integration into magneto-electronic[12] devices[13], which further increases the complexity of the fabrication process.

In the following, I will focus on the fabrication and material properties within the context of magneto-electronic devices, which are the most relevant aspects in the context of this thesis, while only briefly reviewing the characterization methods. I will consider the integration of 3D magnetic structures into electronic devices as one significant aspect of the fabrication.

2.5.1   Fabrication of 3D Nano- and Micro-Magneto-Electronic Devices

The fabrication of a 3D nano- or micro-magneto-electronic device is composed of 3 stages, which might overlap:

---

[11]In this thesis I will consider 3D nanomagnetism and 3D curvilinear (ferro)magnetism to be equivalent and use both interchangeably

[12]I use the term magneto-electronics as an umbrella term for devices combining magnetic and electronic behaviors, thus including spintronics, orbitronics, magnonics, caloritronics, etc.

[13]or magneto-optical devices, but the integration efforts, which are the main aspect here, are similar.
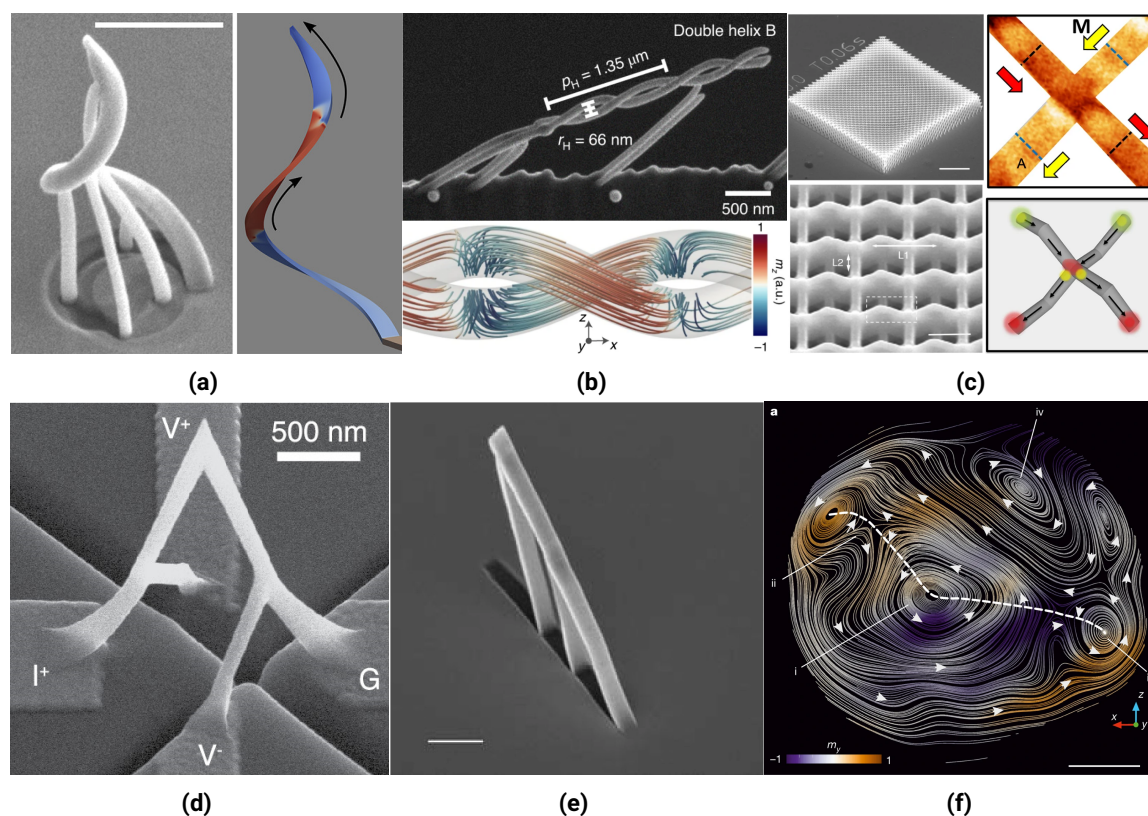
Figure 2.18: Examples of recent developments in 3D nanomagnetism. (a) DW automotion over magnetic helical structures fabricated through FEBID and characterized through shadow X-Ray Magnetic Circular Dichroism (XMCD)-Photoemission Electron Microscopy (PEEM). The DW automotion is driven mainly by thickness gradients and magnetostatic charges. Reproduced from [122]. (b) Observation of a locked DW state and complex free-space magnetic field textures induced by magnetostatic interaction between close nm-scale helical structures. The structures are fabricated with FEBID and characterized with X-ray magnetic laminography based on XMCD. Reproduced from [137]. (c) 3D Artificial spin-ice by electron-beam deposition of magnetic films on MPL fabricated scaffolds. Frustrated spin configurations and monopole excitations are observed at the vertices through magnetic force microscopy. Reproduced from [139, 140]. (d) 3D nano-magneto-electronic device displaying magnetoelectrical signals induced by its non-planar geometry. Device fabricated by FEBID. Reproduced from [54]. (e) Observation of field-induced DW motion over 3D nanomagnetic conduits fabricated by FEBID. Characterization was performed through darkfield MOKE microscopy. Reproduced from [22]. (f) Complex 3D magnetization textures such as vortices, anti-vortices and Bloch points are observed in a soft $GdCo_2$ cylinder through X-ray vector nanotomography based on XMCD. Reproduced with permission from [141].

1. formation of a 3D structure. Should enable general and freeform structures while being highly reproducible and precise, with features at the nano-scale.

2. material functionalization, the attribution of magnetic characteristics to the structure with high-quality material and surface properties that are compatible with the electronic operation of the device.

3. integration into an electronic device, including the device delimitation and the definition of the contacts to the device, in order to enable its electrical characterization.

   So far, the most significant strategies for the fabrication of artificial 3D magnetic devices are self-assembly, scaffold-based or direct fabrication.

Despite the enormous potential of molecular and colloidal self-assembly [142], this approach is yet to produce results that display the flexibility and control in the growth of freeform 3D magnetic structures comparable to the other two approaches and therefore will not be further considered.

2.5.1.1   Scaffold-Based Fabrication of 3D Magnetic Devices

The scaffold-based approach consists of fabricating a complex 3D structure of a passive or sacrificial material, the scaffold, followed by its functionalization into a magnetic structure, e.g., by coating [23], pyrolysis [26] or inversion [31].

The most common approaches for 3D fabrication of the scaffold are MPL, Focused Electron Beam Induced Deposition (FEBID), and the controlled rolling of strained planar membranes [143], including origami-like approaches.

The latter is commonly considered a self-assembly approach and, likewise, is yet to display the same capability to produce general 3D structures as MPL or FEBID. It has, nonetheless, already achieved some results in this scope [129, 144].

FEBID is described in further depth in section 2.5.1.2. While mostly used as a direct fabrication approach for 3D nanomagnetism [14, 54, 137], several recent studies use FEBID made structures as scaffolds [22, 145] (see fig. 2.18a). FEBID provides significantly improved feature sizes and resolutions over standard MPL based approaches and dispenses post-processing, which is beneficial for yielding nanoscale structures. However, its projection base characteristics can lead to discontinuities at the edges between device segments [145]. A multi-step process workflow has been demonstrated for integrating FEBID grown structures into magneto-electronic devices by connecting the device terminals into gold contacts patterned in the substrate [145].

Multi-Photon Lithography

MPL is one of the best suited 3D fabrication techniques for a scaffold-based approach to 3D magneto-electronic devices (e.g., see fig. 2.18c). MPL, as presented in section 2.1, is a lithography technique where a small volume of photoresist is polymerized if the energy deposited in it by a laser goes above a material-dependent threshold. The 3D nature of the method results from a non-linear dependence of the energy absorption on the laser intensity. This absorption process, which starts the polymerization, is controlled to occur only in the vicinity of the laser focus. By scanning the laser focus within the photoresist, virtually any freeform 3D structure can then be produced. Such structure remains after the unpolymerized photoresist is washed away.

The smallest features are typically smaller than 100 nm while the lateral resolution is typically about 200 nm. These values are typically about 3 times larger along the optical axis (z). The feature size, resolution, and aspect ratio can be improved with super-resolution MPL, as discussed in section 2.1.6.

The materials patterned in MPL, i.e., the photoresists, are composed by photoinitiators, typically < 5 % mass, and acrylate polymers. Functional inorganic components can also be added, such as metallic clusters for structure metallization [26] or mineral oils for refractive-index matching in dip-in schemes [146]. However, the concentration of functional components is typically limited to a few % of the total mass in order to avoid agglomeration. MPL produced structures are typically dielectric, transparent for wavelengths above 532 nm and poor thermal conductors.

Being made of a passive material[14], a scaffold needs to be functionalized, i.e., converted into a structure with significant magnetic and electronic properties. This is typically done by Physical Vapour Deposition (PVD), Chemical Vapour Deposition (CVD) or inversion procedures.

PVD methods such as magnetron sputtering, are directional methods, i.e., heterogeneous, where a plasma beam causes the ejection of atoms from a target substrate of the desired material and onto the sample substrate. It is used to deposit high quality thin-films of a large range of relevant materials for magnetism and electronics. They allow thickness control at the Å scale [147], as well as co-sputtering. These methods are, so far, significantly limited for 3D applications because their directionality causes thickness modulation over surfaces with different orientations as well as shadowing effects that are difficult to avoid for non-trivial 3D structures and difficult to control in current deposition systems.

CVD corresponds to processes such as atomic layer deposition where the surface exposure to one or more gaseous precursors leads to their reaction, resulting in the conformal deposition of an atomically thin layer

---

[14]in the context of an magneto-electronic device operation

of material. With the reaction happening simultaneously over the whole structure surface, the deposition time is independent on the surface area, which is advantageous for intricate features such as photonic crystals. While these characteristics are advantageous over PVD, the range of available magnetic materials is more limited [148, 149]. Furthermore, slower deposition rates make for significantly longer depositions [150] which limit the maximum achievable layer thickness and provide for a more demanding precise control over the entire deposition process. CVD processes can be used together with selective scaffold removal, described below, to implement a double inversion procedure [31, 151].

The passive role of the MPL scaffold enables to explore its material properties, and their differences to those of the active layers, to selectively optimize the functionality of the scaffold. Particularly, post-processing strategies that selectively target the scaffold core are essential to achieve the multi-step fabrication processes necessary to realize complex 3D electronic devices. Such strategies have been particularly investigated in recent years, as reviewed next, with many significant results, as shown in fig. 2.19.
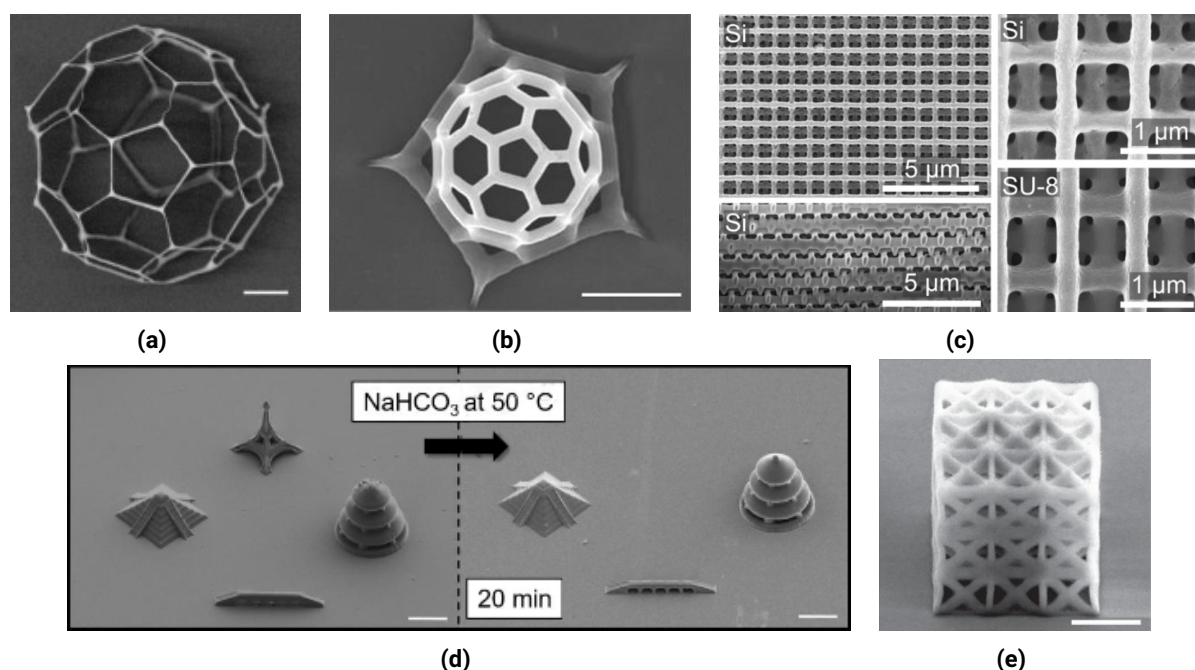
Figure 2.19: Examples of post-processing strategies of MPL scaffolds. (a) Thinning of MPL features through plasma etching. Scale bar is 1 μm. Reproduced with permission from [32]. (b) The removal of the polymer organic backbone through high-temperature processing, i.e., pyrolysis, enables to scale down the structure, keeping only its inorganic components. Scale bar is 1 μm. Reproduced with permission from [32]. (c) Double inversion of a SU-8 MPL scaffold (bottom right) into a Si photonic crystal with the same geometry. Reproduced with permission from [31]. (d) Selective removal of specific photoresist compositions in aqueous solutions. Scale bars are 20 μm. Reproduced from [71]. (e) 3D SiO$_2$ structure fabricated through MPL. Scale bar is 5 μm. Reproduced from [71].

Pyrolysis [32] or dehydration [152] (for hydrogels) of photoresists enable to greatly shrink the fabricated structures, providing access to nanometer scale features and resolution beyond those currently possible through MPL.

To produce functional structures, molecules or clusters can be mixed into or deposited onto the scaffold prior to shrinking. Conductive metallic structures haven been produced using this approach, although with poor conductivity compared to bulk due to inhomogeneous material agglomeration [26, 152].

Another strategy is to pyrolyze a photoresist with inorganic mineral components, such as those compatible with dip-in methods [146], producing a shrunk inorganic scaffold with feature size and resolution improvements [32], as in fig. 2.19b.

When, instead, the scaffold is coated by a thick and self-supporting structure of a material with higher thermal stability, pyrolysis leads to the selective removal of the polymer core without affecting the inverse structure [151].

Pyrolysis, however, is still seen to lead to stretching or discontinuity issues at interfaces [32]. On the other hand, in the hydrogel-based approach, the hydrogel backbone structure in not removed, resulting in a mixed structure [152].

Oxygen plasma etching enables to isotropically etch a photoresist structure, serving two different purposes.
First, it can be used to fine tune the feature size in an MPL polymer structure before further processing, without improving the resolution [32], as shown in fig. 2.19a.
Second, it enables to selectively remove the photoresist from inside a coated scaffold structure, even in highly intricate structures. This has been used for hollowing photonic crystals in double inversion procedures [31].

The direct conversion of MPL scaffolds with nm-scale features into 3D SiO_2 structures (fig. 2.19e), as well as polycrystalline SiO_2, has also been recently shown [64, 153]. While polycrystalline SiO_2 freestanding structures are not yet realizable with this method, it constitutes an important step towards 3D crystalline scaffolds and their use to grow crystalline materials along 3D geometries, an important hallmark for 3D fabrication.

The ability to dissolve MPL photoresists in aqueous solutions has also been recently shown [71] (fig. 2.19d). This would enable a simple procedure for selective scaffold removal, producing freestanding films. However, this must yet be confirmed experimentally, as the intrinsic capillary forces, combined with the lack of mechanical support by the scaffold, make it unlikely for the film to withstand the dissolution, at least without supercritical drying.

Other MPL related developments such as multi-foci approaches [28], which achieves fabrication rates on the order of 10^7 voxels/s, dip-in MPL [46], which enables to work with non-transparent substrates, su-perresolution MPL [87], and improved photoiniator efficiencies [72] are also expected to play an important role in the use of scaffold-based approaches in magnetism and electronics.

2.5.1.2   Direct Fabrication of 3D Magnetic Devices

Direct fabrication of 3D magnetic devices, as the name suggests, refers to the formation of 3D structures having the desired magnetic properties right after they are fabricated. As opposed to the scaffold-based approach, which requires an intermediate passive structure, this strategy merges the formation and functionalization of the structure into a single step. Naturally, this is only possible as long as there are techniques akin to magnetic material deposition with intrinsic 3D capabilities.

Glancing Angle Deposition (GLAD) [154, 155] was one of the first such methods and is based on shadowing effects for depositions directed almost parallel to the substrate. The geometries it enables, and their integration into devices, are quite limited in scope, and therefore they won't be covered in further depth.

Recently, a new method was developed that forms 3D structures by guiding charged nanoparticles through convergent electric field lines [156], as shown in fig. 2.20b. This has shown to be able to produce a large variety of 3D structures with features smaller than 100 nm and to be compatible with several different materials that can be interchanged within the same structure. The precise guidance of individual or small clusters of nanoparticles should enable high material, surface, and structural qualities in a wide range of materials, with the potential of overcoming some of the most significant shortcomings of MPL and FEBID in a single technique. Preliminary results, however, appear to show significant surface roughness and an asymmetry between in-plane and out-of-plane features [156].
Also recently, the direct fabrication of 3D structures from quantum dots [33] (fig. 2.20c), including semi-conductor quantum dots, and nano-crystals [34] was achieved based on direct laser writing through multi-photon absorptions. These methods are based on laser induced increased surface reactivity and thermo-electrically induced nano-crystal formation and erasure, respectively. Although the compatibility of such methods with different materials is shown, the full extent of compatible materials and the achievable material quality in each case remains to be seen. For features below 200 nm some discontinuities appear in the films that likely limit their applications. These methods are also particularly susceptible to effects

such as the refraction index mismatch at the interfaces with these materials, which induce aberrations that affect the maximum structure depth.

(a)   **(b)**   **(c)**
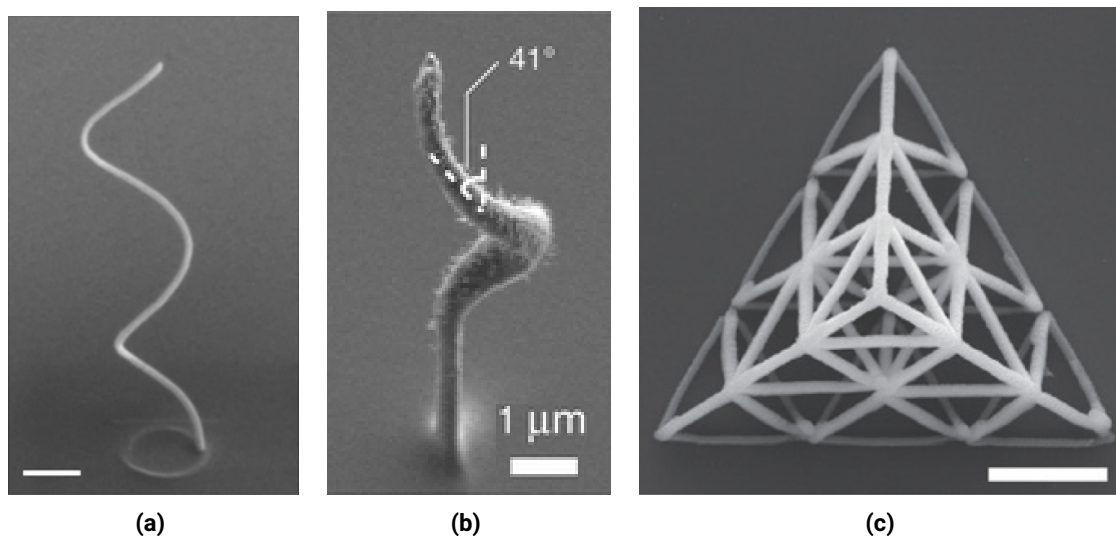
Figure 2.20: Examples of direct fabrication methods. (a) Co nanospirals fabricated through FEBID, with 100 ± 25 nm diameter. Scale bar is 500 nm. Reproduced from [14]. (b) 3D metalic structures fabricated by guiding charged aerosols jets with electric fields. Reproduced with permission from [156]. (c) 3D structures from semiconductor quantum dots through laser-activated surface functionalization. Scale bar is $5\mu m$. Reproduced with permission from [33].

FEBID is, however, the technique providing better structural and material properties for solid magnetic structures at the nanoscale, as exemplified in fig. 2.20a. Therefore, it will now be reviewed.

Focused Electron Beam Induced Deposition

FEBID [157] is a bottom-up maskless deposition technique where a tightly-focused electron beam causes a precursor gas to locally disassociate, leading to the deposition of a solid by-product. The continued exposure of a given location by the electron beam leads to the build up of deposited material into a 3D vertical feature. By controlling the position of the sample substrate relative to that of the electron beam focus, as well as the exposure time at each location, complex 3D structures can be realized [25]. FEBID is capable to achieve both feature sizes and resolutions of ≈ 50 nm [25], being comparable only to e-beam lithography. The fabrication rates are typically about 0.01 to 1 voxel per second, and up to 10^4 for cryo-FEBID, although at a worse resolution [158].

The experimental equipment is similar to a scanning electron microscope. It includes an electron beam column with electron optics and a fine gas nozzle through which to feed the precursor gas. The gas is injected close, i.e., between 50 and 300 μm, to the surface location where the electron beam is focused on. When the gas is injected, the precursor molecules move towards the sample surface where they adsorb, diffuse and desorb at different rates [25]. When the focused electron beam, with typical energies between 1 and 30 keV, reaches the surface, it, and its associated secondary electrons [159], cause the dissociation of the precursor and the deposition of the desired material by-product. Local scattering events can lead to a significant dispersion of the beam [159], and therefore to significant material co-deposition at the substrate [157]. This can be minimized by increasing the electron beam energy or decreasing the electron beam current [157].

The material deposited through FEBID depends on the chosen precursor. A wide range of different materials have already been deposited with different purities [160], and important ferromagnetic materials such as Co, Fe and Ni have been synthesized with 95 %,85 % and 40 % purities, respectively [161]. However, the development of new and high-quality precursors is a long and demanding process and so, recently, FEBID has also been combined with PVD and CVD to increase the range of available materials [159]. In

this case, a FEBID structure acts as a scaffold rather than a magnetic structure directly, as mentioned in section 2.5.1.1.

FEBID is a directional deposition technique and can be thought of as a projection-based deposition where a feature is formed when material can be projected into an existing surface with the desired angle, i.e., when the desired feature is a continuation of another already existing feature and the growth direction is within an accessible angle [159]. Per opposition, for example, a polymerized MPL feature can be made to exist disconnected inside the photoresist and to grow along any desired 3D direction at any point. Thus, the growth of sideways structures like bridges, parallel to the substrate, is particularly difficult using FEBID due to the small projection surface of the electron beam into the existing feature, since it points perpendicular to the beam. To overcome this, FEBID can be realized with the sample mounted onto a rotating stage which enables to rotate the sample with regard to the electron beam and increase the projection area [159], at the cost of an increase in control complexity. To improve the precision of the FEBID process, a simple calibration is ran before each fabrication step [25].

Being based on the dissociation of a gaseous precursor, no post-processing is required in a FEBID process, greatly improving the yield of nanometer-scale structures compared with liquid based techniques as MPL. This aspect is particularly important for studying nanometer sized structures. Furthermore, it is also possible to deposit different materials within the same structure. However, due to scattering-based beam dispersion and projection- based nature of the deposition, the contamination of the substrate with the deposited material cannot be excluded [157] and must be taken into account when preparing the integration of the fabricated structures into electronic devices.

2.5.2   Characterization of 3D Nano- and Micro-Magneto-Electronic Devices

The challenges in the 3D characterization of magnetic and magneto-electronic devices are similar to those in fabrication. These include the variation of the normal orientation over the sample surface, the variation of sample thickness, the complexity of 3D magnetic textures, the reconstruction of 3D magnetization from the acquired data, etc. Ideally, a 3D magnetic characterization technique would enable a nm-precise reconstruction of the vectorial representation of the magnetization within the volume of intricate samples, as well as the characterization of magnetic dynamics with time-resolved measurements at the fs scale.
To approach these requirements, higher energy sources such as electron or X-rays need to be used. Over the last years, X-ray nanotomography techniques such as scanning X-ray transmission microscopy [141], which exploits X-Ray Magnetic Circular Dichroism (XMCD), and its combination with coherent diffraction imaging [162] have seen tremendous development, including the time-resolved measurement of magnetization dynamics [15]. These are now the reference for characterization of 3D magnetic samples, having almost reached the established performance goals [137]. Other such techniques include X-ray photoemission electron microscopy [163], electron holography [164] and Lorentz microscopy [155].
However, these samples take advantage of the last generation of X-ray and electron beam coherent sources for optimal performance, which are not widely available. Within commonly available techniques, Magneto-Optical Kerr Effect (MOKE) microscopy and magnetic force microscopy have proven the best suited. These have been significantly adapted to characterize 3D samples, e.g., through angle resolved dark-field MOKE [22] or integration in SEM setups [165]. Nonetheless, they are only able to probe the surface state of the magnetization in surfaces mostly oriented away from the substrate and, particularly for MOKE, with limited spatial and angular resolution.
Another option is the electrical characterization of 3D magneto-electronic devices. While it is mostly similar to that of planar devices, the study of magnetoresistive samples under applied magnetic fields greatly benefits from the ability to apply fields along a large range of 3D orientations, which is not typically available. Thus, it requires adequate planning of the device geometries and the experimental procedure, as well as extensive modeling.

2.5.3 Perspective on the Fabrication of 3D Nano- and Micro-Magneto-Electronic Devices

My perspective is that, currently, no existing 3D fabrication method is matured enough to achieve fabrication of freeform 3D magneto-electronic devices with sub-μm features and high material quality over a large range of materials. Instead, the available methods offer a complementary set of properties which make them advantageous under different situations, or even in different steps of the same complex fabrication process.

The MPL shortcomings related to limited resolution, capillary forces during sample development and poor thermal stability, are balanced by its more general 3D capabilities, higher fabrication rates and its modularity, i.e., the flexibility in interfacing with other fabrication processes, which is reflected in the development of many promising post-processing techniques.

FEBID, on the other hand, is superior for the fabrication of magnetic structures at the nanoscale, with feature sizes and resolutions of $\approx$ 50 nm, which are typically not feasible with MPL [15], but it is limited by the range of materials for magnetic and electronic devices it can deposit with sufficient purity, as well as by the time-consuming precursor development process and substrate contamination, which can difficult the integration in electronic devices and lower fabrication rates.

I, therefore, consider MPL to be more promising in the context of my project and decided to use it for the experimental works on this thesis because it makes a clear separation between 3D structure fabrication and its functionalization. To elaborate, MPL is chosen for its ability to provide high-quality 3D structures that can be optimized independently of the functional material properties. Reciprocally, a distinct process, such as PVD, can be used to achieve functional surfaces of very high material quality for a wide range of materials without affecting the 3D capabilities. Thus, while PVD is not yet optimized to interface with MPL, it can be so iteratively in the future without compromising any of the current capabilities. For example, PVD could be improved by establishing control over the deposition angle and area during the deposition process, similar to [156]. FEBID, on the other hand, by coupling both structural and material quality together, makes it harder to optimize for both simultaneously.

2.6 Project Aims

Three aims were established for this thesis:

1. The development of a state-of-the-art 3D micro- and nano-fabrication setup using super-resolution multi-photon lithography. The focus is to establish an open and configurable system that can be easily adapted to the changes in the needs and specifications that are expected throughout the project.

2. The establishment of a workflow for the fabrication of 3D spintronic devices with complex geometries. Such a workflow is expected to address the fabrication of general 3D geometries at a scale relevant to the state-of-the-art and the functionalization of such structures with high-quality magnetic film stacks. Ideally, this workflow should be compatible with the material stacks that are being used in high-performance state-of-the-art 2D spintronic devices.

3. The experimental demonstration of clear functional advantages in the operation of the developed 3D complex spintronic devices over known devices. The focus is to demonstrate generational, rather than iterative, improvements to current spintronic devices. The referred advantages are expected to either take the form of direct performance improvements or novel functionalities.

Each established aim is dependent on the completion of the previous. In chapter 8, the achievement of these aims will be reviewed.

---

[15] for comparison, MPL is limited to 50 nm feature size and 120 nm resolution using STED-MPL or 100nm feature size and 250nm resolution without.

Chapter 3

Experimental Methods

3.1   Multi-Photon Lithography

For Multi-Photon Lithography (MPL), a customized INFINITY-line super-resolution STED microscope (Abberior Instruments GmbH) is used. The microscope hardware and software are adapted for performing MPL, as further described in chapter 4. The schematic overview of the system is shown in fig. 3.1. For multi-photon excitation, a 780 nm wavelength femtosecond Er fiber laser (Menlo Systems C-Fiber 780) is used with an 80MHz repetition rate and chirp pre-compensation through pulse compression to pulse widths $\leq 70\ fs$ at the laser output. A 532 nm CW laser is used as the STED-MPL depletion beam and as the fluorescence excitation laser for the confocal experiments in chapter 6. The power of the lasers is controlled through AOMs before being focused on the photoresist through a Nikon Plan Apo Lambda 100x/1.45 Oil objective lens. For STED-MPL, the STED laser point-spread function is shaped into a bottle beam focus[87] by separating the two polarizations of the beam and shaping one into a 2D donut and one into vertical lobes through a single Spatial Light Modulator (SLM) before recombining them. For the confocal fluorescence experiments in chapter 6, no PSF modification is done.

The motion of the objective along the optical axis is achieved by a combination of a motorized focus stage embedded in the microscope (Nikon Ti-2), with 10 mm range and 20 nm precision, and the z axis of an xyz piezoelectric scanning stage (Physik Instrumente P-545.3C8S PInano) with 200 μm range and 1 nm precision in each of the 3 axes. The motion of the sample along xy is achieved through a combination of the xy axis of the mentioned xyz piezoelectric stage, with 200 μm range per axis, and a coarse motion stage (Physik Instrumente U-780 PILine XY-stage) with 135 $mm \times$ 85 mm ($x \times y$) range, on which the piezoelectric stage is mounted. The latter stage extends the available range of motion and therefore the fabrication workspace, which was used for the fabrication of the electrical contact pads in chapters 5 and 7 by implementing a simple stitching procedure. A set of galvanometer-scanners are also available for scanning the lasers in xy with an 80×80 μm maximum range for the specified objective.

At the start of the fabrication the photoresist is drop-casted onto a borosilicate glass coverslip (170 μm thick) which is placed in the microscope sample stage. Determining the glass-photoresist interface position is automated by detecting the increased laser reflection at the glass-photoresist interface with a photodiode. The error in the interface position is less than 200 nm. The fabrication is started with the laser focused into the substrate to improve adhesion. During fabrication, the laser was scanned in xy utilizing the set of galvanometer-scanners while the z motion between layers utilizes the xyz piezoelectric stage.

For the fabrication of the structures in chapters 5 and 7, 0.2 nJ excitation pulses were used at an 80MHz repetition rate, calculated from the average laser power measured with a power meter (S302C, Thorlabs) at the back aperture of the objective, after the acousto-optic modulator. The xy scanning during fabrication was performed at 6.25 mm/s (chapter 5) or 4.5 mm/s (chapter 7) with the galvanometer-scanner, using y as the fast axis. In order to reduce the surface roughness the spacing between parallel lines (along x) and parallel layers (along z) was set to 25 nm. To speed up the fabrication of the electric contact pad delimitation, a coarser fabrication profile was used: $\approx$ 0.35 nJ excitation pulses, 10 mm/s scanning speed and a spacing of 0.2 μm between parallel lines (x) and layers (z).
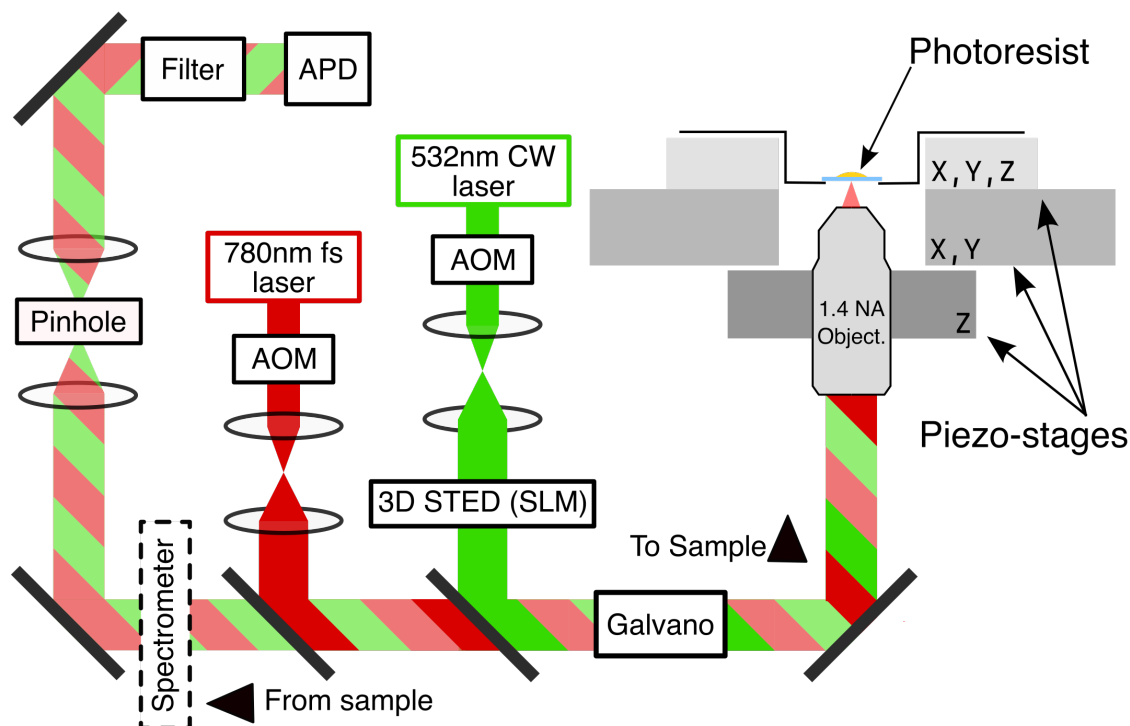
Figure 3.1: Scheme of the experimental setup, consisting of a standard MPL arrangement along a 3D STED module and a confocal acquisition module. Numerical Aperture (NA); Spatial Light Modulator (SLM); Acousto-Optical Modulator (AOM); Avalanche Photo-Detector (APD). The SLM is controlled to either modify the 532 nm laser PSF, e.g., into a 2D donut or a 3D bottle-beam, or not to modify it at all, e.g., as used for the confocal and spectroscopy experiments in chapter 6.

After fabrication, the unpolymerized photoresist is removed by submerging the sample on propylene glycol monomethyl ether acetate (PEGMEA, Merck Sigma-Aldrich) for 25 min, followed by a 5 min submersion on 2-propanol. Finally, the sample is carefully dried with dust-free compressed air to avoid residues on the surface which could impact the deposition step.

MPL fabrication yield is measured to be typically better than 90 % for optimized structures, such as the ones used in chapters 5 and 7.

3.2   Photoresist Preparation

The utilized photoresists are composed by 7-diethylamino-3-thenoyl-coumarin (DETC) (Luxottica Exciton) as photoinitiator, 0.25 wt% concentration, and either Pentaerythritol Triacrylate (PETA) (Merck Sigma-Aldrich) or Pentaerythritol Tetraacrylate (PETTA) (Merck Sigma-Aldrich) as the monomer. The photoresists are prepared from the components, by weighing them to the correct ratio followed by mixing with a magnetic stirrer between 20 to 40 minutes at room temperature until the photoinitiator completely dissolves in the monomer. In some cases it was necessary to grind the DETC crystals before mixing to achieve complete dissolution. These photoresists have been widely used and characterized in past publications, specifically in STED-MPL experiments[27, 47, 166].

3.3   Spectroscopy Measurements

For the spectral analysis presented in chapter 6, a spectrophotometer (Flame-T-VIS-NIR-ES, Ocean Insight) is placed on the optical path of the confocal apparatus of the MPL setup, as seen in fig. 3.1. The fluorescence signal is integrated in 70 millisecond intervals while a reference volume of photoresist is being scanned

by one of the lasers separately or both lasers sequentially. The reference volume scanned during the acquisition corresponds to a $15 \times 15 \times 4 \ \mu m$ cuboid, equivalent to the lower half of the structures shown in section 6.B. The total scan time for each layer was about 9 times higher than the spectral signal integration time, guaranteeing several spectral acquisitions are taken during the scanning phase. The spectra acquired during the transition between layers are filtered out through a peak counts threshold before analysis. In order to minimize effects related to the substrate interface, only the data corresponding to the top end of the cuboid section was accounted for, corresponding to a focus $3 - 4 \ \mu m$ into the photoresist.

3.4   Confocal Fluorescence Microscopy

In chapter 6, the dependence of the fluorescence intensity on the power of the different laser sources is characterized. The confocal fluorescence microscopy arrangement within the MPL setup, described in section 3.1 and fig. 3.1, is used for this purpose. The fluorescence emission is filtered through a pinhole and registered through an Avalanche Photo-Detector (APD) (SPCM-AQRH-13-FC, Excelitas technologies). Given the high sensitivity of the APD, a band-pass filter is utilized to attenuate the incoming fluorescence signal and avoid saturation. A 650-720 nm band-pass filter (ET685/70, AHF GmbH) is used that only transmits 0.095 % of the signal at the wavelengths of the fluorescence emission peaks. A dwell time of 20 μs, i.e., the acquisition time per pixel, is used for all exposures, along a pixel size of $100 \times 100 \ nm$. In order to minimize interface effects, only the fluorescence signals corresponding to focus deeper than 3 μm into the photoresist are considered. Each data point in the analysis corresponds to the average of the fluorescence signal over all exposed pixels in a layer and over 10 layers, i.e., an average over all pixels in a focus depth range of 1 μm. The fluorescence signal progression is analyzed at different focus depths and is seen to produce consistent results.

The average laser power, controlled through an Acousto-Optical Modulator (AOM), is measured with a power meter (S302C, Thorlabs) at the back aperture of the objective. As the 532 nm laser is a CW laser, the exposure energy is calculated instead of pulse energy by accounting for a 20 μs dwell time per pixel.

To determine the scaling order N of the fluorescence signal with a given excitation energy, the function $I_{fluor} = a \times E_{excitation}^{N}$ is fitted to the experimental data using a non-linear least squares method with the proportionality constant a as the only free parameter.

3.5   Sputtering

3.5.1   Magnetron Sputtering of Chiral Spin-Orbit Torque Film Stacks

In chapter 5, a magnetic film stack known to display chiral spin-orbit torques[121] is deposited onto the 3D ribbon-like structures. After the MPL process is completed, the glass substrate is cut into a smaller piece in preparation for deposition. The magnetic film stacks are deposited onto both the polymer structures and glass substrate by magnetron sputtering at an Ar pressure of 1 mTorr at room temperature. The deposition system has a base pressure better than 10^{-9} Torr. A 100 Å thick TaN layer is first deposited to improve the adhesion and the smoothness of the following films. TaN capping layers, 30 and 60 Å thick, are used to prevent the oxidation of the magnetic layers underneath for the Synthetic Anti-Ferromagnet (SAF) and ferromagnetic films, respectively. For the single-layer ferromagnetic film, the stack is: 100 TaN/30 Pt/3 Co/7 Ni/3 Co/60TaN (thicknesses in Å, with the layer on the left being the bottom layer) while for the SAF film the deposited stack is: 100 TaN/30 Pt/3 Co/7 Ni/1.5 Co/9.5 Ru/3.5 Co/7 Ni/3 Co/30TaN (thicknesses in Å, with the layer on the left being the bottom layer). The deposition is done from a direction close to perpendicular to the substrate while the substrate is rotated about the out-of-plane axis in order to promote a uniform coating on the ramp and torsion sections while achieving shadowing in the desired places, such as underneath the electrical contact pad delimitation and underneath the suspended section of the device.

3.5.2   Magnetron Sputtering of CoNi Alloys

In chapter 7, a CoNi magnetic alloy known to display a large Anisotropic Magnetoresistance (AMR) is deposited onto the fabricated 3D coil structures.

After the MPL process is completed, the magnetic film stack is deposited onto both the polymer structures and the glass substrate by magnetron sputtering in an ultra-high vacuum system operating at a base pressure of 3×10^{-9} $mbar$. Argon is used as a sputtering gas with a fixed rate of 55 sccm. A 20 Å thick MgO underlayer is deposited as a substrate passivation layer, followed by a 450 Å thick $Co_{0.3}Ni_{0.7}$ alloy layer and a 60 Å thick MgO capping layer to prevent the oxidation of the magnetic layer underneath. Radio-Frequency (RF) sputtering is used for the MgO layer at a sputtering pressure of 3 mTorr. DC co-sputtering is used for the CoNi layer at a sputtering pressure of 3.5 mTorr. Both deposition steps are done at room temperature. The Co and Ni targets are oriented at 0 ° and 90 °, respectively, which might lead to slight differences in the film stoichiometry over different surfaces of the coils. The substrate is rotated during deposition to improve the uniformity of the grown films, particularly over the outer surfaces of the coils.

3.6   Transport Measurements

In chapter 7, the Anisotropic Magnetoresistance (AMR) response of different coil-based devices is characterized using electrical transport measurements. Major electrical transport measurements were carried out in a physical property measurement system (PPMS, Quantum Design). The electrical transport measurement configuration is represented in fig. 7.3a. A single mid-frequency (Direct Current (DC)-5MHz) Lock-in amplifier (MFLI, Zurich Instruments) is used, providing all the necessary capabilities. As the polymer core is heat sensitive (see section 7.D), the electrical transport measurements were carried out at 220 K and using a maximum probing current of 0.2 mA to minimize Joule heating of the system. Each device is characterized under the following current setpoints: [0.05, 0.1, 0.15, 0.2] mA.

The AMR is measured by rotating the sample about the x axis while an external magnetic field is applied along the $+z$ direction, as shown in fig. 7.3a. Each cycle corresponds to rotating the device in the range $[2, 365]$ °, corresponding to an external field sweep in the yz plane, at a rate of $+0.9$ °$/s$. A data point is acquired every 50 ms. The measurement cycle was repeated at the fixed external magnetic field setpoints of 0.05, 0.1, 0.25, 0.5, 0.75, 1, 2, 4 and 6 T, respectively.

In each acquisition, the first and second harmonic components of the voltage difference are measured at the device terminals, together with the current flowing through the device. The second harmonic component is typically in the order of a few μVs. Thus, to increase the Signal-to-Noise Ratio (SNR), the modulation frequency and the parameters for the low-pass filter applied after demodulation are optimized such that any other peak in the frequency spectrum that is within the range of the low-pass filter has a power spectral density at least 10^{-9} times smaller than that of the central peak. After optimization, a modulation frequency of 433.6Hz is used, along with a 4th order filter with a 0.11 s time constant. Even after optimization, the noise level for the second harmonic component is still observed to be at or above the expected signal variation level across a measurement cycle, i.e., $0.1 - 0.2$ μV, making the measurement unreliable. Even when using higher time constants for the low-pass filter, the signal is seen to fluctuate over the same range within the duration of a measurement cycle, typically 6.5 minutes.

3.7   Kerr Microscopy

Let us consider the polar Magneto-Optical Kerr Effect (MOKE)[167]: The reflection of linearly polarized light[1], e.g., in the xy plane and propagating along z, on the surface of a sample with perpendicular magnetization (along z) will cause the polarization to rotate and to become elliptical, instead of linear. This occurs due to the different velocities and absorptions of the left- and right-handed circular polarization components during the reflection at the magnetized surface.

---

[1]linearly polarized light can be described as a combination of left- and right-handed circular polarization components

In chapter 5, the MOKE is used to probe the out-of-plane magnetization component of the 3D twisted ribbons and measure the current-induced domain wall motion using the experimental system shown in fig. 3.2a. The incoming light is linearly polarized and shines onto the sample. By passing the light reflected from the sample through a quarter waveplate and an analyzer, the resulting signal magnitude is proportional to the sample magnetization along z through the polarization ellipticity it induces [167]. This signal will appear as bright or dark regions when the ellipticity has the same or the opposite sign to that defined by the analyzer, respectively.
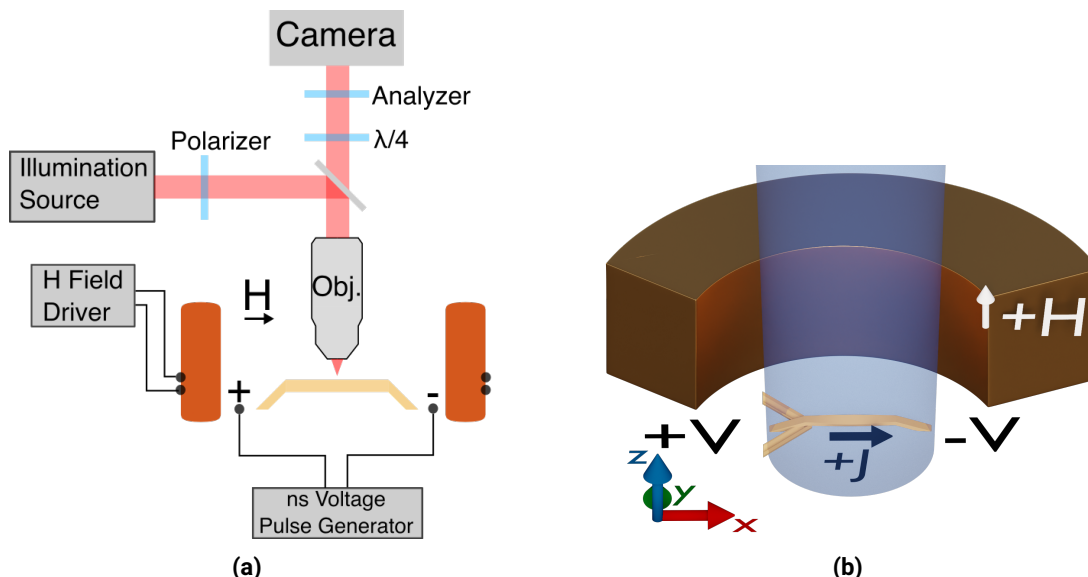
Figure 3.2: Magneto-Optical Kerr Effect (MOKE) microscopy experimental setup for characterization of Current Induced Domain Wall Motion (CIDWM) in 3D magnetic ribbons. (a) Scheme of the functional elements of the MOKE setup, shown with the electromagnet utilized to generate in-plane magnetic field along x. Particularly, the $\lambda/4$ waveplate renders the Kerr ellipticity, rather than the Kerr rotation, detectable, which is more robust to the influence of other optical components in the lightpath. Obj. is the objective lens. (b) A 3D view of the system with the hollow cylinder magnet utilized for generating out-of-plane field, with the Kerr illumination shown in blue. Points +V and -V represent the two electrical contacts and $+J$ the corresponding positive direction of the current.

After the deposition step described in section 3.5, the devices in chapter 5 are wire-bonded with the source (positive) contact bonded to the inside of the fully delimited pad while the ground is bonded to the open contact, such that for a positive voltage pulse, the current flows from the inside to the outside of the fully delimited pad, as represented in fig. 3.2b. The device resistances, typically in the range of 1.7 $k\Omega$ for 2.5 μm wide devices, are measured before and after the characterization to probe for significant changes in the devices such as deformations from Joule heating, with variations typically < 1 %.

A Tektronix PSPL10300B nanosecond pulse generator is used to move the DWs. It is able to generate voltage pulses from 0 to 50V and with pulse lengths between 1-100 ns. The rise and fall times of the voltage pulses are measured, under the utilized experimental conditions, to be about 0.3 and 0.8 ns, respectively. To minimize the uncertainty, a sequence of current pulses with a minimum pulse length t_p = 10 ns is applied between each Kerr image acquisition unless DW nucleation is observed due to heating effects, in which case 8 ns long pulses are used. On the upper bound, t_p is not increased above 50 ns when the current density J is low ($\approx 0.6 \times 10^8$ Acm^{-2}), to limit the impact of thermally-induced DW creep. t_p is reduced as J is increased (up to $\approx 1.7 \times 10^8$ Acm^{-2}) since larger t_p often heats up the suspended 3D structures due to the poor thermal conductivity of the polymer cores.

At the start of each acquisition cycle, a DW is nucleated inside the device. In most cases, the DW is nucleated by field-induced magnetization switching, using an electromagnet to generate out-of-plane fields ([-50;50] mT range) along z, as represented in fig. 3.2b: first, a large field is applied to uniformly magnetize the sample, followed by a smaller field in the opposite direction that switches the magnetization

of the pads but not on the device, creating a DW at each end of the device.

For characterizing the SAF devices and the influence of the H_x field on DW motion, the DW is instead nucleated by current induced magnetization switching [168]. An in-plane electromagnet is used to generate fields along x ([-300;300]mT range), as shown in fig. 3.2a. The nucleation procedure is the following: first, a handheld magnet is used to uniformly magnetize the sample along $\pm z$; second, an in-plane field in the order of a few mT is applied while a current pulse is sent through the sample. The current pulse must be strong enough to thermally nucleate new domains. By adjusting the direction of the uniform magnetization, the in-plane field and the current flow, a DW of a given type is nucleated within the device.

The nucleated DWs are driven into the twisted region by sequences of current pulses, acquiring an image after each pulse sequence. Differential mode Kerr microscopy is employed: an image taken before the pulse sequence is used as background, being subtracted from the acquisition image taken after the pulse sequence is sent, as shown in figs. 3.3a to 3.3c. This process significantly improves the magnetic contrast and resolution of images by minimizing the effect of drift and vibrations on the Kerr contrast, to which 3D structures are particularly susceptible and sensitive. Consequently, the processed Kerr image shows two boundaries in the wire that correspond to the prior and present DWs positions, as in fig. 3.3d. The region between boundaries appears as either dark or bright depending on whether the magnetization changes to be pointing down or up along z in that region, respectively.

Each acquisition cycle, i.e., the nucleation and driving of the DW into the device through several pulse sequences, highlighted in fig. 3.3e, is automated to enable consistent data acquisition and repeated between 3 and 5 times for each experimental condition in order to evaluate reproducibility.

The upper bound of the current density is limited by heating-induced DW nucleation to be $\approx 1.7 \times 10^8 \ Acm^{-2}$, which is worsened by the poor thermal conductivity of the polymer core. The lower bound is defined by the critical current density J_c, considered to be the current density necessary for DW motion with speeds above $5 \ ms^{-1}$, which is measured to be $\approx 0.6 \times 10^8 \ Acm^{-2}$ for devices without torsion.

For the magnetic ribbon with $\zeta = -45\ °$ torsion angle, the sample is placed on a wedge at $22.5\ °$ angle to the stage surface to enhance the Kerr image contrast.

Data processing of the Kerr microscope experimental data, including the calculation of the DW velocity, is described in chapter 4.

3.8   Micromagnetic Simulations

A micromagnetic simulation utilizing a hybrid finite-element/boundary-element method was set up to validate the experimental AMR response for the coil-based devices in chapter 7. The simulation is implemented through the mangum.fe software (version 2.2) from SuessCo Simulations [169]. For the simulation, only the outer surface of a single coil turn is considered. The simulated film is considered to have a cross section of $600 \times 40 \ nm$ (height $\times$ thickness). The meshes are created with a mesh size of 8 nm using the program Gmsh. The saturation magnetization of the material is fixed at $1.128 \times e^3 \ A/m$, as measured for unpatterned films through Vibrating Sample Magnetometry (VSM) (Lakeshore VSM 8600). The magnetization was initialized in the out-of-plane direction (z, i.e., along the main axis of the coil) and full saturation is assumed. An external magnetic field of $H = 1 \ kOe$ is considered and made to rotate in the yz plane in the clockwise direction, as in the experimental setup. The relaxation is calculated using the LLG equation with a damping parameter $\alpha = 1$. The resistivity for the cases where the magnetization is parallel (perpendicular) to the current flow direction are set to $2.388e^{-7} \ \Omega \ m$ ($2.351e^{-7} \ \Omega \ m$), respectively, as measured from the AMR response of the 2D reference device under saturating external fields. The exchange constant is extrapolated from [170], by accounting with the desired $Co_{0.3}Ni_{0.7}$ stoichiometry for the alloy, to be $\approx 1.7e^{-11} \ J/m$. A current density of $8.3e^9 \ A/m^2$ is considered.
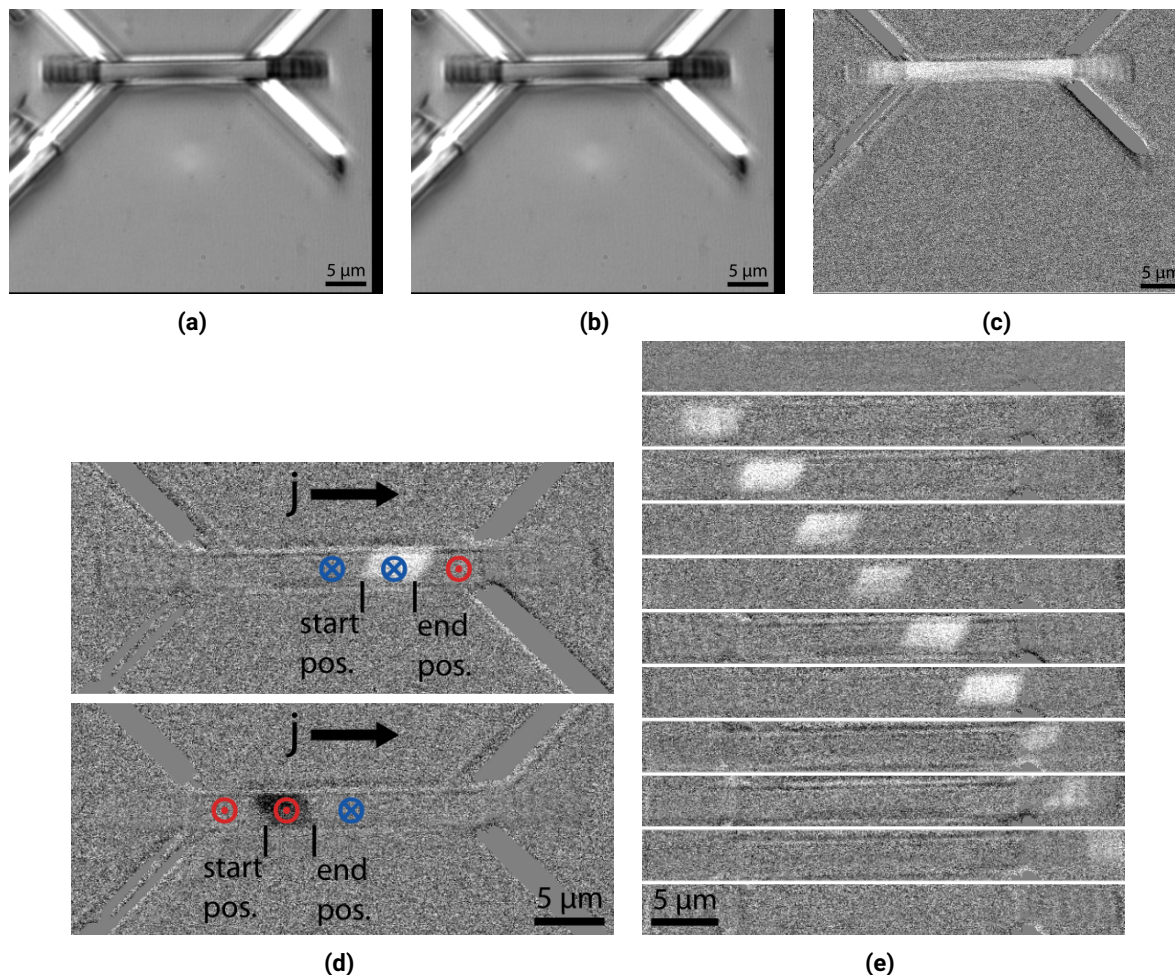
Figure 3.3: Differential Kerr microscopy mode. (a)-(c) Example of the differential processing workflow. (a) Initial acquisition to be used as background. (b) Unprocessed measurement acquisition, e.g., as acquired after each voltage pulse is sent. (c) Processed measurement acquisition, obtained from subtracting (a) from (b). In this case it represents the Kerr ellipticity change after the magnetization is uniformly set along $-z$, i.e., $\otimes$, through the application of an external field at the start of an acquisition sequence. (d) Examples of processed Kerr images showing the current induced DW displacement (top-$\otimes \odot$;bottom-$\odot \otimes$) for a single pulse sequence with $j > 0$, i.e., flowing to the right or along $+x$. Since differential processing is used, the bright or dark shaded regions correspond to the DW displacement due to a single pulse sequence, with the left boundary corresponding to the initial DW position (again, for $j > 0$) and the right to the final DW position, as marked. (e) Representative example of an automated sequence acquisition. After the sample is uniformly magnetized and the DWs nucleated, an initial processed capture is taken (top). Afterwards, a pre-configured number of pulse sequences are sent sequentially, with a new image being taken and processed between each two pulse sequences. To improve robustness, a new background is also acquired before a new pulse sequence is sent.

Chapter 4

Software Architecture and Algorithms

In this section, I will provide an overview of the software architecture and algorithms developed in the context of this thesis. The package for hardware control, which implements the core functionality for the realization of Multi-Photon Lithography (MPL), is presented first, in section 4.1, followed by the algorithms that were developed on top of it to provide additional functionality to the MPL fabrication, in section 4.2, and the algorithms developed for data processing, presented in section 4.3.

The aspects explained in sections 4.1 and 4.2 are not necessary to understand the applications in chapters 5 to 7 but establish the working process by which they were achieved and are therefore a set of results in themselves. Sections 4.1 and 4.2 complement the experimental description of the MPL process presented in section 3.1 by explaining how the scanning process at the core of MPL is implemented and automated. Section 4.3 is an extended description of the algorithms described in chapters 5 and 6.

4.1 Hardware Control

The purpose of the control layer of the software is to manage the hardware resources and implement an efficient, automated and flexible process for the realization of MPL fabrication. The organization and structuring principles that were considered during development are presented in section 4.1.1.

Within the fabrication process, the scanning of the laser between two points is the most critical step as it typically happens more than ten thousand times per fabrication, even in small structures. As presented in section 3.1, the scanning of the laser focus in the xy plane with regard to the photoresist sample can be performed either with a xyz piezoelectric scanning stage or a set of galvanometer scanners. While the piezoelectric stage offers higher positioning precision, the much faster scanning with the galvanometer scanner enables smoother features and fabrications two or more orders of magnitude faster. The difference in scanning speed also has implications on the polymerization process dynamics, as noted in chapter 6. Therefore, two hardware control schemes were implemented, one for piezoelectric stage-based fabrication and another for galvanometer-based fabrication. Since all the structures presented in this thesis are fabricated with a galvanometer-based scanning, only this approach is described (section 4.1.2).

4.1.1 Architecture and Usability

A framework was established that divides the MPL process in two stages. In the configuration stage, the user might choose to thoroughly configure all process variables or simply use a predefined fabrication profile. In this stage, the focus is in the ease of use and accessibility. In the second stage, the fabrication itself, the process should run autonomously and optimize the use of the hardware to maximize fabrication quality and minimize fabrication time. In this stage, the focus is on performance and autonomy.

Our experimental system is based on an Abberior Instruments INFINITY line STED microscope, which implements or interfaces with the drivers for most of the hardware components through Abberior Instuments' Imspector software [171]. Therefore, Imspector is used as an abstraction layer which enables to

address most of the individual hardware components in a consistent manner through a single communication channel. Besides accelerating the development process, this greatly simplifies the control scheme and is central to the user configuration scheme set in place, as described in this section.

The communication with Imspector is established through its Python interface, Specpy, or, equivalently, through Imspector's Transmission Control Protocol (TCP) server in JavaScript Object Notation (JSON) formatted messages. Each single communication element corresponds to reading or setting a given parameter in Imspector, e.g., a laser power, the pinhole aperture or a shutter status, and each message can contain multiple elements. All the implemented functionalities that build upon Imspector are based on two simple functions, set_parameters and get_parameters, that take a list of parameter names, more specifically a Python dictionary, and either set them to the associated value or just read their value. Therefore, at its basis, any complex procedure can be reduced to an ordered sequence of such instructions, as represented in fig. 4.1.
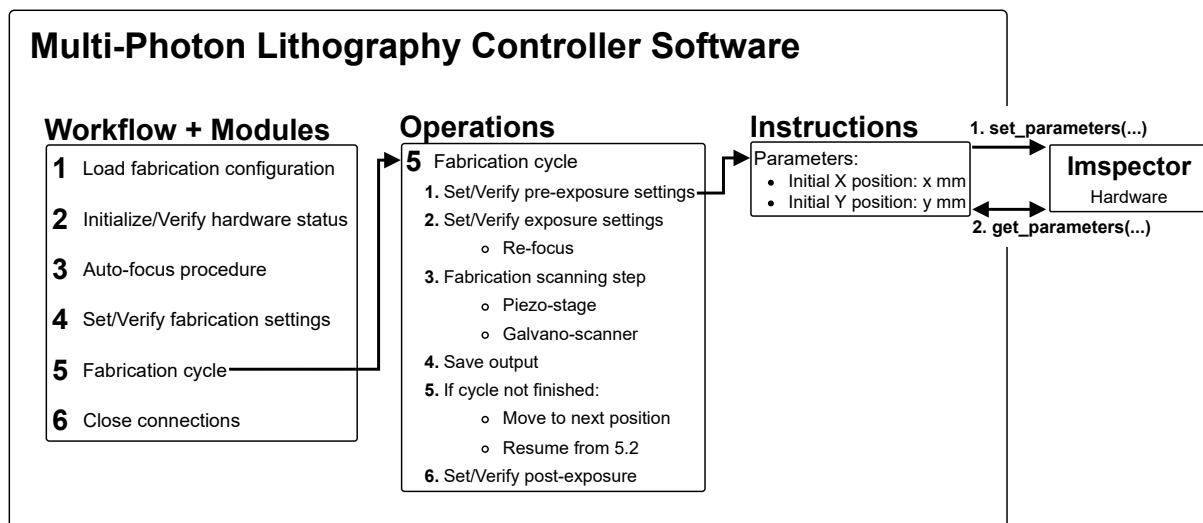
Figure 4.1: Simplified representation of the MPL controller software workflow, showing how the complex MPL process is broken down into modules, operations, and commands. At the lower level, each hardware command corresponds to an ordered list of parameters to be set and/or read through the set/get_parameter commands, which implement the interface with Imspector. The fabrication cycle is only a cycle if configured as such, e.g., in case a structure is to be repeated several times or in the case of a sweep of the fabrication parameters for optimization purposes. The most performance critical step is the fabrication scanning, which can be performed with a piezoelectric stage or a galvanometer-scanner. The characterization step presented in chapter 6, although not specifically mentioned, is configured along with the other fabrication settings in step 4 of the workflow and implemented in the fabrication scanning step, 5.3.

Since Imspector parameter names are human-readable, e.g., the ExpControl/measurement/ channels/0/lasers/3/power/calibrated addresses the power of laser 3 in the measurement channel 0, establishing such complex procedures can, in many cases, be directly imparted to the user by giving the user the possibility to choose which parameters to change at each specific point of the experiment. For example, by providing the user a configuration file that is executed right before the photoresist exposure, the user can freely control the exposure settings based on the list of all available parameters. This concept is at the core of the user interface for the developed software. By expanding the Imspector parameter set with parameters specific to the MPL process, defined along similar human-readable guidelines, and establishing configuration files which provide access to all these parameters at specific and clearly identified process steps such as exposure or auto-focus, the user can either choose to fine tune all the executed parameters at each step of the process or simply start from a pre-defined fabrication profile and adjust a small set of parameters.

An illustrative example of such configuration flexibility is presented in line 23, where a section of the experiment configuration file is shown that defines the pre-exposure, exposure, and post-exposure parameters. In

this simple example the experiment is made to start at stage position $x = 500 \ \mu m$ and the desired structure, which is defined in another configuration file, is to be fabricated three times at different laser powers, namely 5,10 and 15 %, spaced by 100 μm from each other in the x axis. In the post-experience the system is simply made to return to the initial position in the x axis. Parameter sweeps with different settings can be easily compounded within the same configuration file by changing the id number at the start. These are used, for example, to fabricate structure arrays or to optimize sample fabrication by performing a power sweep with spacing in the x direction compounded with a scanning speed sweep spaced in the y axis. Such an extensive set of user-accessible configuration parameters might expose the system to undesirable hardware states that could damage the setup, e.g., having the objective move into the substrate, especially when defined by an inexperienced user. To avoid it, the configurations are checked for the most critical and the most common failure modes and the execution is stopped if a given action is detected to lead to such a state.

```
- 0:                              #step number
  execute: True

  pre_exp:
    parameters:
    ExpControl/scan/range:
    coarse_x/g_off: 500.0e-6

  exp:
    transition_stabilization_time: 1.0             #in sec
    transition:
    add:
      ExpControl/scan/range/coarse_x/g_off: 100.0e-06
    range: [False]
    cycle:
      ExpControl/measurement/channels/0/lasers/3/power/calibrated:
        [5.0,10.0,15.0]

  post_exp:
    parameters:
    ExpControl/scan/range:
    coarse_x/g_off: 500.0e-6
```

Listing 4.1: Section of the configuration file used to define an MPL fabrication run.

Most functional components of the controller software were developed as separate modules. As an example, although the laser scanning control software, along with its process settings, differ for piezo- and galvano-based strategies, they can be interchanged, with remaining steps of the fabrication, such as the auto-focus, pre- and post-process procedures being kept the same. A general overview of the functional modules and their sequence is presented in fig. 4.1. Specific functional modules are further described in sections 4.1.2 and 4.2.

4.1.2   Galvanometer Mirrors Based Scanning

The utilized galvanometer scanner was integrated by Abberior Instruments and is only accessible through Imspector. Since coordinate-based scanning is not supported, a point-by-point scan control algorithm could not be used. Instead, a mask-based exposure was implemented. In this case and for each layer, the galvanometer scanner is made to scan the minimum rectangular region in the xy plane containing all the elements of the structure, e.g., as seen in fig. 4.2, and the laser exposure is controlled synchronously through the AOM, either blocking or transmitting the laser into the sample with a given intensity. In fig. 4.2, the bright and dark pixels represent exposed and non-exposed regions, respectively. The scanning of each layer is done through parallel lines aligned either along the x or y axis.
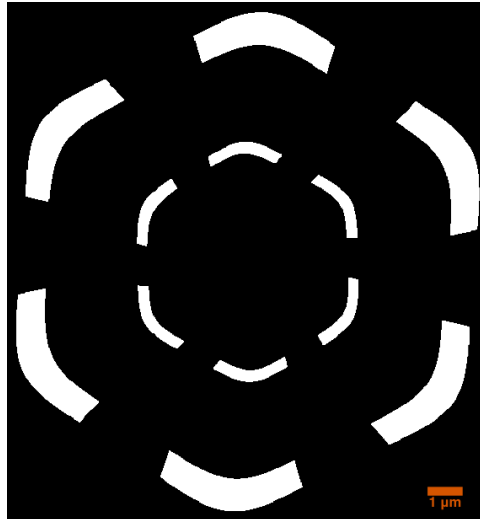
Figure 4.2: Representative mask for exposure of a single layer during galvanometer mirrors based scanning. The whole rectangular area of the mask is scanned by the galvanometer scanner, line-by-line, with the white regions being exposed to the laser while the black regions are not. For the representative case of a negative photoresists, the white regions will undergo polymerization and become insoluble.

The described mask scanning feature was already available in Imspector, where it is implemented in an Field Programmable Gate Array (FPGA) to achieve operation control at the sub-μs range, thus dismissing the development of a new control algorithm. Since performance is taken care of by the FPGA implementation and is no longer a critical aspect, the galvano scanning software module is written in Python.

Prior to the fabrication, the desired 3D structure model needs to be discretized into a step-wise representation. For galvanometer-based scanning, a layer-by-layer discretization, or slicing, is used, with each layer being represented in an image, or mask, as exemplified in fig. 4.2. A new software module is developed that uses 3D Slicer's [172, 173] Medical Reality Modeling Language (MRML) Segmentation Node to discretize a 3D structure into a set of z-spaced parallel layers with given x and y pixel sizes. The slicing process, as well as the remaining parameters necessary for mask-based scanning, can be configured through dedicated configuration files. These configurations are loaded onto the FPGA at the time of fabrication, enabling reliable sub-μs control of the hardware components.

For larger structures whose dimensions exceed that of the galvanometer scanner workspace ($80 \times 80 \, \mu m$), a stitching process is implemented which uses the large-range piezoelectric stage in the system (see section 3.1) to recenter the galvanometer scanner in a contiguous fabrication region. In this process, the more precise xyz piezostage is used to correct any position error introduced by the large-range stage in its motion between two fabrication starting points. Instead of using the full range of the galvanometer scanner, which induces structural deformation due to the laser being scanned in the periphery of the objective lens, the stitching mechanism enables to improve fabrication fidelity by using smaller fabrication regions. Each of these fabrications regions has a dedicated mask representation.

The applications presented throughout this thesis, described in chapters 5 to 7, are achieved with galvanometer-based scanning, rather than piezoelectric stage scanning, since it enables faster fabrications, improved surface quality, as seen in fig. 4.3, and attenuates excited state absorption, as explained in chapter 6.

4.2 Hardware Functionality Algorithms

While the software modules and principles reviewed in section 4.1 establish the basis for hardware control and the core fabrication step, i.e., the scanning of the fabrication laser, these are insufficient to establish a general and automatic fabrication process. To do so, additional modules are built upon such basis to
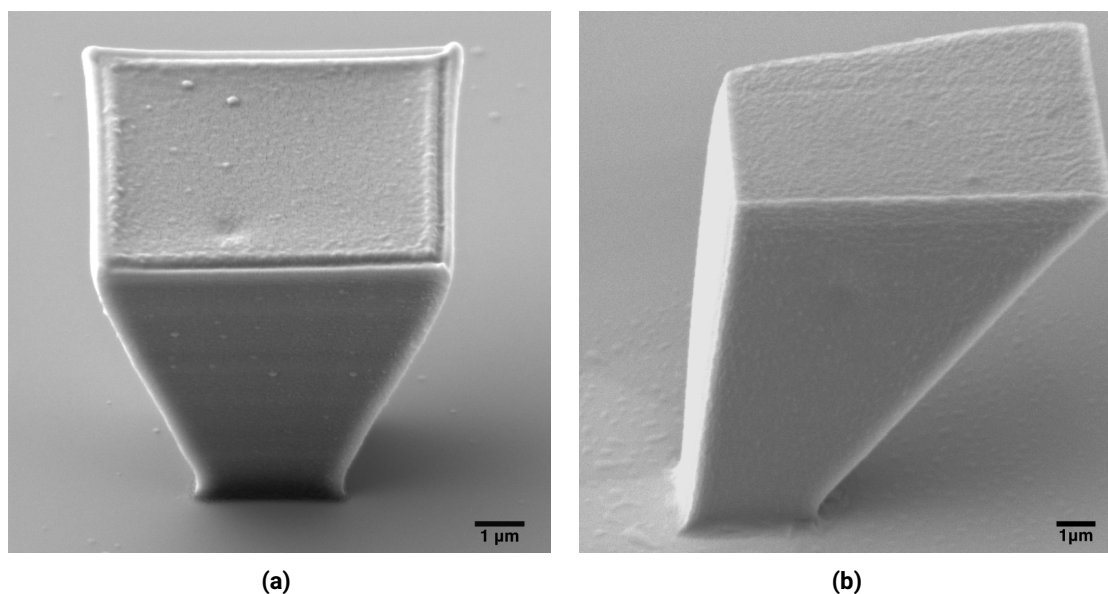
Figure 4.3: Comparison between piezo- (a) and galvano-based (b) scanning on the fabricated structure surface quality. Particularly at the edges and corners, piezo-based scanning leads to non-uniform feature sizes. The increased speed of the galvano scanning enables closer layer packing and smaller pixels, improving surface roughness.

provide added functionality to the whole process. The description of these functional modules is presented in this section.

4.2.1 Auto-Focus

Determining the position of the interface between the substrate and the photoresist is of great importance in the context of MPL as it affects the systematic and successful realization of a structure, i.e., the fabrication yield. A starting focus position inside the substrate but close to the interface is desired [74], as it improves substrate adhesion while having little impact on the fabrication result. Thus, in order to achieve a reliable and precise starting position relative to the substrate-photoresist interface, an auto-focus procedure is implemented.

The auto-focus method utilized in this thesis is based on the faint increase in the reflection signal at the interface between the borosilicate glass substrate and the photoresist, due to the difference in the refraction index of both materials, typically on the order of $\Delta n = 0.03$. Therefore, the implementation of the auto-focus corresponds to the measurement of the reflection signal at regularly spaced positions along z within a given range. The 780 nm laser, the same used for fabrication, is used as the reflection probing source in order to increase the auto-focus precision, but a laser intensity about 100× lower than the polymerization threshold is used to avoid affecting the sample. The signal is averaged over a 5 μm line scanned along x, increasing robustness to local defects while keeping the scanning time low. The reflection signal is registered through a Photo-Multiplier Tube (PMT). After the reflection is measured at all positions in the range, the resulting data is fitted to a Cauchy distribution. If the R-squared parameter of the fit is above a given threshold, the z position corresponding to the fitted maximum is taken as the interface position. This verification step makes the system robust to undesired reflection signals.

For ease of use, the auto-focus process is implemented as an ordered set of instructions that exposes all the relevant parameters to the user, e.g., which piezoelectric stage to use for the z motion and the motion step and range, in an auto-focus configuration file, providing increased flexibility.

Different auto-focus settings are useful in different stages of the fabrication process. While at the start of a fabrication a wide and coarse range auto-focus enables to quickly find the approximate interface position, a finer auto-focus is useful to reacquire the interface after a large displacement in the xy plane. Since, in a single fabrication, several sets of auto-focus parameters are necessary, a profile-based approach

was used, where different subsets of auto-focus parameters are defined under specific keywords, with each keyword, e.g., refocus, corresponding to a specific situation where the auto-focus is executed.

4.2.2 Proportional Controller

An algorithm to control the fabrication laser power and the scanning speed was implemented in the context of the MPL fabrication control described in chapter 6. The algorithm is based on a proportional (P) controller, and acts on the fabrication laser power and the scanning speed to keep the average fluorescence over the masked region, i.e., the process variable, constant throughout all of the fabrication.
The scanning speed is used as a control variable in order to compensate for the dispersion of the fabrication laser and that of the fluorescence emission. By adjusting the scanning speed, the fluorescence signal is integrated over a longer period, compensating for the increased fluorescence emission dispersion as well as for the dispersion of the fabrication laser. By itself, this is not sufficient to maintain a stable exposure dosage over the fabrication process and therefore the fabrication laser power is also compensated, affecting only the fabrication and not the characterization stage. These two control variables are not independent and need to be adjusted adequately. Such a control scheme was chosen as it enables to simplify the implementation. The control algorithm is described in algorithm 1 and below.

Algorithm 1 Exposure control algorithm based on a proportional (P) controller

---

Require: Layer Fluorescence Data
  1: **if** Detected stable additional fluorescence **and** Setpoint tracking not started **then**
  2:      **if** Automatic threshold **then**
  3:          setpoint = average fluorescence in exposed regions
  4:      **else**
  5:          Load setpoint from configuration file
  6:      **end if**
  7:      Start Setpoint tracking
  8: **end if**
  9: **if** Setpoint tracking started **then**
 10:      Update process variable
 11:      Calculate new control variables
 12:      Log controller variables
 13:      **if** Stable additional fluorescence **and** $\|$Setpoint - Process variable$\| \geq$ Error threshold **then**
 14:          Set new control variables values
 15:      **end if**
 16: **end if**

The implemented control algorithm is a P controller with operation and stability ranges. The operation range defines the range of the process variable under which the control is applied. This is defined based on the variance of the process variable over the last 5 layers and works to ensure the control is not applied while some other change is affecting the signal, e.g., the proximity to the substrate or a previous change to the control variables. The stability range defines the acceptable error for the control algorithm. It is defined based on the difference between the value of the process variable and that of the setpoint and works to avoid constant modification of the control parameters due to statistical fluctuations of the process variable. As a whole, this corresponds to a control algorithm which only acts on the control variable once a stable and significant deviation of the process variable relative to the setpoint is detected.

The process variable setpoint can be defined manually or automatically. If the starting exposure settings, such as the fabrication laser and the scanning speed, have been previously optimized and are known to trigger polymerization, then an automatic setpoint definition ensures some robustness to the process signal variability in different fabrication samples, improving reproducibility, and maintains the intended fabrication quality throughout the height of the structure. This is implemented by measuring the process variable variance over 5 layers from the start of the fabrication and registering the process variable value at

which the variance first becomes smaller than a predefined threshold, i.e., the value at which the enhanced fluorescence signal stabilizes for shallow layers. If, instead, the optimal exposure parameters are yet to be defined, a manual fluorescence signal setpoint would enable the exposure parameters to be freely modified by the control algorithm until it converges to stable fabrication settings. This corresponds to in-situ and realtime parameter optimization.

4.3 Data Processing Algorithms

Two data processing algorithms were developed to process the data relative to the studies presented in chapters 5 and 6. These provide significant advantages to the analysis and applications they address and are hereby presented.

4.3.1 Analysis of Domain Wall Motion from MOKE Data

For the analysis presented in chapter 5, more than 25 different devices were analyzed under 8 or more current densities per device and 4 configurations per current density, i.e., $\odot \otimes$ and $\otimes \odot$ DW configurations moving along $+x$ and $-x$. Each configuration was repeated at least 3 times and each repetition is composed of 10 to 35 images. Even the dataset selected for the final analysis consists of more than 50000 images to process. For each image, the objective is to quantify the domain wall displacement induced by the corresponding current pulse, observed as a darker or brighter shade (as in fig. 3.3d), and calculate the DW velocity associated with each pulse, referred to as local velocity, or the whole sequence of pulses, referred to as average velocity over the device. Figure 4.4 shows a few representative examples of raw acquisition images.
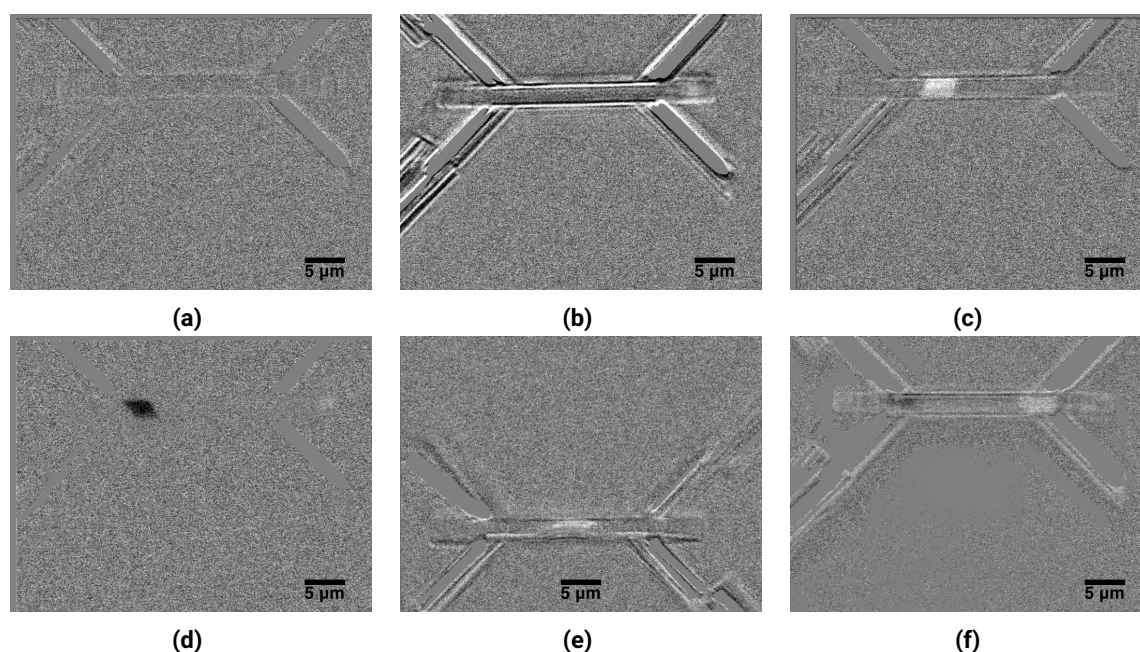
Figure 4.4: Representative MOKE microscope acquisition images for the analysis presented in chapter 5. (a) no DW displacement signal. (b) susceptibility to vibrations causes high noise levels that mask a $\otimes \odot$ (in white) displacement on the right end of the device. (c) $\otimes \odot$ DW displacement (white region) towards the right side. (d) $\odot \otimes$ DW displacement (black region) towards the right side. (e) edge case for a $\otimes \odot$ DW displacement towards the right over a 45 ° torsion device that is made difficult to detect by the torsion angle and vibrations. (f) the compensated magnetic moment of the magnetic layers in a SAF stack decreases the MOKE signal, further complicating the detection of DW displacement as well as the nucleation of DW.

Manual processing of such dataset would be unreliable, imprecise, time-consuming, hard to validate and susceptible to changes in the analysis. On the other hand, the noise level in the images, as in figs. 4.4b

and 4.4e, and the inconsistent number of significant elements in an image, e.g., due to DW nucleation or collapse, creates many different types of edge cases, deeming a fully automated data processing unreliable and difficult to validate.

In this context, a semi-automatic processing program was developed where the detection and measurement of all the shaded regions in an image are automated, improving the analysis speed and precision, while relying on the user to supervise the software operation by selecting, in each image and from a pre-selection of automatically detected regions, the shaded regions that are relevant for the analysis. A verifiable process was set in place that saves the data at each critical point in the analysis and provides the visualization tools for any third party to quickly review the selection criteria used in it. By saving the data at several steps, the developed software also enables to re-do part of the analysis by loading the data of the previous step, without requiring the re-processing of the whole dataset, as well as to do different types of analysis by starting from different sets of processed data.

The data processing steps are now described in further detail with examples. For the image processing steps, the OpenCV [174] Python library is used. One of the biggest obstacles for automated detection of DW displacement is the predominant presence of speckle noise in the raw acquisition images, as seen in fig. 4.5. This noise level is, in part, unavoidable, as it results from a contrast enhancement operation that is necessary for the detection of the shaded regions related to the DW displacement. Filtering out this noise is a complex task which, in most cases, also significantly affects the measured signal, e.g., when using averaging operations such as Gaussian or median blurs, which is not admissible. In this work, such limitation was overcome by utilizing MPRNet [175], a state-of-the-art multi-stage neural network architecture that is able to restore degraded images while keeping local spatial details. As seen in fig. 4.5, the restored image after MPRNet's denoise operation is seen to keep its local features while removing the unwanted noise. To speed up the analysis, the denoise operation was applied as to all images in the dataset as a pre-processing step, and the restored images were saved in a sub-directory.

(a)   (b)
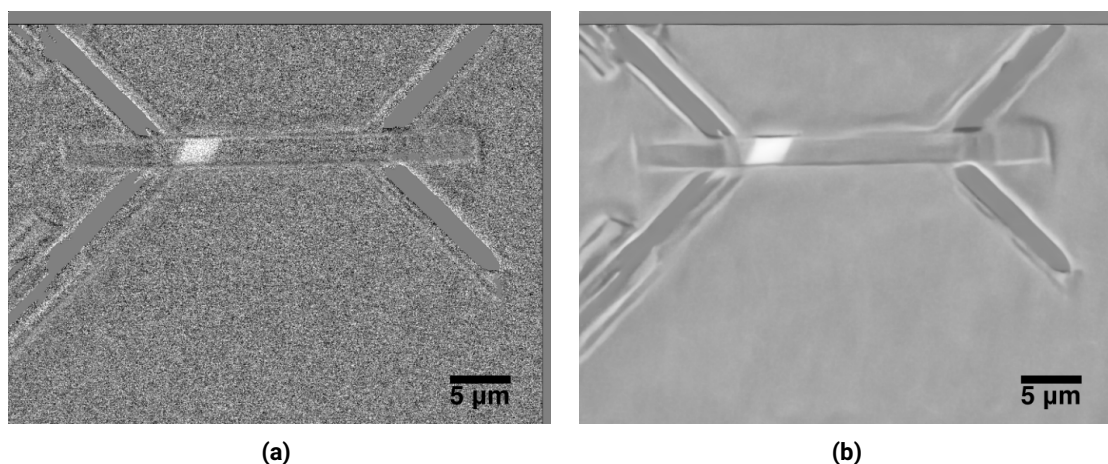
Figure 4.5: Acquisition image (a) and corresponding restoration with MPRNet (b). The restoration almost completely removes speckle noise without significantly affecting the local spatial details, which is essential for the precise and reliable automated detection of DW displacement.

After pre-processing, the first processing step is to isolate the region of the ribbon, i.e., the central part of the device. Edge detection in such 3D devices is hindered by artifacts due to the objective's depth of field and sensitivity to vibrations, as seen in fig. 4.6. Instead, the contours of the ±45 ° angled structures, seen in fig. 4.6, which are always seen to saturate the camera, are used to determine the bounding box of the ribbon through a set of reference points (large white circles in fig. 4.6b). The same bounding box is then used for all images of the acquisition series, but it is re-positioned for each one based on one of the reference points. The determined bounding box is then used to crop the region of interest in the corresponding restored image, as shown in fig. 4.6c.

The detection of the shaded regions is then realized on the cropped image. By incorporating the
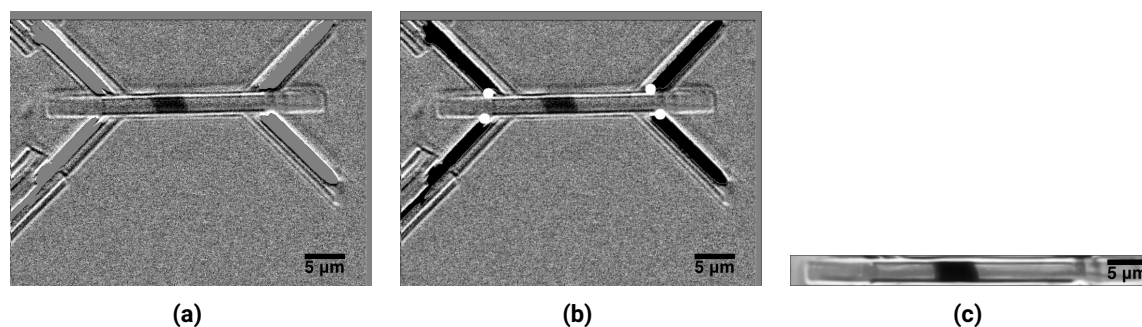
Figure 4.6: Isolating the central section of the device for further processing. (a) Example of an acquisition image where an edge-based detection would be imprecise due to vibration induced noise. (b) Instead, the contours of the overexposed areas of the pad delimiting structures, shown as dark regions, are used to determine a set of points in the bounding box of the central section, here shown in as white circles. (c) After detection of the bounding box, it is used to crop the region of interest from the corresponding MPRNet restored image and the tilting angle is corrected.

knowledge of the DW configuration in each series, defined in the configuration files utilized to run the acquisition, it is possible to determine whether a brighter of darker shade is expected, as explained in section 3.7, and use this knowledge to expand the range of the expected shade. For example, if a brighter shade is expected, the lower half of the 8-bit image range, corresponding to darker shades, is discarded, e.g., by setting its value to a mid-range gray value, and the range of interest is then expanded through a normalization, as shown in fig. 4.7. This step helps to greatly improve the contrast between the background signal level and that of the shaded region associated with DW displacement, as observed in fig. 4.7, and improves the algorithm robustness to slight fluctuations in the values of the shaded regions of interest, improving the precision of the DW displacement measurement.
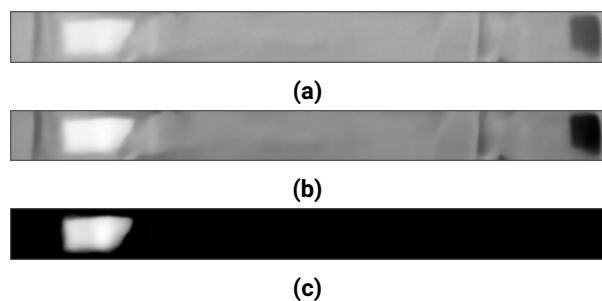
Figure 4.7: Improving shade contrast for DW displacement detection. (a) Starting point for the range extension operation, after the cropping operation described in fig. 4.6. (b) A first normalization and bilateral filtering are applied to further smoothen the image without affecting the edge location. (c) The half of the image range where the DW displacement region is expected is kept, i.e., the white half of the range in this case, while the other half of the range is discarded, i.e., the darker half of the range, and the image is once more normalized, resulting in an effective expansion of the image range.

Despite the significant contrast already achieved in the processed image, contour detection algorithms require binary images. Thus, two different automatic threshold algorithms are applied to the processed image, generating two different binary images. Specifically, two algorithms are used redundantly to provide robustness to the measurement process and increase precision, since each of them is seen to provide better results or fail in different cases, as exemplified in fig. 4.8. The first algorithm, Adaptive Gaussian threshold, determines a local adaptive threshold level based on a Gaussian kernel while the other, Otsu's algorithm, is a global threshold algorithm that minimizes the variance within each of the two classes of pixels in an image [176]. A border-following contour detection algorithm [177] is then applied to each of the binary images to detect the shaded regions.
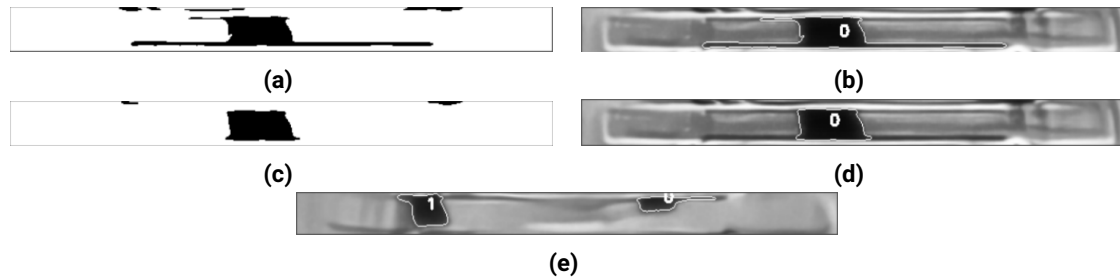
Figure 4.8: Thresholding and selection of the detected contours. Adaptive Gaussian thresholding (a) as well Otsu's algorithm (c) are applied after the processing described in fig. 4.7. Here, the case from fig. 4.6 is represented, with Otsu's algorithm being able to avoid the noise-induced features in the image while the adaptive Gaussian threshold algorithm is not. The user selection display is show in (b) and (d) for the adaptive Gaussian threshold and Otsu's algorithm, respectively. In (e), the user selection display is shown for a case where a DW nucleates near the center, on the right side, due to surface defects, in addition to the expected DW that is nucleated at the left end of the device. In this case, only the one at the left end is selected.

At this point, the contours detected based on each of the two threshold operations are presented to the user for selection, overlapped with the cropped section of the restored image as show in figs. 4.8b and 4.8d. The user is then prompted to select which, if any, of the detected contours best approximates the relevant shaded regions. This workflow enables the user to closely supervise the operation of the algorithm, ensuring that only the contours corresponding to the consistent motion of the injected DW are selected while filtering out others due, for example, to DW nucleation, as seen in fig. 4.8e. As previously referred, the ability to select contours from different threshold algorithms enables to overcome the limitations of each and ensure that at least one precise contour is available for the large majority of the cases, improving the precision of the method.

After the selection phase, if any contour is selected, it will proceed to be measured. The measure of interest is the horizontal displacement of the DW along the x (horizontal) axis, as shown in fig. 4.9. In many cases, however, the boundaries of the displacement region are irregular, which might induce a large measurement error if not properly handled. To robustly measure the displacement width a method was implemented that intersects 10 horizontal lines, equally spaced between the maximum and minimum y (vertical) coordinates of the contour, with the selected contour and measures the average and the standard deviation of the distribution of measurements. If the standard deviation is above a given threshold, which signals an irregular contour boundary, the measured displacement that further deviates from the average is removed and the new average and standard deviation are calculated. This process is repeated until the standard deviation is smaller than the defined threshold. For the large majority of cases, the DW displacement measurement is based on 8 or more points. The filtered set of points used for the displacement measurement is also shown to the user for verification, as in fig. 4.9. At this stage, the displacement is measured in only in pixels.
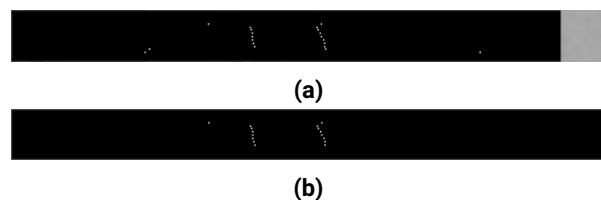
Figure 4.9: Measurement of the user selected DW displacement. Displacement measurement points before (a) and after (b) filtering out outliers. Specifically, it corresponds to the measurement of the contour in fig. 4.8b. Although a complex contour is selected with irregular width, as seen in (a) and fig. 4.8b, an outlier removal step (b) is able to greatly improve the precision of the measurement, increasing the robustness of the algorithm.

This step marks the end of the image processing and image information extraction. At this stage, the

selected contours and the points utilized for displacement measurements for all images in a sequence are saved in a specific file. The analysis software enables any other person to load such files and easily verify the contour selection criteria used during the data processing.

The remaining processing corresponds to the conversion of the extracted image data to data with physical significance and the use of this data to determine relevant physical quantities such as the local and averaged DW velocity. The configuration files utilized to run the experimental data acquisition are used in combination with an additional configuration file which contains all the additional measured or calibrated quantities such as the resistance, width and film thickness of each measured device or the pixel to μm conversion. By combining all this data, it is possible to calculate the local DW velocity associated with each of the validated DW displacements, as well as the averaged DW velocity associated with the cumulative contribution of all the validated DW displacements over each complete sequence of pulses. The whole processing workflow is summarized in fig. 4.10. All these determined quantities are saved in a separate data file for each acquisition series and establish the base dataset for the analysis presented in chapter 5.
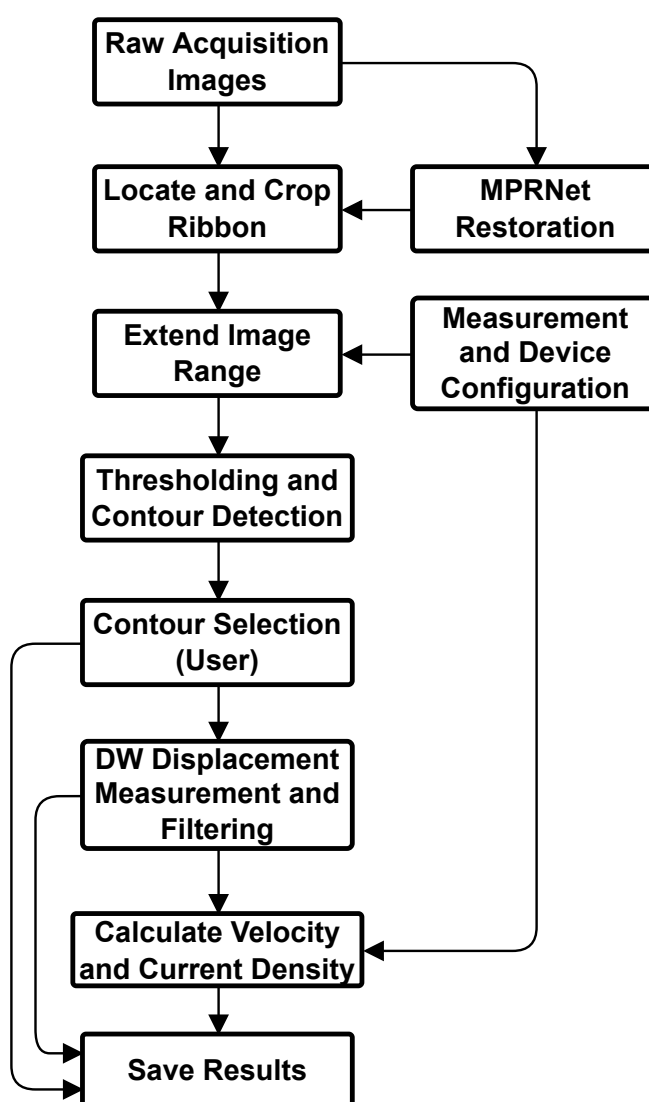
Figure 4.10: Overview of the MOKE data processing algorithm

4.3.2   3D Reconstruction of an MPL Fabricated Structure

Following the observation of an increased fluorescence emission under sequential exposition to the 780 nm MPL laser and a 532 nm CW probe laser, addressed in chapter 6, an algorithm was implemented to perform 3D reconstruction of the fabrication result based on this data. This section describes the implementation of such reconstruction in more detail, complementing the description provided in chapter 6.

The realtime fabrication and characterization method described in chapter 6 produces, for each fabrication run, an equally spaced z-stack of the characterization fluorescence signal. Each layer of the stack represents the fluorescence signal registered at a given height, and is directly related to the fabrication mask used for the same layer at the same height, as can be seen in fig. 4.11. Each pixel in a layer corresponds to the fluorescence emission counts at the corresponding spatial location, as registered by the APD during the dwell time of the scanning, typically between 5 and 30 μs. The objective of the reconstruction process is then to take this data, filter out the unpolymerized regions and use the resulting data to generate a 3D mesh of the resulting structure, balancing the mesh quality and its fidelity.
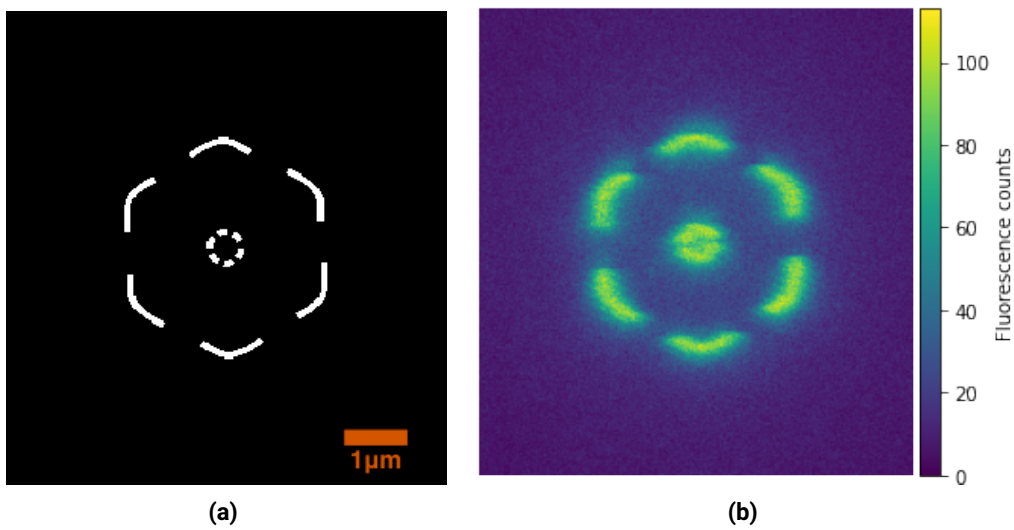
Figure 4.11: Correspondence between fabrication layer mask (a) and increased fluorescence observed at the same focal plane (b).

First, the characterization data corresponding to unpolymerized regions is filtered out. While the signal to noise ratio between polymerized and unpolymerized regions is significant, typically between $4 - 7\times$ as shown in chapter 6, there is a smooth transition region, observed in fig. 4.11b, which can have a large impact on the result of the reconstruction and its fidelity. Filtering out the unpolymerized regions with a simple threshold operation is seen to more precisely match the fabrication result than more complex methods such as adaptive thresholds. The fluoresce threshold value is determined through histogram analysis, by isolating the histogram peak observed at bins corresponding to higher counts, as in fig. 4.12, and analysing its distribution throughout all the layers. Two aspects should be noted. First, applying a constant threshold value throughout the whole structure is only possible because the dispersion of fluorescence signal at higher layers was compensated for by decreasing the scanning speed during fabrication, as explained in chapter 6. Second, a fluorescence threshold needs only to be determined once for each set of fabrication and characterization parameters. Since, in most cases, a fabrication is run based on previously optimized parameters, the corresponding fluorescence threshold can be reused as well, if previously determined.

The statistical nature of fluorescence emission paired with simple thresholding leads to a discretization error that is akin to salt and pepper noise, as observed in fig. 4.13a, resulting in noisy layer representations and rough reconstructions. In order to achieve smoother and cleaner reconstructions, a Gaussian blur is applied in xy and another in z, followed by a bilateral filter. Small Gaussian kernel dimensions corresponding to 100 nm in xy and 150 nm in z, i.e., on the order of the voxel size, and a bilateral filter are
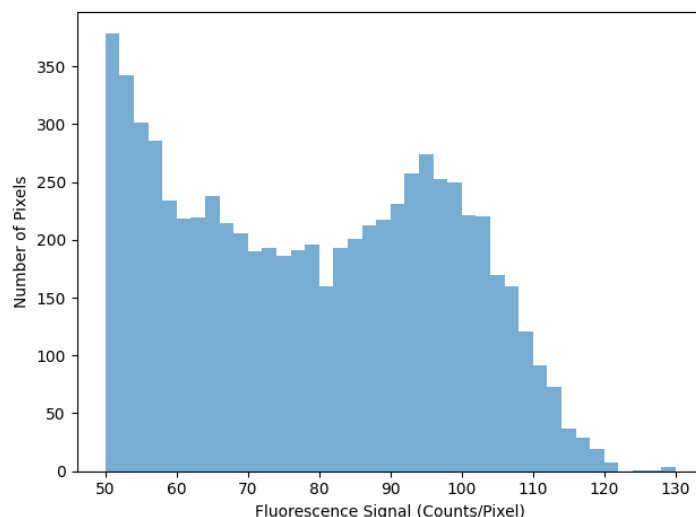
Figure 4.12: Histogram of the fluorescence signal corresponding to a single layer. Although partially masked, a peak is noticeable at the high intensity region, on the right, that corresponds to the desired signal. After analysing the histogram for all layers, the fluorescence intensity threshold value is set at 85 counts per pixel.

chosen to compensate for pixel sizes smaller than the voxel sizes without otherwise significantly affecting the positions of the edges, as shown in fig. 4.13b. At small pixel sizes, e.g., 25 nm, where edges of the polymerized regions can be more precisely estimated, it could also be beneficial to perform a convolution of the polymerized pixels with a voxel sized volume instead of the Gaussian blurring.

(a) (b)
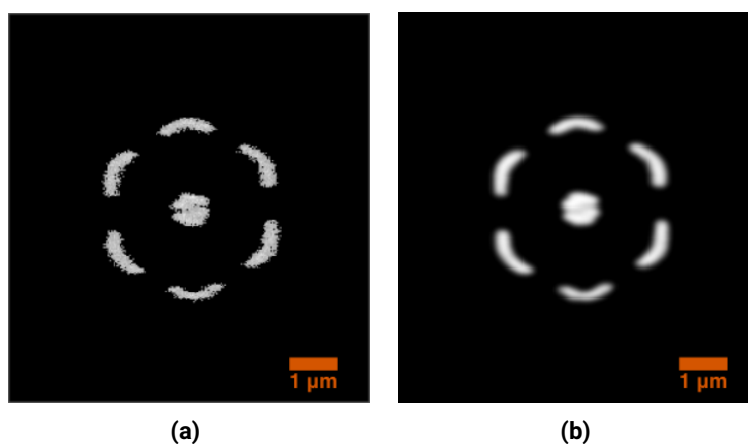
Figure 4.13: Processing of fluorescence signal. Starting from the data in fig. 4.11b, (a) shows the fluorescence signal after threshold, with salt and pepper noise that leads to increased roughness in the reconstructed mesh. (b) shows the result after Gaussian blurring and bilateral filtering, smoothing the signal without affecting the edge positions.

After thresholding, a layer-based binary representation of the fabricated structure is achieved, divided in polymerized and non-polymerized regions. This layer based binary representation is converted into a point cloud, a 3D coordinate-based representation that already incorporates the pixel sizes and layer spacing defined at the fabrication, as observed in fig. 4.14a. All the point cloud and mesh-based operations described here are implemented using Open3D [178, 179]. For the correct meshing of a point cloud, the surface normals must be correctly defined at each point. While the normal axis can be determined by locally fitting a plane to the surface, the exact direction can be difficult to determine. Since we have a volumetric point cloud, the correct normal direction was determined by calculating, for both possible normal directions, the distance to the nearest polymerized point and selecting the one with higher distance, as that will be the one outside of the volume defined by the set of polymerized points.
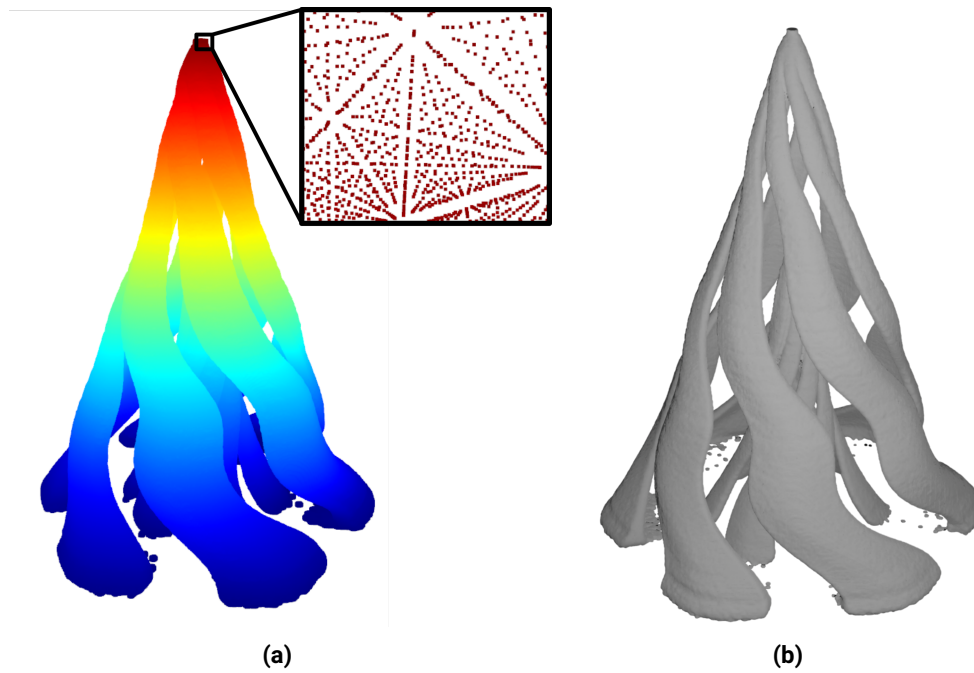
Figure 4.14: Point cloud generation and meshing.(a) Distribution of points in a volumetric point cloud. Zooming in on the point cloud highlights its discrete nature. (b) Resulting mesh after applying a Poisson surface reconstruction on the poinctloud, followed by vortex clustering.

Afterwards, a Poisson surface reconstruction [180] is applied to the point cloud to generate a mesh. In order to capture fine surface details, higher resolution functions are used by setting the tree depth to 11. The mesh is then simplified through a vertex clustering within the volume of a sphere with radius of the size of the scanning pixel, in order to remove any sub-pixel features and make the resulting mesh easier to process. An example of a reconstruction result is shown in fig. 4.14b.

Chapter 5

Interplay of Torsion and Spin Chiralities in Domain Wall Motion Over 3D Magnetic Ribbons

Spin-orbit torque driven domain wall motion [181] (see section 2.3.3) has enabled the achievement of magnetic domain wall logic [115] and magnetic domain-wall memory devices [121], and is a promising candidate for in-memory computing architectures[24] targeting, for example, neuromorphic computing [182]. While SOT drives both configurations[1] of a chiral DW at the same velocity, such a degeneracy can be lifted, in 2D magnetic wires, by geometrical features such as curvature[183] or branching[184] due to DW tilting[185, 186].

Simultaneously, exploration of the magnetic systems with 3D geometrical features such as curvature and torsion has attracted much attention lately. As discussed in section 2.4, theoretical studies show that such geometrical features induce anisotropy and chiral DMI-like exchange interactions. For example, it has been predicted that chiral symmetry breaking due to this DMI-like effect moves DWs along opposite directions in left- and right-handed magnetic helices [187], and it has been experimentally shown that such effects can lead to DW auto-motion in spirals [122]. Furthermore, this geometry-driven DMI is expected to stabilize complex magnetic textures, such as skyrmions, with unique properties [3, 188].

However, as reviewed in section 2.5, while 3D curvilinear magnetic structures have been much studied theoretically, the fabrication and characterization of such structures and their integration into electronic devices are challenging. This has limited experimental demonstration of geometry-induced magneto-chiral effects in 3D structures, especially the current-induced manipulation of chiral topological excitations such as chiral DWs.

In this chapter, I present the realization of a 3D magneto-electronic device with torsion and characterize the current-induced domain wall motion over it. The torsion chirality is seen to interact with the magnetic DW chirality, lifting the degeneracy between the two possible DW configurations and affecting their motion differently. The experimental results are confirmed by results from an analytical model presented in section 5.F. The devices are observed to work as current-controlled DW filters, and a DW diode functionality is predicted. The utilized fabrication workflow provides a significant opportunity to explore a wide range of 3D geometries and their effects in magnetic systems.

5.1   3D Device Design

The device design, shown in fig. 5.1, comprises 3 elements: the ramps, the suspended (or twisted) ribbon section, and the electrical contact pad delimitation.

The ramps provide mechanical support for the suspended section and establish an electrical connection from the substrate to it.

---

[1] i.e., $\odot \otimes$ and $\otimes \odot$

59
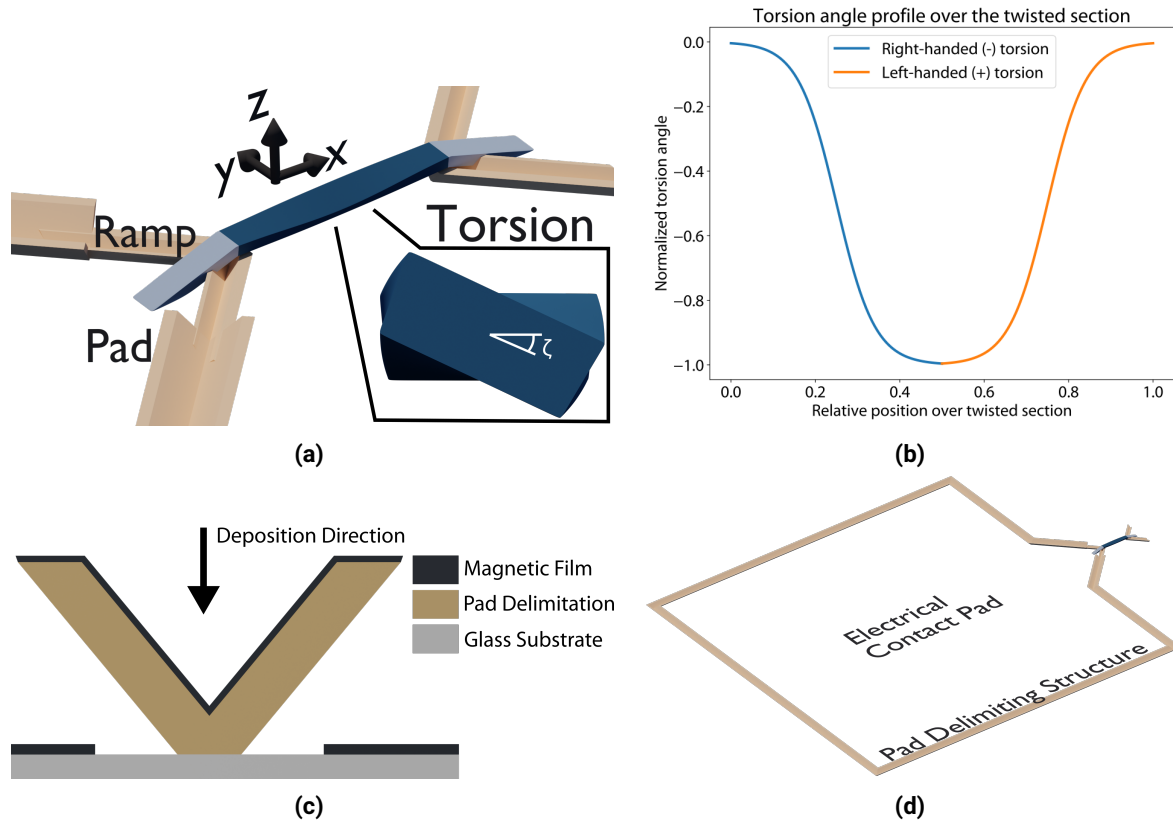
Figure 5.1: 3D twisted ribbon device design. (a) Functional components of the device design, color-coded. A cross section of the twisted region, taken at its midsection, is shown in the inset, displaying the left-handed torsion over the second half of the device. ζ describes the angle between the substrate (horizontal) and the maximum inclination of the surface induced by torsion, verified at the midsection. The inside of the pad is defined by the contact pad delimitation structure shown in light brown. (b) Torsion angle profile over the twisted section, evaluated from the left end (the one in the fully enclosed pad, corresponding to relative position 0) of the device towards its right end (relative position 1). The torsion angle is shown normalized to the maximum angle in the twisted region, verified at its midsection. The maximum torsion angle varies among devices, as explained in the text. The torsion angle proceeds towards negative values because a right-handed torsion is defined as leading to negative torsion angles. Thus, a negative torsion angle in the text is associated with a right-handed torsion in the first (left) half. The torsion is proportional to the derivative of the torsion angle rather than to the torsion angle itself, and is therefore maximum (in modulus) at the 0.25 and 0.75 relative positions over the suspended section. (c) A V-shaped structure shadows the substrate underneath during the magnetron sputtering of the magnetic film, preventing material deposition. (d) By extending a V-shaped cross section along a closed perimeter around one end of the devices, an isolated contact pad is established, such that the connection between the inside and outside is only realized through the device.

The suspended section of the ribbon is the main region of interest throughout this chapter because of its torsion[2]: its cross section is continuously rotated along the longitudinal direction, as shown in figs. 5.1a and 5.1b.

Different halves of the device have different torsion signs such that both device ends are horizontal and parallel to one another and to the substrate. For example, a device with a left-handed or anti-clockwise torsion chirality in the first half has a right-handed or clockwise torsion chirality in the second-half. It follows that the device has mirror symmetry around its midsection. Positive and negative torsions are associated with left- and right-handed torsion chiralities evaluated along $+x$ (see fig. 5.1), respectively. The rotation profile along each half of the device length has the shape of a logistic function, shown in fig. 5.1b, to guarantee surface continuity. Therefore, the torsion, i.e., the rate of rotation, is not constant over the device, being maximum at 1/4 and 3/4 of the suspended section length and 0 at its middle and

---

[2]a twisted structure is a structure with torsion

both its ends.

The angle between the substrate plane and the midsection of the ribbon (see inset of fig. 5.1a) is referred to as the torsion angle ζ of the device and is used to identify different devices. A device with higher ζ has a higher torsion magnitude while a device with ζ=0 is perfectly horizontal.

The electrical contact pads are defined by fabricating a structure with a V-shaped cross section at their boundary that prevents material deposition underneath it, electrically isolating the inside from the outside. This exploits the directionality of the deposition method to create a shadow underneath the structure where no material is deposited (see sections 3.5 and 5.2). Only one fully delimited electrical contact pad with a $150 \times 150 \ \mu m^2$ area is defined per device in order to decrease fabrication times, being enough to electrically isolate both ends of the device.

The devices have a $40 \times 2.5 \ \mu m^2$ footprint, with the suspended section having a $20 \ \mu m$ length. In specific cases that are explicitly identified, devices with 1.25 and $5 \ \mu m$ widths are also tested. Devices with $\zeta = 0, \pm 11, \pm 18, \pm 26, \pm 45$ ° torsion angles were fabricated and tested[3]. All of the devices have ramps with an elevation angle of 18 °. These angles were selected as they minimize the discretization error for equally spaced layers along z, since no adaptive height slicing algorithm [189] was implemented at the time.

5.2   3D Device Fabrication and Characterization

The device design, and in particular the approach to electrical pad definition, greatly simplifies the fabrication process to only 2 steps: the fabrication of 3D polymeric structures and their coating.

MPL is utilized for the fabrication of the 3D polymeric scaffolds, as depicted in figure fig. 2.2 and detailed in section 3.1. During layer-by-layer scanning, the spacing between every two scans is minimized in order to optimize the resulting surface roughness, which is critical to achieving high-performance devices. 25 nm spacings in x and z are achieved, corresponding to about 1/4 of the voxel size. The MPL fabrication yield is about 92 %, evaluated over a set of more than 70 devices, although some are later observed to have point defects that affect their performance.

SEM analysis of the fabricated structures shows that most surfaces are consistently smooth, with only the torsion and ramp sections, at 18 ° angles, generally presenting resolvable steps, as seen for the ramps in the fig. 5.2b. The appearance and severity of such steps at the ramps are influenced by the development step of the MPL process, possibly due to shrinking and hydrodynamic forces, and can be mitigated through future design optimization. Such steps impact the device's performance to an unknown extent but do not compromise its functionality.

The device footprints are measured to be about $37.5 \times 2.35 \ \mu m^2$ instead of the designed $40 \times 2.5 \ \mu m^2$. The length mismatch affects mostly the ramps and is due to starting the fabrication with the laser focused inside the substrate to promote adhesion, while the width mismatch is attributed to shrinking during development.

The resulting 3D structures are used as scaffolds on which the magnetic material stack is deposited by magnetron sputtering, as detailed in section 3.5.1. The stack comprises a thin Co/Ni/Co ferromagnetic layer with perpendicular magnetic anisotropy deposited on top of an heavy metal (Pt) layer. The heavy metal and ferromagnetic layers are delimited by a 100 Å thick TaN adhesion layer underneath, which is made thicker to further improve the surface roughness, and a TaN capping layer above. Some devices are coated with a SAF stack instead, where a second Co/Ni/Co ferromagnetic layer is anti-ferromagnetically coupled with the first through a Ru spacer, as specified in section 3.5.1.

After deposition, an RMS surface roughness of 0.37 nm was measured over the torsion section of a +11 ° torsion device by AFM[4] (Asylum Research Cypher), compared to 0.1 nm over a similar area of the substrate. The device topography is shown in figure fig. 5.2d. All but the biggest surface defect over the device were accounted for.

---

[3]note that the torsion angle, and therefore the device labelling, is defined by the torsion chirality on the left (or first) half of the device, with the torsion in the other half being of the opposite chirality.

[4]the scan was realized in AC mode with 10 nm pixel size, 0.3Hz line scan rate and 600 mV voltage setpoint
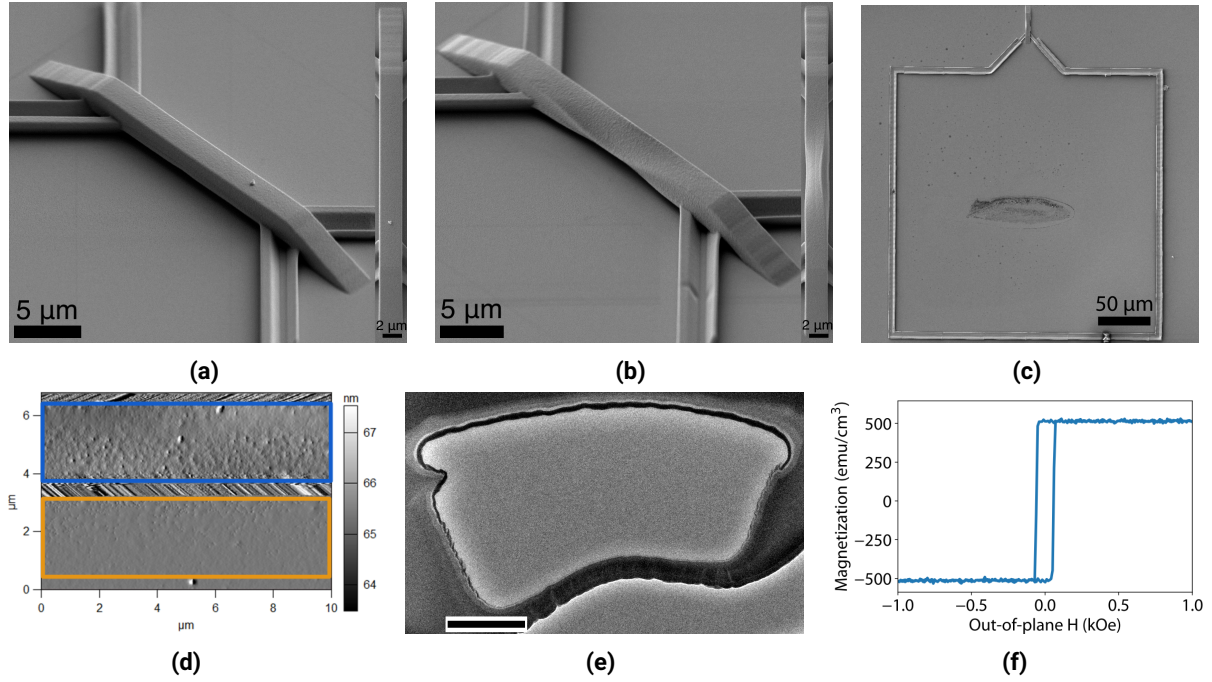
Figure 5.2: Experimental characterization of 3D ribbon devices. Scanning electron micrographs of devices without torsion (a) and with ζ = +45 ° torsion angle (b). The top view of each device is shown on the right panel of each image. (c) Top view of a device with the associated contact pad delimitation structure, after MOKE characterization. Only one fully delimited pad is fabricated per device to shorten fabrication times. (d) Atomic Force Microscopy (AFM) characterization of the surface roughness over the suspended section (blue), after deposition. The Root Mean Square (RMS) value of the roughness in this region (0.37 nm) is compared to that obtained for the contiguous substrate region (orange, 0.1 nm). (e) TEM characterization of a cross sectional slice of a ζ = +11 ° device, near the midsection. The polymer core is the light gray region in the middle and the magnetic film stack is the black line that is mostly on top of it, quickly thinning over the sides. The scale bar is 500 nm. (f) Hysteresis curve of the ferromagnetic film stack, characterized with VSM (Lakeshore VSM 8600) over a section of the same substrate where the devices were fabricated.

cross sectional high-resolution TEM (JEOL JEM-F200, 200 kV acceleration voltage) images of a device with ζ = +11 ° are shown in fig. 5.2e. The metallic film can be seen as a thin black strip around the polymer scaffold, the light-gray region in the center. The slight indentation on the left side is due to deformation during the TEM sample preparation.

The growth is conformal and uniform over the top surface of the device, accompanied by a steep thickness gradient starting at the edges and progressing along the side surfaces, as expected from a directional deposition method. No deposition is observed underneath the device. The thinner regions at the ribbon edges can cause DW pinning during current-driven motion. It was also possible to confirm that the structure was completely suspended over the substrate.

The grown films show excellent perpendicular magnetic anisotropy for both the Ferromagnetic (FM) (fig. 5.2f) and SAF (fig. 5.13) films, with strong anti-ferromagnetic exchange coupling and a small net magnetization for the SAF films.

Current induced domain-wall motion was measured using polar Kerr microscopy in differential mode, as detailed in section 3.7. In the main experiment, devices with ζ = 0, ±11, ±18, ±26, ±45 ° torsion angles and 2.5 μm width were tested. Each device is characterized under a similar set of current densities j. For each density j, a set of current pulses are used to drive the DW into the device. Each acquisition sequence is repeated 3-5 times for evaluating reproducibility. For each device and each current density, the motion of both $\odot\otimes$ and $\otimes\odot$ DWs are evaluated for currents flowing over the device in both the left ($\leftarrow$, -) and right ($\rightarrow$,+) directions.

Other experiments include devices with 1.25 μm and 5 μm width, devices with SAF films, devices combining both rotations side-by-side, and DW propagation under an applied H_x field. These experiments are

explicitly identified throughout the text. The same base protocol for data acquisition (just stated) is applied in these cases as well.

The results and their analysis are presented over the next sections.

5.3 Domain Wall Filtering

In this section, the DW displacement by current pulses in the twisted ferromagnetic ribbons is investigated as a function of the cumulative pulse lengths. First, a qualitative analysis of the torsion effect on DW motion over all devices in the main dataset is done (fig. 5.3), followed by a quantitative analysis over the 0 and ±11 ° devices (fig. 5.4).

The qualitative analysis of the data is presented in fig. 5.3. A set of experimental conditions where the DW overcomes the whole suspended section within the maximum number of current pulses is considered favorable (marked green), being considered unfavorable (marked red) if it does not. In devices with higher torsion, the presence of pinning or nucleation-inducing defects causes the DW to "break" into different segments progressing side-by-side, as can be seen in section 5.B. These cases are identified and considered favorable if all segments go through the suspended section and unfavorable with defects (marked orange) if only some of them do. Each set of conditions is labelled based on its prevalent behavior over the 3-5 runs it corresponds to.

From fig. 5.3, specific combinations of torsion chirality, current flow direction, and DW type seem to determine whether a DW is able to go through the suspended section or not. The set of favorable conditions is consistent for all devices with the same torsion chirality and is inverted when the device's torsion chirality is inverted. The same is true for the set of unfavorable conditions. For the device without torsion all combinations are able to move through the device, as expected [5]. For the $\zeta = \pm 11$ ° devices, the unfavorable combinations at low current densities become favorable at higher current densities, but otherwise, the DW ability to overcome the torsion section appears independent of the torsion magnitude. Devices with higher torsion angles have more surface defects to act as pinning and nucleation defects, difficulting the quantitative analysis of the data. Therefore, for the remainder of the analysis, only the data for $\zeta = 0; \pm 11$ ° devices will be accounted for.

Torsion(°)	0°		-11°		+11°		+18°		-18°		+26°		-26°		-45°	
j (10⁸ A/cm²)	+j(→) ⊙⊗ ⊗⊙	-j(←) ⊙⊗ ⊗⊙	+j(→) ⊙⊗ ⊗⊙	-j(←) ⊙⊗ ⊗⊙	+j(→) ⊙⊗ ⊗⊙	-j(←) ⊙⊗ ⊗⊙	+j(→) ⊙⊗ ⊗⊙	-j(←) ⊙⊗ ⊗⊙	+j(→) ⊙⊗ ⊗⊙	-j(←) ⊙⊗ ⊗⊙	+j(→) ⊙⊗ ⊗⊙	-j(←) ⊙⊗ ⊗⊙	+j(→) ⊙⊗ ⊗⊙	-j(←) ⊙⊗ ⊗⊙	+j(→) ⊙⊗ ⊗⊙	-j(←) ⊙⊗ ⊗⊙
0.5-0.6																
0.7-0.8																
0.8-0.9																
0.9-1.0																
1.0-1.1																
1.1-1.21																
1.25-1.35																
1.4-1.52																
1.57-1.7																
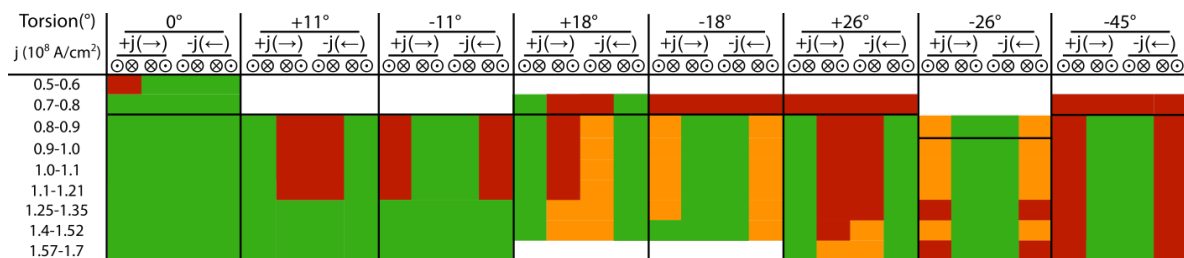
Figure 5.3: Qualitative analysis of DW motion over 3D ribbon devices with different torsions at different current densities j. In conditions marked green the DW is able to overcome the whole device while for conditions marked red it becomes blocked in the twisted section. Conditions marked orange relate to conditions where defects in the device surface affect the measurement outcome, either through nucleation or breaking of the DW into multiple, side-by-side, DWs as shown in section 5.B. For each case, the DW type (⊙⊗ or ⊗⊙) is defined in the direction of the current flow.

The relative DW position over the $\zeta = 0; \pm 11$ ° devices as a function of cumulative pulse duration for current flowing in the $+x$ direction is shown in fig. 5.4a. The corresponding data for current flowing along $-x$ is shown in section 5.C. The data processing is described in section 4.3.1. For low current densities, ⊙⊗ DWs move through the whole suspended section of the +11 ° device while ⊗⊙ remains stuck in the first half of the device. Kerr images relative to this case are seen in figs. 5.4c and 5.4d, displaying the asymmetry in the displacement of different DW types. The opposite is true for the −11 ° device, with

---

[5]The condition where the DW does not move through the device without torsion is due to imperfections of the sample in the very low DW velocity regime. For reference, the black horizontal line in fig. 5.3 corresponds to DW velocity threshold of 5 m/s

the $\odot \otimes$ DW becoming stuck. As the current density j increases and the unfavorable DW types in each case are able to move past the highest torsion point and into the second half of the devices, their velocity increases again, and they are able to reach the end of the twisted section. If the current density is further increased to $j \approx 1.6 \times 10^8 \ Acm^{-2}$, the differences between both DW types over the devices with torsion mostly disappear. As a reference, in the device without torsion, both DW types are able to overcome the suspended section for all j with similar displacements, as expected.

(a)

(b)

(c)

(d)
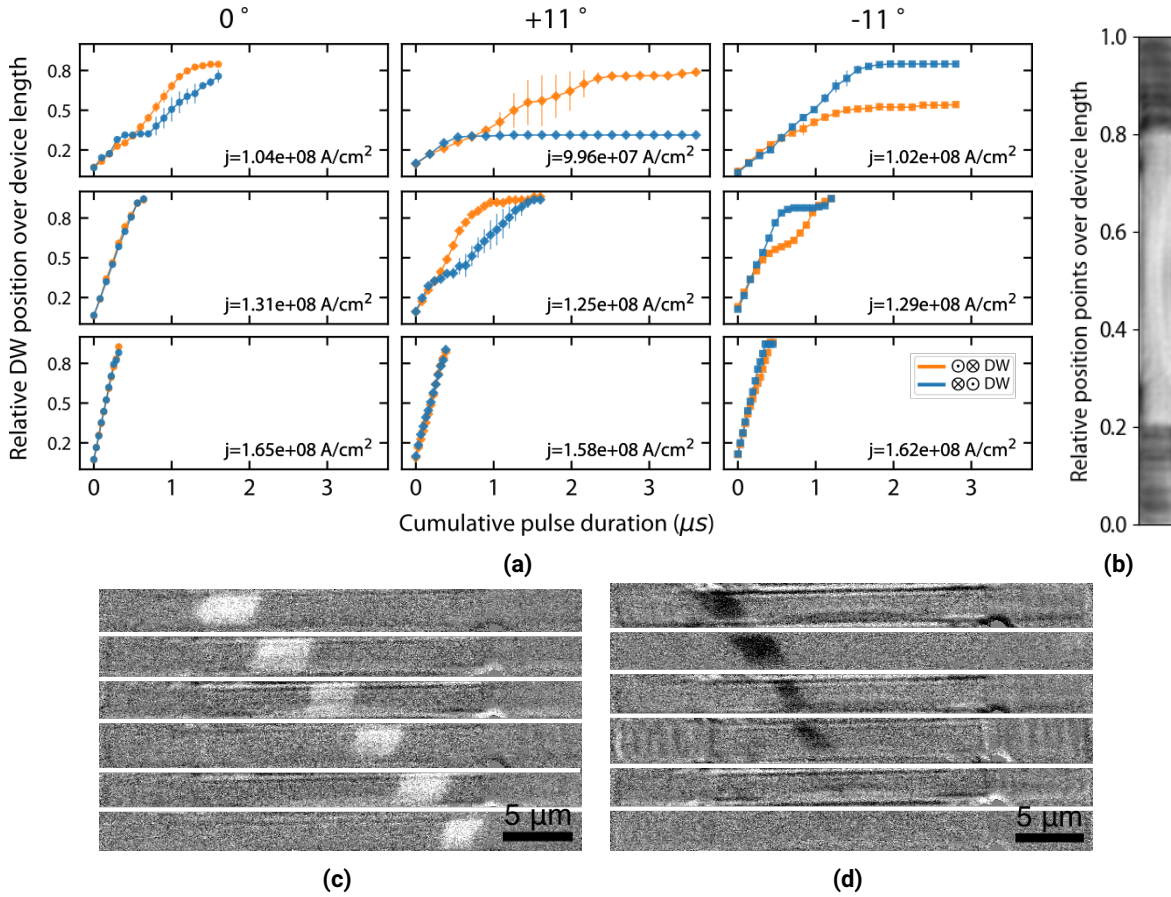
Figure 5.4: Observation of DW filtering. (a) Relative DW position, for both $\odot \otimes$ (orange) and $\otimes \odot$ (blue) DWs, over the device as a function of the cumulative pulse duration for devices with $\zeta = 0; \pm 11$ ° and for different j, with $j > 0$. (b) Top view of a device in the Kerr microscope, showing the scale of relative positions over the device length that is used in (a). The twisted section corresponds to the [0.2;0.8] range of relative positions. (c)-(d) Sequences of differential Kerr images of $\otimes \odot$ (c) and $\odot \otimes$ (d) DWs driven across a $\zeta = -11$ ° torsion device by a sequence of current pulses with the same properties, e.g., pulse length and number of pulses. Corresponds to the $\zeta = -11$ ° torsion device with $j = 1.02 \times 10^8 \ Acm^{-2}$ case in (a). The $\otimes \odot$ DW becomes stuck in the middle of the twisted ribbon (d) while the $\odot \otimes$ passes through the whole ribbon (c).

The selective action of the torsion on different types of DWs for different torsion chiralities equates to a DW filtering functionality. The favorable or unfavorable DW type is opposite for opposite current flow directions because the torsion chirality experienced in each direction is also opposite, as can be seen in figs. 5.1a and 5.2b [6]. Furthermore, the filtering can be activated and deactivated by modulating the current density flowing through the device.

Similarly, the device with $\zeta = 45$ ° displays the ability to selectively nucleate DWs of a particular type, mediated only by current pulses, as shown in section 5.D.

To further assess the impact of torsion, a dual device was also fabricated and tested that combines

---

[6]e.g., for current flowing in the $+x$ direction, the chirality of the torsion over the left half (i.e., the first the current flows through) of a $\zeta = +11$ ° is positive (left-handed) while for current along $-x$, the current goes through the right-half of the device first, which has opposite (negative or right-handed) torsion chirality.

opposite torsion chiralities side-by-side, with the results being presented in section 5.E.

5.4   Domain Wall Velocity Dependence on Torsion and Current Density

The average DW velocity over the whole device is calculated, as explained in section 4.3.1, for current densities above the threshold current density [7], in both current flow directions, and for the torsion angles $\zeta = 0; \pm 11°$. The results are presented in fig. 5.5.
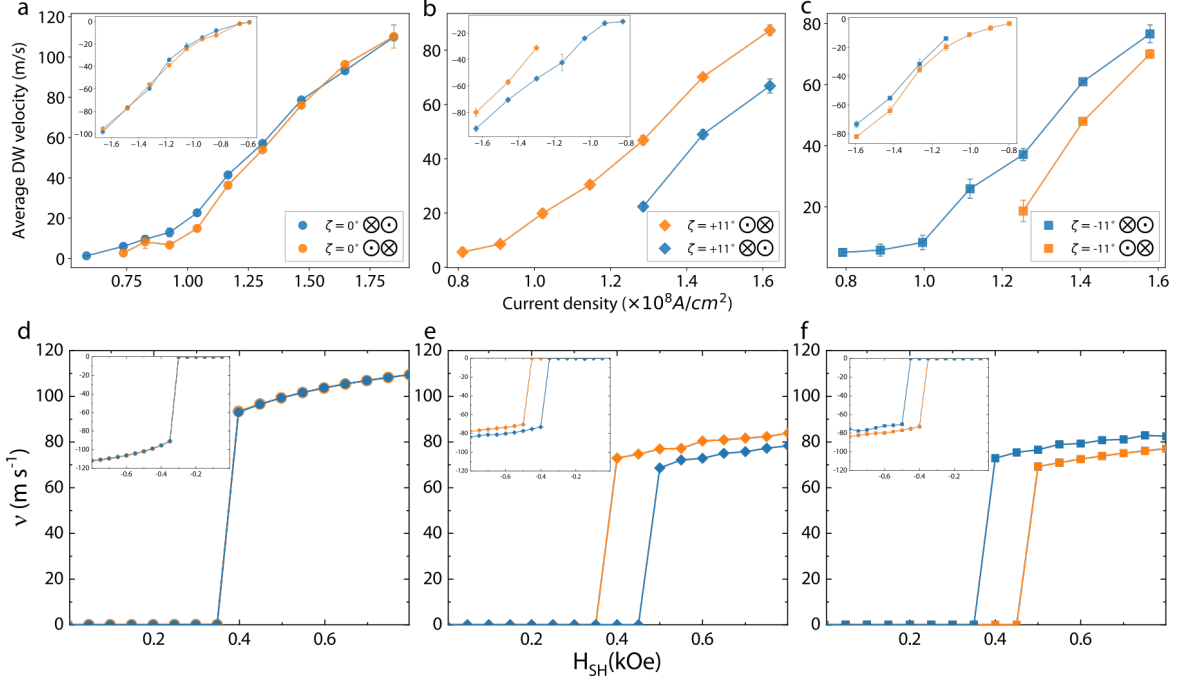
Figure 5.5: Dependence of the average DW velocity on torsion. Orange (blue) represents $\odot \otimes$ ($\otimes \odot$) DW configurations. Circle, diamond and square symbols correspond to 0, +11 ° and −11 °, respectively. (a)-(c), Experimental data showing the average DW velocity for both DW configurations for $j > 0$ and for $\zeta = 0$ ° (a), +11 ° (b) and −11 ° (c). Insets plot the corresponding DW velocity dependence on j for $j < 0$, i.e., current flowing along $-x$. Each point is the average of 2-3 measurement cycles while the error bars correspond to the average deviation. (d)-(f), Analytical model results corresponding to (a)-(c), respectively. The parameters used in the calculations are $\Delta = 5$ (d) and 3 nm (e-f), $\alpha = 0.1$, $H_k = 2 \, kOe$, $H_{DM} = -1 \, kOe$ for $\odot \otimes$ and 1 kOe for $\otimes \odot$, $M_s = 200 \, emu \, cm^{-3}$, $b = 1 \, \mu m$, $A_e x = 5.2 \times 10^{-6} \, erg \, cm^{-1}$, $V = 2 \times 10^5 \, erg \, cm^{-3}$, $q_0 = 4$ (d) and 2 nm (e-f), and $q_{shift} = 10 \, nm$. See section 5.F for more information.

As expected, the DW velocity over the device without torsion is mostly equivalent for both DW types over all combinations of current flow direction and current density. For the devices with torsion, however, two differences are noticeable between the two DW types.
First, a given DW type is consistently and significantly faster than the other, e.g., a $\odot \otimes$ DW is faster for $j > 0$ and $\zeta = +11$ °, with the difference becoming less significative towards higher j (in modulus). This is consistent with the observations in section 5.3 and, as before, the opposite DW type is seen to be faster for opposite current flow directions because the experienced torsion chirality is also opposite in both cases.
Second, the threshold current densities for the slower DW type are seen to be about 50 % higher than for the favorable, or faster, DW type. For example, while a $\odot \otimes$ DW is seen in fig. 5.5b to move over a $\zeta = +11$ ° device for $j \geq 0.8 \times 10^8 \, A \, cm^{-2}$, a $\otimes \odot$ DW only overcomes the torsion section in the same device for $j > 1.2 \times 10^8 \, A \, cm^{-2}$.
In this configuration, the torsion is seen to selectively modulate both the threshold current density and the DW velocity of the different DW types.

---

[7]defined in section 3.7 as the current density corresponding to average DW velocities above 5 m/s.

The experimental results in fig. 5.5 (a-c, top row) are compared with the results of the analytical model (d-f, bottom row) presented in section 5.F, which models the influence of constant torsion chirality and magnitude on DW velocity[8]. The model is able to replicate both a difference in DW velocity and threshold current for different DW types over ribbons with torsion while showing no effect for a device without torsion, in accordance with the experimental data. The interpretation of these results and the analysis of the effect of torsion on the different DW types is done in section 5.5.

To complement the analysis of the average DW velocity over the ribbons, the local DW velocities are also analyzed as a function of the relative position over the devices at which they are registered in order to evaluate the influence of different device regions on the observed effects. The results of the analysis are presented in section 5.G.

5.5   Torsion Effect on DW Motion

Let us consider the energetic equilibrium over a magnetic ribbon with torsion[9]. The global, local and magnetization reference frames over the ribbon are shown in fig. 5.6a.

(a)

(b)

(c)
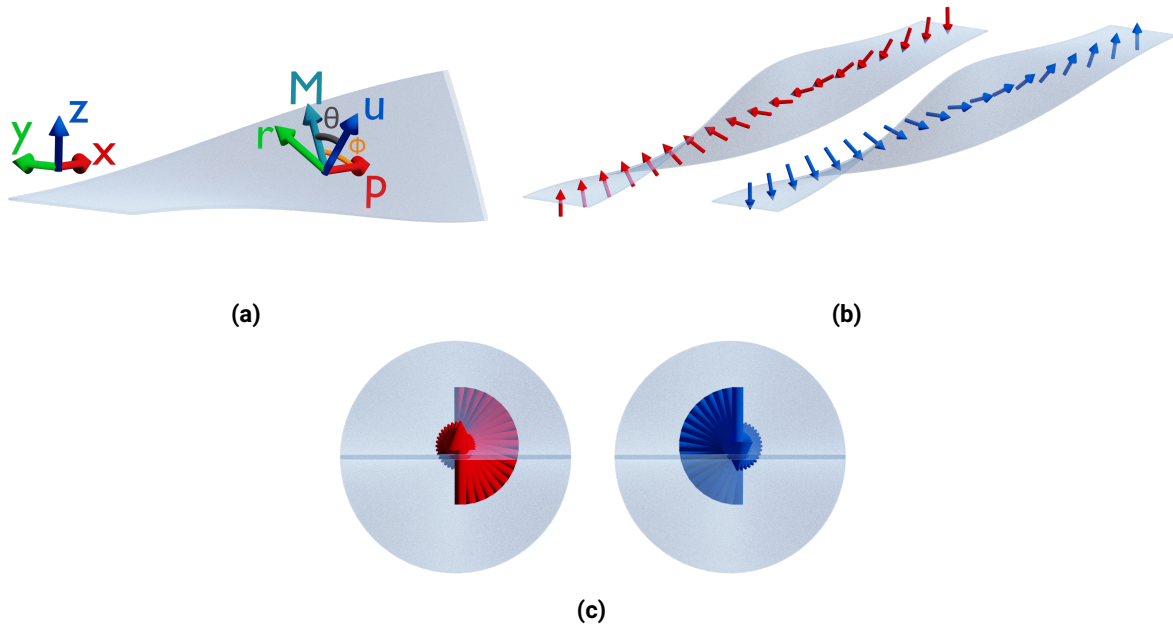
Figure 5.6: Magnetization orientation over the 3D ribbon. (a) To better analyze and model the magnetization over the twisted ribbon a local reference frame is defined over the surface. The axis p is tangent to the ribbon and its guiding curve while axis u is perpendicular to the ribbon surface. (b) Geometry-induced rotation of the magnetization in uniform states, shown for upwards ($\odot$, left, red) and downwards ($\otimes$, blue, right) uniform states. The magnetic anisotropy will act to make the magnetization follow the ribbon geometry. In this case, maintaining perpendicular magnetic anisotropy over the ribbon, i.e., **m**∥**u,** causes a left-handed rotation of the magnetization even for uniform magnetization states. Because sequential spins are no longer aligned, this rotation will cause an increase in the exchange energy (see eq. 5.1). (c) Longitudinal perspective of the anisotropy-induced rotation of the magnetization for upwards (left, red) and downwards (blue,right) uniform magnetization states. This rotation directly follows from maintaining the magnetization normal to the ribbon surface and, therefore, it assumes the specific chirality of the geometry.

The analysis in this section is supported by the model presented in section 5.6 and section 5.F. Correspondingly, this analysis can also be understood in the context of the 3D curvilinear magnetism framework

---

[8]being, therefore, roughly equivalent to the first half of each experimental device.
[9]but no curvature

presented in section 2.4. First, let us consider a uniformly magnetized ribbon. As referred to in section 2.4, the energetic balance of the magnetization is described by the anisotropy, including the magnetostatic contribution in the form of shape anisotropy, exchange and DMI interactions. Since the magnetic film has PMA, the anisotropy will act to align the magnetization along the u axis at any point. Under the torsion-induced rotation, this corresponds to a rotation of the magnetization about the longitudinal direction p[10], as represented in fig. 5.6. As the magnetization rotates under the anisotropy influence, the DW exchange energy, described by

$$E_{ex} = A_{ex}(\nabla \mathbf{m})^2 \tag{5.1}$$

increases. This increase is the same independently of the chirality of torsion.

Let us now consider a magnetic DW over the ribbon, as represented in fig. 5.7. In this case, the intrinsic magnetization rotation of the DW will interplay with the rotation of the magnetization due to torsion, and will do so differently for Bloch and Néel DWs.
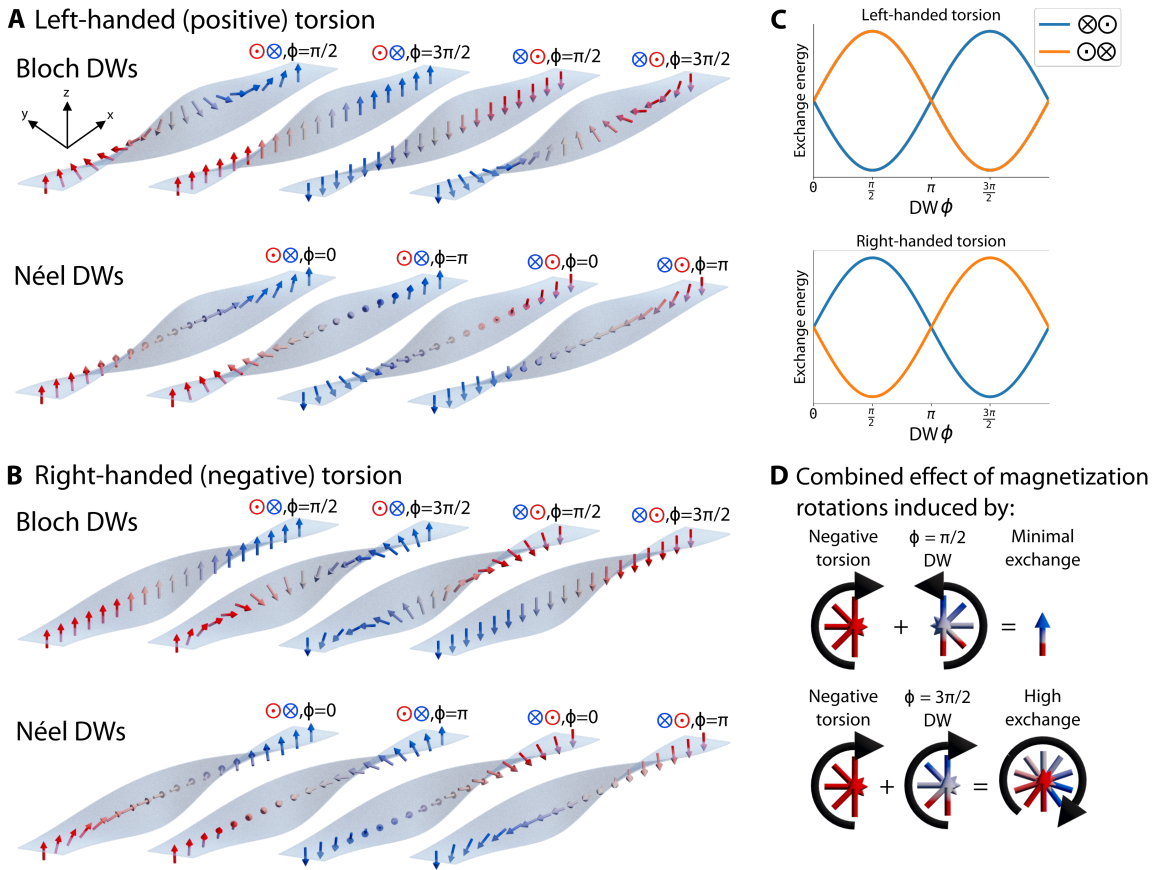
Figure 5.7: Modulation of the exchange energy by a combined effect of torsion- and DW-induced magnetization rotation. For illustrative purposes, the DW width is shown equal to the half-turn ribbon rotation length, i.e., the DW- and torsion-induced rotations occur over the same length, which is not the case experimentally where the former is $> 10^3$ times smaller. (a)-(b) DW magnetization rotation for left- (a) and right-handed (b) torsion chiralities, for Bloch ($\phi = \pi/2; 3\pi/2$, top row) and Néel ($\phi = 0; \pi$, bottom row) DWs and for $\odot\otimes$ and $\otimes\odot$ DW types. For Bloch DWs the DW magnetization rotation occurs in the same axis, x, as the torsion and thus both rotations interact, leading to a chiral symmetry breaking. For pure Néel DWs, the magnetization rotation occurs along y, i.e., perpendicular to that caused by torsion, and therefore both magnetization rotations do not interact. (c) Dependency of the exchange energy on the DW angle ϕ for left- and right-handed torsion and for $\odot\otimes$ (orange) and $\otimes\odot$ (blue) DWs. (d) For Bloch DWs, if the DW and torsion chiralities are opposite (top row), the rotations cancel out and the exchange energy is minimum, otherwise both rotations add up and the exchange energy is maximum (bottom row). Thus, the degeneracy for DWs of opposite chiralities is lifted.

---

[10]which is parallel to x in the global reference frame. Because there is no curvature, these axes can be used interchangeably.

In a Bloch DW, the intrinsic DW magnetization rotation occurs around the same axis p as the torsion-induced magnetization rotation. If the Bloch DW chirality and the torsion chirality are the same, the magnetization rotation will rotate further and, by eq. 5.1, the exchange energy of this configuration will increase, increasing the total configuration energy[11], as seen in fig. 5.7a,d. On the other hand, if the torsion and Bloch DW chiralities are opposite, both magnetization rotations will, at least partially, cancel, decreasing the exchange energy contribution[12] as in fig. 5.7d. An important result follows: for a given torsion chirality, the different Bloch DW chiralities are no longer degenerate, i.e., by influence of the torsion-induced rotation of one Bloch DW chirality will be more energetically stable than the other. This equates to a torsion-induced DW chiral symmetry breaking. Different torsion chiralities will stabilize different Bloch DW chiralities, as represented in fig. 5.7c.

In a Néel DW, the intrinsic DW magnetization rotation occurs around an axis, r, perpendicular to the axis of the torsion-induced rotation (p). As such, the interplay between DW and torsion chiralities is constant for both DW chiralities and both are degenerate (see fig. 5.7c).

In our experimental system, however, the degenerate Néel DWs stabilized by DMI[13] have their magnetization canted towards $\pm r$ by the influence of the SHE-induced spin-polarized current, as described in section 2.3.3.

A Left-handed (positive) torsion
Low E_{ex}
High E_{ex}

B Right-handed (negative) torsion
High E_{ex}
Low E_{ex}

C Combined effect of magnetization rotations induced by:

Negative torsion   SHE canting   Increased exchange energy

Negative torsion   SHE canting   Decreased exchange energy
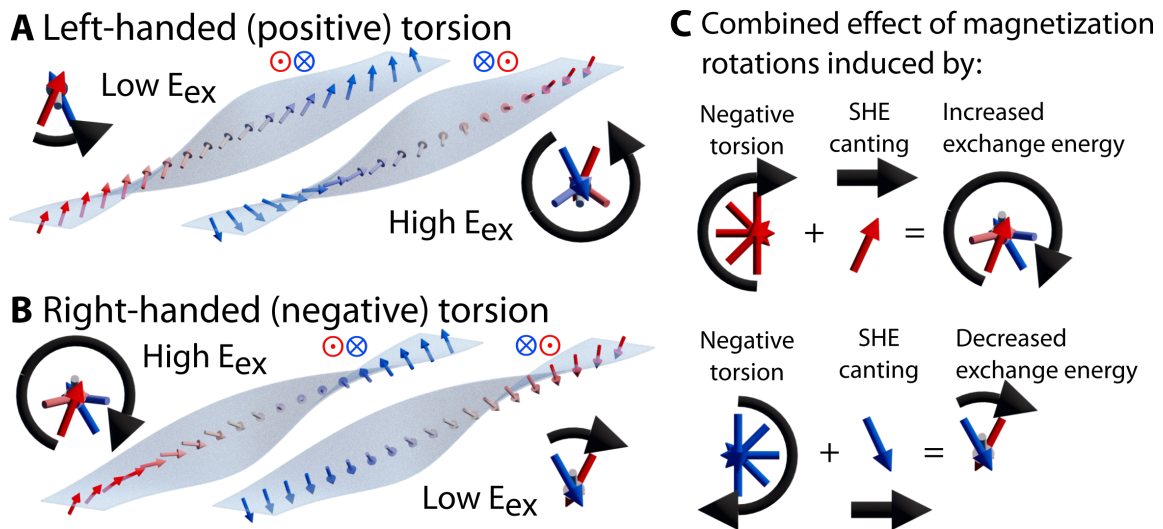
Figure 5.8: Modulation of the exchange energy by a combined effect of torsion- and SHE-induced magnetization canting. For illustrative purposes, the DW width is shown equal to the half-turn ribbon rotation length, while experimentally the former is $> 10^3$ times smaller. (a)-(b) DW magnetization rotation for left- (a) and right-handed (b) torsion chiralities, for Néel ($\phi = 0$) DWs of both $\odot\otimes$ and $\otimes\odot$ configurations. The insets show the longitudinal perspective (along $+x$) over the magnetization rotation along the DW. (c) The canting of the DW by the SHE-induced spin-current along a curved surface leads to a rotation of the DW magnetization that has opposite chirality for $\odot$ and $\otimes$ domains. This rotation interacts with the torsion-induced rotations such that, if both chiralities are the same, the rotations add up and the exchange energy increases, otherwise they partially cancel out and the exchange energy decreases, lifting the degeneracy for DWs of opposite chiralities.

The canting rotates magnetic moments pointing along $+u$ and $-u$ in opposite directions, as shown in fig. 5.8. Thus, when evaluated over the whole DW, the canting either extends or shortens the range of the torsion-induced magnetization rotation about the p axis, as represented in fig. 5.8b, either increasing or decreasing the exchange energy as a consequence, respectively. This contribution is opposite for different

---

[11]As referred in section 2.3.1, the Heisenberg exchange energy contribution is significantly higher than the anisotropy contribution

[12]instead of considering a DW of a fixed type and opposite chiralities, the same result is reached by considering a DW of a fixed chirality and different type, as shown in fig. 5.7a. In this general case both are equivalent.

[13]as explained in section 2.3.2.2, the DMI stabilizes Néel DWs of a particular chirality and therefore the analysis is restricted to different DW types of the same chirality.

DW types, leading to a non-degeneracy between canted Néel DWs of different type, and for different torsion chiralities, thus breaking the chiral symmetry that is present in the case of non-canted Néel DWs. The argument for non-degenerate Néel DWs follows naturally from the 3D curvilinear magnetism framework presented in section 2.4, and particularly from the concept that a curvilinear geometry translates into higher exchange energy states due to the translational invariant nature of the anisotropy. Furthermore, this analysis is also supported by the analytical model presented in section 5.F: the SHE-induced canting causes ϕ to deviate from $\phi = 0; \pi$ in opposite directions, i.e., towards larger or smaller angles, for different DW types and opposite torsion chiralities, which is shown in fig. 5.7c to lead to the non-degenerate states[14].

Because both DW configurations have different exchange energies, it follows from eq. 2.28 that a new effective magnetic field component will appear along $\pm r$ to align the magnetization in the less energetic configuration. Because the most stable configuration is defined by the torsion, and particularly its chirality, this field component is referred to as the torsion-induced magnetic field. In turn, this magnetic field will give rise to a torque on the magnetization that is, according to eq. 2.27, described by

$$\tau_{torsion} = -\gamma \mathbf{m} \times \mathbf{H}^{torsion}$$
$$= -\gamma \, m_p \, H_r^{torsion} \, \hat{\mathbf{u}}. \tag{5.2}$$

The dependence on the DW type is present through m_p, which is opposite for $\odot \otimes$ and $\otimes \odot$ DW, while the dependency on the torsion chirality is present through $H_r^{torsion}$. This torque is parallel to the DMI-induced torque responsible for the current-induced DW motion (see section 2.3.3) and, depending on the torsion and DW type, can either align along or against the latter, as is shown in fig. 5.9 for the configurations tested experimentally. If both torques are aligned, the velocity component of both will add up, driving the DW faster, otherwise the torsion-induced torque will act to slow the current-induced DW motion, as indicated in fig. 5.9. This leads to the modulation of the current-induced DW motion by the torsion that is observed in the experimental results.

5.6   3D Analytical Model for the Torsion Effect on DW Motion

The analysis presented in section 5.5 is based on and informed by an analytical 3D model of DW motion over a magnetic ribbon with torsion. The model and its results are summarized here and are fully specified in section 5.F.

By updating the 1D model discussed in section 2.3 to account for the 3D geometry of the twisted ribbon, new torsion-driven terms appear in the exchange energy contribution, in accordance with the analysis presented in section 2.4.

The predominant geometry-driven term introduces a $\frac{\sin \phi}{b}$ [15] dependence on the exchange energy, as shown in fig. 5.7c, with b being a parameter associated with torsion[16], as explained in section 5.F. Néel DWs have energies between those of the favorable and unfavorable Bloch DWs, independent on their (or the torsion) chirality, as can be visually inferred from fig. 5.7c.

Furthermore, the equations of motion are obtained by using the Rayleigh-Lagrange and the Landau-Lifshitz-Gilbert equations while accounting for all the relevant energy terms in the system (see section 2.3.2.2). Within the geometry-driven terms in the resulting equations of motion, presented in section 5.F, there is one predominant geometry-driven contribution to the DW velocity, described by

$$\dot{q}_{torsion} = -\frac{\pi \, \gamma \, A_{ex}}{b \, M_s} \cos \phi. \tag{5.3}$$

This term matches the expectations established by the analysis in section 5.5 and the results in section 5.4, i.e., it is dependent on both the DW type trough ϕ and the torsion chirality through b and can either align

---

[14]this can also be thought of as the Néel DWs acquiring Bloch-like DW components of opposite chiralities, due to the SHE-induced canting, that lift their degeneracy

[15]as referred to in section 2.3.2.1, Bloch and Néel DWs correspond to $\phi = \pi/2; 3\pi/2$ and $\phi = 0; \pi$, respectively.

[16]the sign of b is the same as that of torsion, and an increase in b correlates to an increase in torsion
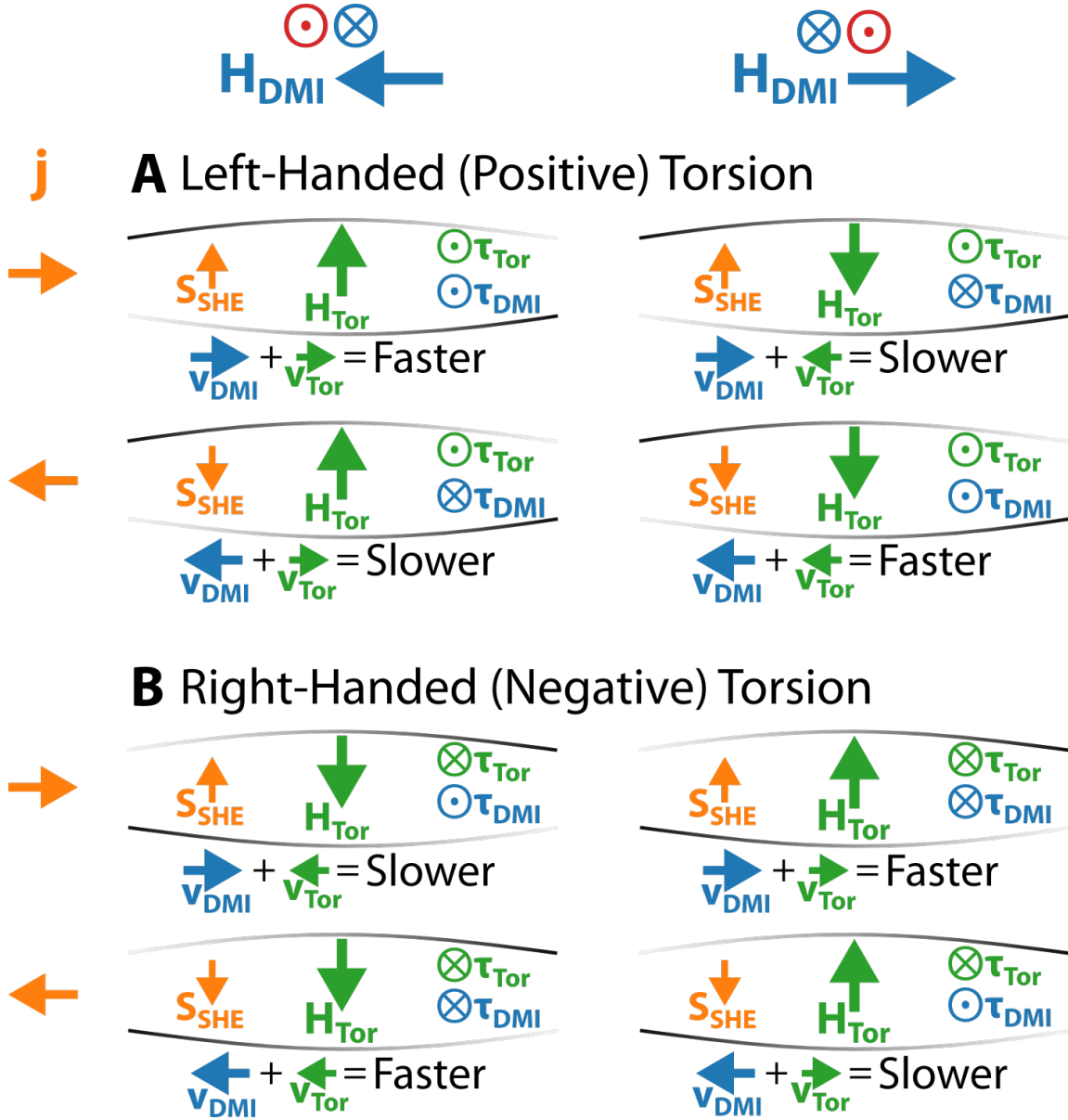
Figure 5.9: Mapping of the different torsion chiralities (a, left-handed; b, right-handed) and magnetic parameters of the system to the resulting torques and CIDWM velocity components. Particularly, it should be noted that H_{DMI}, along p, acts on the magnetization component along r while $H_{Torsion}$, along r, acts on the magnetization component along p such that both torques, given by $\tau = -\mathbf{m} \times \mathbf{H}$, point along u.

with or against the current-induced DW motion contribution. Whether this term is parallel or anti-parallel to the DMI-driven DW velocity contribution will determine if the DW motion over the torsion section is favorable or unfavorable.

The results predicted by this model for each tested experimental condition are compared with the experimental data in each section, if relevant.

5.7 Influence of Device Width on the Torsion-Driven Effects

Devices with 1.25 μm and 5 μm were also fabricated and tested to evaluate the impact of the device width on the torsion-driven effects. The DW velocity as a function of j is shown in fig. 5.10 for devices with $\zeta = +11$ °. A significant difference in the threshold current density is observed between the two DW types in the 5 μm wide device but not in the 1.25 μm device, despite being predicted by the analytical model for

both devices, as seen in fig. 5.10b. Differences in the DW velocity of different DW types are seen for both devices, particularly for $j \geq 1.2 \times 10^8 \, A/cm^2$, but no significant difference or trend is discerned between the progression of the DW velocities in devices with 1.25, 2.5 (section 5.4) and 5 μm. From the analytical model, and particularly eq. 5.3, the torsion contribution to the DW velocity has no dependence on the device width and therefore no difference is expected between the different device widths, as is observed experimentally.
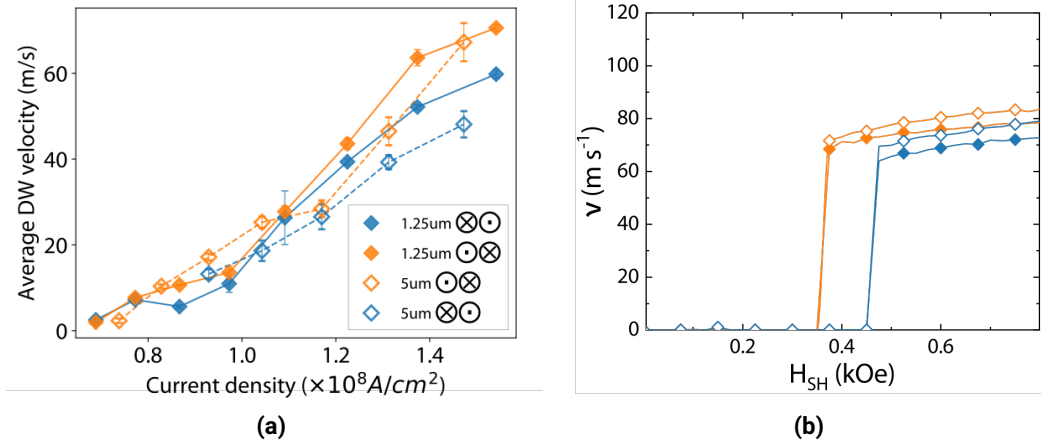
Figure 5.10: Dependence of the average DW velocity and the torsion effect on device width. Orange (blue) represent $\odot\otimes$ ($\otimes\odot$) DW configurations. (a) Average DW velocity dependence on j for $j > 0$ and $\zeta = +11\,°$ with device widths of 1.25 (solid) and 5 μm (open), respectively. (b) Analytical model results corresponding to (a). The parameters used in the calculations are $\Delta = 3nm$, $\alpha = 0.1$, $H_k = 2\,kOe$, $H_D M = -1\,kOe$ for $\odot\otimes$ and $1kOe$ for $\otimes\odot$, $M_s = 200\,emu\,cm^{-3}$, $b = 1\,\mu m$, $A_e x = 5.2 \times 10^{-6}\,erg\,cm^{-1}$, $V = 2 \times 10^5\,erg\,cm^{-3}$, $q_0 = 2\,nm$, and $q_s hift = 10\,nm$. See section 5.F for more information.

5.8 Influence of $\mathbf{H_x}$ on Current Induced Domain Wall Motion

As presented in section 2.3.3 and shown in fig. 5.9, the current-induced DW motion is driven by a torque τ_{DMI} induced by an effective DMI field $\mathbf{H}_{DMI}$ that points along $\pm x$. Thus, if an external field $\mathbf{H}_x$ is applied along $\pm x$, it will either add to or subtract from the $\mathbf{H}_{DMI}$, modulating the velocity of DWs, as previously shown [121]. Since $\mathbf{H}_{DMI}$ points along opposite directions for different DW types, the external $\mathbf{H}_x$ will speed up one DW type while slowing down, or even stopping, the other. This experiment enables to quantify the strength of the DMI field $\mathbf{H}_{DMI}$ in a given system, as well as its symmetry.

Figure 5.11 shows the results, as well as the modeled response, for driving DW motion over $\zeta = 0; +11\,°$ devices under different $\mathbf{H}_x$ fields. For this analysis, only the motion through the left half of the device is considered, corresponding to the $[0.2, 0.5]$ relative position range (see fig. 5.4b). This is done to avoid compounded effects due to having both torsion chiralities over a single device and to enable a more direct comparison with the developed model which accounts for constant torsion.

For the device without torsion, the typical response for 2D devices is observed: the dependency of the DW velocity on $\mathbf{H}_x$ is the same for both current flow directions, i.e., increasing $\mathbf{H}_x$ causes the DW velocity of a given DW type to increase or decrease (in modulus) in both directions of j, while being inverse for different DW types, i.e., increasing $\mathbf{H}_x$ causes the DW velocity of one DW type to increase and that of the other DW type to decrease.

For the device with torsion, however, the response is asymmetric both on the current flow direction and DW type, as seen in fig. 5.11b. This results from the interaction between DMI- and torsion-induced torques. Upon inversion of the current flow direction or the DW type, this interaction inverts and such torques go from being parallel to anti-parallel or vice-versa[17], as established in fig. 5.9. Thus, for example,

---

[17] i.e., from adding up to subtracting from one another
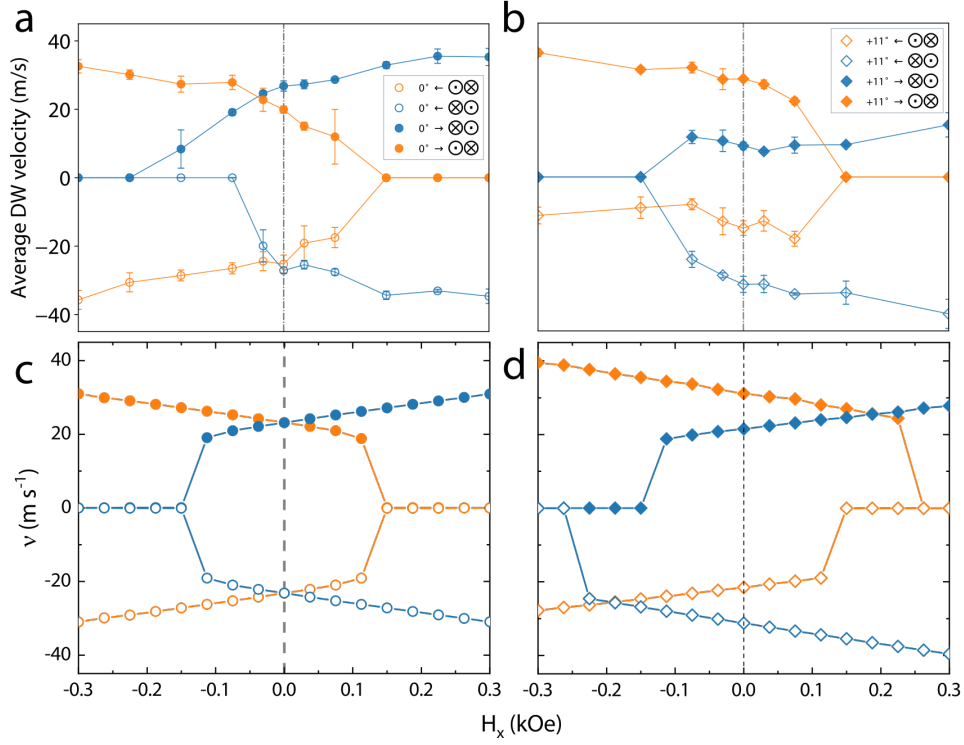
Figure 5.11: Average DW velocity as a function of the applied field along x. Orange (blue) represent $\odot\otimes$ ($\otimes\odot$) DW configurations while solid (hollow) markers represent DW motion along $+x$ ($-x$). a-b, Experimental data for devices with $\zeta = 0\,°$ (a) and $\zeta = +11\,°$ (b). c-d Corresponding theoretical model calculation for the devices with with $\zeta = 0\,°$ (c) and $\zeta = +11\,°$ (d). The parameters used in the calculations are $\Delta = 5$ (c) and $3\,nm$ (d), $\alpha = 0.1$, $H_k = 2\,kOe$, $H_{DM} = -1\,kOe$ for $\odot\otimes$ and $1\,kOe$ for $\otimes\odot$, $M_s = 200\,emu\,cm^{-3}$, $b = 1\,\mu m$, $A_e x = 5.2\times10^{-6}\,erg\,cm^{-1}$, $V = 2 \times 10^5\,erg\,cm^{-3}$, $q_o = 4$(c) and $2\,nm$(d), and $q_s hift = 10\,nm$. See section 5.F for more information.

the velocity of a $\odot\otimes$ DW moving along $+x$ ($j > 0$) on a device with $\zeta > 0\,°$ is increased by the torsion contribution to the DW velocity while, for $j < 0$, the DW velocity is decreased by the torsion contribution. This causes a shift of the $\odot\otimes$ DW velocity response under $\mathbf{H}_x$ towards positive velocities for both $j > 0$ and $j < 0$. Because the interaction is opposite for the $\otimes\odot$ DW, as can be observed from fig. 5.9, the DW velocity response under $\mathbf{H}_x$ response is, instead, shifted towards negative velocities.

The experimental data is consistent with the model predictions apart from the offsets in the threshold fields necessary for DW motion to occur. This difference could be due to the influence of pinning sites, the presence of an undesired out-of-plane field component contributing to the DW motion, or just a discretization error due to the set of experimentally tested $\mathbf{H}_x$ fields.

5.9   Synthetic Anti-Ferromagnetic Devices with Torsion

The torque influence on DW motion is intrinsically related to the ferromagnetic nature of the film stack because it depends on the exchange-mediated chiral selection of the magnetization rotation and its influence on the DMI- and SHE-induced DW driving mechanism. Synthetic anti-ferromagnetic films, on the other hand, are much more robust to such effects because of the magnetic moment compensation in the different layers, as previously shown for curved 2D wires [183]. Furthermore, the current-induced DW motion in such systems is driven by an additional torque component, the exchange coupling torque [110, pp. 37–39].

To test this hypothesis, devices with $\zeta = \pm11\,°$ were fabricated with SAF rather than ferromagnetic films. As seen in fig. 5.12 for a $\zeta = +11\,°$ device, the average DW velocity over the device and the threshold current for both DW types no longer show the significant differences observed in fig. 5.5. Again, this is

expected because the direct exchange interaction driving the torsion effect in ferromagnetic films is much less significant in SAF films due to inter-layer exchange and magnetic moment compensation.
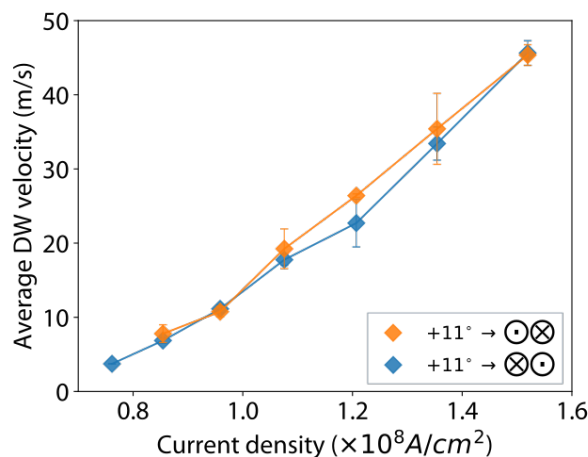
Figure 5.12: Average DW velocity as a function of the current density j for $j > 0$ and for a device with a SAF magnetic film stack and ζ = +11 °. Orange (blue) represent $\odot \otimes$ ($\otimes \odot$) DW configurations.

5.10 Discussion

The dataset presented in this chapter supports the hypothesis that intrinsically 3D geometrical features are able to break the chiral symmetry of a magnetic system, lifting the degeneracy of different magnetic configurations such as DWs of different chirality or type. In accordance with the presented model, as well as the model in section 2.4, this effect is attributed to a combined action of the anisotropy, which makes the magnetization follow the geometry, and the exchange energy, which helps stabilize particular magnetic configurations.

The verification of theoretically predicted features in such a complex 3D magneto-electronic device validates the fabrication method. This fabrication strategy is simple and compatible with a wide range of intrinsic 3D geometries. Nevertheless, minimizing surface defects for devices with $\zeta > 11$ ° is necessary to allow their quantitative analysis.

The presented devices improve on the state of the art by achieving current-induced DW motion in 3D through spin-orbit torques, particularly through SHE and DMI, which are of particular relevance in the current context of spintronics . The ability to model the current-induced DW motion through spin-orbit torques in 3D magnetic systems with PMA is also of relevance to the current state-of-the-art.

The ability to consistently drive DW motion in 3D suspended structures by current at relevant speeds, up to ≈ 120 m/s, is achieved. The ability to modulate the DW velocity and threshold current by torsion chirality and DW type is also shown, leading to a DW filter capability that can be deactivated at large current densities. Furthermore, other functionalities are predicted by the developed model that could not be definitely proven, such as the DW diode function of a similar device with constant and non-zero torsion.

Nonetheless, many questions are raised by this study. Particularly, understanding the influence of the region where the torsion chirality is inverted, as well as understanding why a DW is able to overcome an unfavorable torsion chirality in the second half of the device after overcoming a favorable torsion chirality in the first are the most important.

To follow up, it would be beneficial to fabricate devices with a single torsion chirality. Also, to further understand the observations presented in this chapter, it would be beneficial to improve the utilized model to account for the continuous torsion variation and the torsion chirality inversion in the same device, e.g., by applying the framework presented in section 2.4.

Despite the relevant observations, the fabricated system width and length are much larger than the

characteristic lengths of the fundamental magnetic interactions. Thus, although it is relevant to note that geometry-driven effects are still observable over these large ranges, a much wider variety of effects and combinations are expected in nm-scale structures such as those achievable by FEBID or STED-MPL.

5.11   Conclusion

In this chapter, a new fabrication workflow combining MPL and PVD is presented that simplifies the fabrication of scaffold-based magneto-electronic devices with complex 3D structural properties. This method was employed to fabricate high-quality 3D-suspended magnetic ribbons with torsion. Current induced DW motion driven by spin-orbit torques, particularly by a torque induced by SHE and DMI, was consistently verified, which is of particular relevance for spintronic applications. In doing so, a novel DW filtering effect was demonstrated that results from the interplay of magnetic DW chirality and geometrical torsion chirality. By modeling the system, the geometry is seen to give rise to an unidirectional effective magnetic field that lifts the energetic degeneracy between any two states characterized by different ϕ angles if $\phi \neq 0; \pi$. This corresponds to a geometry-driven anti-symmetric exchange[7], which is shown to lead to a chiral symmetry breaking in the system similar to the one induced by DMI[18].

The results hereby achieved have significant practical relevance. On one side, they provide simplified means, in the form of the presented fabrication workflow, to realize complex 3D magnetic structures and easily integrate them into electronic devices. On the other, they show new and significant functionality in the context of spintronics and do so based on widely used mechanisms such as current driven DW motion. It is my expectation that further exploration of different geometries in this context will enable to achieve DW-based logic.

As shown here, the ability to tune device properties and functionality not through its material properties but through its 3D geometry enables a new and promising design paradigm in spintronics and electronics in general. In this context, the achievement of new functionalities and improved performances is directly tied to the extent of the geometrical parameter space one can realize with the available fabrication and characterization methods. Therefore, any method which contributes to the exploration of new geometries and new regions of the parameter space in magnetic and electronic devices is a significant improvement to the state of the art.

---

[18]which results in the stabilization of Néel DWs of a specific chirality, as seen in section 2.3.2.2

Appendix 5.A   SAF Film Stack Hysteresis Curve

Beyond the ferromagnetic film, some devices were also coated with a SAF stack. To verify its magnetic properties, the film was characterized using VSM (Lakeshore VSM 8600), and the resulting hysteresis curve is shown in fig. 5.13. The film is seen to have a good magnetic moment compensation between both ferromagnetic layers of the SAF stack. Furthermore, the clear spin-flop transition and large saturation field of about 10 kOe indicate a strong interlayer exchange coupling.
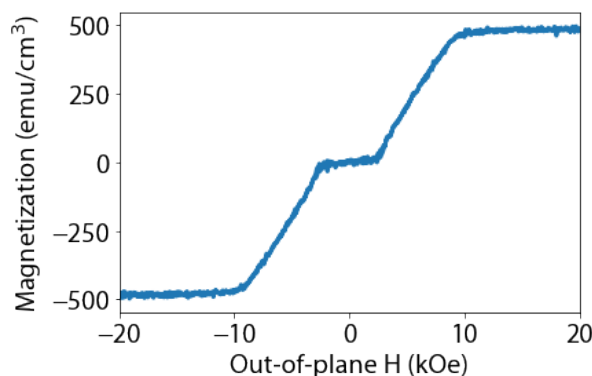
Figure 5.13: Magnetization hysteresis curve of the deposited SAF films, taken from the same substrate as the devices.

Appendix 5.B   DW Motion Failure Cases

As mentioned in section 5.3, the higher density of defects in devices with $\zeta \geq 18$ ° interfered with the DW motion by either inducing DW "breaking" in unfavorable cases (fig. 5.14a) or by inducing nucleation of new DWs in favorable cases (fig. 5.14b)
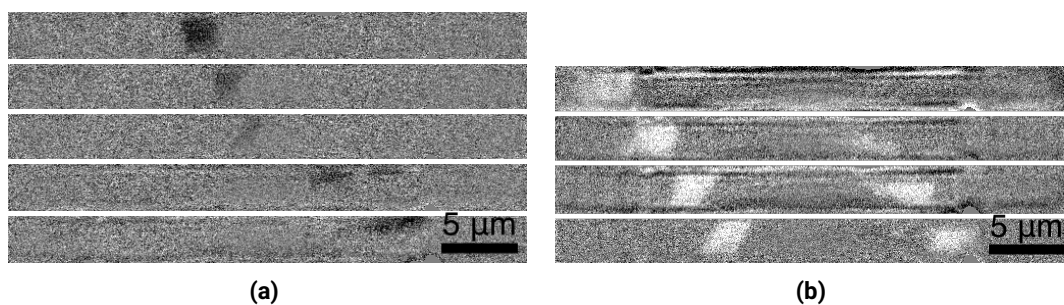
Figure 5.14: Defect induced DW motion types in devices with $\zeta \geq 18$ °. (a) In cases where the DW would be blocked by the torsion effect, defects can cause the DW to "break" into two sections side-by-side, with one of them still advancing. (b) Defect-induced nucleation interferes with the expected DW motion by dividing it into two sequential passages.

Appendix 5.C   Data for DW Motion for j < 0

Throughout the main text, the analysis tends to focus on the cases with currents flowing in the $+x$ direction, i.e., $j > 0$. The data for the inverse current flow direction ($j < 0$), i.e., for DWs moving along $-x$, is shown in here, in fig. 5.5, in fig. 5.11, and in fig. 5.18. The effects observed in the data and their interpretation are the same as for $j > 0$.

Particularly, it should be noted that when a DW of a given type moves along a device in $-x$ direction, the first torsion chirality it encounters is opposite to that in the $+x$ direction, such that the DW driving torques have the opposite alignment as for DW motion along $+x$, as seen in fig. 5.9. It then results that when the DW motion over a torsion section is favorable in one direction, it will be unfavorable in the opposite direction.

A convention that is typically used, as noted in section 5.3, and which simplifies the analysis for the cases with $j < 0$ is to define the DW type in the direction of the current flow, i.e., to assume a local referential with $+x$ in the direction of the current flow. Under this convention, the current direction is always positive and therefore, when a DW of a given type is moved through a device with torsion along $j > 0$ and $j < 0$, the only changing parameter is the torsion chirality. This convention can also be used to simplify the analysis of fig. 5.9 by ignoring the rows corresponding to $j < 0$.

Defects can cause significant differences between the data for $j > 0$ and $j < 0$, but these are sparse and inconsistent.
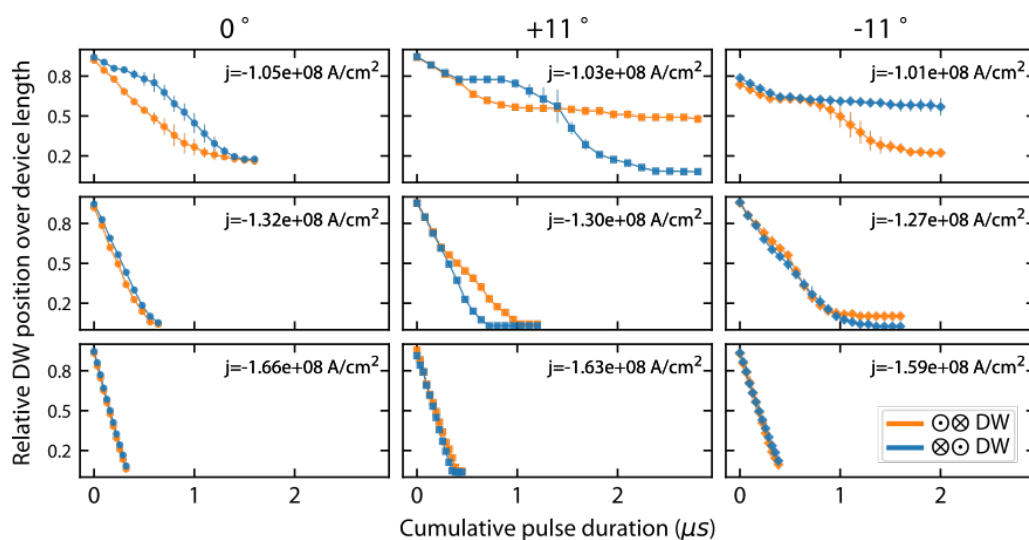
Figure 5.15: Observation of DW filtering. Relative DW position, for both $\odot \otimes$ (orange) and $\otimes \odot$ (blue) DWs, over the device as a function of the cumulative pulse duration for devices with $\zeta = 0; \pm 11\,°$ and for different j, with $j < 0$. The filtered DWs are different from the ones for $j > 0$ because a DW moving in opposite directions over the device experiences the opposite torsion chirality.

Appendix 5.D   Selective DW Nucleation by Current

A device with $\zeta = 45\,°$ rotation is characterized using Kerr microscopy while placed on a 22.5 $°$ wedge. On this device, it is possible to selectively nucleate DWs of a specific type by current action alone. After uniformly magnetizing the whole sample with an out-of-plane external field along $\pm z$, the application of a current pulse with density $j \geq 1e8\ A\ cm^{-2}$ leads to the nucleation of a DW in the region of highest torsion in the device. When the specific DW type created is favoured to move over the specific torsion chirality of the device, it is possible to move the given DW out of the system, as shown in fig. 5.16, otherwise no DW would be output. By tuning the initial magnetization of the system and the direction of current flow, it is possible to selectively output DWs of a specific type from the system. Devices with opposite torsion chirality output different DW types.

The origin of the observed effect is unclear. While it is likely caused by surface defects or a heterogeneous thickness of the film it that region, it could also potentially be due to the torsion. This could have significant practical uses and would need to be confirmed after further improving the surface quality.
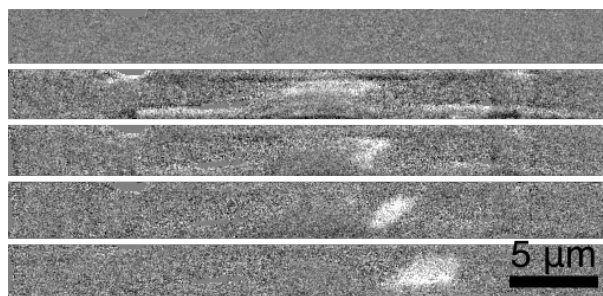
Figure 5.16: Selective nucleation of $\otimes\odot$ DWs in devices with $\zeta = -45$ °. After uniformly magnetizing the 3D ribbon device with an external field, the application of $j \geq 1e8\ A\ cm^{-2}$ consistently nucleates $\odot\otimes$ DWs at the central region. This is attributed to a combined effect of the DW filtering effect and the abrupt geometrical torsion feature, e.g., which leads to increased nucleation points. Oppositely, the nucleation of $\odot\otimes$ DWs is consistently observed in devices with $\zeta = +45$ °

Appendix 5.E   Device With Opposite Torsion Chiralities Side-by-Side

The importance of torsion to the DW filtering effect, discussed in section 5.3, is further confirmed by fabricating a 5 μm wide device with opposite torsion chiralities side-by-side ($\zeta = \pm26$ °), as seen in fig. 5.17. While a DW can be consistently nucleated along the whole device width, it only moves through the whole suspended section in the half-width where the given DW type is favorable, becoming stuck in the other, as seen in fig. 5.17b. The function of this device is typically affected by defect-induced nucleation due to the high torsion angle, similar to the $\zeta = 26$ ° devices in fig. 5.3.

This concept could be used, for example, to separate DWs of different types into different channels.

(a)   (b)
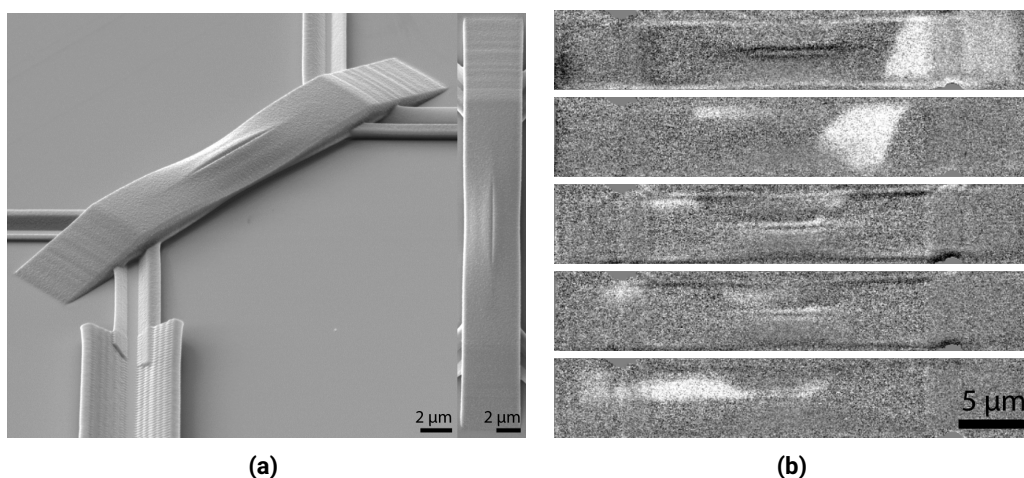
Figure 5.17: By combining two torsions of opposite chirality side-by-side in the same device ($\zeta = +26$ ° top, $\zeta = -26$ ° bottom) (a) a $\otimes\odot$ injected from the right side ($j < 0$) is able to overcome the top half but not the bottom half (b).

Appendix 5.F   Analytical Model for Chiral Torsion Fields and Torques

In order to better evaluate the experimental results, an analytical model for the CIDWM in the 3D twisted ribbons was developed by Dr.See-Hun Yang. It was used to establish the expected behavior to which the experimental data is compared to, e.g., in fig. 5.5, and is now presented.

A twisted magnetic ribbon can be described by the following parametric equations, when the torsional

axis, around which the magnetic ribbon is twisted, is x:

$$p = x \tag{5.4}$$

$$r = y \cos \frac{x}{b} \tag{5.5}$$

$$u = y \sin \frac{x}{b} \tag{5.6}$$

where (x, y, z) are the stationary cartesian coordinates while (p, r, u) correspond to the coordinates fixed on the twisted ribbon surface, as shown in fig. 5.6a. b measures how much the ribbon is twisted such that the torsion $\xi = \frac{b}{b^2+y^2}$ is determined by b. Note that the sign of b corresponds to the chirality of torsion. $\hat{p}$ and $\hat{r}$ are unit tangential vectors, and $\hat{u}$ is a unit normal vector for the moving frame:

$$\hat{p} = \text{sign}(b) \frac{b\hat{x} + y\hat{z}}{\sqrt{b^2 + y^2}} \tag{5.7}$$

$$\hat{r} = -\text{sign}(b) \sin \frac{x}{b} \frac{y\hat{x} - b\hat{z}}{\sqrt{b^2 + y^2}} + \hat{y} \cos \frac{x}{b} \tag{5.8}$$

$$\hat{u} = -\text{sign}(b) \cos \frac{x}{b} \frac{y\hat{x} - b\hat{z}}{\sqrt{b^2 + y^2}} - \hat{y} \sin \frac{x}{b} . \tag{5.9}$$

Then the unit magnetization $\hat{m}$ can be written as

$$
\begin{aligned}
\hat{m} =& \sin \theta \cos \phi \, \hat{p} + \sin \theta \sin \phi \, \hat{r} + \cos \theta \, \hat{u} \\
=& \text{sign}(b) \frac{b \sin \theta \cos \phi - y \sin \theta \sin \phi \sin \frac{x}{b} - y \cos \theta \cos \frac{x}{b}}{\sqrt{b^2 + y^2}} \hat{x} \\
&+ \left(\sin \theta \sin \phi \cos \frac{x}{b} - \cos \theta \sin \frac{x}{b} \right) \hat{y} \\
&+ \text{sign}(b) \frac{y \sin \theta \cos \phi + b \cos \theta \cos \frac{x}{b} + b \sin \theta \sin \phi \sin \frac{x}{b}}{\sqrt{b^2 + y^2}} \hat{z}
\end{aligned}
\tag{5.10}
$$

θ and ϕ are the polar and azimuthal angles of DW magnetization with respect to $\hat{u}$ and $\hat{p}$ directions, respectively. Consequently, the exchange energy per unit volume is

$$
\begin{aligned}
E_{ex} =& A_{ex} (\nabla \hat{m})^2 \\
=& A_{ex} \left[\left(\frac{\partial m_x}{\partial x} \right)^2 + \left(\frac{\partial m_y}{\partial x} \right)^2 + \left(\frac{\partial m_z}{\partial x} \right)^2 + \left(\frac{\partial m_x}{\partial y} \right)^2 + \left(\frac{\partial m_y}{\partial y} \right)^2 + \left(\frac{\partial m_z}{\partial y} \right)^2 \right]
\end{aligned}
\tag{5.11}
$$

where A_{ex} is the exchange stiffness constant. Since $\theta = 2\arctan \exp \left[\pm \frac{(x-q) \cos \chi + y \sin \chi}{\Delta} \right]$ for the DW magnetization,

$$
\begin{aligned}
E_{ex} =& A_{ex} \left[\frac{\sin^2 \theta}{\Delta^2} - \frac{2}{b} \frac{\sin \theta}{\Delta} \sin \phi \cos \chi - 2\xi \frac{\sin \theta}{\Delta} \cos \phi \sin \chi - \frac{1}{b^2} \sin^2 \theta \cos^2 \phi \right. \\
& \left. + \xi^2 \left(\sin^2 \theta \sin^2 \phi \sin^2 \frac{x}{b} - \sin^2 \theta \cos^2 \frac{x}{b} + \sin^2 \theta \cos^2 \phi + \frac{1}{2} \sin 2\theta \sin \phi \sin \frac{2x}{b} \right) \right],
\end{aligned}
\tag{5.12}
$$

where q is the DW position, χ is the DW tilting angle with respect to $\hat{r}$, and Δ is the DW width parameter.

The equations of motion are, then,

$$
\begin{aligned}
(1+\alpha^2)\dot{q} = {}& \mp \frac{\gamma\Delta}{M_s} K_0 \sin 2(\phi-\chi)\sec\chi \pm \frac{\pi\gamma\Delta}{2}\sec\chi\left[H_p\sin(\phi-\phi_H)+H_{DMI}\sin(\phi-\chi)\right]\\
& \mp \frac{\pi}{2}\alpha\gamma H_{SH}\Delta\cos\phi\sec\chi - \frac{\pi\gamma A_{ex}}{bM_s}\cos\phi\\
& + 4\gamma A_{ex}\sin\frac{\pi\Delta\sec\chi}{2b}\left(\frac{b}{\Delta}\sin\phi\cos\chi\cos\frac{q}{b}-\alpha\cos\phi\sin\frac{q}{b}\right)\\
& \left[0.4\cot\chi\left(1-\cos\frac{w\tan\chi}{2b}\right)+\left(1-\frac{0.2w}{b}\right)\sin w\,\tan\frac{\chi}{2b}\right]\\
& + \frac{\gamma A_{ex}\Delta}{2b^2 M_s}\sin 2\phi\sec\chi - \frac{\gamma A_{ex}}{2wM_s}\sin\frac{2\Delta\sec\chi}{b}\cot\chi\\
& \left[\sin 2\phi\cos\frac{2q}{b}+\frac{2\alpha\Delta}{b}\sec\chi(1+\sin^2\phi)\sin\frac{2q}{b}\right]\\
& \left[0.3\cot\chi\left(1-\cos\frac{w\tan\chi}{b}\right)+\left(1-\frac{0.3w}{b}\right)\sin\frac{w\tan\chi}{b}\right]\\
& -\frac{2\alpha\gamma A_{ex}\Delta}{wbM_s}\left[0.3\cot\chi\left(\cot\chi-\cot\chi\cos\frac{w\tan\chi}{b}-\frac{w}{b}\sin\frac{w\tan\chi}{b}\right)\right.\\
& \left.\left(\sin\frac{2q}{b}+\sin\frac{\pi\Delta\sec\chi}{b}\cos\frac{2q}{b}\right)+\cot\chi\sin\frac{\pi\Delta\sec\chi}{b}\left(\sin\frac{2q}{b}+\cos\frac{2q}{b}\right)\right],
\end{aligned}
\tag{5.13}
$$

$$
\begin{aligned}
(1+\alpha^2)\dot{\phi} = {}& \frac{\alpha\gamma}{M_s}K_0\sin 2(\phi-\chi)-\frac{\alpha\pi\gamma}{2}\left[H_p\sin(\phi-\phi_H)+H_{DMI}\sin(\phi-\chi)\right]\\
& -\frac{\pi}{2}\gamma H_{SH}\cos\phi\pm\frac{\alpha\pi\gamma A_{ex}}{bM_s\Delta}\cos\phi\cos\chi\\
& \mp\frac{4\gamma A_{ex}}{wM_s\Delta}\cos\chi\sin\frac{\pi\Delta\sec\chi}{2b}\left(\frac{\alpha b}{\Delta}\sin\phi\cos\chi\cos\frac{q}{b}+\cos\phi\sin\frac{q}{b}\right)\\
& \left[0.4\cot\chi\left(1-\cos\frac{w\tan\chi}{2b}\right)+\left(1-\frac{0.2w}{b}\right)\sin\frac{w\tan\chi}{2b}\right]\\
& \mp\frac{\alpha\gamma A_{ex}\Delta}{2b^2 M_s}\sin 2\phi\pm\frac{\gamma A_{ex}}{2wM_s\Delta}\sin\frac{2\Delta\sec\chi}{b}\cot\chi\\
& \left[\alpha\cos\chi\sin 2\phi\cos\frac{2q}{b}-\frac{2\Delta}{b}(1+\sin^2\phi)\sin\frac{2q}{b}\right]\\
& \left[0.3\cot\chi\left(1-\cos\frac{w\tan\chi}{b}\right)+\left(1-\frac{0.34w}{b}\right)\sin\frac{w\tan\chi}{b}\right]\\
& \mp\frac{2\gamma A_{ex}}{wbM_s}\left[0.3\cot\chi\left(\cot\chi-\cot\chi\cos\frac{w\tan\chi}{b}-\frac{w}{b}\sin\frac{w\tan\chi}{b}\right)\right.\\
& \left.\left(\sin\frac{2q}{b}+\sin\frac{\pi\Delta\sec\chi}{b}\cos\frac{2q}{b}\right)+\cot\chi\sin\frac{\pi\Delta\sec\chi}{b}\left(\sin\frac{2q}{b}+\cos\frac{2q}{b}\right)\right],
\end{aligned}
\tag{5.14}
$$

$$\frac{\pi^2 \alpha}{6\gamma}\left[\left(\frac{w}{\pi\Delta}\right)^2 \sec^2\chi + \tan^2\chi\right]\dot{\chi} = -\frac{\sigma}{M_s\Delta}\tan\chi + \pi H_{DM}\sin(\phi-\chi) - H_k\sin 2(\phi-\chi)$$

$$\mp \frac{4A_{ex}}{wM_s\Delta}\cos\phi\cos\frac{q}{b}\left(\frac{b}{\Delta}\sin 2\chi\sin\frac{\pi\Delta\sec\chi}{2b} - \pi\sin\chi\cos\frac{\pi\Delta\sec\chi}{2b}\right)$$

$$\left[0.4\cot\chi\left(1 - \cos\frac{w\tan\chi}{2b}\right) + \left(1 - \frac{0.2w}{b}\right)\sin\frac{w\tan\chi}{2b}\right] \mp \frac{8bA_{ex}}{wM_s\Delta^2}\cos\phi\cos\frac{q}{b}$$

$$\sin\frac{\pi\Delta\sec\chi}{2b}\left\{0.4\cot\chi\left[\cot\chi\left(1 - \cos\frac{\pi\Delta\sec\chi}{2b}\right) - \frac{w}{2b}\sin\frac{\pi\Delta\sec\chi}{2b}\right]\right.$$

$$\left. -\left(1 - \frac{0.2w}{b}\right)\frac{w}{2b}\cos\frac{\pi\Delta\sec\chi}{2b}\right\} \pm \frac{A_{ex}}{wM_s\Delta}(1 + \sin^2\phi)\cos\chi\cos\frac{2q}{b}$$

$$\left\{\left(\frac{2\Delta}{b}\sec\chi\cos\frac{2\Delta\sec\chi}{b} - \csc^2\chi\sin\frac{2\Delta\sec\chi}{b}\right)\left[0.3\cot\chi\left(1 - \cos\frac{w\tan\chi}{b}\right)\right.\right.$$

$$\left. + \left(1 - \frac{0.3w}{b}\right)\sin\frac{w\tan\chi}{b}\right] + 0.34\sin\frac{2\Delta\sec\chi}{b}\cot\chi\left[\csc^2\chi\left(\cos\frac{2\Delta\sec\chi}{b} - 1\right)\right]$$

$$\left. + \frac{w}{b}\sec\chi\left(\csc\chi\sin\frac{w\tan\chi}{b} - \sec\chi\cos\frac{w\tan\chi}{b}\right)\right\} \mp \frac{2A_{ex}}{wM_s\Delta}\cos\chi\csc^2\chi$$

$$\left[0.3\cot\chi\left(\cot\chi - \cot\chi\cos\frac{w\tan\chi}{b} - \frac{w}{b}\sin\frac{w\tan\chi}{b}\right)\left(\cos\frac{2q}{b}\right.\right.$$

$$\left. -\sin\frac{\pi\Delta\sec\chi}{b}\sin\frac{2q}{b}\right) + \sin\frac{\pi\Delta\sec\chi}{b}\left(\cos\frac{2q}{b} - \sin\frac{2q}{b}\right)\right] \pm \frac{2A_{ex}}{wM_s\Delta}\cos\chi\cot\chi$$

$$\left\{0.3\left[\csc^2\chi\left(\cos\frac{w\tan\chi}{b} - 1\right) + \frac{w}{b}\sec\chi\left(\csc\chi\sin\frac{w\tan\chi}{b} - \sec\chi\cos\frac{w\tan\chi}{b}\right)\right]\right.$$

$$\left(\cos\frac{2q}{b} - \sin\frac{\pi\Delta\sec\chi}{b}\sin\frac{2q}{b}\right) + \frac{\pi\Delta\sec\chi\tan\chi}{b}\cos\frac{\pi\Delta\sec\chi}{b}$$

$$\left.\left.\left[\cos\frac{2q}{b} - \sin\frac{2q}{b}\left[1 + 0.3\left(\cot\chi - \cot\chi\cos\frac{w\tan\chi}{b} - \frac{w}{b}\sin\frac{w\tan\chi}{b}\right)\right]\right]\right\}\right\}, \qquad (5.15)$$

where upper and lower signs correspond to $\odot\otimes$ and $\otimes\odot$, respectively, and $\sigma = 4\sqrt{A_{ex}K_0} + K_0\Delta\sin(\phi-\chi) - \pi\Delta M_s H_p\cos(\phi-\phi_H) - \pi\Delta M_s H_{DM}\cos(\phi-\chi)$.

Note that many terms are much smaller than the dominant other terms since $b, w \gg \Delta$, which leads to the following equations of motion:

$$(1+\alpha^2)\dot{q} \approx \mp\frac{\gamma\Delta}{M_s}K_0\sin 2(\phi-\chi)\sec\chi \pm \frac{\pi\gamma\Delta}{2}\sec\chi\left[H_p\sin(\phi-\phi_H) + H_{DMI}\sin(\phi-\chi)\right]$$

$$\mp\frac{\pi}{2}\alpha\gamma H_{SH}\Delta\cos\phi\sec\chi - \frac{\pi\gamma A_{ex}}{bM_s}\cos\phi, \qquad (5.16)$$

$$(1+\alpha^2)\dot{\phi} \approx \frac{\alpha\gamma}{M_s}K_0\sin 2(\phi-\chi) - \frac{\alpha\pi\gamma}{2}\left[H_p\sin(\phi-\phi_H) + H_{DMI}\sin(\phi-\chi)\right]$$

$$-\frac{\pi}{2}\gamma H_{SH}\cos\phi \pm \frac{\alpha\pi\gamma A_{ex}}{bM_s\Delta}\cos\phi\cos\chi, \qquad (5.17)$$

$$\frac{\pi^2\alpha}{6\gamma}\left[\left(\frac{w}{\pi\Delta}\right)^2\sec^2\chi + \tan^2\chi\right]\dot\chi \approx -\frac{\sigma}{M_s\Delta}\tan\chi + \pi H_{DM}\sin(\phi-\chi) - H_k\sin 2(\phi-\chi)$$
$$\mp \frac{4A_{ex}}{wM_s\Delta}\cos\phi\cos\frac{q}{b}\left(\frac{b}{\Delta}\sin 2\chi\sin\frac{\pi\Delta\sec\chi}{2b} - \pi\sin\chi\cos\frac{\pi\Delta\sec\chi}{2b}\right)$$
$$\left[0.4\cot\chi\left(1-\cos\frac{w\tan\chi}{2b}\right) + \left(1-\frac{0.2w}{b}\right)\sin\frac{w\tan\chi}{2b}\right]\mp\frac{8bA_{ex}}{wM_s\Delta^2}\cos\phi\cos\frac{q}{b}$$
$$\sin\frac{\pi\Delta\sec\chi}{2b}\left\{0.4\cot\chi\left[\cot\chi\left(1-\cos\frac{\pi\Delta\sec\chi}{2b}\right) - \frac{w}{2b}\sin\frac{\pi\Delta\sec\chi}{2b}\right]\right.$$
$$\left.-\left(1-\frac{0.2w}{b}\right)\frac{w}{2b}\cos\frac{\pi\Delta\sec\chi}{2b}\right\}. \tag{5.18}$$

The most important term that is related to the torsion torque is $-\frac{\pi\gamma A_{ex}}{bM_s}\cos\phi$, which corresponds to the mechanism of the torsion-induced effect that is shown in figs. 5.7 to 5.9.

Appendix 5.G   Local Domain Wall Velocity Over the Device Length

Over the length of a device, the torsion varies in magnitude [19] and in chirality. Any torsion-related effect should, therefore, vary accordingly. To evaluate it, the DW displacements after each pulse sequence were used to calculate local DW velocities in different regions over the device. This local DW velocity data was accumulated over the 3-5 repetitions for each experimental condition and is shown in fig. 5.18 for different DW types moving over $\zeta = 0; \pm 11\,^\circ$ devices with different current densities j and directions.

DWs in favorable cases move consistently faster than those in unfavorable cases. Particularly, the points where torsion peaks, at 0.35 and 0.65 in the relative position scale (see fig. 5.4b), and the chirality inverts, at 0.5 in the relative position scale, display the largest differences. For each set of conditions, the unfavorable DW type starts to slow down over the region with maximum torsion, and proceeds to become stuck in the point where the torsion chirality changes, rather than the points with maximum torsion magnitude. On the other hand, the velocity of favorable DW type in each case typically peaks around one of the points with maximum torsion magnitude.

If a given DW type is able to overcome the region where the torsion chirality inverts, then it is highly likely to move through the whole twisted section, even though, in the second half, the torsion chirality is inverted. This is unexpected since an inversion of the torsion chirality in the second half of the device would be expected to render the motion of a DW type that moves through the first half unfavorable. For example, this is seen when the torsion chirality of the first half of a device is inverted, as is the case with $\zeta = +11\,^\circ$ and $\zeta = -11\,^\circ$ devices. In some cases, the DW velocity shows local peaks at the location of both torsion maxima, despite their opposite chiralities. A detailed analysis of the DW progression over the variable torsion region, particularly the region where the torsion chirality inverts, is necessary to understand this effect. This is, so far, not contemplated in the model of section 5.F, which models a constant torsion throughout the device.

In general, DW velocity varies less over the device without torsion. However, the presented data is too inconsistent and, in many cases, too sparse for a conclusive analysis. The acquisition settings, particularly the pulse length, would need to be optimized to acquire more and more consistent data points for such analysis.

Appendix 5.H   Error Analysis

Two different error analysis are employed in the analysis of the experimental data.

The first measures the data dispersion within the 3-5 repetitions done for each experimental condition, as mentioned in section 5.2, by measuring the average of the deviations to the average of the measurements.

---

[19] as explained in section 5.1, this is necessary for the magnetic film surface to be continuous at the start and middle of the twisted section
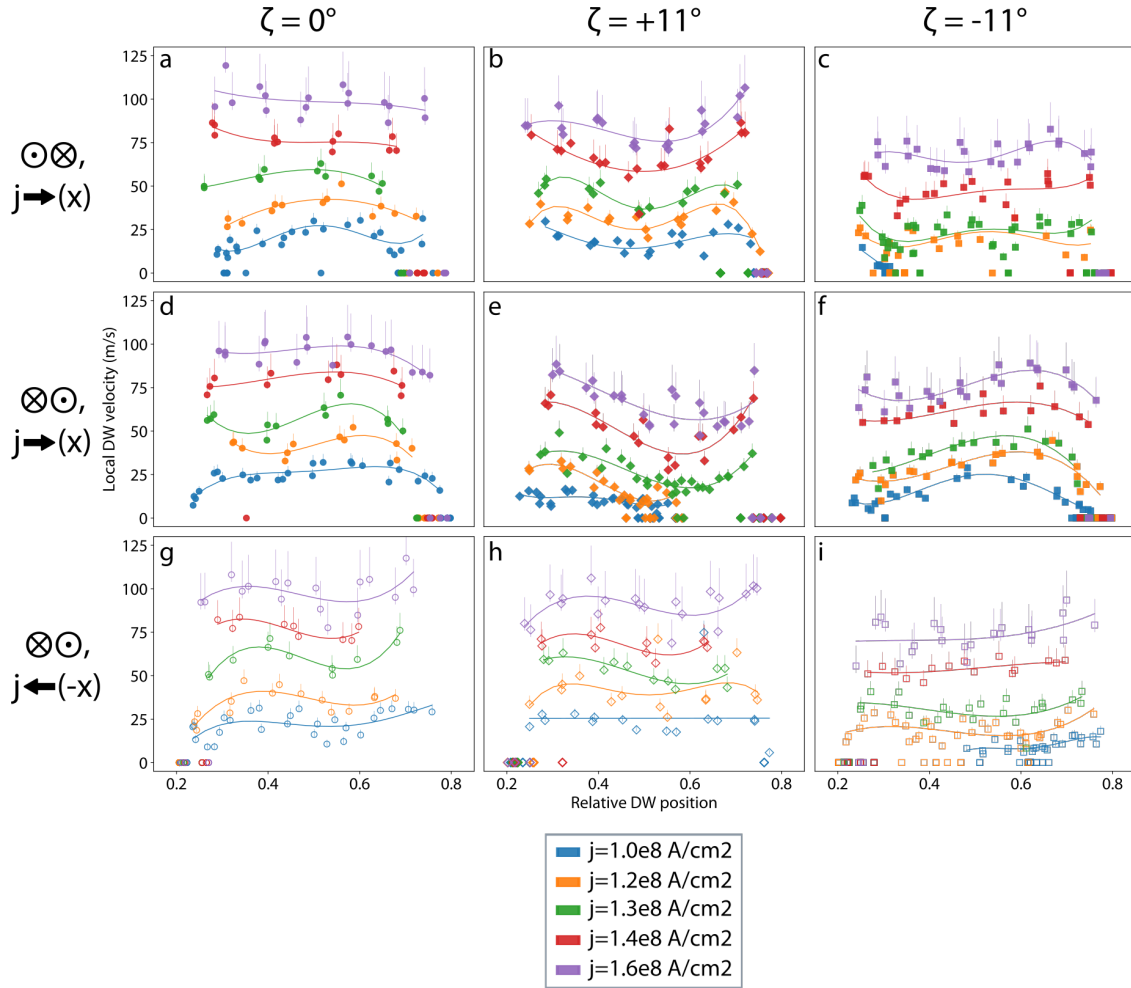
Figure 5.18: Local DW velocity as a function of the relative DW position over the device and the current density j (color-coded according to the legend on the bottom) for devices with $\zeta = 0\,°$ (a,d,g), $\zeta = +11\,°$ (b,e,h) and $\zeta = -11\,°$ (c,f,i) and for $\odot\otimes$, for $j > 0$ (a,b,c), and $\otimes\odot$, for both $j > 0$ (d,e,f) and $j < 0$ (g,h,i). The lines are only guides to the eye, corresponding to fits to polynomials of order ≤ 4.

Because the amount of repetitions is small, the estimated error is not statistically relevant and thus the standard deviation is not presented instead. This is used, for example, in the plots showing the average DW velocity over the device as a function of the current density in section 5.4 and is easily identified by the symmetric error bars.

The second error type measures the inaccuracy of the data acquisition and quantification methods. It accounts for errors in determining the boundaries to calculate the DW velocity, which are small, but most importantly it accounts for the error in the pulse lengths due to the rise and fall times of the pulses, as mentioned in section 3.7. Because the effective pulse length is always smaller than the set value, this error contribution is asymmetric towards higher velocities and is proportional to the measured velocity. This is used in the evaluation of the local DW velocity over the device in section 5.G and is easily identified by the asymmetric error bars.

Chapter 6

Real-Time Controlled and Verified Multi-Photon Lithography

As reviewed in section 2.1, Multi-Photon Lithography (MPL) is a diverse research field with an important role in 3D applications at the nano- and micro-scale over a wide range of topics [9], including electronics [53, 54], photonics [17, 55], cell scaffolding [19, 58], microfluidics [18], robotics [60], and material science [63, 64]. Such widespread adoption has greatly accelerated MPL development, as well as the development of a wide range of complementary processes [9, 31, 32]. In this context, significant improvements to the MPL process can translate to many applications.

Today, MPL maturity and ease of use are such that inexperienced user is able to significantly adapt the fabrication characteristics and materials [72] to their needs while reliably achieving small features over large ranges in short fabrication times [28].

Compared to such an efficient fabrication, the MPL-compatible characterization methods have seen little progress and are now the bottleneck in the fabrication optimization process, inhibiting shorter iteration cycles. Mostly used characterization methods are asynchronous and ex-situ. For example, Scanning Electron Microscopy (SEM) provides high resolution but is time-consuming for detailed analysis and might damage sensitive samples. Standard microscopy-based techniques such as bright-field microscopy enable quick but very coarse analysis while confocal fluorescence microscopy still requires sample development. Alternatives have been developed [190–193], but remain limited in applicability, i.e., they are either ex-situ or asynchronous, or in resolution.

In this chapter, I present a real-time and in-situ characterization process for MPL that enables fabrication control and high-fidelity 3D reconstruction of the fabrication result without any post-processing. This process enables to correct for fabrication defects during the fabrication and to perform optimization of the fabrication parameters in-situ.

The presented process is based on the polymerization-induced stabilization of subspecies of the photoinitiator with a red-shifted fluorescence absorption, which results in a polymer-specific fluorescence emission under excitations to the far red of the absorption.

Combining fabrication and characterization in a single process improves fabrication yields and, particularly, the time efficiency of the optimization process, and directly translates into shorter iterations times and more efficient research in all MPL dependent applications.

6.1 MPL Characterization

The outcome of an MPL process is, to some extent, dependent on the structure being fabricated because of the intricate features the latter might have. While pre-defined fabrication profiles provide good initial results, optimization of fabrication parameters is often necessary to achieve the desired results, particularly for structures with small, high-resolution or overhanging features.

The standard optimization process comprises fabricating the same structure under different parame-

ters followed by characterization, usually with SEM. While SEM-based optimization provides a reliable high-resolution characterization which is so far unmatched, it is usually a time-consuming process that involves iterative fabrication and characterization of several samples and requires specific post-processing. Furthermore, it is susceptible to parallax errors, to partial or total shadowing of structural elements [50], and to e-beam-induced damage [194].

On the other hand, methods such as Two-Photon Excited Fluorescence (TPEF) [192] and Third-Harmonic Generation (THG) [191] are not hindered by shadowing effects nor require post-processing besides the development step. Beyond TPEF and THG, Coherent Anti-Stokes Raman Spectroscopy (CARS) [190] achieves the same capabilities while in-situ and real-time through selective characterization of the polymerized regions. Thus, while not matching SEM resolution, CARS provides real-time non-invasive characterization without shadowing effects even before sample development, similar to the method presented in this paper.

Fourier-Domain Optical Coherence Tomography (FD-OCT) [193] is an in-situ characterization technique with fast acquisition cycles that is sensitive to local differences in the refractive index. However, it is also sensitive to the fabrication settings and is limited to a resolution of $\approx 2 \ \mu m$.

6.2   Environment Sensitive Fluorescence

Fluorescent dyes are known to be sensitive to distinct environmental properties, prompting their use as environmental probes [195]. In the particular context of this paper, the fluorescence response of the DETC dye, used as photoinitiator, is known to be sensitive to the solvent polarity [196], known as solvatochromism, and appears to be sensitive to medium rigidity [197], through effects known as red-edge effects [104], reviewed in section 2.2. Previously, such fluorescence effects have been used to monitor UV-induced polymerization of polymer films [198, 199].
DETC is a known fluorescence dye with typical absorption in the 300-480 nm range and emission in the 420-600 nm range [196, 197]. Although thoroughly used in stimulated emission depletion STED-MPL [101, 200], DETC-PETA photoresist is a rather complex molecular system with several different possible pathways for polymerization- and depletion-inducing phenomena [166, 197].

6.3   Experimental Setup

For the study presented in this chapter, the STED-MPL experimental setup shown in fig. 6.1a was utilized. It consists of an MPL system with a 780 nm fs excitation laser, used as excitation beam to induce polymerization, a 3D STED module with a 532 nm CW depletion laser, a spatial light modulator for modulation of the point spread function, and a confocal microscope arrangement with an avalanche photo-detector for fluorescence characterization. Further information can be found in section 3.1.

We utilize photoresists consisting of 0.25 wt% DETC as photoinitiator and 99.75 wt% of either PETA or PETTA as monomers. These photoresists compositions have been extensively used in STED-MPL research [66, 101, 200], enabling several successful applications. Furthermore, the molecular mechanisms of DETC-PETA photoresist in STED-MPL have been comprehensively investigated, serving as basis for this study [197]. Figures 6.1d to 6.1f show the molecular structure of the photoresist components while fig. 6.1g depicts the arrangement of DETC and PETA in an unbranched polymer chain.

6.4   Polymer-Specific Fluorescence

As the core observation for the following study, an increased fluorescence signal was noted in the regions of the photoresist that are sequentially exposed to the polymerization-inducing beam and, after an interval ranging from hundreds of μs to minutes, to the 532 nm laser. This increased fluorescence signal is shown
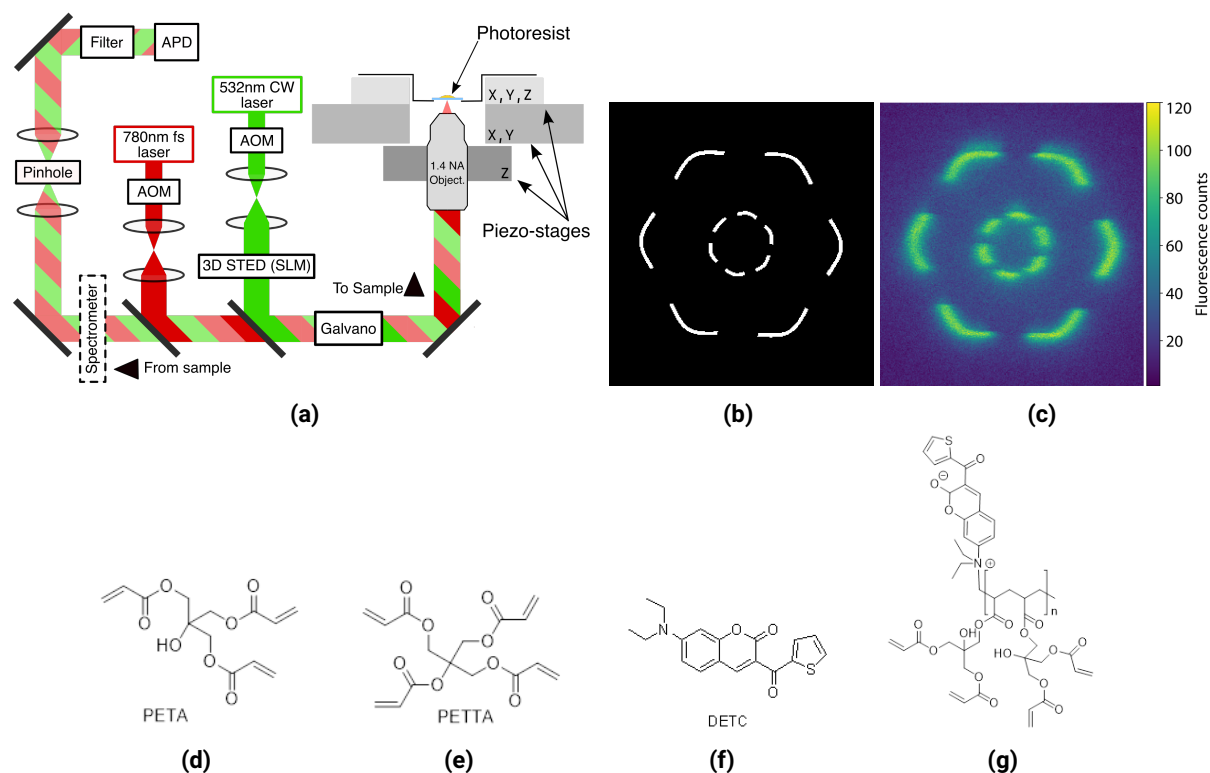
Figure 6.1: Experimental setup for observation of enhanced fluorescence. (a) Scheme of the experimental setup, consisting of a standard MPL arrangement along a 3D STED module and a confocal acquisition module. (b) Example of a layer exposure mask, with the white regions being exposed to the 780 nm fs laser. (c) By scanning the region of the layer exposure mask (b) with the 532 nm CW laser a few ms after the exposure scan, an enhanced fluorescence is observed in the areas exposed to both lasers. (d)-(f) Molecular structures of the photoresist components: PETA (d), PETTA (e), DETC (f). (g) Arrangement of PETA and DETC in an unbranched polymer chain.

in fig. 6.1b and fig. 6.1c. The enhanced fluorescence under such combined exposure scheme is clearly distinguishable from the background fluorescence signal, defined by the fluorescence emission of the photoresist under 532 nm exposure only. As the lifetime of STED-associated states is on the order of ns for singlet states to few μs for triplet states [166, 200], and the polymerization starts approximately 100 μs after exposure [84], the enhanced fluorescence is observed beyond such timescales and cannot be attributed to these events. Instead, as will we show and as had been previously proposed [197], this effect appears to be associated with the stabilization of DETC mesomeric structures, or subspecies, with red-shifted fluorescence responses in the polymerized volumes [104].

6.5   Spectral Analysis of DETC Fluorescence Emission

In order to characterize the enhanced fluorescence, we performed both spectral and power-dependent analyses of DETC fluorescence emission. While the spectral analysis provides further insight into specific transitions in the molecules' pathway, the power-dependent analysis provides insight into the nature of a molecule's interaction with the light it is exposed to. To acquire the emission spectra, we place a spectrophotometer in the beam path of the confocal section (fig. 6.1a), and integrate the signal for 70 ms intervals while continuously scanning the laser, focused deep into the photoresist, over a large area of the material. The fluorescence spectra for DETC-PETA photoresist under combined exposure, i.e., sequential exposure to the 780 nm and 532 nm with a few ms interval in between, is shown in fig. 6.2. Spectra for fluorescence emission under single laser exposure and for the PETTA-DETC photoresist can be found in section 6.A. Further experimental details are described in section 3.3. The measured emission spectra

differ significantly from the expected [196]. At 504 nm wavelength, the central emission peak for DETC, the fluorescence is barely above the noise level while a sharp peak appears at 529 nm, due to exposure to the 532 nm laser, and a broad group of peaks appears in the 750-800 nm range due to exposure to the 780 nm laser.
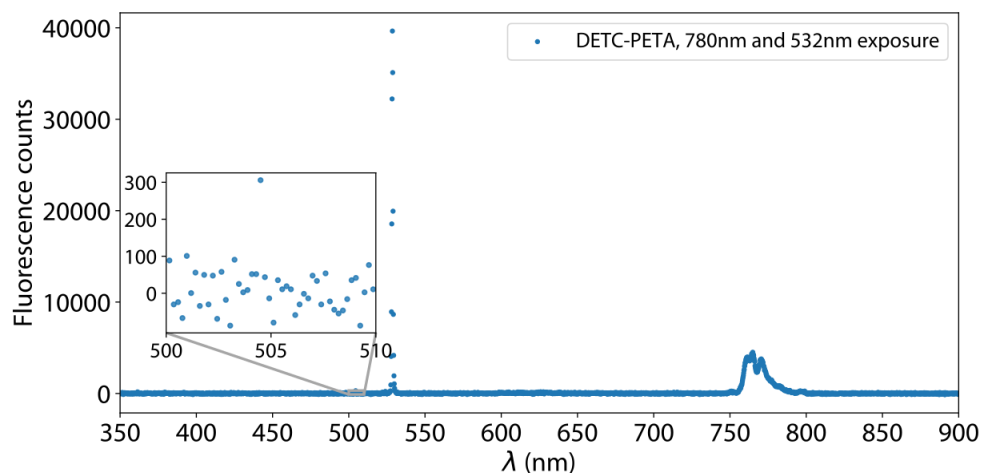
Figure 6.2: Fluorescence emission spectra of the DETC-PETA photoresist under sequential exposure to the 780 nm and 532 nm laser sources in polymerization-inducing conditions.

The 504 nm wavelength peak matches the central peak for the DETC fluorescence emission [196] but it is barely significant, even at higher laser powers. This suggests that the fluorescence emission induced by two-photon absorption from the 780 nm source is, compared to other pathways, unlikely.

As previously observed and interpreted [197], the 529 nm is an anti-stokes peak caused by the 532 nm source. Although this source is at the far-red of the DETC absorption band, the fluorescence emission induced by it can be explained by red-edge effects [104] (see section 2.2): the interaction of DETC with the surrounding viscous medium stabilizes a distribution of DETC mesomeric structures, or subspecies, that causes an inhomogeneous broadening of its energy states. This broadening of a molecule's energy states might occur particularly at the ground state, e.g., by hindered rotation of a molecular group that disables complete relaxation, at the excited state, e.g., by stabilization of an excited state through interaction with the solvent, or at both, and contributes to a red-shifted fluorescence absorption and/or emission [104] [1]. This is consistent with previous observations of the sensitivity of DETC fluorescence [196], and that of other coumarins [198], to changes in the molecules' environment, such as changes in solvent polarity.

More surprising, however, are the fluorescence emission peaks at the 750-800 nm band, caused by the 780 nm excitation. Based on previous studies, a TPA triggered by the 780 nm laser was to be expected for DETC, followed by a one-photon emission at the 420-600 nm range [197]. Instead, this observation signals a more complex molecular pathway. These peaks become more pronounced with increasing laser power, but are still present well below the polymerization threshold. As for the 529 nm fluorescence peak, the main emission wavelength components of these peaks are shorter than the excitations', possibly due to dipolar relaxation-inducing an anti-Stokes shift [104]. To further understand the appearance of this peak, a power-dependent analysis of the fluorescence signal is realized.

---

[1] as discussed in section 2.2, the energy state with highest dipole moment is typically the one with highest contribution to the red-edge effect, which for DETC would be excited state [196].

6.6   Power Dependency of DETC Fluorescence Emission

Fluorescence emission enabled by an N-photon absorption process is expected to follow an N-order scaling with the energy of the excitation source, i.e.

$$I_{fluor} \propto E_{exc}^{N}. \tag{6.1}$$

In order to further characterize the molecular mechanisms in DETC-initiated polymerization, we measure the dependency of each fluorescence signal (presented in section 6.5 and section 6.A) on the energy of the corresponding excitation source(s). For each exposure configuration, we scan a reference volume (see section 6.B) of the photoresist with a given laser source and measure the resulting confocal fluorescence signal at the APD. We repeat this process for different laser powers and exposure schemes, e.g., exposure to the 780 nm and 532 nm sources separately or both sequentially. The fluorescence signal dependence on the 532 nm source energy is shown in section 6.C. Further experimental details can be found in section 3.4.

The 780 nm laser-induced fluorescence results are presented in fig. 6.3a. Although we observe the expected [197] N=2 scaling at lower pulse energies, possibly connected to the fluorescent emission peak at 504 nm, an N=4 scaling, associated with the fluorescence emission at 750-800 nm range, becomes dominant for excitation pulse energies above 0.055 nJ. Such scaling continues until the polymerization threshold is reached, with the fluorescence signal saturating for excitation pulse energies higher than the threshold.

The observation of an increased significance of the 4th-order process when compared to earlier studies [197] is attributed to differences in the exposure. We use a laser scanning speed of 5 mm/s, 50 times higher than previously, greatly decreasing the cumulative exposure dose [2]. Excited state absorption events like the triplet state absorption in the three-photon initiation mechanism [197], shown faded in fig. 6.3c, are strongly dependent on the temporal extent of the exposure [93] and are greatly reduced under shorter exposures as in our case, while non-linear processes are not.

Furthermore, the shorter exposure requires about 2.5 times higher pulse energy for polymerization to occur, an energy range where the N=4 process is much more significant due to the scaling defined by eq. 6.1. Since both N=2 and N=4 scaling processes are associated with a different polymerization initiation mechanism, respectively a 3- and 4-photon initiation mechanism (fig. 6.3c), the predominance of the 4-photon excitation also implies the predominance of the 4-photon initiation mechanism.

The 4-photon pathway is expected to lead to a highly excited but unstable singlet state, S3. It is therefore likely that the associated fluorescence emission at the 750-800 nm range occurs from the highly excited singlet state rather than the corresponding triplet state. Under this hypothesis, corresponding to the Jablonski diagram of fig. 6.3c, the observed fluorescence emission is directly correlated with the polymerization initiation mechanism. The intersystem crossing would then take place from this less excited S2 state, followed by radical generation.

However, considering the de-excitation through fluorescence emission in the 750-800 nm range to a less-energetic S2 state, as shown in fig. 6.3c, opens the possibility for a 4-photon process consisting of a two-photon non-linear absorption followed by two one-photon excited state absorptions, which would also lead to a scaling with an N=4 component [92]. Furthermore, it could also mean that the radical formation occurs from the same triplet-state, T2, as in the 3-photon pathway that was previously identified [197], shown faded in fig. 6.3c. Even though we use 70 fs-short pulses and 12.5 ns pulse intervals[3], which are expected to limit the extent of excited state absorptions, investigating these possibilities would require additional time-resolved measurements [93, 197] of the fluorescence and polymerization processes.

The saturation of the 780 nm laser-induced fluorescence, corresponding to fluorescence emission that occurs before the start of the polymerization, is attributed to the saturation of the excitation itself, with the large majority of the DETC molecules in the volume corresponding to a pixel being excited by the 780 nm

---

[2]this is achieved by utilizing a galvano scanner for scanning the laser beam rather than a piezoelectric stage.

[3]i.e., significantly higher than the S1 lifetime [200]
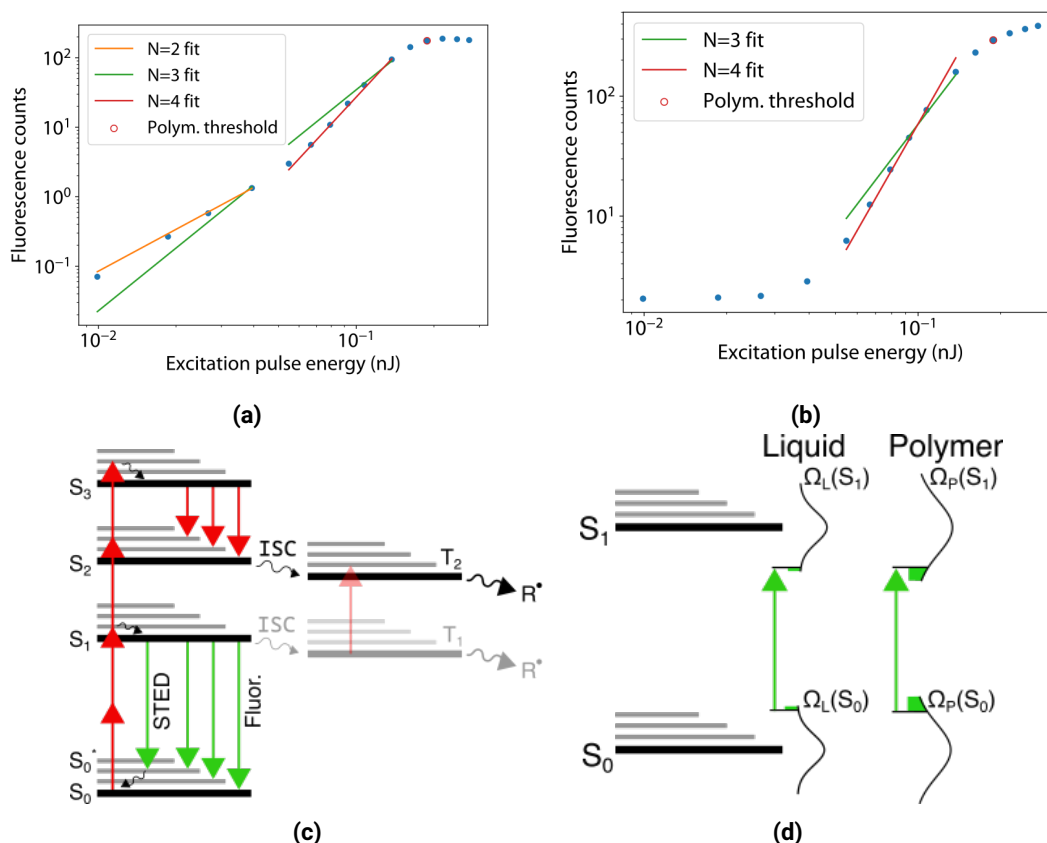
Figure 6.3: Dependency of the DETC fluorescence on the exposure laser pulse energy. (a) 780 nm induced fluorescence of the DETC-PETA photoresist as a function of the 780 nm pulse energy. Curves represent fits of the experimental data to the function $I_{fluor} = a * E_{780nm}^{N}$ with N=2,3 and 4 scalings. (b) DETC-PETA fluorescence signal under sequential 780 nm and 532 nm laser exposures as a function of the 780nm pulse energy. The interval between exposures is on the order of milliseconds. Curves represent fits of the experimental data to the function $I_{fluor} = a * E_{780nm}^{N}$ with N=3 and 4 scalings. (c) Jablonski diagram of the molecular model developed based on the fluorescence characterization. The 3-photon pathway, involving triplet-triplet absorption, is faded, as even though it has been shown to be possible, it is not considered to play a very significant role in the conditions studied here. S^{*} states, in gray, correspond to vibrational states. (d) Impact of solute-solvent interactions on the molecule's energy levels and its red-edge absorption. The interaction between DETC and the monomer generates a distribution of DETC mesomeric structures, or subspecies, with slightly different energies, leading to a dispersion of the energy levels of the ensemble, i.e., inhomogeneous broadening, and enabling fluorescence excitation at the red end of the absorption. As the range of interaction energies between solute and solvent increases, e.g., through polymerization, the variance of the energy level distributions increases, increasing the number of subspecies excited by a red-edge excitation (shown as green regions) and therefore increasing the resulting fluorescence signal. The distribution of each energy state is independent and specific to the DETC-monomer interactions.

laser focus.

As for the increased fluorescence emission signal under sequential exposure to 780 nm and 532 nm sources, referred to as combined exposure, its dependency on 780 nm pulse energy is shown in fig. 6.3b. With no fluorescence signal dependence at low pulse energies, an N=4 scaling is observed for pulse energies greater than 0.055 nJ that closely matches that of the 780 nm induced fluorescence (fig. 6.3a). As with the 780 nm induced fluorescence, the fluorescence signal also saturates for pulse energies above the polymerization threshold.

The increased fluorescence signal can be promptly explained in the context of red-edge effects associated with polymer matrix formation [104]: as polymerization changes the interaction landscape of the medium, it enables a larger range of interaction energies (see section 2.2), enabling a further stabilization the DETC

energetic states, e.g., through the incorporation of DETC in polymeric chains or through improved dipole-dipole stabilization, but also a further hindrance of DETC relaxation, e.g., by frustrated rotations in a rigid polymer matrix. As a whole, a larger range of solute-solvent interaction energies results in a more dispersed energetic band structure, i.e., a larger inhomogeneous broadening, as represented in fig. 6.3d. Therefore, a red-shifted fluorescence excitation source like the 532 nm laser is able to excite more subspecies in a polymerized volume than in a non-polymerized volume, resulting in an increased fluorescence signal that is specific to the polymerized regions.

Under this hypothesis, it becomes clear that the 4-photon process driving the 780 nm laser-induced fluorescence is the same driving the polymerization, since the polymerization-driven fluorescence signal displays the same scaling as the former. This fourth-order scaling for the enhanced fluorescence is consistent with previous observations [197]. Under the tested experimental conditions, the 4-photon initiation thus seems more efficient than the alternative 3-photon initiation mechanism, given it is seen to drive the polymerization-induced fluorescence signal.

6.7 Influence of Monomer Polarity and Polymer Rigidity

Solvent polarity is an important parameter for both inhomogeneous broadening [104] and DETC fluorescence emission in liquids [196], and is therefore expected to impact the observed fluorescence. To investigate its impact, we characterize the enhanced fluorescence signal under combined exposure for the PETTA-DETC resist and compare it with that of the PETA-DETC in fig. 6.4. While the PETA monomer has a hydroxyl group that increases its polarity, the PETTA monomer has an extra vinyl group in its place, an extra branching domain that enables a more rigid polymer structure.
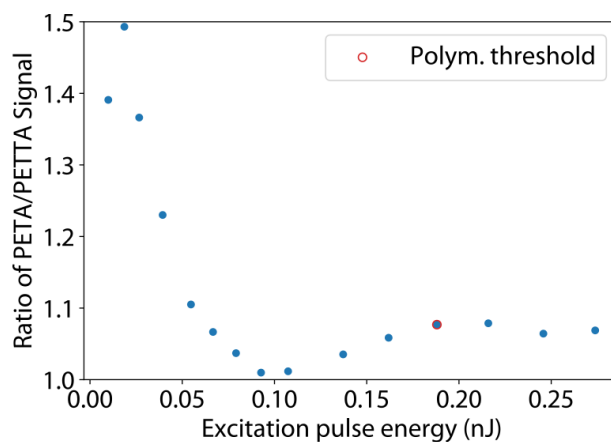
Figure 6.4: Ratio of the fluorescence signals in DETC-PETA and DETC-PETTA photoresists, respectively, under combined exposure as a function of the 780nm pulse energy.

While PETA increased polarity is expected to increase inhomogeneous broadening, resulting in an increased fluorescence signal through a red-shifted fluorescence, inhomogeneous broadening is also sensitive to the increased rigidity of the PETTA polymer matrix. The ratio presented in fig. 6.4 weighs the impact of both factors.

Before the polymerization starts, at pulse energies < 0.05 nJ, the effect of increased polarity is clearly dominant, with a 35-50 % increased fluorescence signal for the PETA-DETC photoresist despite increased viscosity of the PETTA-DETC resist. As polymer matrices start to form, however, the effect of PETA's increased polarity is mostly compensated by the increased rigidity of the PETTA polymer matrix. Under sparse polymerization conditions, at pulse energies of about 0.1 nJ, the difference in polymer rigidity between both photoresists is likely maximum, fully compensating for the polar effect. Past the polymerization threshold, the difference in the rigidity of the polymer matrices likely decreases and the polymer densities

saturate, such that the polar effect becomes predominant again, netting a 5-8 % increase in fluorescence intensity.

Regarding the comparison of the emission spectra of both photoresists, and particularly the 532 nm fluorescence peak, no measurable differences were found within the experimental wavelength resolution of 0.2 nm.

6.8   Enhanced Fluorescence as a Probe of the Local Polymerization State

In the context of the presented results, the DETC molecule is seen to function as a probe for the local environment it is in. That we are able to observe an increased fluorescence for excitation pulse energies well below the polymerization threshold means that the underlying fluorescence mechanism is sensitive to changes in the local environment well before a material density is reached that leads to appreciable features, as established by the polymerization threshold. For excitation pulse energies above the polymerization threshold, there is a saturation of the photo-excitation and of the polymer matrix density, leading to a saturation of the polymerization-induced fluorescence. Such environment-sensitive fluorescence has been previously observed for the photoresist [196] we use as well as other fluorescence dyes [195]. Furthermore, this signal has been used to monitor polymerization processes in films [198, 199].

By associating the enhanced fluorescence signal to the polymerization conversion level, it is possible to locally characterize the polymerization state based on the enhanced fluorescence signal at a given point (see fig. 6.1c). This correspondence enables, for any specific set of exposure parameters, to characterize and control the fabrication based on the registered fluorescence signal.

To evaluate the sensitivity of this approach, we compare the fluorescence signals under combined exposure and under 532 nm laser exposure only, with the latter constituting the background signal. Both signals are acquired in contiguous areas of the same scanning experiment and thus at the same depth and under the same conditions. The ratio between both signals is presented in fig. 6.5 for different excitation pulse energies, establishing the Signal-to-Noise Ratio (SNR) for using the enhanced fluorescence as a characterization of the polymerization state. Past the polymerization threshold, the SNR is seen to go up to 7, achieving significant specificity. That the fluorescence signal ratio is seen to saturate before the polymerization threshold and greatly increase afterwards is strong evidence of a significant transition at that point. In the context of red-edge effects, this can be interpreted as a generation of many new subspecies in the DETC ensemble as a result of the increased polymer matrix rigidity or solute-solvent interaction past the polymerization threshold, leading to a greater inhomogeneous broadening.
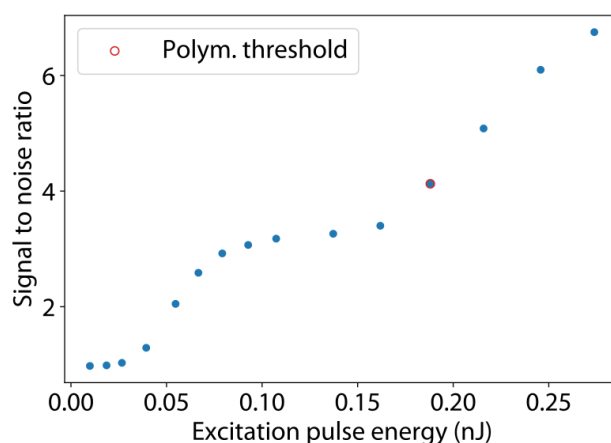
Figure 6.5: Ratio of the fluorescence signals under combined exposure and under exposure to the 532 nm laser only as a function of the 780 nm pulse energy. Both fluorescence signals were measured in contiguous areas of the same scan. This ratio quantifies the SNR of the enhanced fluorescence under combined excitation.

6.9 MPL with Real-Time Characterization

Based on the presented results, an improved MPL process is established where, a few ms after the exposure of a given area to the excitation beam, the same area and its close vicinities are scanned with the 532 nm laser and the resulting fluorescence signal is registered through a confocal detection scheme. The 532 nm laser exposure dose is kept minimum, at 25 nJ, so as not to affect the fabrication or saturate the APD.

By processing the registered fluorescence signal, the fabricated regions can be extracted. Direct processing with a simple threshold operation is used, although accounting with PSF deconvolution is expected to provide improved results.

This improved MPL process achieves layer-by-layer real-time characterization of the fabrication. Since the fluorescence excitation is done on the red-edge of the DETC absorption spectra, it is highly specific to DETC subspecies in polymerized volumes due to inhomogeneous broadening therein.

The red edge effects provide a mechanism to balance between the specificity of the excitation and the magnitude of the acquired signal, since a fluorescence excitation wavelength that is further red-shifted will more specifically excite species in the more densely polymerized regions but will consequently reduce the acquired signal overall because such species are rarer even in densely polymerized regions [104]. Such increased specificity has no fundamental limit [104] and could potentially be explored to approach super-resolution through stochastic excitation of sparse molecules, similar to Stochastic Optical Reconstruction Microscopy (STORM) and Photo Activated Localization Microscopy (PALM).

The advantages of such an improved MPL process are demonstrated in the next sections.

6.10 Real-Time Closed Loop Control of MPL Fabrication

Beyond the intrinsic value of the characterization, the presented method further enables the implementation of closed-loop real-time control of the fabrication process. Two particular cases are considered in the scope of this chapter[4]: the compensation of the beam dispersion over increasing focus depths and the modification of the exposure masks to improve structural fidelity, i.e., dynamic masking.

In the first case, as the exposure laser is focused deeper into the sample during fabrication, the laser dispersion in the material leads to a smaller exposure dose at the focus and therefore a decreased fluorescent signal. This can be corrected by increasing the exposure dose through an increase in the excitation laser power and/or decreasing the scanning speed.

To automate the control, a proportional (P) controller was implemented for the laser power and one for the scanning speed. The measured process variable is the average 532 nm induced fluorescence signal in the masked regions of a given layer, e.g., the white regions in fig. 6.1c, and the process setpoint can be set either manually or automatically, e.g., based on the value the process variable stabilizes on at the start of the fabrication.

While the power controller directly modulates the fabrication exposure dose, the scanner controller adjusts the scanning speed which is the same for the fabrication and characterization steps, and thus compensates not only for the decreased fabrication exposure dose but also for the increasing dispersion of the acquired fluorescence signal at increased depths. While other control architectures avoid a shared variable between the fabrication and acquisition step, the one presented here simplifies the overall implementation.

The fabrication results were seen to greatly improve following the implementation of this algorithm, as can be seen in figs. 6.6a to 6.6b. In fig. 6.6f, it is possible to see the progression of the process variable, the average fluorescence in the masked regions of a layer, with the layer number, for the case with (fig. 6.6a) and without (fig. 6.6b) fabrication control. In this figure, higher layer numbers correspond to having the laser focused deeper into the sample. The process variable is seen to steadily decrease with increasing focus depth for the case without fabrication control while keeping stable for the controlled case. This process is also compatible with STED-MPL, which leads to improved feature size and resolution, as shown in fig. 6.6e and further discussed in section 6.D.

---

[4]many others are, however, made available by the presented method
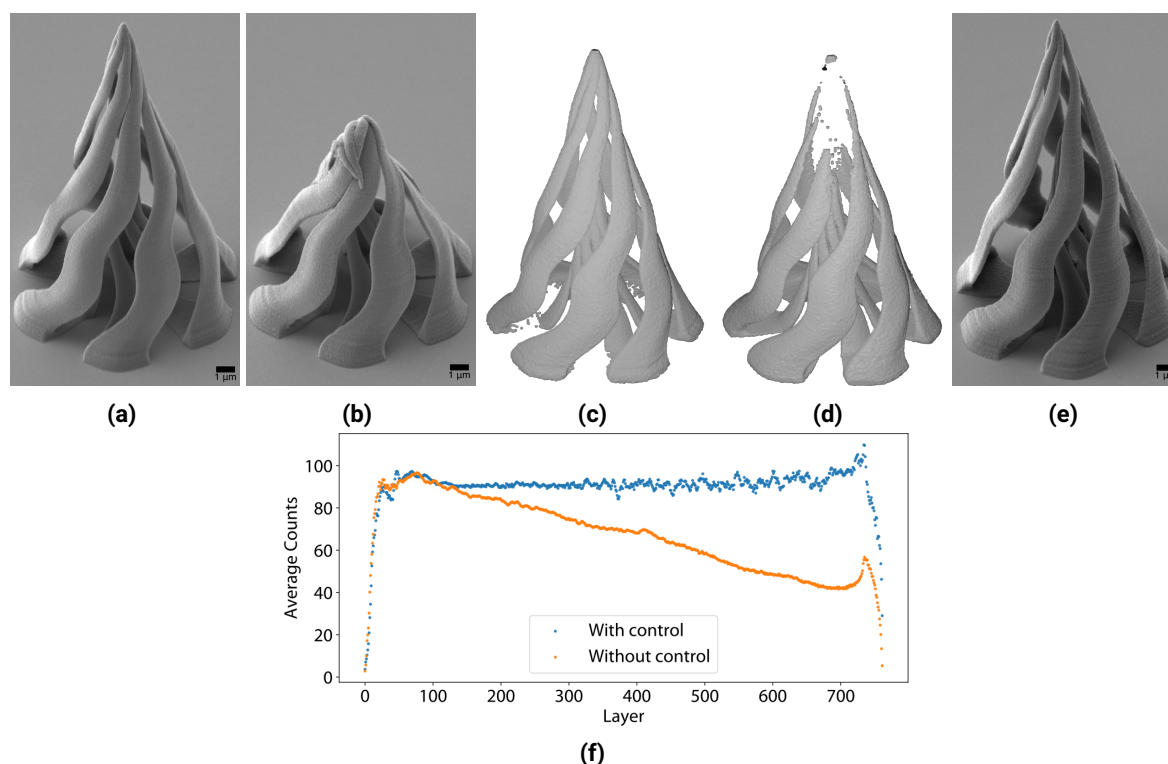
Figure 6.6: Application of the improved MPL process. (a)-(b) Reference 3D structure fabricated with (a) and without (b) exposure dose compensation. (c)-(d) Reconstruction of the reference 3D structures fabricated with (c), equivalent to (a), and without (d), equivalent to (b), exposure dose compensation. (c) corresponds to (a) while (d) corresponds to (d). (e) Reference structure fabricated combining STED and dose compensation, achieving improved feature size and resolution. (f) Progression of the fluorescence signal averaged over the exposed regions with (blue, corresponds to (a)) and without (orange, corresponds to (b)) as a function of the layer number. Higher layer numbers correspond to deeper laser focusing onto the sample.

As for the second application case, by comparing the fabricated region in each layer to the desired result, specified by the original design or mask, as done in section 6.E, it is possible to dynamically adapt the fabrication mask to more closely match the desired results. While similar algorithms have been developed based on fabrication models for pre-optimization of fabrication masks [201], the improved MPL process enables us to achieve this in real-time, through a faster iterative process of mask optimization based on direct characterization. Such an algorithm has, however, not been implemented in the context of this work. Furthermore, this method is also compatible with the usage of machine learning for mask optimization.

6.11   3D Reconstruction of the Fabrication Results

Another novel application is demonstrated based on the improved MPL method: the 3D reconstruction of the fabricated structure based on the characterization data acquired over the whole fabrication run. An algorithm was implemented that automatically performs this reconstruction. The polymerization threshold is approximated by a simple threshold in the fluorescence signal, and proximity effects are considered through Gaussian blurring. A point cloud is then generated and a Poisson surface reconstruction performed. A detailed description of the implementation can be found in section 4.3.2.

The reconstructed models corresponding to the structures shown in figs. 6.6a to 6.6b are shown in figs. 6.6c to 6.6d, respectively. The reconstructed 3D models closely match most features of the actual fabricated structure. Such reconstruction is of particular importance as, when compared to SEM, it provides a quick characterization method that requires no post-processing of the sample and enables the measurement between any two points on the sample surface, even inner surfaces which would be difficult to image. Furthermore, it does so without parallax-induced errors and provides access to all perspectives

into the structure without having to perform multiple acquisitions. Although SEM provides nm-scale resolution, it is also prone to damage small features with polymer backbone due to heating effects, which is also avoided through the presented 3D reconstruction.

The proposed reconstruction method is able to detect exposure-related defects in the fabrication but fails to account for effects related to the sample development step, such as shrinking, which would have to be modeled, and capillary forces, which are usually a fabrication bottleneck and are difficult to predict.

A characterization of the reconstruction fidelity is shown in section 6.F. The presented algorithm can be further improved by performing PSF deconvolution on the acquired signal [202] and by accounting for voxel size modulation based on the fluorescence signal.

6.12   Discussion

Polymerization-induced changes in fluorescence have been used to monitor polymerization processes in the past [198, 199]. Here, this concept is extended by using it for precise real-time layer-by-layer monitoring and control of an MPL process. We achieve increased SNR and reduced implementation complexity compared to similar methods [190]. This improved process enables, for example, to correct for deviations in local excitation energy dosage as well as to adjust the fabrication mask based on the characterization signal from previous layers so as to replicate the desired structure with increased fidelity. Furthermore, it enables to characterize the fabrication result by performing a 3D reconstruction of it.

The presented applications are achieved by taking advantage of DETCs' red-shifted fluorescence absorption when in a polymer. This shift is due to red-edge effects and the underlying inhomogeneous broadening, i.e., the stabilization of a larger range of DETC subspecies when in a more rigid or polar environment. The stabilization of subspecies unique to the polymerized regions enables site-selective excitation and probing of polymerized regions through a laser source red-shifted relative to the DETC absorption peak.

The improved MPL method proposed here is not exhausted in its capabilities. Not only can its precision be improved through PSF deconvolution or further tuning of the fluorescence excitation wavelength, but the implemented control and reconstruction schemes are greatly simplified and can be improved. Furthermore, the utilized red-edge effects are likely not restricted to the current molecular system and might be accessible in other photoresists, even if with a different fluorescence excitation source.

The presented characterization method is limited by the effects of the development steps, which can cause a structure to significantly differ from its 3D reconstruction. Furthermore, when different fabrication exposure conditions are used, the fluorescence baseline signal varies significantly, and therefore an absolute analysis of the fluorescence signal, and its comparison between different exposures, is not immediate.

6.13   Conclusion

An improved MPL process is presented which achieves real-time monitoring and control of the fabrication, as well as 3D reconstruction of the fabrication result even before sample development. It is based on the confocal layer-by-layer detection of an increased fluorescence signal in the regions where polymerization has occurred. The enhanced fluorescence is attributed to red-edge effects in DETC mesomeric structures stabilized inside a polymer matrix, which result in a red-shift in fluorescence absorption of these polymer-specific DETC subspecies. The proposed implementation is simpler and achieves higher SNR than previous ones [190]. Furthermore, the resolution of the method is configurable by the scanning parameters and the fluorescence excitation wavelength and can be easily improved. Regarding applications, the improved MPL enables in-situ fabrication optimization without further processing and is compatible with super-resolution MPL through STED [101].

The integration of structure fabrication and analysis in a single process with little added complexity provides unique opportunities for improving the fabrication outcome and the efficiency of the optimization process, as well as providing further insight into MPL. The improvements presented here are applicable to most of the use cases that benefit from MPL, with potential for a wide-ranging impact.

Appendix 6.A   Fluorescence Emission Spectra

The fluorescence emission spectra of the utilized photoresists are characterized under different excitation sources and exposure schemes. First, the emission spectra under the 780 nm fs and the 532 nm CW lasers are measured separately. Afterwards, the fluorescence spectrum under combined exposure is measured, i.e., sequential exposure to the 780 nm and 532 nm lasers with a 4 ms interval in between. The spectrum for PETA-DETC under combined exposure is shown in fig. 6.2. The spectra for PETA-DETC photoresist under separate 780 nm and 532 nm excitations, and for the PETTA-DETC photoresist under combined excitation are shown in fig. 6.7. As mentioned in the main text, the 529 nm emission peak is due to the 532 nm laser exposure while the peaks at the 750-800 nm range are due to the 780 nm laser exposure. Both photoresists present very similar spectra under combined and separate excitations.

Both the 529 nm and 750-800 nm fluorescence peaks under sequential excitation from the 780 nm and 532 nm laser sources produce $2.5 - 15$ % less counts than the corresponding peaks under single laser excitation by each source. However, when considering that the same volume is addressed in both sequential and single exposure cases, it must be noted that the fluorescence under sequential exposure is actually the sum of the counts of both peaks, therefore resulting in much higher fluorescence counts for the same volume of material.

Appendix 6.B   Reference Volume Scan

A reference laser scanning process is established to enable the characterization of the photoresists' fluorescence spectra and fluorescence dependency on the excitation power under similar and reproducible conditions. For single laser excitation the laser is scanned layer-by-layer along a $15 \times 15 \times 8$ μm cuboid with 0.1 μm spacing between layers and 5 mm/s scanning speed, totaling 62 ms per layer, producing the structure shown in fig. 6.8a under polymerization-inducing conditions.

Under combined exposure, and in order to compare the enhanced fluorescence and the background fluorescence signals, the top half of the cuboid is exchanged with a 4 μm high intricate sculpture-like feature, producing the structure seen in fig. 6.8b under polymerization-inducing conditions. In this case, while the 780 nm laser is scanned within a masked region in each layer, e.g., as seen in fig. 6.1b, so as to produce the reference structure from fig. 6.8b, the fluorescence characterization scanning with the 532 nm laser, occurring 4 ms afterwards, is performed over the whole layer, corresponding to the same scanning pattern that would produce the structure in fig. 6.8a but without inducing polymerization. This enables to characterize the fluorescence signal under 532 nm exposure only and under combined exposure within the same layer. For the spectral analysis only the bottom half of the reference structures is accounted for, corresponding to a $15 \times 15 \times 4$ μm cuboid.

During combined exposure experiments in polymerization-inducing conditions, the 532 nm laser is seen to contribute to increased polymerization at exposure dosages above 450 nJ, as well as to lead to the saturation of the APD signal. Therefore, the 532 nm laser exposure dose during fabrication characterization, e.g., for the structures in fig. 6.6, is kept low, at about 25 nJ, contributing to an increased SNR and avoiding interfering with polymerization.

Appendix 6.C   Fluorescence Dependency on 532nm Laser Exposure Energy

The fluorescence signal dependency on the 532 nm laser exposure energy is presented in fig. 6.9. fig. 6.9a presents the fluorescence signal under exposure to the 532 nm laser only while fig. 6.9b presents it under exposure to the 532 nm laser 4 ms after exposure to the 780 nm laser in polymerization inducing conditions. While under 532 nm exposure alone the fluorescence scales with $N = 0.7$ and the fluorescence intensity is small, under combined exposure in polymerization-inducing conditions the fluorescence intensity is ≈ 30 times higher, leading to a saturation of the APD even at small 532 nm laser exposure energies and with the signal attenuation from the band-pass filter (see section 3.4). The APD saturation (at about 600 counts) under enhanced fluorescence emission impedes the characterization of its scaling.
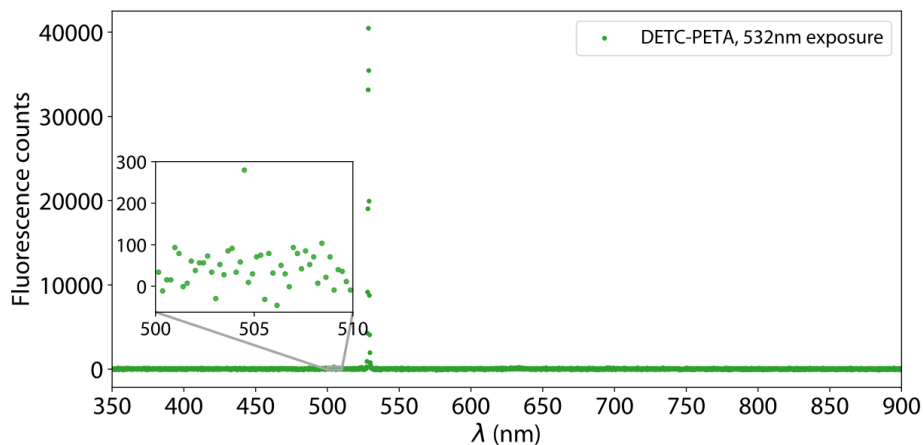
(a)
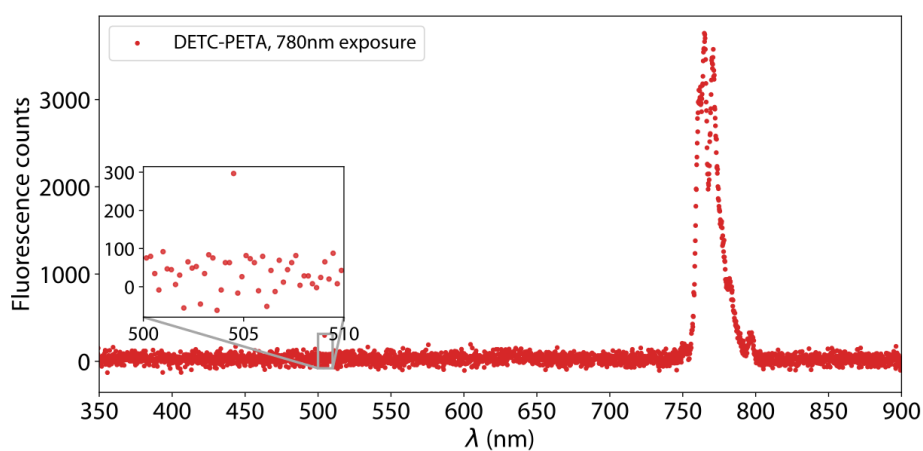
(b)
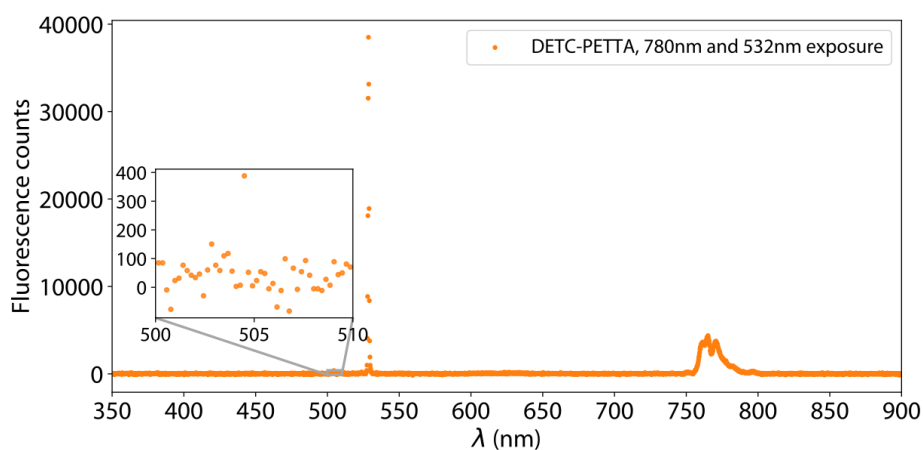
(c)

Figure 6.7: Emission spectra for PETA- and PETTA-DETC photoresists under different excitation sources. (a) PETA-DETC photoresist fluorescence emission spectrum under 532 nm laser excitation. (b) PETA-DETC photoresist fluorescence emission spectrum under 780 nm laser excitation. (c) PETTA-DETC photoresist fluorescence emission spectrum under combined excitation.

(a)   **(b)**
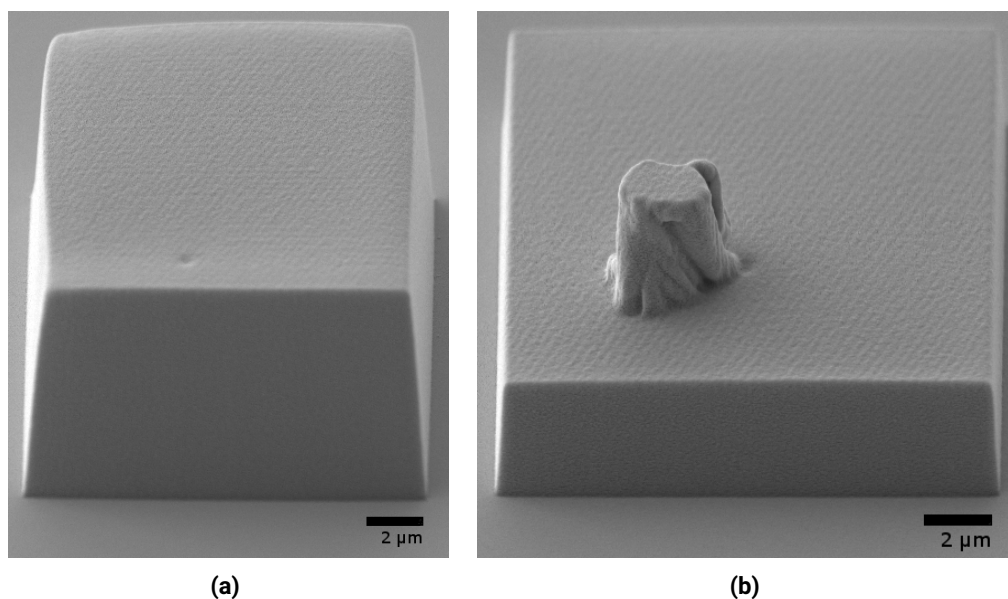
Figure 6.8: Reference structures resulting from the reference volume scanning under polymerization-inducing conditions. (a) Volume scanned during single laser exposure experiments and during the characterization scan (with the 532 nm laser) in combined exposure experiments. (b) Volume scanned by the 780 nm laser during combined exposure experiments.

(a)   **(b)**
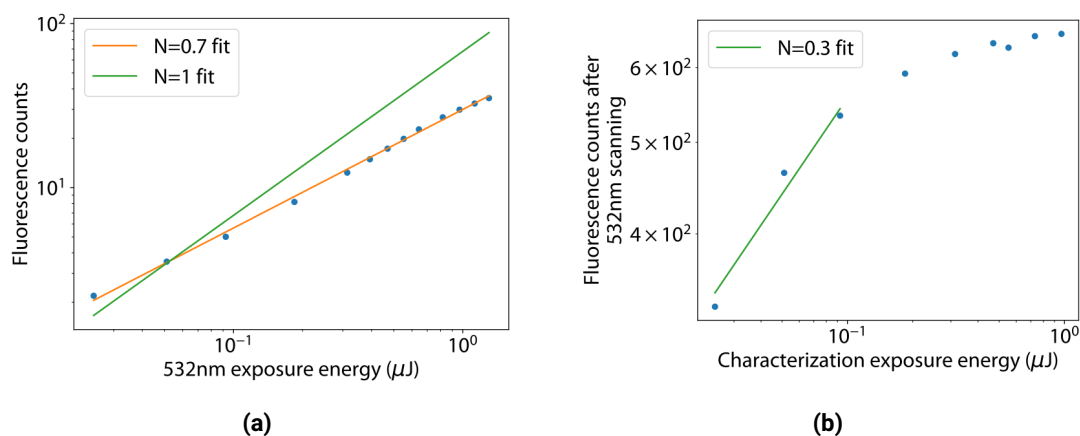
Figure 6.9: Fluorescence signal dependency on 532 nm laser exposure energy. (a) Fluorescence under 532 nm laser exposure only. (b) Fluorescence under combined exposure in polymerization induced conditions.

Appendix 6.D   Enhanced Fluorescence Signal During STED-MPL

The improved MPL process proposed in this chapter is compatible with STED-MPL [101]. To characterize the impact of STED, the enhanced fluorescence signal is acquired under STED-MPL combined exposure and compared to the enhanced signal under MPL combined exposure. STED-MPL combined exposure consists of a first simultaneous scan of the polymerization-inducing 780 nm fs laser and the depletion-inducing 532 nm CW laser with a modified 3D donut PSF followed by a second scan, 4 ms after the first, of the 532 nm laser with the same modified 3D donut PSF, that is now used to trigger the enhanced fluorescence signal.

The results for the fluorescence signal dependency on the 780 nm pulse energy are presented in fig. 6.10. The ratio between the signals, presented in fig. 6.10a, is maximum close to the point where the polymerization is expected to start, i.e., where the $N = 4$ scaling becomes dominant in fig. 6.3a. Since the depletion acts to reduce the effective energy dose at a given location, this peak in the signal ratio can be attributed to a shift in the 780 nm pulse energy at which the polymerization starts under STED-MPL, as

previously observed [47] and apparent in fig. 6.10b. On the left edge of the peak in fig. 6.10a, the start of a sparse polymerization in the MPL process drives the increase of the enhanced fluorescence while in the STED-MPL process little to no enhanced fluorescence is registered because the polymerization start is shifted towards higher excitation energies. For laser excitation energies above the MPL polymerization threshold, the enhanced fluorescence is about $25 - 30$ % higher in the MPL case. This can be due to the decrease in the effective exposure dose under STED-MPL, the bleaching of the enhanced fluorescence signal contribution of layers underneath by the STED exposure, and even the effect of the modified 3D donut PSF of the 532 nm laser.
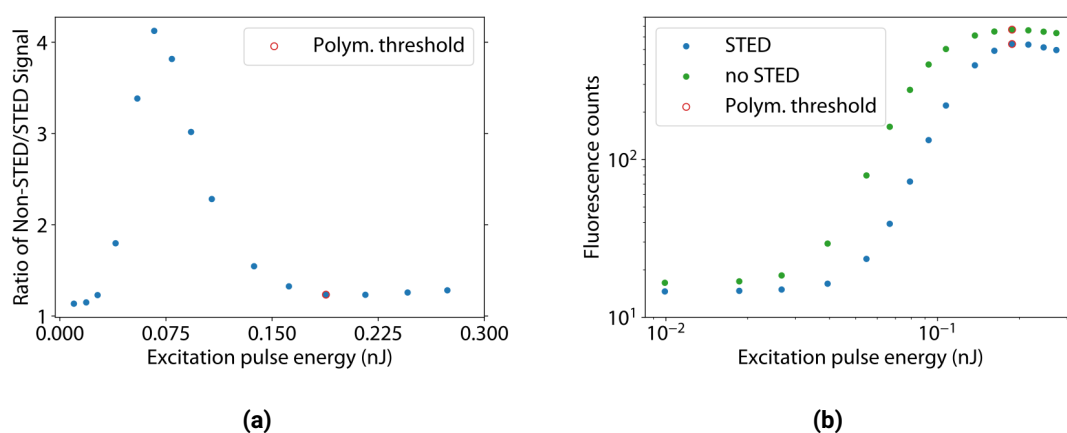
Figure 6.10: Comparison of the enhanced fluorescence signal under MPL and STED-MPL conditions. (a) Ratio of the enhanced fluorescence signals. (b) Enhanced fluorescence signals.

Appendix 6.E   Comparison Between Fabrication Mask and Outcome

Another important factor for fabrication control is the correlation between the fabrication mask and the resulting fabricated region. This is compared in fig. 6.11. By applying the fabrication control algorithm described in section 6.10, the area of the fabricated region is seen to reproduce the area of the fabrication mask to a much greater extent than without fabrication control, as seen in fig. 6.11a. It should be noted that this improvement is achieved without directly controlling the fabricated area during the fabrication process, validating the implemented control algorithm. Still, it can be observed in fig. 6.11b that the fabricated region, in blue, extends beyond the fabrication mask, in white (underneath). This opens the possibility to utilize the presented characterization method to dynamically adjust the fabrication mask in order to more closely match the desired fabrication result, e.g., by applying an erosion morphological operation to the fabrication mask in fig. 6.11b or by using a machine learning model developed for the purpose.

Appendix 6.F   3D Reconstruction Fidelity

In order to quantify the fidelity of the 3D reconstruction method presented in section 6.11, the reconstructed 3D model of a reference structure is compared to the SEM characterization of the same structure by measuring the same features in both methods. The results are shown in fig. 6.12. In general, the errors in the measurements of the 3D reconstructed features are only a few % when compared to the measurement of the same features in SEM, demonstrating the high precision and reliability of the developed 3D reconstruction method. This is achieved even in sub-optimal acquisition conditions for the reconstruction method, as explained in the following.

The fidelity of the 3D reconstruction is closely related to the pixel size used during the data acquisition step, as expected. When using a larger pixel size, e.g., 100nm as in fig. 6.12b, a reasonable fidelity is still
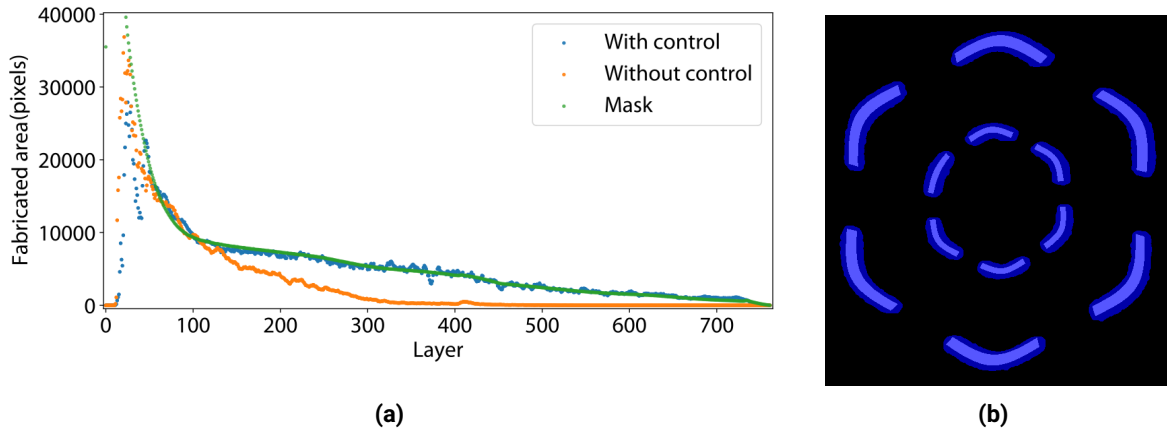
Figure 6.11: Comparison between fabrication mask and fabrication outcome. (a) Effect of fabrication control on the fabricated area in each layer. (b) Comparison between the mask, in white (underneath), and the resulting fabricated region, in blue.

possible if no blur (see section 4.3.2) is applied to the fluorescence data at the cost of a more irregular reconstructed mesh, as seen in fig. 6.12b.
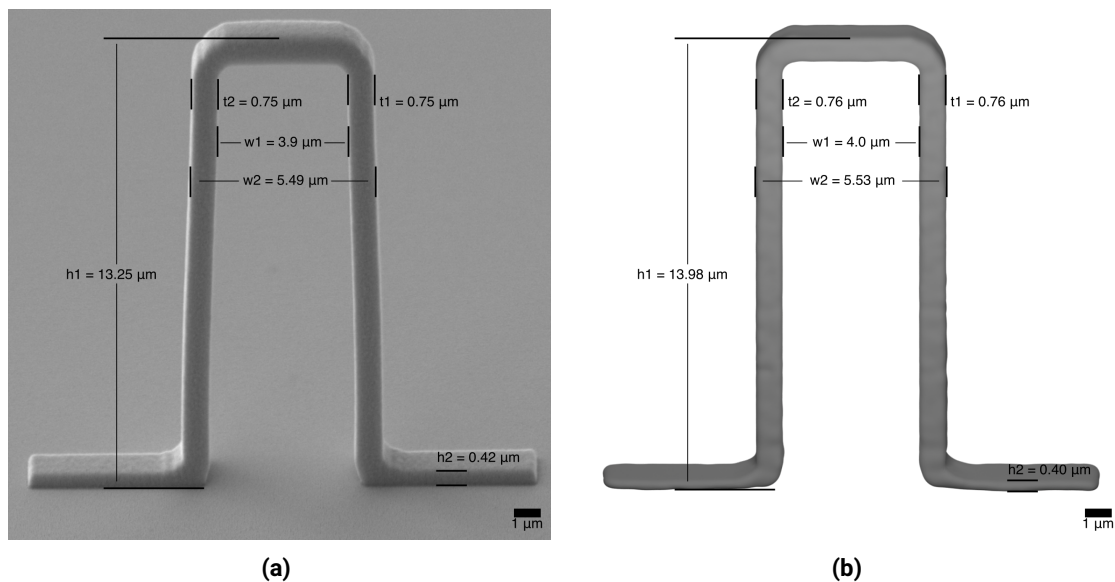
Figure 6.12: Comparison between SEM based measurement (a) and 3D reconstruction based measurement (b) of a fabricated structure.

Any effects related to the development step which are not compensated for during the fabrication itself, e.g., shrinking, will lead to significant differences between the reconstructed model and the actual fabrication result, e.g., in the total height h_1 in fig. 6.12. While this limits the applicability of the 3D reconstruction as a general characterization method, particularly for small or fragile structures, it can be used to provide additional insight into the development stage of the fabrication and to compensate for common development-related effects during fabrication.

An improved reconstruction process would subdivide the point cloud into smaller steps in x, y and z and interpolate between them, such that the mesh could be smoothed more precisely without significantly affecting its boundaries.

Chapter 7

Chiral 3D Anisotropic Magnetoresistance at the Sub-Micron Scale

The promise and challenges of 3D magnetic and magneto-electronic devices are established in sections 2.4 and 2.5. In chapter 5, a simplified workflow for the fabrication of general 3D magneto-electronic devices based on polymer scaffolds is shown. The results achieved therein, and their applications[1], are greatly significant to the state-of-the-art in curvilinear ferromagnetism. However, they refer to mostly planar structures with mostly out-of-plane normals and widths much larger than the characteristic lengths of the fundamental magnetic interactions, thus not fully representing the expected complexity of a general freeform 3D magnetic structure.

In this chapter, I apply the workflow developed in chapter 5 to investigate another 3D curvilinear magneto-electronic device, with more complex geometry and smaller features than in chapter 5[2]. Two particular objectives are established. The first is to probe and identify the limits of the presented methodology and, when applicable, the limits of the state-of-the-art in the fabrication of 3D magnetic systems. This applies in terms of both structural and integration complexity. The second is to study the interplay between the magnetoresistance of a material, a shape-driven self-induced magnetic field, and the additional components of the exchange interaction induced by a 3D curvilinear structure. The chiral symmetry breaking provided by both the self-induced field and the exchange-driven effects induced by the 3D curved geometry is expected to manifest directly in the anisotropic magnetoresistance of the device through unique signatures.

Here, I utilize the simplified two-step fabrication process from chapter 5 to fabricate magnetic 3D coils with sub-μm features, and proceed to validate the fabrication process through comprehensive characterization. After fabrication, the transport properties of the 3D coil structures are characterized. The geometry-induced magnetic interactions and the self-induced fields lead to a chirality-dependent asymmetric AMR responses. Furthermore, the coil chirality affects the AMR ratio of the whole structure. In order to interpret and validate the observed transport measurement response, finite element simulations of the 3D coils are performed.

This study replicates a previous study [203], extending it by using a fabrication method with improved 3D capabilities. This enables to achieve features at a sub-micron scale, i.e., more than 100 × smaller than in the original study, and to realize more elaborate device designs, such as combining two coils in one device. While past results establish a baseline for the device measurements, at the μm scale the local magnetic interactions have increased relevance and therefore the balance between the self-induced field and curvature effects is expected to differ significantly.

---

[1]such as a controllable DW filter
[2]although using a less complex and sensitive material stack.

7.1 Device Fabrication and Characterization

The spintronic 3D coil devices consist of an organic polymer core that serves as a scaffold for a magnetic thin film. The devices are fabricated through a two-step process, represented in fig. 7.1a, and detailed in section 3.1. First, the scaffold is fabricated using MPL, using a photoresist composed of DETC, .25 wt%, as photoinitiator, and PETA, as monomer. The photoresist preparation is described in section 3.2. Afterwards, the scaffold is coated with a $CoNi$ alloy with a targeted stoichiometry of $Co_{0.3}Ni_{0.7}$, known to display AMR of $\approx$ 6 % [204], and 45 nm thickness, deposited through magnetron sputtering, as detailed in section 3.5.2.
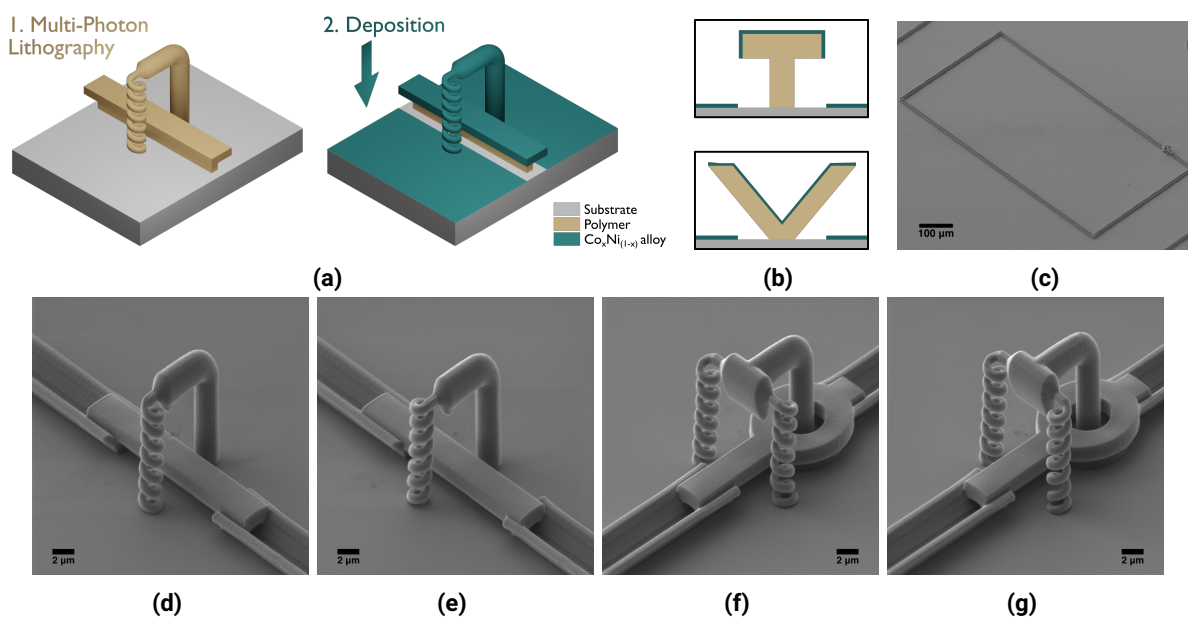
Figure 7.1: Fabrication workflow for the realization of 3D AMR coil devices. (a) Scheme of the two-step fabrication process utilized for the realization of the active devices, comprising a MPL step (1) and a magnetic material deposition step (2). (b) Working principle for the contact pad definition, which takes advantage of the coarse directionality of the deposition step to prevent the deposition of the material underneath the structures with the depicted cross sections, thus disconnecting the regions to the left and right of it. (c) By utilizing the structures from (b) to establish a fully closed boundary, inside and outside pads are formed that are electrically disconnected apart from the coil device bridging them. (d)-(g) Single left-handed, single right-handed, dual same-chirality and dual opposite-chirality coil devices, respectively.

The electrical contact pad definition is the critical step in the simplified two-step fabrication. The pads are defined by taking advantage of the directionality of the deposition method. By fabricating a closed contact pad boundary that shadows the substrate underneath it, the material deposition therein is prevented across the whole boundary extent, insulating its interior from the exterior, as shown in fig. 7.1b. The function of the contact pad delimitation structures was tested by fabricating them without any coil device and verifying that a high resistance, on the order of MΩ, is measured between the inside and the outside regions of the pad delimitation.

Coil devices with one or two coil elements are used. For the single coil designs, the coils are either left-handed or right-handed, as seen in figs. 7.1d and 7.1e. For the dual coil devices, the two coil segments are either of the same chirality, both left-handed, or opposite chiralities, as seen in figs. 7.1f and 7.1g. In the dual coil devices, an additional column is necessary to ensure the structural stability of the device. This element is integrated into the electronic device design by adjusting the pad delimitation structure around it to form a floating terminal, as seen in figs. 7.1f and 7.1g. For each coil device type, a reference device is fabricated that substitutes the coil element with a single vertical column, as seen in section 7.A. The coil elements are designed to have 1.4 μm pitch, 0.5 μm internal radius, 0.6 $\times$ 0.6 μm square cross section and 7 turns in total. A square cross section is used for the coil turns to avoid curvature effects on multiple axis

and to minimize the locally varying surface normals, which affect the AMR response. A $0.6 \times 0.6 \ \mu m$ square cross section is also used for the vertical column in the 3D reference devices.

A reference 2D device consisting of a $4 \times 20 \ \mu m$ strip of *CoNi* film between two *Au* contact pads is fabricated through standard lithography, lift-off and etching, in order to characterize the full AMR ratio of the material without being affected by the 3D geometries. All devices are deposited simultaneously. Furthermore, all 3D devices are fabricated in the same substrate, ensuring the same magnetic film deposition conditions.

The device geometry is characterized through SEM, as seen in figs. 7.1d to 7.1g. To characterize the *CoNi* alloy deposition, the cross section of a coil device was prepared with Focused Ion Beam (FIB) and analyzed with high-resolution TEM. The results are shown in fig. 5.2e. The film is mostly on the outer and top faces of the coils turns, as these are most exposed to the sputtering fume. The thickness varies continuously in the $[10; 34] \ nm$ range over each deposited face of the device and is measured to be, on average, 53 % higher for the coil turns shown on the left side of fig. 5.2e than in those shown on the right. Significant thickness variations have been shown to lead to unique magnetic responses in the past, e.g., as in [122], and could potentially contribute to the effects observed in sections 7.2 to 7.6. Based on Energy-Dispersive X-ray Spectroscopy (EDX) measurements (TESCAN FERA 2), the film stoichiometry is estimated to be $Co_{0.38}Ni_{0.62}$ over the lateral outer surface of the coils, with a standard deviation error of ±0.063.
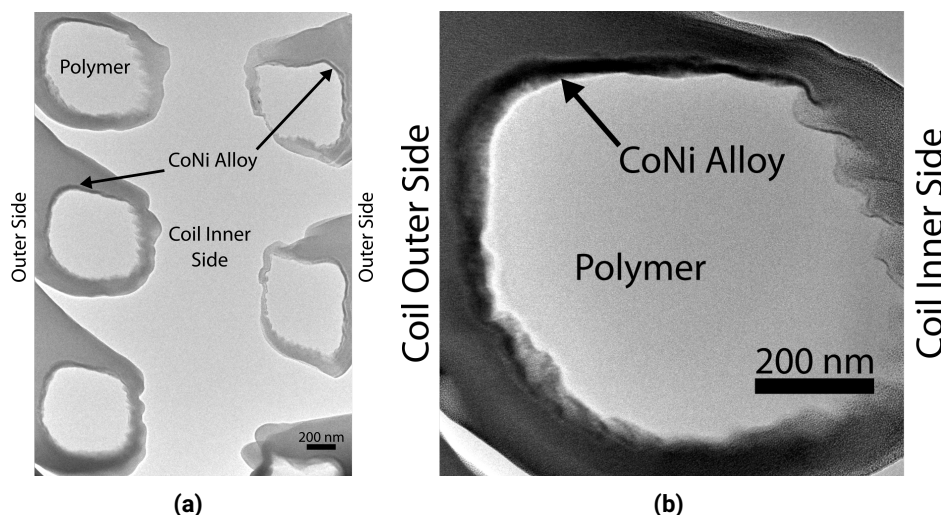
Figure 7.2: TEM characterization of a coil device cross section. (a) Overview of a coil device cross section, particularly the bottom 2.5 turns. The CoNi alloy is observed to be deposited mostly on the top and outer surfaces of each turn and to be asymmetrically deposited on surfaces on the left and the equivalent surfaces on the right. The alloy thickness varies significantly over the surfaces where it was deposited. (b) Closer inspection of the coil turn cross section shown at the top left corner of (a), where the variation of the CoNi alloy thickness is further visible.

7.2 Electrical Transport Measurements

After the fabrication, the AMR response of each coil device type is measured. The measurement configuration scheme is shown in fig. 7.3a. As the device resistances are in the $[140; 320] \ \Omega$ range, a four-probe measurement configuration is used to avoid the error induced by the contact resistance. While measuring, the voltage difference at the device terminals and the current flowing through through the circuit are registered to precisely determine the device resistance. The first and second-harmonics of the resistance are measured with a lock-in amplifier. Further details of the measurement can be found in section 3.6.

All single and double coil devices are measured to have similar resistances, in the $[281, 312] \ \Omega$ range, despite the latter being expected to have about 2 times larger resistance[3]. Possible causes are the connection

---

[3]the dual coil devices have about 1.65 times the length of a single coil device. Accounting with the measured film resistivity

of a few sequential coil turns in the dual coil devices, due to their slightly less stable structure, or the influence of a parallel parasitic connection through the electric pad delimitation, although in this case the AMR responses and ratios, presented below, would be expected to be more similar. As a control, the 3D reference devices present much smaller resistances, about 150 Ω, as expected. Further testing of the device and pad delimitation designs is necessary.
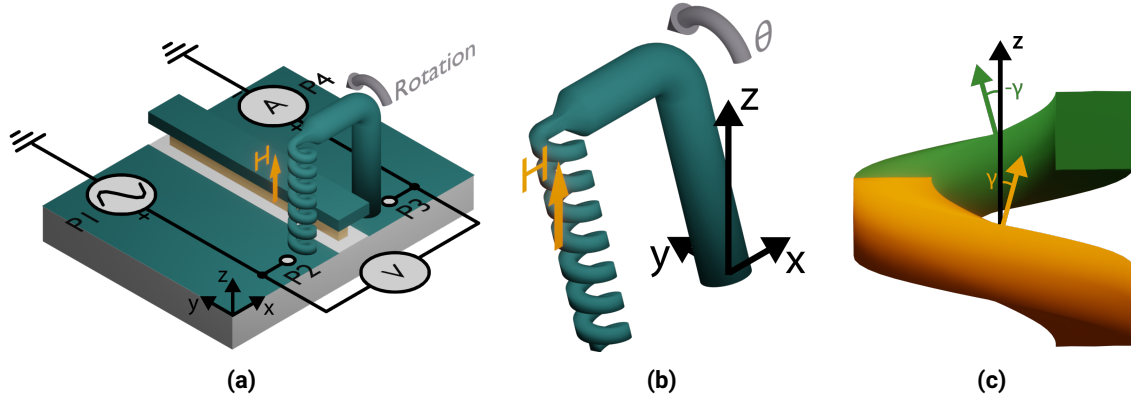
Figure 7.3: Transport measurement configuration. (a) Configuration of the electrical transport measurement setup. A four-probe measurement configuration, with the probe contact points labeled P1-P4. The voltage drop is measured close to the coil terminals while the current injection contacts are placed in the opposite end of the pads, see fig. 7.1c. (b) During the AMR characterization the coil is made to rotate about the x axis, while the magnetic field H is kept directed along z. The angular position is described by θ, as shown. (c) Each coil turn can be decomposed into two separate sections, each with a normal vector to the surface that deviates from z by an angle γ. The resistance in each section is minimized when its normal is aligned with the external field, i.e., $\theta = \pm\gamma$, leading to the appearance of two minima around $\theta = 0; 180$ ° in the single coils AMR response. For the coil design presented here $\gamma = 17$ °.

The AMR response of the devices is characterized by continuously measuring the device resistance under an external magnetic field applied along the $+z$ direction while the devices are made to rotate 360 ° about the x axis, as represented in fig. 7.3b. The angular position is characterized by θ (fig. 7.3b), the angle describing the anti-clockwise deviation of the coil main axis from the $+z$ direction in the yz plane. The AMR characterization of each device is repeated for each external magnetic field setpoint in the following set: $[0.05, 0.1, 0.25, 0.5, 0.75, 1, 2, 4, 6]$ T, and for each applied current setpoint in the following set: $[0.05, 0.1, 0.15, 0.2]$ mA.

The response curves for the first harmonic resistance component under the highest applied current, 0.2 mA, and a representative external field setpoint of 0.5 T, are presented in fig. 7.4 for the two single coil devices and the two double coil devices. The corresponding curves for the single and dual coil 3D reference devices, as well as the 2D reference device can be found in section 7.B.

The corresponding AMR ratio, defined as

$$\frac{\Delta R}{R_{min}} = \frac{R_{max} - R_{min}}{R_{min}}, \tag{7.1}$$

is calculated for all devices as a function of the external field magnitude. It is presented, for the coil devices, in fig. 7.5 for a 0.2 mA current setpoint. The corresponding data for the reference devices can be found in section 7.B.

The results and analysis of the second-harmonic signal are presented in section 7.C. Due to the small inductance of the fabricated coils and small applied current, the second-harmonic signal produced by the devices is not large enough to be discerned from the background noise level, even after optimization of the acquisition parameters and therefore it cannot be used to characterize the function of the devices.

---

and geometry of different sections, the dual coil devices are expected to have 2 times larger resistance.
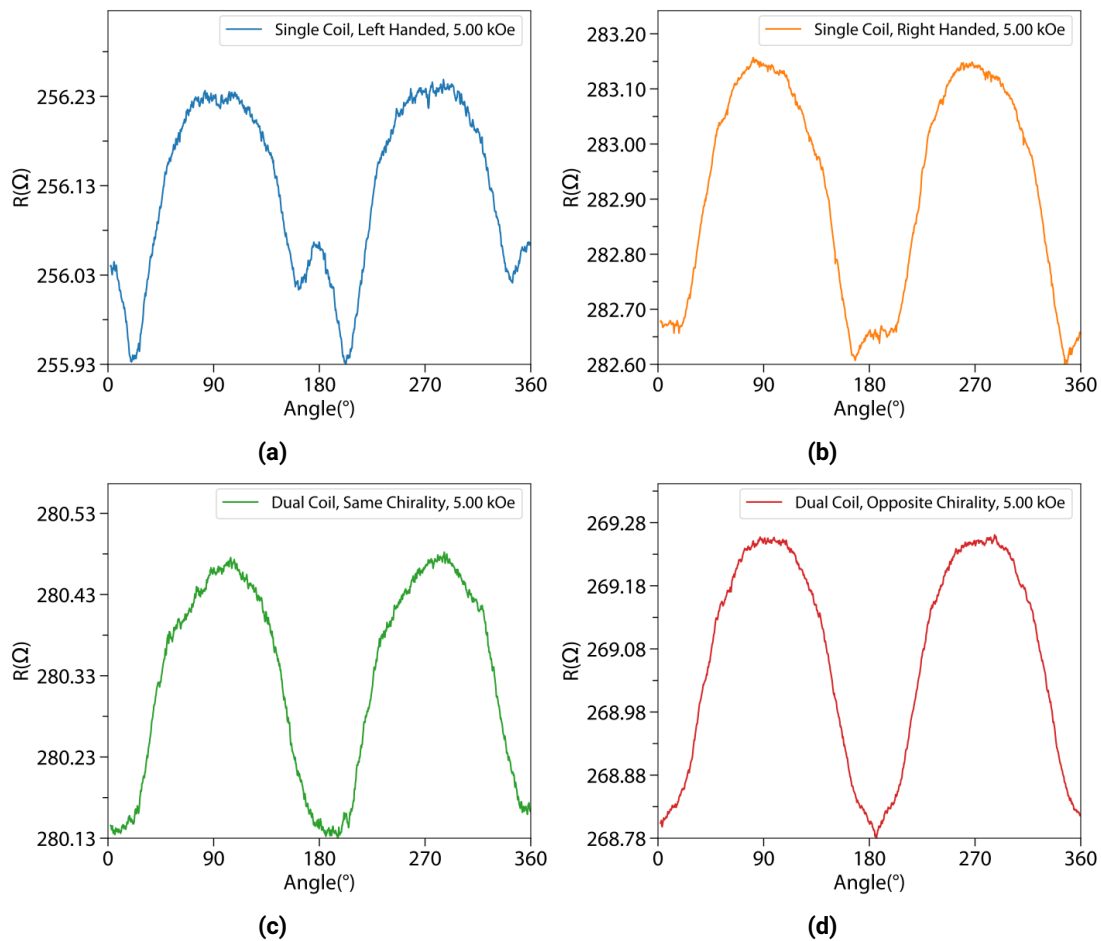
Figure 7.4: First-harmonic AMR response of the 3D coil devices. (a)-(d) First harmonic AMR signal for single left-handed, single right-handed, dual same-chirality and dual opposite-chirality coil devices, respectively, for the representative external field H=0.5 T. The shape of the responses curves are seen to vary significantly. The corresponding curve for reference devices is found in supplementary section 7.B.

7.3 Asymmetric AMR response

The first noticeable aspect in the figs. 7.4a to 7.4b curves for the single coil devices is the presence of two minimum resistance points rather than a single one as in the 3D and 2D reference devices. Such a signature has been previously observed [203]. It occurs because a coil turn is composed of two angled segments and, for fields aligned along $\pm z$, neither are at a minimum resistance configuration, as shown in fig. 7.3c. Instead, the minima occur when the external field is perpendicularly aligned to one of these two coil sections, which, for the utilized coil geometry, occur at $\gamma \approx \pm 17$ ° offset from the $\pm z$ position (i.e., $\theta = 0; \pi$).

However, unlike in previous observations, both local minima are significantly different, resulting in an asymmetrical AMR response. Furthermore, AMR responses for the left and right-handed coils are mirrored (see also fig. 7.6), possibly indicating a connection to the coil chirality.

The AMR curve for the corresponding reference device, shown in section 7.B, has its main features shifted by 90 ° in the angular position, as expected for the vertical column feature. Therefore, the features observed for the coil devices can be attributed to the coil section.

7.4 Chirality-Sensitive AMR Ratio

The AMR ratio of the right-handed single coil is consistently higher than that of left-handed single coil, as seen in fig. 7.5. Furthermore, their absolute difference is proportional to the externally applied field.
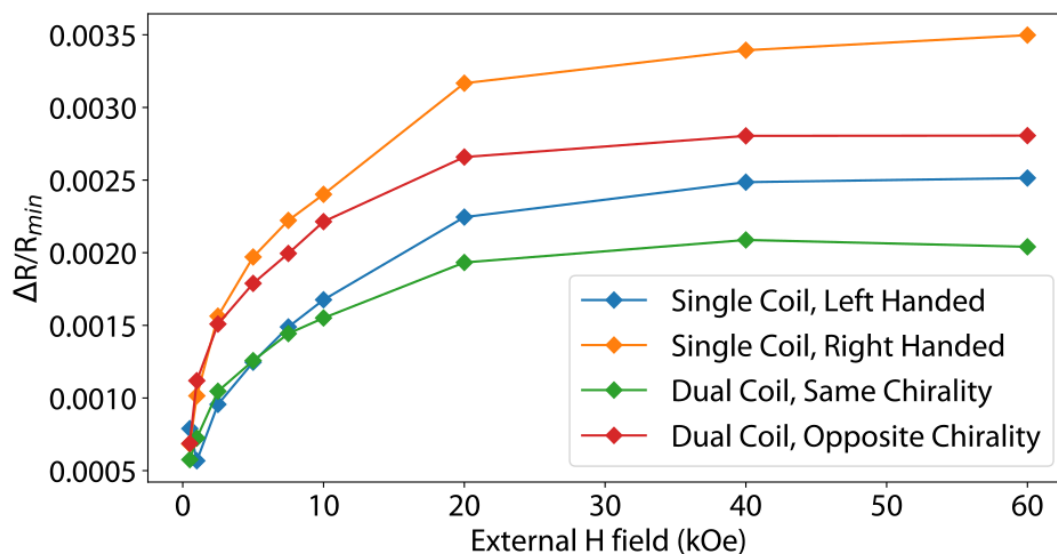
Figure 7.5: AMR ratios for the 3D coil devices as a function of the applied external magnetic field. Devices with left-handed coils have a decreased AMR ratio compared to those with a right-handed coil. The corresponding curve for reference devices is found in Supplementary section 7.B.

Conversely, the AMR ratio of the 3D single coil reference device is mostly independent of the field in the characterized field range, as seen in fig. 7.10c, and thus the observed particular features in the coil devices can be attributed to the coil section of each device.

If the differences in the AMR ratio were due to the self-induced field only, the opposite AMR ratio progression would be expected. That is, the difference in the AMR ratio of coils with opposite chirality would be expected to be maximum at lower externally applied fields, when the relative magnitude of the self-induced field is higher, and it would be expected to decrease for increasing fields, as seen in [203], eventually converging to zero at high fields.

Since the AMR response of the devices is dependent upon the chirality of the coil sections and the AMR ratio dependency on the externally applied field is inconsistent with the effect of self-induced fields, it is plausible that the observed AMR responses are mostly driven by the exchange effects induced by the curvilinear 3D geometry of the coils.

For the single left- and right-handed coil devices it is possible to find different external field setpoints where the AMR ratio of both devices is similar. At these different setpoints, e.g., shown in fig. 7.6, the response of the devices is more closely mirrored than when analyzed at the same field setpoint, as in figs. 7.4a and 7.4b.

Furthermore, as is shown in section 7.5, the changes in the AMR response under increasing field is mostly driven by the decrease of resistance for $\theta \approx 0; 180$ °, i.e., when the external field axis and the main coil axis are collinear or close. This enables us to pinpoint and focus on the alignment conditions that further contribute for the increasing difference in the AMR ratios shown in fig. 7.5.

7.5   Progression of AMR Response with External Field

In fig. 7.7, the progression of the AMR response of a left-handed single coil device under increasing external field is presented. Both maxima and minima resistances are seen to decrease under increasing external field. Nonetheless, the decrease of the AMR response minima, corresponding to $\theta = 0; 180$ °, is approximately 2 times larger than that of the maxima, at $\theta = 90; 270$ °, such that the minima are the dominant driving factor for the variations analyzed in section 7.4.
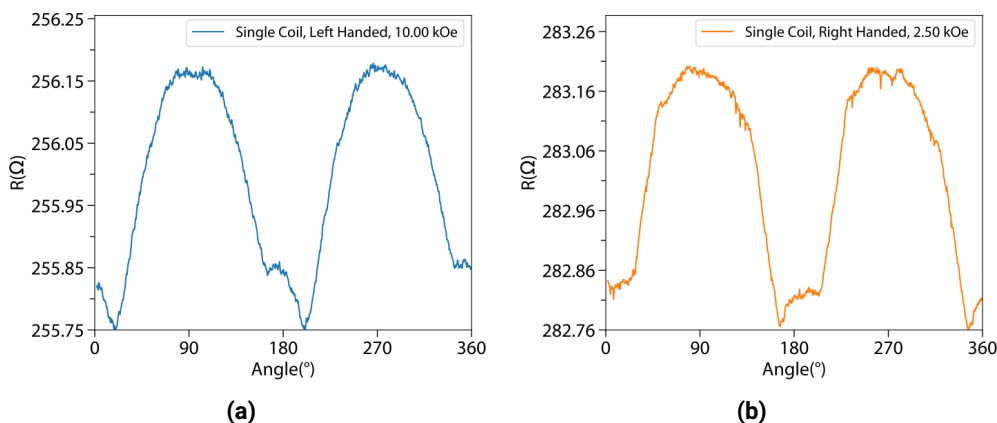
Figure 7.6: At different fields, the single left (a) and right (b) handed coil devices can have almost mirrored AMR responses.
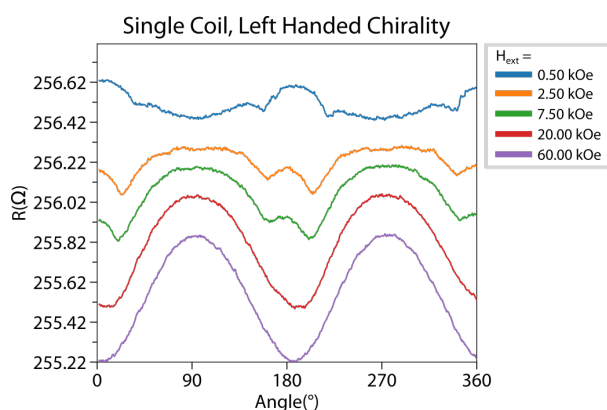
Figure 7.7: AMR response for a single coil device with left-handed chirality as a function of the magnitude of the externally applied field H_{ext}.

7.6   Double Coil Devices

The 1st harmonic response of the double coil devices, seen in figs. 7.4c to 7.4d, is also unexpected. Particularly, while the two different minima near the $\theta = 0; 180$ ° positions disappear, the resulting features around these positions still differ, with the device with coils of the opposite chirality displaying a more abrupt variation resulting in a sharp valley-like minimum, and the device with coils of the same chirality displaying a slower, plateau-like, variation.

Regarding the AMR ratios in fig. 7.5, it is possible to observe that while the double coil device with two left-handed coils displays an even smaller AMR ratio than the device with a single, left-handed coil, the double coil device with a left- and a right-handed coil displays an AMR ratio above that of the single left-handed coil device but smaller than the single right-handed coil device.

As before, the difference in the AMR ratios of the double coil devices increases with the externally applied field. This establishes a consistent relationship between the chirality of the coils in a device and its AMR ratio. Particularly, a right-handed coil appears to increase the AMR ratio of the device while a left-handed coil decreases it. As explained in section 7.4, the self-induced field is insufficient to explain the increased difference in the AMR ratios for increasing external fields. Other factors, like the geometry-driven exchange effects are likely to play a major role.

As for the single coil devices, the double coil 3D reference device displays no unique features in their AMR response, with a response very similar to that of the single coil 3D reference device, and its AMR ratio is also mostly independent on the field over the utilized field range, enabling to attribute the features observed in fig. 7.7 to the coil elements.

7.7   Discussion

The proposed fabrication method is useful for prototyping 3D electronic devices but still presents short-comings in significant aspects.

First, the material deposited at the contact pads is the same active material deposited at the device to be tested, contributing a small, $\approx 1\%$, but undesired component to the measured AMR signal. This could be overcome through multiple a multi-step liftoff process, as made possible by soluble MPL photoresists[71] and explained in section 8.3.

Second, the reduced thermal conductivity of the devices' polymer core limits the applicable electrical current before the device structure is seen to deform, as shown in section 7.D. To overcome this, it would be necessary to either use more heat-tolerant scaffold materials, such as SiO_2, or integrate post-processing techniques such as pyrolysis and plasma etching.

Third, the achievable device feature sizes are limited by their structural stability. While features ≤ 100 nm are possible with MPL and STED-MPL, even slight variations of the presented geometry, such as the addition of a single turn or the rescaling of the cross section, would cause either the sideways deformation of the coils or the adherence of different turns during the development step. Supercritical drying should alleviate the effect of the capillary forces during development but it was not available at the time.

Regarding the transport measurement of the coil devices, specific signatures are observed in the devices with coil sections that are not observed in the corresponding reference devices. These signatures, in particular the AMR ratio progression with increasing external magnetic field, appear to contradict the hypothesis that the effects are mostly driven by the self-induced magnetic field of the coils and to point towards effects driven by the exchange contributions induced by the 3D curvilinear geometry.

However, the data acquired and presented in this chapter is, so far, insufficient to reach a conclusion regarding the cause of the observed effects or to provide an understanding of how these effects, e.g., the geometry-induced magnetic exchange components, could translate into the observed AMR responses. While the data appears to consistently point to an AMR component driven by the coil sections that is chirality-dependent, further experiments are necessary. Particularly, measuring the inductance of the coil devices, in order to better estimate the self-induced field, and understanding why the double coil devices have similar resistances to the single coil devices would be necessary. Furthermore, unwanted factors such as the apparent heterogeneous thickness around the outer surface of the coil, as noted in fig. 5.2e, could also contribute to the observed effects and would need to be further investigated.

Due to a particularly high noise level in the acquisition setup, it was not possible to characterize the second-harmonic signal at the same range of values as done in previous studies [203]. Therefore, the influence of the self-induced field of the coils on the AMR response of the devices could not be directly measured and accounted for.

The AMR response of a single left-handed and a single right-handed coil turn was simulated using the finite-element method to provide further insight into the experimental observations. The simulations take into account the Oersted field generated by a complete coil section (7 turns) of the same chirality. By simulating the magnetic film over different surfaces of the coil turn, based on the TEM profile of fig. 7.2b, the experimentally observed AMR response could be attributed to the magnetic film over the outer surface of the coil turn. While an asymmetric AMR response is simulated for the outer surface of the coil, the AMR response is the same for coil turns of opposite chirality, as shown in fig. 7.8, and therefore the driving mechanism for the experimentally observed effects could not be identified so far.

7.8   Conclusion

In this chapter, 3D magneto-electronic devices with complex coil geometries and sub-μm features are fabricated and their AMR response is characterized. The chosen design and dimensions enable to further validate the fabrication workflow initially used in chapter 5 as well as to probe its limitations. The function of the presented device design could be verified through transport measurements but further decreasing
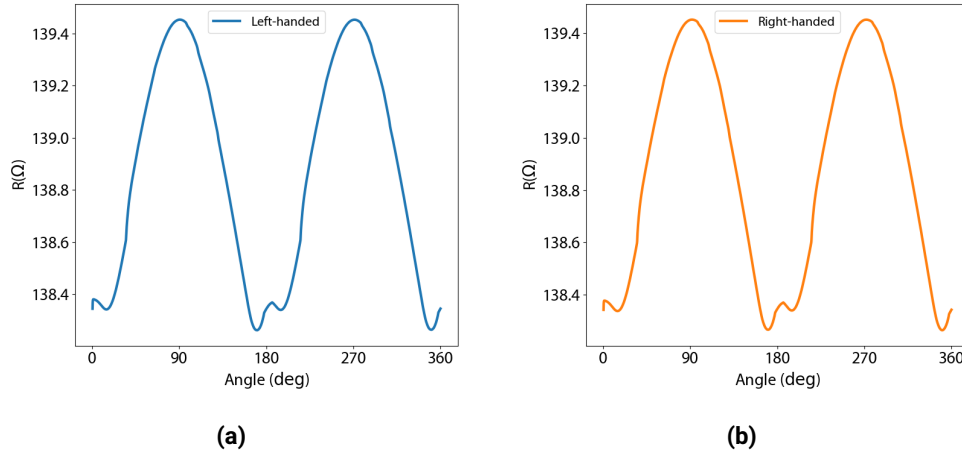
Figure 7.8: Micromagnetic simulations of the AMR response of coil turns with different chirality are unable to replicate the experimentally observed differences, providing undistinguishable responses for both cases. The parameters utilized for the simulation are specified in section 3.8.

the feature sizes to less than 500 nm is seen to result in mechanical instability of the structures.

Regarding the AMR response of the devices, while characteristic features observed in past studies could be replicated [203], local magnetic interactions at the sub-μm scale lead to new signatures in the AMR response that appear to be associated with the 3D curvilinear shape of the devices, and particularly the chirality of the coils. Such particular responses are not observed in reference devices.

However, limitations in the experimental apparatus have, so far, hindered the complete characterization of the devices. Simulating the devices through finite-element methods has been able to replicate the asymmetric AMR response but not the AMR response mirroring for devices with opposite chirality. Thus, further experiments are necessary to identify and comprehend the driving mechanisms behind the chiral-dependent AMR responses.

Appendix 7.A   Reference Devices

Along with the coil devices shown in fig. 7.1, a set of reference devices is designed in order to isolate the coil responses from that of the other 3D elements of the devices. Three reference devices are designed and fabricated: a 2D device that consists of a simple strip of AMR material with 4 probe pad configuration and two 3D reference devices that consist of the single and dual coil designs but with the coil sections substituted with a vertical column with the same 0.6×0.6 μm square cross section as the coils, as seen in fig. 7.9.

(a)   **(b)**
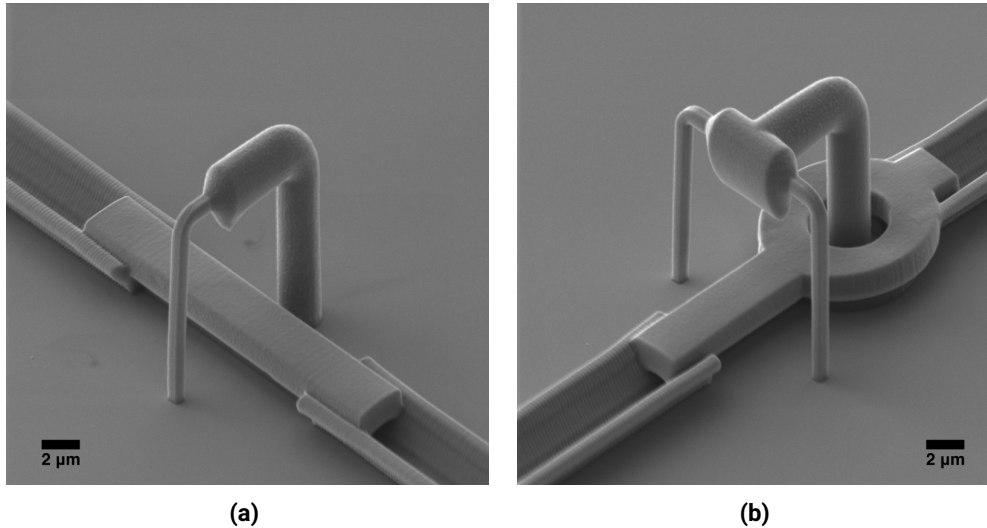
Figure 7.9: Electron micrographs of the single (a)) and dual (b)) 3D reference devices utilized in this study.

Appendix 7.B   Transport Measurements of Reference Devices

The AMR responses of the 3D reference devices, as well as the corresponding AMR ratio dependency on the externally applied field, are shown in fig. 7.10.

The AMR response of the reference devices is observed to differ greatly from that of the coil devices, as expected, given the different orientations the main components of the devices. Not only are the minima and maxima shifted by 90 °, the minima are also seen to be much sharper.

Furthermore, as can be observed in fig. 7.10c, the AMR ratio of the 3D reference devices is seen to saturate even before $H_{ex} = 50$ mT, the minimum applied field for sample characterization, while the coil devices are only seen to saturate only for much higher external fields, above 1T, as seen in fig. 7.5.

As for the 2D reference device, its AMR response and AMR ratio progression with the external magnetic field are shown in fig. 7.11. Given the planar 2D design of the device, its saturation AMR ratio is used as the characteristic AMR ratio of the material, which is not possible to determine from the 3D devices due to the varying surface normals. This is used to validate the material deposition step as well as to establish a base reference for the 3D device response. As expected, the AMR ratio is significantly larger, about 10×, than that of the 3D devices. The AMR response of the 2D reference device is seen to saturate at about 3.1 % AMR ratio for external fields field ≥ 2 T. The 2D reference device is seen to saturate at approximately the same external field setpoint as the 3D coil devices.

Appendix 7.C   second-harmonic Magnetoresistive Response

The second-harmonic component of the AMR responses is shown in fig. 7.12. No systematic characteristic response could be confidently extracted from the data. Despite the optimization of the lock-in low-pass filter, the acquired data, in the μV-range, is particularly affected by measurement noise from varied sources

(a)

(b)

(c)
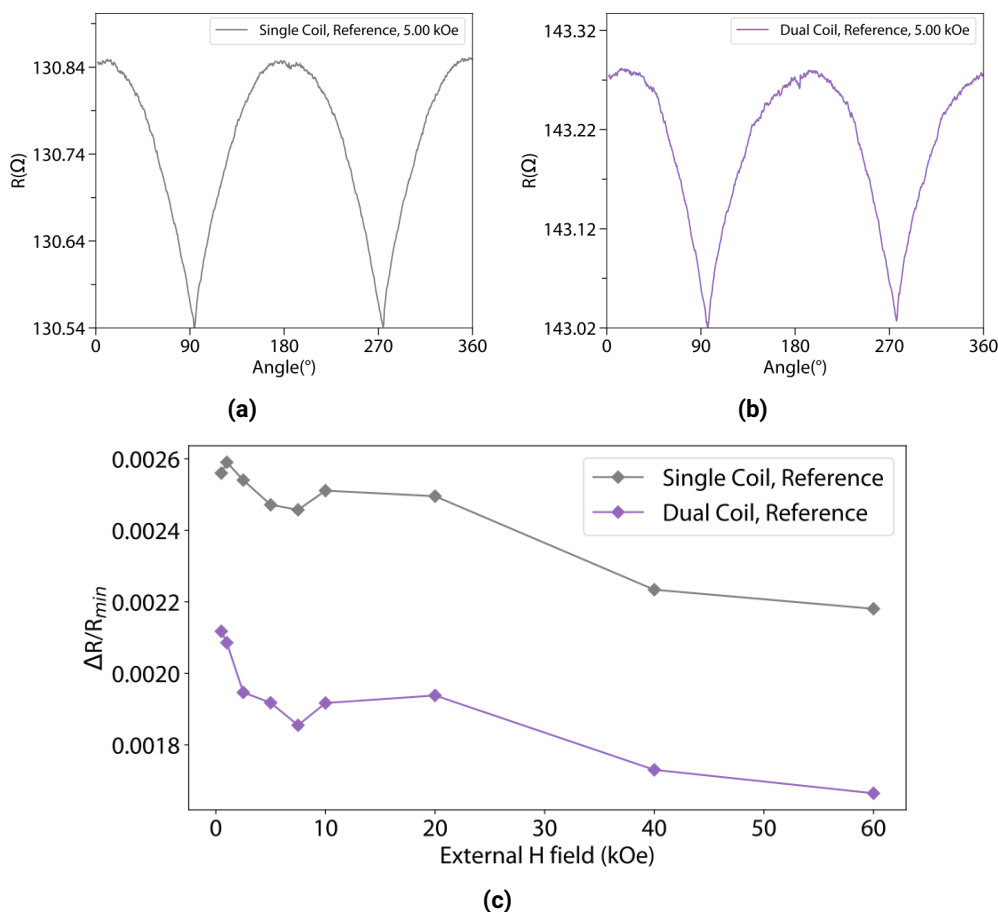
Figure 7.10: AMR response of the single (a) and dual (b) 3D reference devices for the representative external field $H_{ex} = 0.5\ T$. (c) AMR ratio of the single and dual 3D reference devices as a function of the applied external field.

which cannot be systematically characterized and de-convoluted. Particularly, any signal variation that could potentially be attributed to an AMR response is seen to greatly vary between each two field setpoints, both for the coil and for the 3D reference devices.

While directly measuring the inductance of the coil devices would enable to establish an expectation for the second-harmonic signal range, measuring the second-harmonic signal would require improving the experimental apparatus by identifying and removing noise sources.

Appendix 7.D   Thermally Induced Deformation of the Polymer Cores

At room temperatures, even currents in the order of $0.2\ mA$ cause the signal baseline resistance to steadily increase over long periods of time, signaling changes in the device properties. This results from heating of the polymer core of the devices, which causes the device to deform and its electrical properties to change. Such deformation was confirmed through the continued application of currents $> 0.5\ mA$ at room temperatures, which is seen in fig. 7.13 to lead to the evaporation of the polymer core. To avoid any changes to the device during the timeframe of its measurement, the devices are cooled down to 220 K before being characterized.

(a)

(b)

(c)
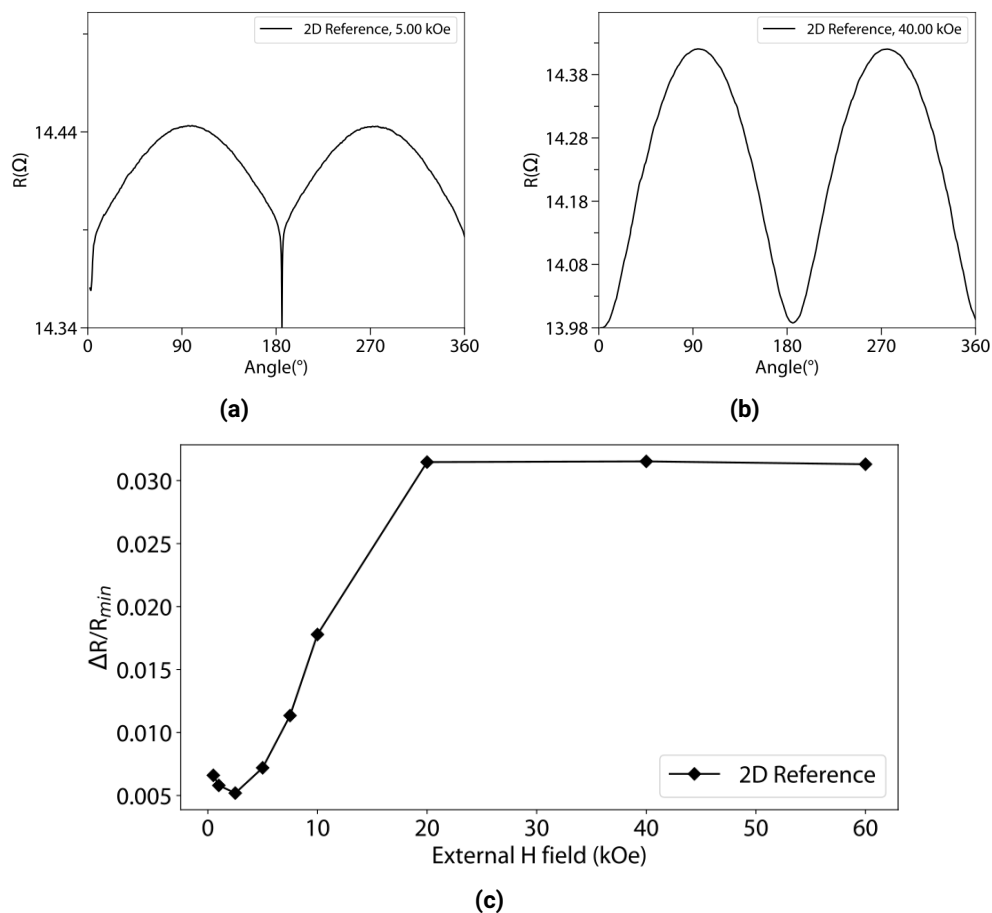
Figure 7.11: Transport measurement results for the 2D reference device. AMR response of the 2D reference device for the representative external field H_{ext} = 0.5 T (a) and for H_{ext} = 4 T (b). (c) AMR ratio as a function of the applied external field.

(a)   **(b)**   **(c)**

(d)   **(e)**   **(f)**
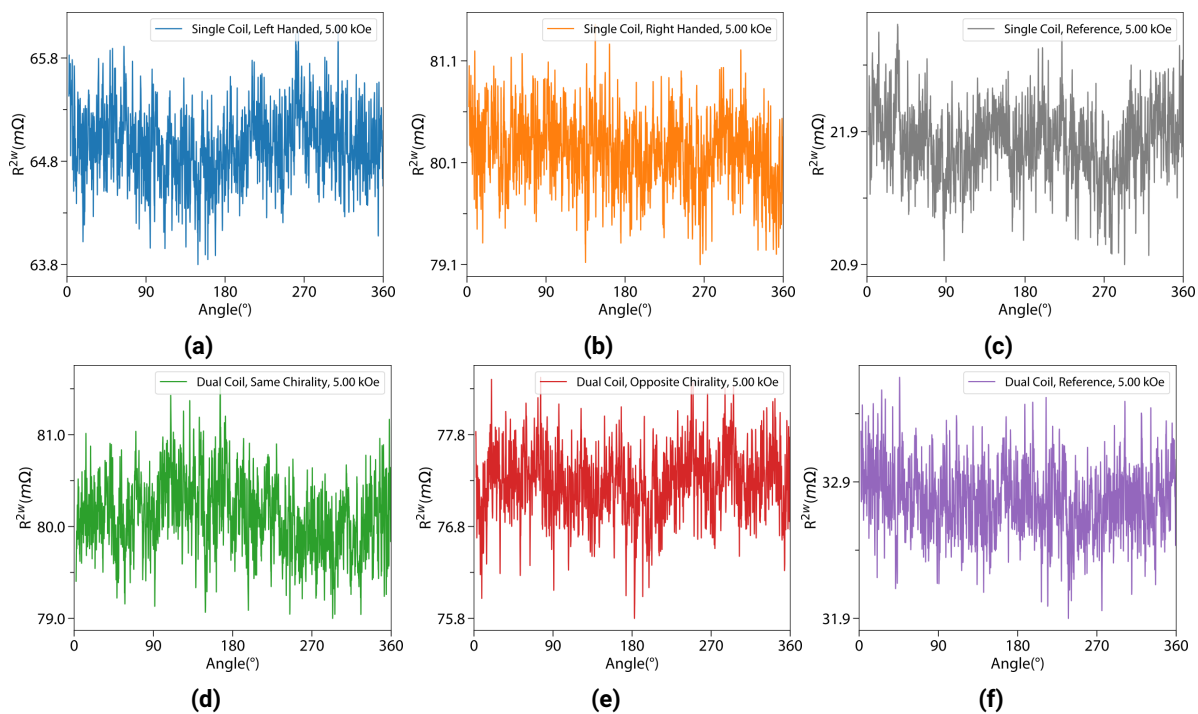
Figure 7.12: Representative second-harmonic signals for the characterized 3D devices at the highest characterization current of about 0.2 mA.
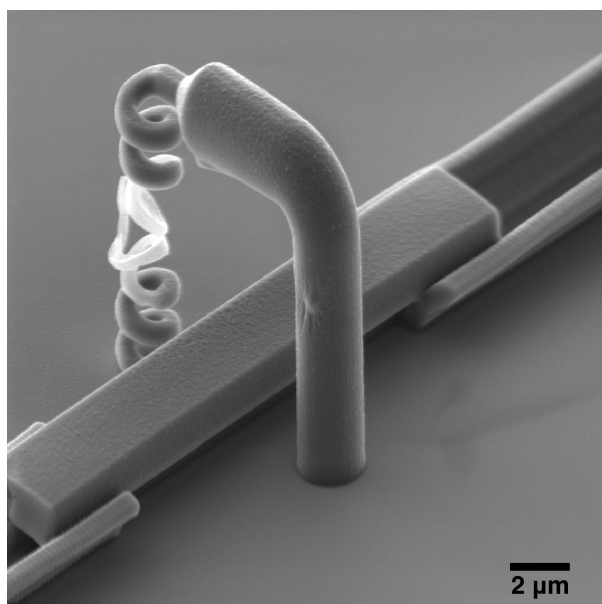
Figure 7.13: Evaporation of the polymer core of a coil due to current induced heating, along with deformation of the remaining CoNi alloy.

Chapter 8

Discussion

In chapters 5 to 7, the results achieved therein are discussed within the specific context of the experiments and closely-related research. Here, I will go beyond it by discussing the relevance of this work as a whole. I will do so in an incremental scope, starting by reviewing the achieved results in the context of the proposed aims, followed by the analysis of the relevance of this work to the field and finishing with my perspective regarding the future of this work and the field it is part of.

8.1 Reviewing the Aims

The aims for the project associated with this thesis are specified in section 2.6. Based on the results presented in chapters 5 to 7, all the aims are considered to be achieved, although in manners that differ from the initial expectation. To see how, each aim is further reviewed separately.

The first aim was fully realized. A state-of-the-art MPL setup with super-resolution capabilities was implemented that combines the benefits of high-end STED microscope hardware with the benefits of an open and fully modifiable architecture that can be easily adapted to the specifics of the intended application. The ability to freely modify both the software and hardware was, for example, critical to achieve the real-time characterization and control of the MPL process presented in chapter 6 and to understand the mechanisms behind it, respectively.

Regarding the second aim, a workflow for the fabrication of general 3D spintronic devices was successfully established. The two-step fabrication process greatly simplifies the fabrication when compared to more standard workflows [145], enabling the fast prototyping of spintronic devices with general 3D geometries by exploiting the directionality of PVD methods.

Nonetheless, this method has a more limited scope than initially intended, as it falls short of showing the same flexibility provided by photolithography to the fabrication of 2D devices. First, while the combination of MPL and PVD in multi-step workflows, e.g., as proposed in fig. 8.1, is expected to enable selective 3D material processing akin to etching and liftoff in 2D devices, this was not experimentally demonstrated. This would enable selective PVD coating of specific surfaces, e.g., as typically used to differentiate the active components of the device from the contact pads [145]. Second, unintended interactions between the active surface and the polymer core of the scaffold, as in chapter 7, might interfere with the device's function. Finally, the proposed method is particularly susceptible to the orientation of the material target relative to that of the 3D geometry surfaces during deposition, which can lead to film inhomogeneity, undesired shadowing and parasitic parallel resistances.
Improving upon these aspects would still require non-trivial research. Particularly, it would require the incorporation of dip-in MPL [46], supercritical drying and chemical [31, 71], plasma-based [151] or thermal-based [32] removal of the photoresist into the proposed workflow, as well as implementing the improvements to PVD described in section 8.3.

Regarding the third aim, it was accomplished by demonstrating the interplay between the 3D geometry and the functionality of a spintronic device, such as the DW filtering under current-induced DW motion in chapter 5. In its initial conception, this objective had particularly targeted the increase in the surface- and volume-to-footprint ratios when transitioning to 3D, e.g., as explored in the 3D racetrack memory [1]. In this context, the aim was unexpectedly superseded by experimentally demonstrating a new degree of freedom in the control of the magnetic properties of a system, one encompassing a vast and mostly unexplored parameter space.

8.2   Relevance

This work was started in a context where the influence of the 3D geometry on the properties of magnetic and magneto-electronic devices had been predicted theoretically [2, 124, 126, 127, 130, 134, 205], but not significantly shown in experiments due to difficulties in the realization and characterization of active devices with relevant magnetic film stacks and complex 3D geometries at the micro- and nano-scale. That several significant developments occurred in this scope during the realization of this project, including new geometry-driven functionalities and applications [22, 54, 122, 137], extensive improvements to characteriza- tion methods [15, 22, 137, 141, 162, 163, 165] and new post-processing [32, 64, 68, 71, 152] and deposition [33, 34, 156] techniques, demonstrates the relevance of the topic and the interest of a considerable international community in it.

Within this topic, I focused on the fabrication of 3D spintronic devices combining complex magnetic stacks and complex 3D geometries. The objective was to realize such systems by extrapolating into 3D fabrication the benefits provided by photolithography and photoresist materials in 2D spintronics. In the latter, the magnetic material properties and quality are decoupled from device patterning through selective processing methods such as etching and lift-off. To achieve this objective, scaffold-based fabrication using MPL and PVD, which was mostly unexplored in this context, was considered the most promising approach.

The significant results achieved through the proposed workflow establish it as an important alternative for the future exploration of the 3D geometry effects in spintronic devices. Particularly, the results in chapter 5 establish interesting new research directions and could, for example, potentially lead to DW logic. And yet, the merit of the proposed workflow is not a particular system but the ability to fabricate a wide range of geometries, easily integrated onto electronic devices, while maintaining compatibility with high-quality materials through PVD. In this regard, the techniques presented in this thesis are far from exhausted. This idea is further reinforced by recent exploration of magnetic and spintronic devices achieved through FEBID-based scaffolds coated with PVD [122, 145].

In choosing the main strengths of the approach I wanted to pursue and the techniques I would use to do it, I also incurred the particular set of limitations that are inherent to it.

First, capillary forces present during the MPL development step (see section 3.1) limit the minimum feature size of freestanding out-of-plane features to $\geq 500\ nm$, as seen in chapter 7. Although supercritical drying is expected to significantly improve this figure, it is likely difficult to achieve freestanding structures with sub-50 nm features, even though these are enabled by the super-resolution capabilities of our system. By comparison, freestanding structures with features on the sub-100 nm range are possible through FEBID [14], which has no development step.

Furthermore, the incorporation of polymer scaffolds into the active devices is prone to interfere with the electrical measurements, e.g., due to heating effects as seen in chapter 7, and therefore either polymer removal, e.g., through plasma etching [32], or scaffold cores with improved properties, e.g., SiO_2 scaffold cores [64], would have to be incorporated into the fabrication workflow.

Finally, the proposed method is also affected by shadowing effects and the specific deposition directions defined by the orientation of the material targets in the utilized PVD chamber, which are static in current systems. By comparison, FEBID takes advantage of a sample micromanipulator to control the direction of the material deposition during the fabrication [159].

On the application side, novel functionalities are shown in spintronic devices. The chirality of the device

geometry is seen to induce chirality in magnetic systems, as in chapter 7, or to interface with the already existing chiralities, as in chapter 5, breaking the chiral symmetry of the system in new ways. Particularly, this leads to the modulation current-induced DW motion thresholds and velocities for different DW types over devices with torsion, implementing a DW filter as seen in chapter 5, and to asymmetric AMR responses and the modulation of the AMR ratios over coils of opposite chirality, as seen in chapter 7. The former effect had not been previously observed for current-induced DW motion in 3D.

Beyond the applications in spintronics, an improved MPL fabrication process is developed that incorporates real-time characterization and control, enabling to correct for fabrication mismatches on-the-fly and to generate precise 3D reconstructions of the fabrication result without any further post-processing of the sample. This process greatly improves and simplifies the optimization of fabrication settings, the fabrication yield and the fidelity of the resulting structure. While addressing a widely sought functionality, the proposed implementation improves on the precision and implementation of previously developed methods [190, 193].

For the studies presented in chapters 5 and 7, readily available standard characterization methods were favored over intrinsically 3D characterization methods, as the former require less setup adaptation and simpler preparation and therefore enable shorter the design iteration cycles. However, this has significantly limited the insights provided by the characterization. Having stabilized the devices' design, the studies presented in this thesis would greatly benefit from the precise 3D characterization offered by intrinsically 3D methods in order to better understand the impact of the different geometrical features on the device function and the associated underlying effects. For example, the device in chapter 5 would benefit from orientation-sensitive dark-field MOKE [22], which would filter out the substrate signal, while the devices in both chapter 5 and chapter 7 would benefit from time-resolved XMCD-based nanotomography [141] to evaluate the DW behavior in different sections, if such technique is proven compatible with the presence of the polymer cores.

As a whole, the fabrication workflow that was developed throughout this work significantly advances the capability to achieve structures with general 3D geometries and functionalize them into magneto-electronic devices. This capability is proven by the observation of new geometry-driven functionalities in the context of spintronics. The presented method is aligned with the other developments achieved by the community over the same period, and improves on them in some aspects, which further validates its relevance for the current context and state-of-the-art. Despite its freeform 3D capabilities, it remains to be seen if the limitations of the method presented here will impede its general adoption. My perspective towards the future of general and high-performance 3D spintronic devices, informed by the work developed throughout this thesis, is presented next.

8.3 Outlook and Future Perspectives

As shown in chapters 5 and 7, the exploration of general 3D spintronic devices is now possible. Currently, the most feasible methods to do so are direct fabrication through FEBID [54] as well as scaffold-based methods using FEBID [122] or MPL. Upon the start of a new project in this scope, the decision of the approach to pursue will be mostly dependent on the particular objective of the project, as the different approaches provide significantly different advantages that might either facilitate a given application or hinder it, as is summarized next.

Direct fabrication approaches, particularly using FEBID, have the advantage of being a one-step fabrication process with no required postprocessing before measuring, but are limited by the available precursors and the attainable material purity, which is typically subpar to that of PVD, and the resulting properties thereof.

Scaffold-based fabrication, which can be implemented through either FEBID or MPL, overcomes the material purity limitations of direct fabrication by establishing workflows that use PVD. However, this results in more challenging fabrication processes. Particularly, both FEBID and MPL scaffolds increase the complexity of the resulting structures, either due to parasitic deposition [159] or to undesired properties of the scaffold material, such as the poor thermal conductivity in chapter 7.

Within scaffold-based approaches, the bottlenecks for the fabrication of 3D electronic devices are currently the scaffold material properties, the establishment of multi-step patterning processes and the interface of 3D and standard fabrication techniques. Nonetheless, all these three aspects have significant perspectives for improving, as identified next.

Ideally, scaffolds would be made of materials typically used as substrates, e.g., Si or SiO_2, or others with similar properties. For example, scaffolds with higher glass-transition temperatures would already enable integration with higher temperature processing steps and withstand increased Joule heating during characterization. Recent demonstrations of SiO_2 3D structures at the nanoscale through MPL [64] are, so far, the most promising in this context. Although not yet optimized, such an approach constitutes significant progress towards 3D SiO_2 polycrystalline or crystalline scaffolds, and consequently towards active 3D crystalline structures. On the other hand, scaffolds with increased robustness have also been shown using highly resistive materials patterned through FEBID [145].

The realization of 3D multi-step patterning, including etching and lift-off, as envisioned in fig. 8.1, should be readily feasible since all the necessary tools are already available. The ability to perform MPL over opaque substrates and surfaces is achievable through dip-in MPL [46], although conformal patterning over dense structures will likely prove very difficult. On the other hand, the selective removal of MPL polymers can be achieved through oxygen plasma etching [31, 32], which avoids any capillary forces, pyrolysis, which causes inconsistent interfaces [32], and the combination between scaffold dissolution [71] and supercritical drying. To a more limited extent, the integration of FEBID with 2D photolithography for achieving liftoff in more complex processing workflows has already been shown [145]

The integration with standard techniques is also critical, particularly PVD and reactive ion etching. The biggest hurdle so far is the fixed direction of the deposition and etching on existing systems, which can even vary for different materials in the same deposition chamber. This leads to uncontrolled shadowing effects and non-uniform film deposition or etching. The integration of micromanipulator stages, deposition focusing, e.g., through electro-magnetic shutters (or lenses) as in [156], and 3D deposition control algorithms into current PVD systems should enable a major improvement in the deposition of uniform and high-quality films over complex 3D structures. Particularly, this would also enable a much more extensive exploration of shadowing effects in order to more precisely control where the deposition of each material occurs.

Simultaneously, a wide range of 3D-compatible techniques has been appearing very recently that improve upon some shortcomings of current approaches. Direct fabrication methods such as electric-field controlled 3D PVD [156] and laser processing of active materials [33, 34] have the potential to combine the material purity of PVD methods with the benefits of direct fabrication, such as the avoidance of post-processing and the nm-small features and resolution. Other techniques, like the freestanding deposition of high-quality films over 3D structures [206], although more limited in scope, could possibly improve the robustness of the magnetic films to small defects on the surface of the devices, e.g., as observed in chapter 5.

Significantly different materials typically require different deposition methods in different chambers. Thus, the development of laser processing methods for direct processing of different materials [33, 34] which could potentially be integrated into the same MPL-like experimental setup is highly beneficial for the development of multi-step processing of complex structures.

Over the long term, 3D direct fabrication methods are, in principle, better suited to satisfy the requirements for general 3D nano-magnetism: nm features and resolutions over a wide range of high-purity materials. However, as these methods approach the milestone of bottom-up 3D atomic synthesis, such demanding simultaneous requirements are extremely difficult to develop towards. Currently, the methods that better approach this perspective are direct laser processing [33, 34], FEBID [25] and field-controlled deposition of charged particles [156], as reviewed in section 2.5. These techniques all still present a limited range of compatible high-purity materials and, apart from FEBID, relatively large feature sizes and

1. Base MPL **2.** Sacrificial MPL **3.** Coating **4.** Selective Removal (2)

(a)

1. Base MPL **2.** Coating **3.** Protective MPL **4.** Etching+ Sel. Removal (3)

(b)
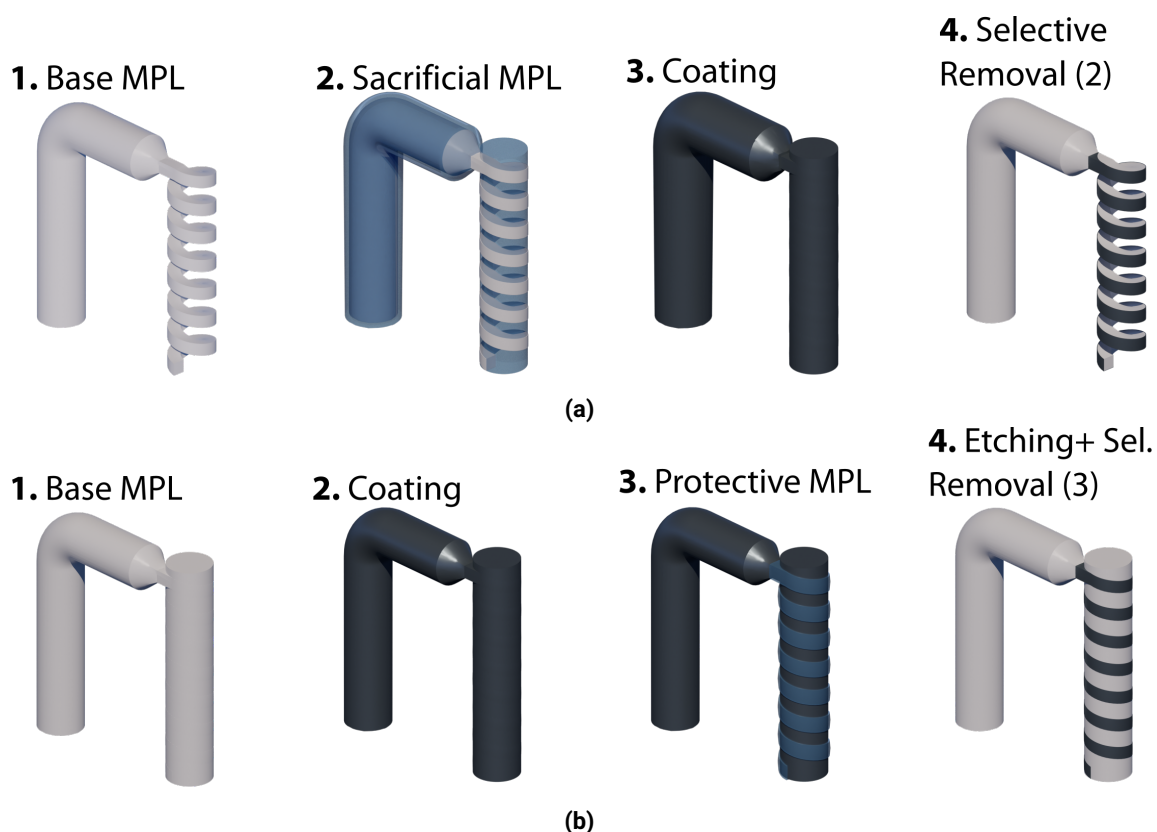
Figure 8.1: Proposal for multi-step 3D processing workflows, exemplified with the devices from chapter 7. (a) 3D liftoff taking advantage of the selective MPL photoresist removal as shown in [71]. (b) 3D etching.

resolutions.

Nonetheless, even if all such requirements were achieved at significant fabrication rates, the ability to pattern materials at the nm-range comes with a high scalability cost [72]. It is therefore likely that in the future different techniques will be used to bridge greatly different scales, e.g., imagine a 1 *cm* cube-like meta-material with many 100×100 μm electrical pads connecting to 1 nm helix-shaped electronic devices. The fabrication workflow I present in this thesis enables 3D scaffolding and processing of active materials over a large range of scales with high fabrication rates, as enabled by MPL [28]. It is therefore, in my perspective, an important addition to the toolbox of techniques necessary to achieve the widespread realization of 3D spintronics and electronics.

Currently, the curvilinear ferromagnetism modeling framework presented in section 2.4 enables to understand and explain observations in experimentally realized 3D magnetic and magneto-electronic systems. As more systems are realized and studied, the mapping between a given geometrical feature and the functionality it provides will be established and improved upon. Once enough knowledge is attained, it should be possible to effectively design new devices with improved function simply through the combination of modular geometrical components. Once this point is reached, the established modeling framework [7] will rather take the role of a device design tool that will enable to fine-tune the device function at an early stage. For example, based on what is known today, it should already be possible to combine specific DW nucleation, DW automotion [122], and DW filtering in a single system. As further specific geometries are mapped to the function they allow, this will likely enable the bit-like manipulation of DWs over 3D devices and, potentially, advanced applications such as DW logic. Beyond the racetrack memory is likely an ecosystem of devices that uses the full extent of their 3D geometry to implement abstract functionality that could be used, for example, in computation. The integration of 3D DW-based memories with DW logic, and other advanced functions, in the same framework would result in an highly energy efficient, dense, and fast computational system that could prove very impactful, for example, in in-

memory logic architectures that are highly desirable in current state-of-the-art computational research [24].

The improved MPL process proposed in this thesis provides access to the fabrication result in real-time. The large number of fabrication parameters, including the fabrication mask itself, can now be leveraged to better match the fabrication result to the desired model, providing an added degree of control. This improved control is particularly impactful when combined with algorithms for automated fabrication optimization and control.

Besides the automatic fabrication control already presented in chapter 6, the most significant application in the short term will be the initial optimization of the baseline fabrication settings to a specific structure. Currently, this is realized through the fabrication of several copies of the same structure under slight variations of a given fabrication preset. Upon implementation of automatic optimization, the convergence towards the optimal settings should mostly occur within tens of layers rather than tens of structures or more. Such convergence should be possible even when no suitable fabrication presets exist.

In the longer term, once enough characterization data is collected, the most impactful application will likely be the training and usage of automatic fabrication pre-optimizers [1] through machine learning. Besides globally optimizing a given set of fabrication parameters for a whole structure, this will enable to locally optimize settings for a given feature or layer. Through the local modulation of fabrication parameters, both the fidelity of the fabrication result and the fabrication time should be significantly and simultaneously improved. The utilization of machine learning in this context, already attempted in the past [201], will enable to take full advantage of the complete fabrication parameter space beyond what is possible to achieve manually.

The provided characterization method can be adjusted for improved speed, e.g., by only scanning every few layers, or resolution and should therefore be suitable for use in most cases. Particularly, the focus on improved resolution will render precise, possibly super-resolution, 3D reconstructions of the fabrication result providing a significant alternative to SEM without the associated sample preparation, time-consuming acquisition, and parallax errors.

---

[1] pre-optimization, as opposed to live optimization, is done before the fabrication is started, i.e., during slicing, and reflects an extensive knowledge of the fabrication process

Chapter 9

Conclusion

A new scaffold-based workflow for the fabrication of freeform 3D spintronic devices is demonstrated. By using 3D features to selectively shadow the substrate during PVD of the magnetic film stacks, working devices are achieved after only two steps, MPL and PVD. While this simplified procedure is particularly advantageous for prototyping and exploring new concepts, a generalization of it compatible with multi-step processing is also proposed. The control over the MPL fabrication provided by the system implemented in this work enables to achieve particularly small surface roughness over the fabricated surfaces, which is crucial to the device performance.

Two different spintronic device concepts are realized with the proposed workflow. Both present a significant coupling between the 3D geometrical properties of the scaffold and the magnetic response of the devices. Particularly, the torsion in 3D ribbons is seen to modulate the DW current threshold and velocity depending upon the DW type and the torsion chirality, enabling the implementation of a DW filter. Furthermore, the chirality of coil-based devices appears to lead to asymmetric AMR responses for coils of opposite chirality.

An improved MPL process is demonstrated that enables in-situ and real-time characterization and control. This process is used to correct errors during fabrication and improve the capabilities of the apparatus. Furthermore, the acquired characterization data is used to perform a high-fidelity 3D reconstruction of the fabricated structures, establishing a new 3D characterization method.

This thesis establishes improved tools for prototyping 3D spintronic devices. By employing them, new and unexpected phenomena and applications were discovered. And yet, as most of the parameter space for 3D geometries remains unexplored, one is led to wonder about all the exciting possibilities lying just ahead. To paraphrase Feynman [8], it is apparent that once we are able to freely arrange nano-electronic devices in 3D we will get an enormously greater range of possible properties that substances can have, and of different things that we can do.

Bibliography

[1]   Stuart S. P. Parkin, Masamitsu Hayashi, and Luc Thomas. "Magnetic Domain-Wall Racetrack Memory". Science 320.5873 (Apr. 11, 2008), pp. 190–194.
DOI: 10.1126/science.1145799.   (Pages v, vii, 1, 19, 114)

[2]   Yuri Gaididei et al. "Magnetization in Narrow Ribbons: Curvature Effects". Journal of Physics A: Mathematical and Theoretical 50.38 (Sept. 2017), p. 385401. ISSN: 1751-8121.
DOI: 10.1088/1751-8121/aa8179.   (Pages v, vii, 1, 25, 26, 28, 114)

[3]   Volodymyr P. Kravchuk et al. "Multiplet of Skyrmion States on a Curvilinear Defect: Reconfigurable Skyrmion Lattices". Physical Review Letters 120.6 (Feb. 8, 2018), p. 067201.
DOI: 10.1103/PhysRevLett.120.067201.   (Pages v, vii, 1, 27, 59)

[4]   Amalio Fernández-Pacheco et al. "Three-Dimensional Nanomagnetism". Nature Communications 8.1 (1 June 9, 2017), p. 15756. ISSN: 2041-1723.
DOI: 10.1038/ncomms15756.   (Pages v, vii, 1, 3, 28)

[5]   Peter Fischer et al. "Launching a New Dimension with 3D Magnetic Nanostructures". APL Materials 8.1 (Jan. 2020), p. 010701.
DOI: 10.1063/1.5134474.   (Pages v, vii, 28)

[6]   Denis D. Sheka. "A Perspective on Curvilinear Magnetism". Applied Physics Letters 118.23 (June 7, 2021), p. 230502. ISSN: 0003-6951.
DOI: 10.1063/5.0048891.   (Pages v, vii, 1, 25, 28)

[7]   Denis D. Sheka et al. "Fundamentals of Curvilinear Ferromagnetism: Statics and Dynamics of Geometrically Curved Wires and Narrow Ribbons". Small 18.12 (2022), p. 2105219. ISSN: 1613-6829.
DOI: 10.1002/smll.202105219.   (Pages v, vii, 25–28, 74, 117)

[8]   Richard P Feynman. "Plenty of Room at the Bottom" (), p. 7.   (Pages 1, 119)

[9]   V. Harinarayana and Y.C. Shin. "Two-Photon Lithography for Three-Dimensional Fabrication in Micro/Nanoscale Regime: A Comprehensive Review". Optics & Laser Technology 142 (Oct. 2021), p. 107180. ISSN: 00303992.
DOI: 10.1016/j.optlastec.2021.107180.   (Pages 1, 3, 83)

[10] Tian-Yun Huang et al. "3D Printed Microtransporters: Compound Micromachines for Spatiotemporally Controlled Delivery of Therapeutic Agents". Advanced Materials 27.42 (2015), pp. 6644–6650. ISSN: 1521-4095.
DOI: 10.1002/adma.201503095.   (Page 1)

[11] Christian Peters et al. "Degradable Magnetic Composites for Minimally Invasive Interventions: Device Fabrication, Targeted Drug Delivery, and Cytotoxicity Tests". Advanced Materials 28.3 (2016), pp. 533–538. ISSN: 1521-4095.
DOI: 10.1002/adma.201503112.   (Page 1)

[12] Tobias Abele et al. "Two-Photon 3D Laser Printing Inside Synthetic Cells". Advanced Materials 34.6 (2022), p. 2106709. ISSN: 1521-4095.
DOI: 10.1002/adma.202106709.   (Pages 1, 3)

[13]   Joachim Fischer, Tolga Ergin, and Martin Wegener. "Three-Dimensional Polarization-Independent Visible-Frequency Carpet Invisibility Cloak". Optics Letters 36.11 (June 1, 2011), pp. 2059–2061. ISSN: 1539-4794.
DOI: 10.1364/OL.36.002059.   (Page 1)

[14]   Amalio Fernández-Pacheco et al. "Three Dimensional Magnetic Nanowires Grown by Focused Electron-Beam Induced Deposition". Scientific Reports 3.1 (1 Mar. 20, 2013), p. 1492. ISSN: 2045-2322.
DOI: 10.1038/srep01492.   (Pages 1, 30, 33, 114)

[15]   Claire Donnelly et al. "Time-Resolved Imaging of Three-Dimensional Nanoscale Magnetization Dynamics". Nature Nanotechnology 15.5 (5 May 2020), pp. 356–360. ISSN: 1748-3395.
DOI: 10.1038/s41565-020-0649-x.   (Pages 1, 34, 114)

[16]   Hao Zeng et al. "Light-Fueled Microscopic Walkers". Advanced Materials 27.26 (2015), pp. 3883–3887. ISSN: 1521-4095.
DOI: 10.1002/adma.201501446.   (Page 1)

[17]   Timo Gissibl et al. "Two-Photon Direct Laser Writing of Ultracompact Multi-Lens Objectives". Nature Photonics 10.8 (8 Aug. 2016), pp. 554–560. ISSN: 1749-4893.
DOI: 10.1038/nphoton.2016.121.   (Pages 1, 4, 83)

[18]   Francesca Bragheri, Rebeca Martínez Vázquez, and Roberto Osellame. "Chapter 12.3 - Microfluidics". Three-Dimensional Microfabrication Using Two-Photon Polymerization (Second Edition). Ed. by Tommaso Baldacchini. Micro and Nano Technologies. William Andrew Publishing, Jan. 1, 2020, pp. 493–526. ISBN: 978-0-12-817827-0.
DOI: 10.1016/B978-0-12-817827-0.00057-6.   (Pages 1, 4, 83)

[19]   Anastasia Koroleva et al. "In Vitro Development of Human iPSC-Derived Functional Neuronal Networks on Laser-Fabricated 3D Scaffolds". ACS Applied Materials & Interfaces 13.7 (Feb. 24, 2021), pp. 7839–7853. ISSN: 1944-8244.
DOI: 10.1021/acsami.0c16616.   (Pages 1, 3, 4, 83)

[20]   Zemin Liu et al. "Creating Three-Dimensional Magnetic Functional Microdevices via Molding-Integrated Direct Laser Writing". Nature Communications 13.1 (1 Apr. 19, 2022), p. 2016. ISSN: 2041-1723.
DOI: 10.1038/s41467-022-29645-2.   (Pages 1, 4)

[21]   Tobias Frenzel, Muamer Kadic, and Martin Wegener. "Three-Dimensional Mechanical Metamaterials with a Twist". Science 358.6366 (Nov. 24, 2017), pp. 1072–1074. ISSN: 0036-8075, 1095-9203.
DOI: 10.1126/science.aao4640.   (Pages 1, 3, 4)

[22]   Dédalo Sanz-Hernández et al. "Fabrication, Detection, and Operation of a Three-Dimensional Nanomagnetic Conduit". ACS Nano 11.11 (Nov. 28, 2017), pp. 11066–11073. ISSN: 1936-0851.
DOI: 10.1021/acsnano.7b05105.   (Pages 1, 28–30, 34, 114, 115)

[23]   Gwilym Williams et al. "Two-Photon Lithography for 3D Magnetic Nanostructure Fabrication". Nano Research 11.2 (Feb. 1, 2018), pp. 845–854. ISSN: 1998-0000.
DOI: 10.1007/s12274-017-1694-0.   (Pages 1, 3, 30)

[24]   Abu Sebastian et al. "Memory Devices and Applications for In-Memory Computing". Nature Nanotechnology 15.7 (7 July 2020), pp. 529–544. ISSN: 1748-3395.
DOI: 10.1038/s41565-020-0655-z.   (Pages 1, 59, 117)

[25]   Luka Skoric et al. "Layer-by-Layer Growth of Complex-Shaped Three-Dimensional Nanostructures with Focused Electron Beams". Nano Letters 20.1 (Jan. 8, 2020), pp. 184–191. ISSN: 1530-6984.
DOI: 10.1021/acs.nanolett.9b03565.   (Pages 1, 33, 34, 116)

[26]   Andrey Vyatskikh et al. "Additive Manufacturing of 3D Nano-Architected Metals". Nature Communications 9.1 (1 Feb. 9, 2018), p. 593. ISSN: 2041-1723.
DOI: 10.1038/s41467-018-03071-9.   (Pages 1, 30, 31)

[27]   Thomas A. Klar, Richard Wollhofen, and Jaroslaw Jacak. "Sub-Abbe Resolution: From STED Microscopy to STED Lithography". Physica Scripta 2014.T162 (2014), p. 014049. ISSN: 1402-4896. DOI: 10.1088/0031-8949/2014/T162/014049.   (Pages 3, 38)

[28]   Vincent Hahn et al. "Rapid Assembly of Small Materials Building Blocks (Voxels) into Large Functional 3D Metamaterials". Advanced Functional Materials 30.26 (2020), p. 1907795. ISSN: 1616-3028.
       DOI: 10.1002/adfm.201907795.   (Pages 3, 4, 32, 83, 117)

[29]   Pol Cabanach et al. "Zwitterionic 3D-Printed Non-Immunogenic Stealth Microrobots". Advanced Materials 32.42 (2020), p. 2003013. ISSN: 1521-4095.
       DOI: 10.1002/adma.202003013.   (Pages 3, 4)

[30]   Christoph A. Spiegel et al. "4D Printing at the Microscale". Advanced Functional Materials 30.26 (2020), p. 1907615. ISSN: 1616-3028.
       DOI: 10.1002/adfm.201907615.   (Pages 3, 4)

[31]   N. Tétreault et al. "New Route to Three-Dimensional Photonic Bandgap Materials: Silicon Double Inversion of Polymer Templates". Advanced Materials 18.4 (Feb. 17, 2006), pp. 457–460. ISSN: 1521-4095.
       DOI: 10.1002/adma.200501674.   (Pages 3, 30–32, 83, 113, 116)

[32]   G. Seniutinas et al. "Beyond 100 nm Resolution in 3D Laser Lithography — Post Processing Solutions". Microelectronic Engineering 191 (May 5, 2018), pp. 25–31. ISSN: 0167-9317.
       DOI: 10.1016/j.mee.2018.01.018.   (Pages 3, 4, 31, 32, 83, 113, 114, 116)

[33]   Shao-Feng Liu et al. "3D Nanoprinting of Semiconductor Quantum Dots by Photoexcitation-Induced Chemical Bonding". Science 377.6610 (Sept. 2, 2022), pp. 1112–1116.
       DOI: 10.1126/science.abo5345.   (Pages 3, 32, 33, 114, 116)

[34]   Xiaoyi Xu et al. "Femtosecond Laser Writing of Lithium Niobate Ferroelectric Nanodomains". Nature 609.7927 (7927 Sept. 2022), pp. 496–501. ISSN: 1476-4687.
       DOI: 10.1038/s41586-022-05042-z.   (Pages 3, 32, 114, 116)

[35]   Jürgen Stampfl, Robert Liska, and Aleksandr Ovsianikov, eds. Multiphoton Lithography: Techniques, Materials and Applications. Weinheim, Germany: Wiley-VCH Verlag GmbH & Co. KGaA, 2017. 386 pp. ISBN: 978-3-527-33717-0.   (Page 4)

[36]   Soichiro Tottori et al. "Magnetic Helical Micromachines: Fabrication, Controlled Swimming, and Cargo Transport". Advanced Materials 24.6 (Feb. 7, 2012), pp. 811–816. ISSN: 09359648.
       DOI: 10.1002/adma.201103818.   (Page 4)

[37]   Lucas R. Meza et al. "Resilient 3D Hierarchical Architected Metamaterials". Proceedings of the National Academy of Sciences 112.37 (Sept. 15, 2015), pp. 11502–11507. ISSN: 0027-8424, 1091-6490.
       DOI: 10.1073/pnas.1509120112.   (Page 4)

[38]   Anna Guell Izard et al. "Ultrahigh Energy Absorption Multifunctional Spinodal Nanoarchitectures". Small 15.45 (Nov. 2019), p. 1903834. ISSN: 1613-6810, 1613-6829.
       DOI: 10.1002/smll.201903834.   (Page 4)

[39]   Cornelius Fendler et al. "Microscaffolds by Direct Laser Writing for Neurite Guidance Leading to Tailor-Made Neuronal Networks". Advanced Biosystems 3.5 (May 2019), p. 1800329. ISSN: 2366-7478, 2366-7478.
       DOI: 10.1002/adbi.201800329.   (Page 4)

[40]   Benjamin W. Pearre et al. "Fast Micron-Scale 3D Printing with a Resonant-Scanning Two-Photon Microscope". Additive Manufacturing 30 (Dec. 2019), p. 100887. ISSN: 22148604.
       DOI: 10.1016/j.addma.2019.100887.   (Page 4)

[41]   Maria Göppert-Mayer. "Über Elementarakte Mit Zwei Quantensprüngen". Annalen der Physik 401.3 (1931), pp. 273–294. ISSN: 1521-3889.
       DOI: 10.1002/andp.19314010303.   (Pages 3, 9, 10)

[42]   Shoji Maruo, Osamu Nakamura, and Satoshi Kawata. "Three-Dimensional Microfabrication with
       Two-Photon-Absorbed Photopolymerization". Optics Letters 22.2 (Jan. 15, 1997), pp. 132–134. ISSN:
       1539-4794.
       DOI: 10.1364/OL.22.000132.   (Page 3)

[43]   En-Shinn Wu et al. "Two-Photon Lithography for Microelectronic Application". Optical/Laser
       Microlithography V. Optical/Laser Microlithography V. Vol. 1674. SPIE, June 1, 1992, pp. 776–782.
       DOI: 10.1117/12.130367.   (Page 3)

[44]   Winifried Denk, James H. Strickler, and Watt W. Webb. "Two-Photon Laser Scanning Fluorescence
       Microscopy". Science 248.4951 (Apr. 6, 1990), pp. 73–76.
       DOI: 10.1126/science.2321027.   (Page 3)

[45]   James H. Strickler and Watt W. Webb. "Three-Dimensional Optical Data Storage in Refractive
       Media by Two-Photon Point Excitation". Optics Letters 16.22 (Nov. 15, 1991), pp. 1780–1782. ISSN:
       1539-4794.
       DOI: 10.1364/OL.16.001780.   (Page 3)

[46]   Tiemo Bückmann et al. "Tailored 3D Mechanical Metamaterials Made by Dip-in Direct-Laser-
       Writing Optical Lithography". Advanced Materials 24.20 (2012), pp. 2710–2714. ISSN: 1521-4095.
       DOI: 10.1002/adma.201200584.   (Pages 3, 32, 113, 116)

[47]   Joachim Fischer and Martin Wegener. "Ultrafast Polymerization Inhibition by Stimulated Emission
       Depletion for Three-dimensional Nanolithography". Advanced Materials 24.10 (2012), OP65–OP69.
       ISSN: 1521-4095.
       DOI: 10.1002/adma.201103758.   (Pages 3, 38, 97)

[48]   Satoshi Kawata et al. "Finer Features for Functional Microdevices". Nature 412.6848 (6848 Aug.
       2001), pp. 697–698. ISSN: 1476-4687.
       DOI: 10.1038/35089130.   (Page 3)

[49]   Martin Straub and Min Gu. "Near-Infrared Photonic Crystals with Higher-Order Bandgaps
       Generated by Two-Photon Photopolymerization". Optics Letters 27.20 (Oct. 15, 2002), pp. 1824–
       1826. ISSN: 1539-4794.
       DOI: 10.1364/OL.27.001824.   (Page 3)

[50]   Georg von Freymann et al. "Three-Dimensional Nanostructures for Photonics". Advanced Func-
       tional Materials 20.7 (2010), pp. 1038–1052. ISSN: 1616-3028.
       DOI: 10.1002/adfm.200901838.   (Pages 3, 84)

[51]   Xiaoqin Zhou, Yihong Hou, and Jieqiong Lin. "A Review on the Processing Accuracy of Two-
       Photon Polymerization". AIP Advances 5.3 (Mar. 2015), p. 030701. ISSN: 2158-3226.
       DOI: 10.1063/1.4916886.   (Pages 3, 4)

[52]   Claire Donnelly et al. "Element-Specific X-Ray Phase Tomography of 3D Structures at the Nanoscale".
       Physical Review Letters 114.11 (Mar. 16, 2015), p. 115501.
       DOI: 10.1103/PhysRevLett.114.115501.   (Page 3)

[53]   Matthew Hunt et al. "Harnessing Multi-Photon Absorption to Produce Three-Dimensional Mag-
       netic Structures at the Nanoscale". Materials 13.3 (3 Jan. 2020), p. 761. ISSN: 1996-1944.
       DOI: 10.3390/ma13030761.   (Pages 4, 83)

[54]   Fanfan Meng et al. "Non-Planar Geometrical Effects on the Magnetoelectrical Signal in a Three-
       Dimensional Nanomagnetic Circuit". ACS Nano 15.4 (Apr. 27, 2021), pp. 6765–6773. ISSN: 1936-
       0851.
       DOI: 10.1021/acsnano.0c10272.   (Pages 4, 28–30, 83, 114, 115)

[55]   Johnny Moughames et al. "Three-Dimensional Waveguide Interconnects for Scalable Integration
       of Photonic Neural Networks". Optica 7.6 (June 20, 2020), pp. 640–646. ISSN: 2334-2536.
       DOI: 10.1364/OPTICA.388205.   (Pages 4, 83)

[56] Alexandra M. Greiner, Benjamin Richter, and Martin Bastmeyer. "Micro-Engineered 3D Scaffolds for Cell Culture Studies". Macromolecular Bioscience 12.10 (), pp. 1301–1314. ISSN: 1616-5195.
DOI: 10.1002/mabi.201200132. (Page 4)

[57] Aleksandr Ovsianikov et al. "Engineering 3D Cell-Culture Matrices: Multiphoton Processing Technologies for Biological and Tissue Engineering Applications". Expert Review of Medical Devices 9.6 (Nov. 1, 2012), pp. 613–633. ISSN: 1743-4440.
DOI: 10.1586/erd.12.48. pmid: 22943308. (Page 4)

[58] Xiaoyu Sun et al. "Chapter 12.4 - Cell Motility and Nanolithography". Three-Dimensional Micro-fabrication Using Two-Photon Polymerization (Second Edition). Ed. by Tommaso Baldacchini. Micro and Nano Technologies. William Andrew Publishing, Jan. 1, 2020, pp. 527–540. ISBN: 978-0-12-817827-0.
DOI: 10.1016/B978-0-12-817827-0.00058-8. (Pages 4, 83)

[59] Sangwon Kim et al. "Fabrication and Characterization of Magnetic Microrobots for Three-Dimensional Cell Culture and Targeted Transportation". Advanced Materials 25.41 (Nov. 2013), pp. 5863–5868. ISSN: 09359648.
DOI: 10.1002/adma.201301484. (Page 4)

[60] Fatemeh Rajabasadi et al. "3D and 4D Lithography of Untethered Microrobots". Progress in Materials Science 120 (July 1, 2021), p. 100808. ISSN: 0079-6425.
DOI: 10.1016/j.pmatsci.2021.100808. (Pages 4, 83)

[61] T. Bückmann et al. "An Elasto-Mechanical Unfeelability Cloak Made of Pentamode Metamaterials". Nature Communications 5.1 (1 June 19, 2014), p. 4130. ISSN: 2041-1723.
DOI: 10.1038/ncomms5130. (Page 4)

[62] Muamer Kadic et al. "On the Practicability of Pentamode Mechanical Metamaterials". Applied Physics Letters 100.19 (May 7, 2012), p. 191901. ISSN: 0003-6951.
DOI: 10.1063/1.4709436. (Page 4)

[63] Airán Ródenas et al. "Three-Dimensional Femtosecond Laser Nanolithography of Crystals". Nature Photonics 13.2 (2 Feb. 2019), pp. 105–109. ISSN: 1749-4893.
DOI: 10.1038/s41566-018-0327-9. (Pages 4, 83)

[64] Xiewen Wen et al. "3D-printed Silica with Nanoscale Resolution". Nature Materials 20.11 (11 Nov. 2021), pp. 1506–1511. ISSN: 1476-4660.
DOI: 10.1038/s41563-021-01111-2. (Pages 4, 32, 83, 114, 116)

[65] Zongsong Gan et al. "Three-Dimensional Deep Sub-Diffraction Optical Beam Lithography with 9 Nm Feature Size". Nature Communications 4.1 (Oct. 2013), p. 2061. ISSN: 2041-1723.
DOI: 10.1038/ncomms3061. (Page 4)

[66] Richard Wollhofen et al. "120 Nm Resolution and 55 Nm Structure Size in STED-lithography". Optics Express 21.9 (May 6, 2013), pp. 10831–10840. ISSN: 1094-4087.
DOI: 10.1364/OE.21.010831. (Pages 4, 84)

[67] Alexander Münchinger et al. "Multi-Photon 4D Printing of Complex Liquid Crystalline Microstructures by In Situ Alignment Using Electric Fields". Advanced Materials Technologies 7.1 (2022), p. 2100944. ISSN: 2365-709X.
DOI: 10.1002/admt.202100944. (Page 4)

[68] Richard Wollhofen et al. "Multiphoton-Polymerized 3D Protein Assay". ACS Applied Materials & Interfaces 10.2 (Jan. 17, 2018), pp. 1474–1479. ISSN: 1944-8244.
DOI: 10.1021/acsami.7b13183. (Pages 4, 114)

[69] Tamara Aderneuer et al. "Two-Photon Grayscale Lithography for Free-Form Micro-Optical Arrays". Optics Express 29.24 (Nov. 22, 2021), pp. 39511–39520. ISSN: 1094-4087.
DOI: 10.1364/OE.440251. (Page 4)

[70]   Andrea Bertoncini et al. "Advancement in Two-Photon Grayscale Lithography". 3D Printed Optics
       and Additive Photonic Manufacturing III. 3D Printed Optics and Additive Photonic Manufacturing
       III. Ed. by Georg von Freymann, Alois M. Herkommer, and Manuel Flury. Strasbourg, France:
       SPIE, May 20, 2022, p. 1. ISBN: 978-1-5106-5602-4.
       DOI: 10.1117/12.2620974.   (Page 4)

[71]   David Gräfe et al. "Adding Chemically Selective Subtraction to Multi-Material 3D Additive Manu-
       facturing". Nature Communications 9.1 (1 July 17, 2018), p. 2788. ISSN: 2041-1723.
       DOI: 10.1038/s41467-018-05234-0.   (Pages 4, 31, 32, 106, 113, 114, 116, 117)

[72]   Pascal Kiefer et al. "Sensitive Photoresists for Rapid Multiphoton 3D Laser Micro- and Nanoprint-
       ing". Advanced Optical Materials 8.19 (2020), p. 2000895. ISSN: 2195-1071.
       DOI: 10.1002/adom.202000895.   (Pages 4, 7, 10, 11, 32, 83, 116)

[73]   Barbara Spagnolo et al. "Tapered Fibertrodes for Optoelectrical Neural Interfacing in Small Brain
       Volumes with Reduced Artefacts". Nature Materials 21.7 (7 July 2022), pp. 826–835. ISSN: 1476-
       4660.
       DOI: 10.1038/s41563-022-01272-8.   (Page 4)

[74]   Hong-Bo Sun and Satoshi Kawata. "Two-Photon Photopolymerization and 3D Lithographic
       Microfabrication". NMR • 3D Analysis • Photopolymerization. Ed. by N. Fatkullin et al. Berlin,
       Heidelberg: Springer, 2004, pp. 169–273. ISBN: 978-3-540-40000-4.
       DOI: 10.1007/b94405.   (Pages 4–6, 9, 11, 49)

[75]   Joachim Fischer. Three-dimensional optical lithography beyond the diffraction limit. 2012.
       DOI: 10.5445/IR/1000028704. URL: https://publikationen.bibliothek.kit.edu/
       1000028704 (visited on 08/07/2022).   (Pages 4, 7, 10, 11)

[76]   Henry E. Williams et al. "Fabrication of Three-Dimensional Micro-Photonic Structures on the
       Tip of Optical Fibers Using SU-8". Optics Express 19.23 (Nov. 7, 2011), pp. 22910–22922. ISSN:
       1094-4087.
       DOI: 10.1364/OE.19.022910.   (Page 5)

[77]   Justyna K. Gansel et al. "Gold Helix Photonic Metamaterial as Broadband Circular Polarizer".
       Science 325.5947 (Sept. 18, 2009), pp. 1513–1515.
       DOI: 10.1126/science.1177031.   (Page 5)

[78]   Ioanna Sakellari et al. "3D Chiral Plasmonic Metamaterials Fabricated by Direct Laser Writing:
       The Twisted Omega Particle". Advanced Optical Materials 5.16 (2017), p. 1700200. ISSN: 2195-1071.
       DOI: 10.1002/adom.201700200.   (Page 5)

[79]   Mei-Ling Zheng and Xuan-Ming Duan. "Photoinitiators for Multiphoton Absorption Lithography".
       Multiphoton Lithography. Ed. by Jürgen Stampfl, Robert Liska, and Aleksandr Ovsianikov. Wiley-
       VCH Verlag GmbH & Co. KGaA, 2016, pp. 133–165. ISBN: 978-3-527-68267-6.
       DOI: 10.1002/9783527682676.ch6.   (Pages 5, 9)

[80]   "Efficiency of a Photopolymerization Reaction". Photoinitiators for Polymer Synthesis. John Wiley
       & Sons, Ltd, 2012, pp. 103–122. ISBN: 978-3-527-64824-5.
       DOI: 10.1002/9783527648245.ch7.   (Page 6)

[81]   Anton Bauhofer. "Multiscale Effects of Photochemical Shrinkage in Direct Laser Writing". Doctoral
       Thesis. ETH Zurich, 2019.
       DOI: 10.3929/ethz-b-000339159.   (Page 6)

[82]   Magali Dewaele et al. "Volume Contraction in Photocured Dental Resins: The Shrinkage-Conversion
       Relationship Revisited". Dental Materials 22.4 (Apr. 1, 2006), pp. 359–365. ISSN: 0109-5641.
       DOI: 10.1016/j.dental.2005.03.014.   (Page 6)

[83]   S. Loshaek and T. G. Fox. "Cross-Linked Polymers. I. Factors Influencing the Efficiency of Cross-linking in Copolymers of Methyl Methacrylate and Glycol Dimethacrylates1". Journal of the American Chemical Society 75.14 (July 1, 1953), pp. 3544–3550. ISSN: 0002-7863. DOI: 10.1021/ja01110a068. (Page 6)

[84]   Jonathan B. Mueller et al. "Polymerization Kinetics in Three-Dimensional Direct Laser Writing". Advanced Materials 26.38 (2014), pp. 6566–6571. ISSN: 1521-4095. DOI: 10.1002/adma.201402366. (Pages 6, 85)

[85]   Alexander Pikulin and Nikita Bityurin. "Modeling of Polymerization Processes". Multiphoton Lithography. Ed. by Juergen Stampfl, Robert Liska, and Aleksandr Ovsianikov. Wiley-VCH Verlag GmbH & Co. KGaA, 2016, pp. 65–93. ISBN: 978-3-527-68267-6. DOI: 10.1002/9783527682676.ch3. (Pages 6, 10, 11)

[86]   Photoinitiators for Polymer Synthesis. 1st ed. John Wiley & Sons, Ltd, 2012. DOI: 10.1002/9783527648245. (Page 6)

[87]   Joachim Fischer and Martin Wegener. "Three-Dimensional Optical Laser Lithography beyond the Diffraction Limit". Laser & Photonics Reviews 7.1 (Jan. 1, 2013), pp. 22–44. ISSN: 1863-8899. DOI: 10.1002/lpor.201100046. (Pages 8, 11, 13, 32, 37)

[88]   Nonlinear Optical Properties of Organic Molecules and Crystals V2 - 1st Edition. URL: https://www.elsevier.com/books/nonlinear-optical-properties-of-organic-molecules-and-crystals-v2/chemla/978-0-12-170612-8 (visited on 08/13/2022). (Pages 7, 8)

[89]   Bernhard Dick and Georg Hohlneicher. "Importance of Initial and Final States as Intermediate States in Two-photon Spectroscopy of Polar Molecules". The Journal of Chemical Physics 76.12 (June 15, 1982), pp. 5755–5760. ISSN: 0021-9606. DOI: 10.1063/1.442971. (Page 9)

[90]   Joshua Jortner, Mark A. Ratner, and International Union of Pure and Applied Chemistry, eds. Molecular Electronics. A "Chemistry for the 21st Century" Monograph. Osney Mead, Oxford [England] ; Malden, MA, USA: Blackwell Science, 1997. 485 pp. ISBN: 978-0-632-04284-5. (Pages 9, 10)

[91]   O. Sonnich Mortensen and E. No/rby Svendsen. "Initial and Final Molecular States as "Virtual States" in Two-photon Processes". The Journal of Chemical Physics 74.6 (Mar. 15, 1981), pp. 3185–3189. ISSN: 0021-9606. DOI: 10.1063/1.441512. (Page 9)

[92]   Richard L. Sutherland et al. "Excited-State Characterization and Effective Three-Photon Absorption Model of Two-Photon-Induced Excited-State Absorption in Organic Push-Pull Charge-Transfer Chromophores". JOSA B 22.9 (Sept. 1, 2005), pp. 1939–1948. ISSN: 1520-8540. DOI: 10.1364/JOSAB.22.001939. (Pages 9, 87)

[93]   Eric W. Van Stryland and David J. Hagan. "Characterization of 2PA Chromophores". Multiphoton Lithography. Ed. by Jürgen Stampfl, Robert Liska, and Aleksandr Ovsianikov. Wiley-VCH Verlag GmbH & Co. KGaA, 2016, pp. 25–64. ISBN: 978-3-527-68267-6. DOI: 10.1002/9783527682676.ch2. (Pages 9, 87)

[94]   Vincent Hahn et al. "Two-Step Absorption Instead of Two-Photon Absorption in 3D Nanoprinting". Nature Photonics 15.12 (12 Dec. 2021), pp. 932–938. ISSN: 1749-4893. DOI: 10.1038/s41566-021-00906-8. (Pages 9, 11)

[95]   Liang Yang et al. "On the Schwarzschild Effect in 3D Two-Photon Laser Lithography". Advanced Optical Materials 7.22 (2019), p. 1901040. ISSN: 2195-1071. DOI: 10.1002/adom.201901040. (Pages 10, 11)

[96]   M. B. Masthay et al. "A Theoretical Investigation of the One- and Two-photon Properties of Porphyrins". The Journal of Chemical Physics 84.7 (Apr. 1986), pp. 3901–3915. ISSN: 0021-9606. DOI: 10.1063/1.450827. (Page 10)

[97]   P. R. Monson and W. M. McClain. "Polarization Dependence of the Two-Photon Absorption of Tumbling Molecules with Application to Liquid 1-Chloronaphthalene and Benzene". The Journal of Chemical Physics 53.1 (July 1970), pp. 29–37. ISSN: 0021-9606.
DOI: 10.1063/1.1673778.   (Page 10)

[98]   Mai Trang Do et al. "Submicrometer 3D Structures Fabrication Enabled by One-Photon Absorption Direct Laser Writing". Optics Express 21.18 (Sept. 9, 2013), pp. 20964–20973. ISSN: 1094-4087.
DOI: 10.1364/OE.21.020964.   (Page 11)

[99]   M. Thiel et al. "Direct Laser Writing of Three-Dimensional Submicron Structures Using a Continuous-Wave Laser at 532 Nm". Applied Physics Letters 97.22 (Nov. 29, 2010), p. 221102. ISSN: 0003-6951.
DOI: 10.1063/1.3521464.   (Page 11)

[100]   3-D Laser Nanoprinting. URL: https://www.optica-opn.org/home/articles/volume_30/october_2019/features/3-d_laser_nanoprinting/ (visited on 10/16/2022). (Page 12)

[101]   Joachim Fischer and Martin Wegener. "Three-Dimensional Direct Laser Writing Inspired by Stimulated-Emission-Depletion Microscopy [Invited]". Optical Materials Express 1.4 (Aug. 1, 2011), pp. 614–624. ISSN: 2159-3930.
DOI: 10.1364/OME.1.000614.   (Pages 12, 84, 93, 96)

[102]   Linjie Li et al. "Achieving λ/20 Resolution by One-Color Initiation and Deactivation of Polymerization". Science 324.5929 (May 15, 2009), pp. 910–913. ISSN: 0036-8075, 1095-9203.
DOI: 10.1126/science.1168996. pmid: 19359543.   (Page 12)

[103]   Robert R. McLeod, Benjamin A. Kowalski, and Michael C. Cole. "Two-Color Photo-Initiation/Inhibition Lithography". Advanced Fabrication Technologies for Micro/Nano Optics and Photonics III. Advanced Fabrication Technologies for Micro/Nano Optics and Photonics III. Vol. 7591. SPIE, Feb. 16, 2010, pp. 9–16.
DOI: 10.1117/12.845850.   (Page 12)

[104]   Alexander P. Demchenko. "The Red-Edge Effects: 30 Years of Exploration". Luminescence 17.1 (2002), pp. 19–42. ISSN: 1522-7243.
DOI: 10.1002/bio.671.   (Pages 13–15, 84–86, 88, 89, 91)

[105]   Nicolai A. Nemkovich, Anatolyi N. Rubinov, and Vladimir I. Tomin. "Inhomogeneous Broadening of Electronic Spectra of Dye Molecules in Solutions". Topics in Fluorescence Spectroscopy: Principles. Ed. by Joseph R. Lakowicz. Topics in Fluorescence Spectroscopy. Boston, MA: Springer US, 2002, pp. 367–428. ISBN: 978-0-306-47058-5.
DOI: 10.1007/0-306-47058-6_8.   (Pages 14, 15)

[106]   Alexander P. Demchenko. "On the Nanosecond Mobility in Proteins: Edge Excitation Fluorescence Red Shift of Protein-Bound 2-(p-Toluidinylnaphthalene)-6-Sulfonate". Biophysical Chemistry 15.2 (May 1, 1982), pp. 101–109. ISSN: 0301-4622.
DOI: 10.1016/0301-4622(82)80022-7.   (Page 15)

[107]   Michael J. E. Morgenthaler, Keitaro Yoshihara, and Stephen R. Meech. "Red-Edge Excitation Fluorescence Study of the Inhomogeneous Broadening of Electronic Transitions in Solution". Journal of the Chemical Society, Faraday Transactions 92.4 (1996), pp. 629–635.
DOI: 10.1039/FT9969200629.   (Page 15)

[108]   Gregorio Weber and Meir Shinitzky. "Failure of Energy Transfer between Identical Aromatic Molecules on Excitation at the Long Wave Edge of the Absorption Spectrum". Proceedings of the National Academy of Sciences 65.4 (Apr. 1970), pp. 823–830.
DOI: 10.1073/pnas.65.4.823.   (Page 15)

[109]   V. T. Koyava and V. I. Popechits. "Directed Energy Transfer in Solid Polar Dye Mixtures". Journal of Applied Spectroscopy 31.6 (Dec. 1979), pp. 1484–1488. ISSN: 0021-9037, 1573-8647.
DOI: 10.1007/BF01100259.   (Page 15)

[110]   Robin Bläsing. "Highly Efficient Domain Wall Motion in Ferrimagnetic Bi-layer Systems at the
        Angular Momentum Compensation Temperature" (2019).
        DOI: 10.25673/32178.   (Pages 16–22, 24, 72)

[111]   Principles of Nanomagnetism.   (Pages 16, 17)

[112]   Manuel Vázquez, ed. Magnetic Nano- and Microwires: Design, Synthesis, Properties and Applica-
        tions. Second edition. Woodhead Publishing Series in Electronic and Optical Materials. Duxford
        Cambridge, MA Kidlington: Woodhead Publishing, 2020. 984 pp. ISBN: 978-0-08-102832-2.   (
        Page 16)

[113]   "Ferromagnetism". The Physical Principles of Magnetism. John Wiley & Sons, Ltd, 2001, pp. 259–
        331. ISBN: 978-0-470-54658-1.
        DOI: 10.1002/9780470546581.ch6.   (Page 16)

[114]   D. A. Allwood et al. "Magnetic Domain-Wall Logic". Science 309.5741 (Sept. 9, 2005), pp. 1688–
        1692.
        DOI: 10.1126/science.1108813.   (Page 19)

[115]   Zhaochu Luo et al. "Current-Driven Magnetic Domain-Wall Logic". Nature 579.7798 (7798 Mar.
        2020), pp. 214–218. ISSN: 1476-4687.
        DOI: 10.1038/s41586-020-2061-y.   (Pages 19, 59)

[116]   Volodymyr P. Kravchuk. "Influence of Dzialoshinskii–Moriya Interaction on Static and Dynamic
        Properties of a Transverse Domain Wall". Journal of Magnetism and Magnetic Materials 367
        (Oct. 1, 2014), pp. 9–14. ISSN: 0304-8853.
        DOI: 10.1016/j.jmmm.2014.04.073.   (Page 19)

[117]   A. Bogdanov and A. Hubert. "Thermodynamically Stable Magnetic Vortex States in Magnetic
        Crystals". Journal of Magnetism and Magnetic Materials 138.3 (Dec. 1, 1994), pp. 255–269. ISSN:
        0304-8853.
        DOI: 10.1016/0304-8853(94)90046-9.   (Pages 21, 23)

[118]   Eduardo Martinez et al. "Current-Driven Dynamics of Dzyaloshinskii Domain Walls in the
        Presence of in-Plane Fields: Full Micromagnetic and One-Dimensional Analysis". Journal of
        Applied Physics 115.21 (June 7, 2014), p. 213909. ISSN: 0021-8979.
        DOI: 10.1063/1.4881778.   (Pages 21, 23)

[119]   Gong Chen et al. "Unlocking Bloch-type Chirality in Ultrathin Magnets through Uniaxial Strain".
        Nature Communications 6.1 (1 Mar. 23, 2015), p. 6598. ISSN: 2041-1723.
        DOI: 10.1038/ncomms7598.   (Page 21)

[120]   J. H. Franken et al. "Tunable Chiral Spin Texture in Magnetic Domain-Walls". Scientific Reports
        4.1 (1 June 11, 2014), p. 5248. ISSN: 2045-2322.
        DOI: 10.1038/srep05248.   (Page 21)

[121]   Kwang-Su Ryu et al. "Chiral Spin Torque at Magnetic Domain Walls". Nature Nanotechnology 8.7
        (7 July 2013), pp. 527–533. ISSN: 1748-3395.
        DOI: 10.1038/nnano.2013.102.   (Pages 21, 24, 39, 59, 71)

[122]   L. Skoric et al. "Domain Wall Automotion in Three-Dimensional Magnetic Helical Interconnec-
        tors". Oct. 9, 2021. arXiv: 2110.04636 [cond-mat, physics:physics]. (Pages 25, 27–29, 59,
        101, 114, 115, 117)

[123]   Denys Makarov et al. "New Dimension in Magnetism and Superconductivity: 3D and Curvilinear
        Nanoarchitectures". Advanced Materials 34.3 (2022), p. 2101758. ISSN: 1521-4095.
        DOI: 10.1002/adma.202101758.   (Pages 25, 28)

[124]   Oleksandr V. Pylypovskyi et al. "Coupling of Chiralities in Spin and Physical Spaces: The M\"obius
        Ring as a Case Study". Physical Review Letters 114.19 (May 15, 2015), p. 197204.
        DOI: 10.1103/PhysRevLett.114.197204.   (Pages 25, 114)

[125]   Denis D. Sheka et al. "Nonlocal Chiral Symmetry Breaking in Curvilinear Magnetic Shells".
        Communications Physics 3.1 (1 July 20, 2020), pp. 1–7. ISSN: 2399-3650.
        DOI: 10.1038/s42005-020-0387-2.   (Pages 25, 27)

[126]   Yuri Gaididei, Volodymyr P. Kravchuk, and Denis D. Sheka. "Curvature Effects in Thin Magnetic
        Shells". Physical Review Letters 112.25 (June 25, 2014), p. 257203.
        DOI: 10.1103/PhysRevLett.112.257203.   (Pages 26, 28, 114)

[127]   Denis D. Sheka, Volodymyr P. Kravchuk, and Yuri Gaididei. "Curvature Effects in Statics and
        Dynamics of Low Dimensional Magnets". Journal of Physics A: Mathematical and Theoretical
        48.12 (Mar. 2015), p. 125202. ISSN: 1751-8121.
        DOI: 10.1088/1751-8113/48/12/125202.   (Pages 26, 28, 114)

[128]   Wolfgang Kühnel and Bruce Hunt. Differential Geometry: Curves, Surfaces, Manifolds. Third
        edition. Student Mathematical Library volume 77. Providence, Rhode Island: American Mathe-
        matical Society, 2015. 402 pp. ISBN: 978-1-4704-2320-9.   (Page 26
)

[129]   Robert Streubel, Evgeny Y. Tsymbal, and Peter Fischer. "Magnetism in Curved Geometries".
        Journal of Applied Physics 129.21 (June 7, 2021), p. 210902. ISSN: 0021-8979.
        DOI: 10.1063/5.0054025.   (Pages 27, 28, 30)

[130]   Kostiantyn V. Yershov et al. "Curvature and Torsion Effects in Spin-Current Driven Domain Wall
        Motion". Physical Review B 93.9 (Mar. 15, 2016), p. 094418.
        DOI: 10.1103/PhysRevB.93.094418.   (Pages 27, 114)

[131]   Oleksii M. Volkov et al. "Experimental Observation of Exchange-Driven Chiral Effects in Curvi-
        linear Magnetism". Physical Review Letters 123.7 (Aug. 15, 2019), p. 077201.
        DOI: 10.1103/PhysRevLett.123.077201.   (Pages 27, 28)

[132]   Kostiantyn V. Yershov et al. "Geometry-Induced Motion of Magnetic Domain Walls in Curved
        Nanostripes". Physical Review B 98.6 (Aug. 22, 2018), p. 060409.
        DOI: 10.1103/PhysRevB.98.060409.   (Pages 27, 28)

[133]   Lukas Körber et al. Experimental Observation of the Curvature-Induced Asymmetric Spin-Wave
        Dispersion in Hexagonal Nanotubes. Sept. 4, 2020.
        DOI: 10.48550/arXiv.2009.02238. arXiv: 2009.02238 [cond-mat]. URL: http://arxiv.
        org/abs/2009.02238 (visited on 08/22/2022). preprint.   (Pages 27, 28)

[134]   Denis D. Sheka et al. "Torsion-Induced Effects in Magnetic Nanowires". Physical Review B 92.5
        (Aug. 10, 2015), p. 054417.
        DOI: 10.1103/PhysRevB.92.054417.   (Pages 27, 114)

[135]   Oleksandr V. Pylypovskyi et al. "Curvilinear One-Dimensional Antiferromagnets". Nano Letters
        20.11 (Nov. 11, 2020), pp. 8157–8162. ISSN: 1530-6984.
        DOI: 10.1021/acs.nanolett.0c03246.   (Page 28)

[136]   E. Y. Vedmedenko et al. "The 2020 Magnetism Roadmap". Journal of Physics D: Applied Physics
        53.45 (Aug. 2020), p. 453001. ISSN: 0022-3727.
        DOI: 10.1088/1361-6463/ab9d98.   (Page 28)

[137]   Claire Donnelly et al. "Complex Free-Space Magnetic Field Textures Induced by Three-Dimensional
        Magnetic Nanostructures". Nature Nanotechnology (Dec. 20, 2021), pp. 1–7. ISSN: 1748-3395.
        DOI: 10.1038/s41565-021-01027-7.   (Pages 28–30, 34, 114)

[138]   M. Schöbitz et al. "Fast Domain Wall Motion Governed by Topology and \OE{}rsted Fields in
        Cylindrical Magnetic Nanowires". Physical Review Letters 123.21 (Nov. 21, 2019), p. 217201.
        DOI: 10.1103/PhysRevLett.123.217201.   (Page 28)

[139]   A. May et al. "Magnetic Charge Propagation upon a 3D Artificial Spin-Ice". Nature Communica-
        tions 12.1 (1 May 28, 2021), p. 3217. ISSN: 2041-1723.
        DOI: 10.1038/s41467-021-23480-7.   (Pages 28, 29)

[140] Andrew May et al. "Realisation of a Frustrated 3D Magnetic Nanowire Lattice". Communications Physics 2.1 (Dec. 2019), p. 13. ISSN: 2399-3650.
DOI: 10.1038/s42005-018-0104-6. (Page 29)

[141] Claire Donnelly et al. "Three-Dimensional Magnetization Structures Revealed with X-ray Vector Nanotomography". Nature 547.7663 (7663 July 2017), pp. 328–331. ISSN: 1476-4687.
DOI: 10.1038/nature23006. (Pages 29, 34, 114, 115)

[142] Daniil Karnaushenko, Tong Kang, and Oliver G. Schmidt. "Shapeable Material Technologies for 3D Self-Assembly of Mesoscale Electronics". Advanced Materials Technologies 4.4 (2019), p. 1800692. ISSN: 2365-709X.
DOI: 10.1002/admt.201800692. (Page 29)

[143] Changhao Xu et al. "Rolled-up Nanotechnology: Materials Issue and Geometry Capability". Advanced Materials Technologies 4.1 (2019), p. 1800486. ISSN: 2365-709X.
DOI: 10.1002/admt.201800486. (Page 30)

[144] Robert Streubel et al. "Retrieving Spin Textures on Curved Magnetic Thin Films with Full-Field Soft X-ray Microscopies". Nature Communications 6.1 (1 July 3, 2015), p. 7612. ISSN: 2041-1723.
DOI: 10.1038/ncomms8612. (Page 30)

[145] Fanfan Meng et al. "Fabrication of a 3D Nanomagnetic Circuit with Multi-Layered Materials for Applications in Spintronics". Micromachines 12.8 (8 Aug. 2021), p. 859. ISSN: 2072-666X.
DOI: 10.3390/mi12080859. (Pages 30, 113, 114, 116)

[146] Magi Mettry et al. "Refractive Index Matched Polymeric and Preceramic Resins for Height-Scalable Two-Photon Lithography". RSC Advances 11.37 (2021), pp. 22633–22639.
DOI: 10.1039/D1RA01733K. (Pages 30, 31)

[147] Jiho Yoon et al. "Local and Global Energy Barriers for Chiral Domain Walls in Synthetic Antiferromagnet–Ferromagnet Lateral Junctions". Nature Nanotechnology 17.11 (11 Nov. 2022), pp. 1183–1191. ISSN: 1748-3395.
DOI: 10.1038/s41565-022-01215-z. (Page 30)

[148] Booyong S. Lim, Antti Rahtu, and Roy G. Gordon. "Atomic Layer Deposition of Transition Metals". Nature Materials 2.11 (Nov. 1, 2003), pp. 749–754. ISSN: 1476-1122, 1476-4660.
DOI: 10.1038/nmat1000. (Page 31)

[149] R. Mantovan et al. "Atomic Layer Deposition of Magnetic Thin Films". Acta Physica Polonica A 112.6 (Dec. 2007), pp. 1271–1280. ISSN: 0587-4246, 1898-794X.
DOI: 10.12693/APhysPolA.112.1271. (Page 31)

[150] Miling Zhang et al. "Comparison of Sputtering and Atomic Layer Deposition Based Ultra-Thin Alumina Protective Layers for High Temperature Surface Acoustic Wave Devices". Journal of Materials Research and Technology 15 (Nov. 1, 2021), pp. 4714–4724. ISSN: 2238-7854.
DOI: 10.1016/j.jmrt.2021.10.081. (Page 31)

[151] Andreas Frölich et al. "Titania Woodpiles with Complete Three-Dimensional Photonic Bandgaps in the Visible". Advanced Materials 25.26 (2013), pp. 3588–3592. ISSN: 1521-4095.
DOI: 10.1002/adma.201300896. (Pages 31, 113)

[152] Daniel Oran et al. "3D Nanofabrication by Volumetric Deposition and Controlled Shrinkage of Patterned Scaffolds". Science 362.6420 (Dec. 14, 2018), pp. 1281–1285.
DOI: 10.1126/science.aau5119. (Pages 31, 32, 114)

[153] Frederik Kotz et al. "Three-Dimensional Printing of Transparent Fused Silica Glass". Nature 544.7650 (7650 Apr. 2017), pp. 337–339. ISSN: 1476-4687.
DOI: 10.1038/nature22061. (Page 32)

[154] John G. Gibbs et al. "Nanohelices by Shadow Growth". Nanoscale 6.16 (July 24, 2014), pp. 9457–9466. ISSN: 2040-3372.
DOI: 10.1039/C4NR00403E. (Page 32)

[155]   Charudatta Phatak et al. "Visualization of the Magnetic Structure of Sculpted Three-Dimensional
         Cobalt Nanospirals". Nano Letters 14.2 (Feb. 12, 2014), pp. 759–764. ISSN: 1530-6984.
         DOI: 10.1021/nl404071u.   (Pages 32, 34)

[156]   Wooik Jung et al. "Three-Dimensional Nanoprinting via Charged Aerosol Jets". Nature 592.7852
         (7852 Apr. 2021), pp. 54–59. ISSN: 1476-4687.
         DOI: 10.1038/s41586-021-03353-1.   (Pages 32, 33, 35, 114, 116)

[157]   R. Winkler et al. "High-Fidelity 3D-Nanoprinting via Focused Electron Beams: Growth Fundamen-
         tals". ACS Applied Nano Materials 1.3 (Mar. 23, 2018), pp. 1014–1027. ISSN: 2574-0970, 2574-0970.
         DOI: 10.1021/acsanm.8b00158.   (Pages 33, 34)

[158]   Amalio Fernández-Pacheco et al. "Writing 3D Nanomagnets Using Focused Electron Beams".
         Materials 13.17 (17 Jan. 2020), p. 3774.
         DOI: 10.3390/ma13173774.   (Page 33)

[159]   Dédalo Sanz-Hernández et al. "Fabrication of Scaffold-Based 3D Magnetic Nanowires for Domain
         Wall Applications". Nanomaterials 8.7 (7 July 2018), p. 483. ISSN: 2079-4991.
         DOI: 10.3390/nano8070483.   (Pages 33, 34, 114, 115)

[160]   A. Botman, J. J. L. Mulders, and C. W. Hagen. "Creating Pure Nanostructures from Electron-Beam-
         Induced Deposition Using Purification Techniques: A Technology Perspective". Nanotechnology
         20.37 (Aug. 2009), p. 372001. ISSN: 0957-4484.
         DOI: 10.1088/0957-4484/20/37/372001.   (Page 33)

[161]   J. M. De Teresa et al. "Review of Magnetic Nanostructures Grown by Focused Electron Beam
         Induced Deposition (FEBID)". Journal of Physics D: Applied Physics 49.24 (May 2016), p. 243003.
         ISSN: 0022-3727.
         DOI: 10.1088/0022-3727/49/24/243003.   (Page 33)

[162]   Franz Pfeiffer. "X-Ray Ptychography". Nature Photonics 12.1 (1 Jan. 2018), pp. 9–17. ISSN: 1749-
         4893.
         DOI: 10.1038/s41566-017-0072-5.   (Pages 34, 114)

[163]   A. Wartelle et al. "Transmission XMCD-PEEM Imaging of an Engineered Vertical FEBID Cobalt
         Nanowire with a Domain Wall". Nanotechnology 29.4 (Dec. 2017), p. 045704. ISSN: 0957-4484.
         DOI: 10.1088/1361-6528/aa9eff.   (Pages 34, 114)

[164]   Christophe Gatel et al. "Size-Specific Spin Configurations in Single Iron Nanomagnet: From Flower
         to Exotic Vortices". Nano Letters 15.10 (Oct. 14, 2015), pp. 6952–6957. ISSN: 1530-6984.
         DOI: 10.1021/acs.nanolett.5b02892.   (Page 34)

[165]   Chen Yang et al. "Probing the Morphology and Evolving Dynamics of 3D Printed Nanostructures
         Using High-Speed Atomic Force Microscopy". ACS Applied Materials & Interfaces 9.29 (July 26,
         2017), pp. 24456–24461. ISSN: 1944-8244.
         DOI: 10.1021/acsami.7b07762.   (Pages 34, 114)

[166]   Benjamin Harke et al. "Polymerization Inhibition by Triplet State Absorption for Nanoscale
         Lithography". Advanced Materials 25.6 (Feb. 13, 2013), pp. 904–909. ISSN: 1521-4095.
         DOI: 10.1002/adma.201204141.   (Pages 38, 84, 85)

[167]   Z. Q. Qiu and S. D. Bader. "Surface Magneto-Optic Kerr Effect". Review of Scientific Instruments
         71.3 (Mar. 2000), pp. 1243–1255. ISSN: 0034-6748, 1089-7623.
         DOI: 10.1063/1.1150496.   (Pages 40, 41)

[168]   Luqiao Liu et al. "Current-Induced Switching of Perpendicularly Magnetized Magnetic Layers
         Using Spin Torque from the Spin Hall Effect". Physical Review Letters 109.9 (Aug. 29, 2012),
         p. 096602.
         DOI: 10.1103/PhysRevLett.109.096602.   (Page 42)

[169]   Welcome to Magnum.Fe's Documentation! — Magnum.Fe 2.2.2 Documentation. URL: `http://micromagnetics.org/magnum.fe/` (visited on 11/27/2022).   (Page 42)

[170]   P. Talagala et al. "Determination of Magnetic Exchange Stiffness and Surface Anisotropy Constants in Epitaxial ${\mathrm{Ni}}_{1\ensuremath{-}x}{\mathrm{Co}}_{x}(001)$ Films". Physical Review B 66.14 (Oct. 31, 2002), p. 144426.
DOI: `10.1103/PhysRevB.66.144426`.   (Page 42)

[171]   AI Support Server. URL: `https://imspector.abberior-instruments.com/#` (visited on 03/20/2022).   (Page 45)

[172]   3D Slicer Image Computing Platform. 3D Slicer. URL: `https://slicer.org/` (visited on 03/27/2022).   (Page 48)

[173]   Andriy Fedorov et al. "3D Slicer as an Image Computing Platform for the Quantitative Imaging Network". Magnetic resonance imaging 30.9 (Nov. 2012), pp. 1323–1341. ISSN: 0730-725X.
DOI: `10.1016/j.mri.2012.05.001`. pmid: 22770690.   (Page 48)

[174]   OpenCV team. About. OpenCV. URL: `https://opencv.org/about/` (visited on 04/03/2022).
                                                                                    (Page 52)

[175]   Syed Waqas Zamir et al. "Multi-Stage Progressive Image Restoration". Mar. 16, 2021. arXiv: `2102.02808 [cs]`.   (Page 52)

[176]   Digital Image Processing, 4th Edition. URL: `https://www.pearson.com/content/one-dot-com/one-dot-com/us/en/higher-education/program.html` (visited on 04/03/2022).   (Page 53)

[177]   Satoshi Suzuki and KeiichiA be. "Topological Structural Analysis of Digitized Binary Images by Border Following". Computer Vision, Graphics, and Image Processing 30.1 (Apr. 1, 1985), pp. 32–46. ISSN: 0734-189X.
DOI: `10.1016/0734-189X(85)90016-7`.   (Page 53)

[178]   Open3D – A Modern Library for 3D Data Processing. URL: `http://www.open3d.org/` (visited on 04/03/2022).   (Page 57)

[179]   Qian-Yi Zhou, Jaesik Park, and Vladlen Koltun. "Open3D: A Modern Library for 3D Data Processing". Jan. 29, 2018. arXiv: `1801.09847 [cs]`.   (Page 57)

[180]   Michael Kazhdan, Matthew Bolitho, and Hugues Hoppe. "Poisson Surface Reconstruction". The Eurographics Association, 2006. ISBN: 978-3-905673-24-1.
DOI: `10.2312/SGP/SGP06/061-070`.   (Page 57)

[181]   Satoru Emori et al. "Current-Driven Dynamics of Chiral Ferromagnetic Domain Walls". Nature Materials 12.7 (7 July 2013), pp. 611–616. ISSN: 1476-4660.
DOI: `10.1038/nmat3675`.   (Page 59)

[182]   Qiming Shao et al. "Roadmap of Spin–Orbit Torques". IEEE Transactions on Magnetics 57.7 (July 2021), pp. 1–39. ISSN: 1941-0069.
DOI: `10.1109/TMAG.2021.3078583`.   (Page 59)

[183]   Chirag Garg et al. "Dramatic Influence of Curvature of Nanowire on Chiral Domain Wall Velocity". Science Advances 3.5 (May 5, 2017), e1602804.
DOI: `10.1126/sciadv.1602804`.   (Pages 59, 72)

[184]   Chirag Garg et al. "Highly Asymmetric Chiral Domain-Wall Velocities in Y-Shaped Junctions". Nano Letters 18.3 (Mar. 14, 2018), pp. 1826–1830. ISSN: 1530-6984.
DOI: `10.1021/acs.nanolett.7b05086`.   (Page 59)

[185] O. Boulle et al. "Domain Wall Tilting in the Presence of the Dzyaloshinskii-Moriya Interaction in Out-of-Plane Magnetized Magnetic Nanotracks". Physical Review Letters 111.21 (Nov. 20, 2013), p. 217203.
DOI: 10.1103/PhysRevLett.111.217203.   (Page 59)

[186] Kwang-Su Ryu et al. "Current Induced Tilting of Domain Walls in High Velocity Motion along Perpendicularly Magnetized Micron-Sized Co/Ni/Co Racetracks". Applied Physics Express 5.9 (Sept. 6, 2012), p. 093006. ISSN: 1882-0786.
DOI: 10.1143/APEX.5.093006.   (Page 59)

[187] Oleksandr V. Pylypovskyi et al. "Rashba Torque Driven Domain Wall Motion in Magnetic Helices". Scientific Reports 6.1 (Sept. 2016). ISSN: 2045-2322.
DOI: 10.1038/srep23316. arXiv: 1510.04725.   (Page 59)

[188] Vagson L. Carvalho-Santos et al. "Shifts in the Skyrmion Stabilization Due to Curvature Effects in Dome- and Antidome-Shaped Surfaces". Physical Review B 102.2 (July 29, 2020), p. 024444.
DOI: 10.1103/PhysRevB.102.024444.   (Page 59)

[189] Dong Wu et al. "High Numerical Aperture Microlens Arrays of Close Packing". Applied Physics Letters 97.3 (July 19, 2010), p. 031109. ISSN: 0003-6951.
DOI: 10.1063/1.3464979.   (Page 61)

[190] Tommaso Baldacchini and Ruben Zadoyan. "In Situ and Real Time Monitoring of Two-Photon Polymerization Using Broadband Coherent Anti-Stokes Raman Scattering Microscopy". Optics Express 18.18 (Aug. 30, 2010), p. 19219. ISSN: 1094-4087.
DOI: 10.1364/OE.18.019219.   (Pages 83, 84, 93, 115)

[191] Puskal Kunwar et al. "Third-Harmonic Generation Imaging of Three-Dimensional Microstructures Fabricated by Photopolymerization". Optics Express 24.9 (May 2, 2016), pp. 9353–9358. ISSN: 1094-4087.
DOI: 10.1364/OE.24.009353.   (Pages 83, 84)

[192] Warren R. Zipfel, Rebecca M. Williams, and Watt W. Webb. "Nonlinear Magic: Multiphoton Microscopy in the Biosciences". Nature Biotechnology 21.11 (11 Nov. 2003), pp. 1369–1377. ISSN: 1546-1696.
DOI: 10.1038/nbt899.   (Pages 83, 84)

[193] Roman Zvagelsky et al. "Towards In-Situ Diagnostics of Multi-Photon 3D Laser Printing Using Optical Coherence Tomography". Light: Advanced Manufacturing 3.2 (2022), p. 1. ISSN: 2831-4093.
DOI: 10.37188/lam.2022.039.   (Pages 83, 84, 115)

[194] R. F. Egerton, P. Li, and M. Malac. "Radiation Damage in the TEM and SEM". Micron. International Wuhan Symposium on Advanced Electron Microscopy 35.6 (Aug. 1, 2004), pp. 399–409. ISSN: 0968-4328.
DOI: 10.1016/j.micron.2004.02.003.   (Page 84)

[195] Andrey S. Klymchenko. "Solvatochromic and Fluorogenic Dyes as Environment-Sensitive Probes: Design and Biological Applications". Accounts of Chemical Research 50.2 (Feb. 21, 2017), pp. 366–375. ISSN: 0001-4842.
DOI: 10.1021/acs.accounts.6b00517.   (Pages 84, 90)

[196] Jana Basavaraja, S. R. Inamdar, and H. M. Suresh Kumar. "Solvents Effect on the Absorption and Fluorescence Spectra of 7-Diethylamino-3-Thenoylcoumarin: Evaluation and Correlation between Solvatochromism and Solvent Polarity Parameters". Spectrochimica Acta Part A: Molecular and Biomolecular Spectroscopy 137 (Feb. 25, 2015), pp. 527–534. ISSN: 1386-1425.
DOI: 10.1016/j.saa.2014.08.118.   (Pages 84, 86, 89, 90)

[197] Joachim Fischer et al. "Exploring the Mechanisms in STED-Enhanced Direct Laser Writing". Advanced Optical Materials 3.2 (2015), pp. 221–232. ISSN: 2195-1071.
DOI: 10.1002/adom.201400413.   (Pages 84–87, 89)

[198]   Wolter F. Jager, Andries A. Volkers, and D. C. Neckers. "Solvatochromic Fluorescent Probes for
        Monitoring the Photopolymerization of Dimethacrylates". Macromolecules 28.24 (Nov. 1, 1995),
        pp. 8153–8158. ISSN: 0024-9297.
        DOI: 10.1021/ma00128a027.   (Pages 84, 86, 90, 93)

[199]   Bernd Strehmel et al. "New Intramolecular Fluorescence Probes That Monitor Photoinduced
        Radical and Cationic Cross-Linking". Macromolecules 32.22 (Nov. 1, 1999), pp. 7476–7482. ISSN:
        0024-9297.
        DOI: 10.1021/ma990773b.   (Pages 84, 90, 93)

[200]   Benjamin Harke et al. "Photopolymerization Inhibition Dynamics for Sub-Diffraction Direct
        Laser Writing Lithography". ChemPhysChem 13.6 (Apr. 23, 2012), pp. 1429–1434. ISSN: 1439-7641.
        DOI: 10.1002/cphc.201200006.   (Pages 84, 85, 87)

[201]   Shang Yang, Libin Zhang, and Yayi Wei. "Model-Based Image Quality Optimization for Submicron
        Direct Laser Writing". AIP Advances 10.12 (Dec. 2020), p. 125121.
        DOI: 10.1063/6.0000595.   (Pages 92, 118)

[202]   Jean-Baptiste Sibarita. "Deconvolution Microscopy". Microscopy Techniques: -/-. Ed. by Jens
        Rietdorf. Advances in Biochemical Engineering. Berlin, Heidelberg: Springer, 2005, pp. 201–243.
        ISBN: 978-3-540-31545-2.
        DOI: 10.1007/b102215.   (Page 93)

[203]   Henrik Maurenbrecher et al. "Chiral Anisotropic Magnetoresistance of Ferromagnetic Helices".
        Applied Physics Letters 112.24 (June 11, 2018), p. 242401. ISSN: 0003-6951, 1077-3118.
        DOI: 10.1063/1.5027660.   (Pages 99, 103, 104, 106)

[204]   T. McGuire and R. Potter. "Anisotropic Magnetoresistance in Ferromagnetic 3d Alloys". IEEE
        Transactions on Magnetics 11.4 (July 1975), pp. 1018–1038. ISSN: 1941-0069.
        DOI: 10.1109/TMAG.1975.1058782.   (Page 100)

[205]   Carmine Ortix. "Quantum Mechanics of a Spin-Orbit Coupled Electron Constrained to a Space
        Curve". Physical Review B 91.24 (June 11, 2015), p. 245412.
        DOI: 10.1103/PhysRevB.91.245412.   (Page 114)

[206]   Ke Gu et al. "Three-Dimensional Racetrack Memory Devices Designed from Freestanding Mag-
        netic Heterostructures". Nature Nanotechnology 17.10 (10 Oct. 2022), pp. 1065–1071. ISSN: 1748-
        3395.
        DOI: 10.1038/s41565-022-01213-1.   (Page 116)

[207]   "Approach of the Photochemical and Chemical Reactivity". Photoinitiators for Polymer Synthesis.
        John Wiley & Sons, Ltd, 2012, pp. 89–101. ISBN: 978-3-527-64824-5.
        DOI: 10.1002/9783527648245.ch6.

[208]   Kevin D. Belfield et al. "Multiphoton-Absorbing Organic Materials for Microfabrication, Emerging
        Optical Applications and Non-Destructive Three-Dimensional Imaging". Journal of Physical
        Organic Chemistry 13.12 (2000), pp. 837–849. ISSN: 1099-1395.
        DOI: 10.1002/1099-1395(200012)13:12<837::AID-POC315>3.0.CO;2-5.

[209]   J. D. Bhawalkar, G. S. He, and P. N. Prasad. "Nonlinear Multiphoton Processes in Organic and
        Polymeric Materials". Reports on Progress in Physics 59.9 (Sept. 1996), pp. 1041–1070. ISSN: 0034-
        4885.
        DOI: 10.1088/0034-4885/59/9/001.

[210]   Robert W. Boyd. "Chapter 1 - The Nonlinear Optical Susceptibility". Nonlinear Optics (Second
        Edition). San Diego: Academic Press, 2003, pp. 1–65. ISBN: 978-0-12-121682-5.
        DOI: 10.1016/B978-012121682-5/50002-X.

[211]   C. Burrowes et al. "Non-Adiabatic Spin-Torques in Narrow Magnetic Domain Walls". Nature
        Physics 6.1 (1 Jan. 2010), pp. 17–21. ISSN: 1745-2481.
        DOI: 10.1038/nphys1436.

[212]   Marco Carlotti, Omar Tricinci, and Virgilio Mattoli. "Novel, High-Resolution, Subtractive Pho-
        toresist Formulations for 3D Direct Laser Writing Based on Cyclic Ketene Acetals". Advanced
        Materials Technologies n/a.n/a (), p. 2101590. ISSN: 2365-709X.
        DOI: 10.1002/admt.202101590.

[213]   Frederik Claeyssens et al. "Three-Dimensional Biodegradable Structures Fabricated by Two-Photon
        Polymerization". Langmuir 25.5 (Mar. 3, 2009), pp. 3219–3223. ISSN: 0743-7463.
        DOI: 10.1021/la803803m.

[214]   J. L. Clark, P. F. Miller, and G. Rumbles. "Red Edge Photophysics of Ethanolic Rhodamine 101 and
        the Observation of Laser Cooling in the Condensed Phase". The Journal of Physical Chemistry A
        102.24 (June 1, 1998), pp. 4428–4437. ISSN: 1089-5639.
        DOI: 10.1021/jp980589c.

[215]   Héctor Corte-León et al. "Magnetic Imaging Using Geometrically Constrained Nano-Domain
        Walls". Nanoscale 11.10 (Mar. 7, 2019), pp. 4478–4488. ISSN: 2040-3372.
        DOI: 10.1039/C8NR07729K.

[216]   Jiahe Cui et al. "Generalised Adaptive Optics Method for High-NA Aberration-Free Refocusing in
        Refractive-Index-Mismatched Media". Optics Express 30.7 (Mar. 28, 2022), pp. 11809–11824. ISSN:
        1094-4087.
        DOI: 10.1364/OE.454912.

[217]   Cura. Ultimaker, Mar. 21, 2022.

[218]   S. Da Col et al. "Observation of Bloch-point Domain Walls in Cylindrical Magnetic Nanowires".
        Physical Review B 89.18 (May 12, 2014), p. 180405.
        DOI: 10.1103/PhysRevB.89.180405.

[219]   R. A. Duine et al. "Synthetic Antiferromagnetic Spintronics". Nature Physics 14.3 (3 Mar. 2018),
        pp. 217–219. ISSN: 1745-2481.
        DOI: 10.1038/s41567-018-0050-y.

[220]   Xuanyao Fong et al. "Spin-Transfer Torque Devices for Logic and Memory: Prospects and Perspec-
        tives". IEEE Transactions on Computer-Aided Design of Integrated Circuits and Systems 35.1 (Jan.
        2016), pp. 1–22. ISSN: 1937-4151.
        DOI: 10.1109/TCAD.2015.2481793.

[221]   Paola Gentile et al. Curved Electronics: Geometry-Induced Effects at the Nanoscale. July 19, 2022.
        DOI: 10.48550/arXiv.2207.09392. arXiv: 2207.09392 [cond-mat]. URL: http://arxiv.
        org/abs/2207.09392 (visited on 08/21/2022). preprint.

[222]   Anya Grushina. "Direct-Write Grayscale Lithography". Advanced Optical Technologies 8.3-4
        (June 1, 2019), pp. 163–169. ISSN: 2192-8584.
        DOI: 10.1515/aot-2019-0024.

[223]   Wojciech Haske et al. "65 Nm Feature Sizes Using Visible Wavelength 3-D Multiphoton Lithogra-
        phy". Optics Express 15.6 (Mar. 19, 2007), pp. 3426–3436. ISSN: 1094-4087.
        DOI: 10.1364/OE.15.003426.

[224]   Laura J. Heyderman et al. "Mesoscopic Magnetic Systems: From Fundamental Properties to
        Devices". Applied Physics Letters 119.8 (Aug. 23, 2021), p. 080401. ISSN: 0003-6951.
        DOI: 10.1063/5.0064083.

[225]   Georg Hohlneicher and Bernhard Dick. "Two-photon Spectroscopy of Dipole-forbidden Transi-
        tions. II. Calculation of Two-photon Cross Sections by the CNDO–CI Method". The Journal of
        Chemical Physics 70.12 (June 15, 1979), pp. 5427–5437. ISSN: 0021-9606, 1089-7690.
        DOI: 10.1063/1.437454.

[226] Barry Honig, Joshua Jortner, and Abraham Szöke. "Theoretical Studies of Two-Photon Absorption Processes. I. Molecular Benzene". The Journal of Chemical Physics 46.7 (May 3, 2004), p. 2714. ISSN: 0021-9606.
DOI: 10.1063/1.1841103.

[227] R. Inführ et al. "3D-structuring of Optical Waveguides with Two Photon Polymerization". MRS Online Proceedings Library 1179.1 (Dec. 1, 2009), pp. 1–7. ISSN: 1946-4274.
DOI: 10.1557/PROC-1179-BB01-07.

[228] Jingchao Jiang and Yongsheng Ma. "Path Planning Strategies to Optimize Accuracy, Quality, Build Time and Material Use in Additive Manufacturing: A Review". Micromachines 11.7 (7 July 2020), p. 633. ISSN: 2072-666X.
DOI: 10.3390/mi11070633.

[229] Johannes Kepler. "Technische Wissenschaften" (2017), p. 98.

[230] Julian Köpfler et al. "Fused-Silica 3D Chiral Metamaterials via Helium-Assisted Microcasting Supporting Topologically Protected Twist Edge Resonances with High Mechanical Quality Factors". Advanced Materials 33.40 (2021), p. 2103205. ISSN: 1521-4095.
DOI: 10.1002/adma.202103205.

[231] Thomas R Kramer, Frederick M Proctor, and Elena Messina. "The NIST RS274NGC Interpreter - Version 3" (), p. 121.

[232] Ning Li et al. "Metallic Glass Nanostructures: Forming Strategies and Functional Applications". Materials Today Advances 15 (Aug. 1, 2022), p. 100253. ISSN: 2590-0498.
DOI: 10.1016/j.mtadv.2022.100253.

[233] YanJun Liu et al. "Improvement of the Diffraction Properties in Holographic Polymer Dispersed Liquid Crystal Bragg Gratings". Optics Communications 218.1 (Mar. 15, 2003), pp. 27–32. ISSN: 0030-4018.
DOI: 10.1016/S0030-4018(03)01171-4.

[234] S. Maruo and S. Kawata. "Two-Photon-Absorbed near-Infrared Photopolymerization for Three-Dimensional Microfabrication". Journal of Microelectromechanical Systems 7.4 (Dec. 1998), pp. 411–415. ISSN: 1941-0158.
DOI: 10.1109/84.735349.

[235] Wayne M. Moreau. "Optical Exposure". Semiconductor Lithography: Principles, Practices, and Materials. Ed. by Wayne M. Moreau. Microdevices. Boston, MA: Springer US, 1988, pp. 355–408. ISBN: 978-1-4613-0885-0.
DOI: 10.1007/978-1-4613-0885-0_8.

[236] Optics & Photonics News - Speed vs. Feature Size: Additional References. URL: https://www.optica-opn.org/home/articles/volume_30/october_2019/features/3-d_laser_nanoprinting/speed_vs_feature_size_additional_references/ (visited on 08/07/2022).

[237] Stuart Parkin and See-Hun Yang. "Memory on the Racetrack". Nature Nanotechnology 10.3 (3 Mar. 2015), pp. 195–198. ISSN: 1748-3395.
DOI: 10.1038/nnano.2015.41.

[238] The Physical Principles of Magnetism | IEEE eBooks | IEEE Xplore. URL: https://ieeexplore.ieee.org/book/5263396 (visited on 08/16/2022).

[239] Oleksandr V. Pylypovskyi et al. "Curvature-Driven Homogeneous Dzyaloshinskii–Moriya Interaction and Emergent Weak Ferromagnetism in Anisotropic Antiferromagnetic Spin Chains". Applied Physics Letters 118.18 (May 3, 2021), p. 182405. ISSN: 0003-6951.
DOI: 10.1063/5.0048823.

[240] Sourabh K. Saha et al. "Radiopaque Resists for Two-Photon Lithography To Enable Submicron 3D Imaging of Polymer Parts via X-ray Computed Tomography". ACS Applied Materials & Interfaces 10.1 (Jan. 10, 2018), pp. 1164–1172. ISSN: 1944-8244.
DOI: 10.1021/acsami.7b12654.

[241] Simon Sayer et al. "Guiding Cell Migration in 3D with High-Resolution Photografting". Scientific Reports 12.1 (1 May 23, 2022), p. 8626. ISSN: 2045-2322.
DOI: 10.1038/s41598-022-11612-y.

[242] Ganapathi Subramania et al. "Log-Pile TiO_2 Photonic Crystal for Light Control at Near-UV and Visible Wavelengths". Advanced Materials 22.4 (2010), pp. 487–491. ISSN: 1521-4095.
DOI: 10.1002/adma.200902264.

[243] Aniwat Tandaechanurat et al. "Lasing Oscillation in a Three-Dimensional Photonic Crystal Nanocavity with a Complete Bandgap". Nature Photonics 5.2 (2 Feb. 2011), pp. 91–94. ISSN: 1749-4893.
DOI: 10.1038/nphoton.2010.286.

[244] Xingyu Wu et al. "Investigation of Two-Photon Polymerized Microstructures Using Fluorescence Lifetime Measurements". Polymer Chemistry (Mar. 21, 2022). ISSN: 1759-9962.
DOI: 10.1039/D1PY01728D.

[245] Muhammad A. Zeeshan et al. "Hybrid Helical Magnetic Microrobots Obtained by 3D Template-Assisted Electrodeposition". Small 10.7 (Apr. 2014), pp. 1284–1288. ISSN: 16136810.
DOI: 10.1002/smll.201302856.

Eidesstattliche Erklärung

Ich, André Miguel Alves Farinha, erkläre hiermit, dass ich die vorliegende Arbeit, Emergent Magnetic Effects in Spintronic Devices with 3D Chiral Geometries, selbständig und ohne fremde Hilfe verfasst habe. Es wurden keine anderen Quellen oder Hilfsmittel als die von mir ausdrücklich angegebenen verwendet. Elemente, die direkt aus solchen Quellen zitieren oder auf solche Quellen verweisen, sind als solche gekennzeichnet.

Ich erkläre ferner, dass ich diese Arbeit, eine ihr wesentlich ähnliche Fassung oder einen wesentlichen Teil davon nicht für einen Abschluss, ein Diplom oder eine andere Qualifikation an einer anderen Universität oder einer ähnlichen Einrichtung eingereicht habe und dies auch nicht vorhabe.

Göttingen, May 2, 2024 André Miguel Alves Farinha

Acknowledgements

In such an arduous and tolling path as that of my Ph.D., the kindness and help from people with little to gain from it were one of the most inspiring and impactful aspects, in my Ph.D. and beyond it. I keep many endearing memories and have much gratitude to acknowledge. I hope to do them justice here.

First and foremost, I thank Prof. Stuart Parkin, my supervisor, for entrusting me with such an ambitious project and providing me with extensive resources while still allowing me significant independence to manage it. This gave me a unique chance to grow and develop confidence in my abilities. Thank you as well for the continuous motivation and openness to talk.

I would also like to thank Prof. Joyce Poon for her selfless support throughout the years, for receiving me in her group in Toronto, for all of the valuable advice regarding both the big-picture and the tiny details, and for always finding time to meet when I needed it.

At the Max Planck Institute for Microstructure Physics, I was fortunate to meet and work with many fantastic people and make great friends. I extend my gratitude to all administrative and supporting staff, and particularly to Michael Strauch and Simone Jäger, for going to great lengths to create the necessary conditions for this project to thrive and allow me to focus on research; to Winfried Heichler, for the support with the tendering process; to Daniel Meyer, for his proactivity and for helping me to make sense of polymer chemistry; to See-Hun Yang for all the ideas, discussions and explanations; to Tianping Ma, for his patience in explaining all things magnetism and for always being attentive and considerate in the lab; to Abhay Srivastava, for always being available to help with the FIB.

I want to thank Jae-Chun Cheon for the unofficial guidance in all sorts of matters, for all the criticism and dinners, Andrea Migliorini for being a kind and attentive friend, especially in the toughest of times, and Lukas Fischer, for always being supportive and cheerful.

I am also profoundly grateful to Jiho Yoon for his unwavering support at any time of the day, his kindness and availability; Amine Wahada for his willingness to help even when overwhelmed with work; Edouard Lesne for the guidance at the start and frankness; Jiho, Amine, Edouard, James Taylor, and Alessandro Fumarola, for their friendship and support, even when I made it difficult.

To Berthold Rimmler, I am grateful for all the side projects we got into and the stories we accrued, and to all the CuriosiTea group members for making it such a relevant and impactful initiative.

I also heartily acknowledge all who helped revise and improve this thesis.

Outside the Max Planck, I extend my sincere gratitude to Prof. Bernard Dick for helping me navigate and understand the fascinating theory behind MPL; to Jakob Bierwagen for the availability and for expertly advising me towards the MPL system I sought just when I needed it the most; to Markus Köhler for always being cheerful and supportive even when facing the most out-of-the-box requests.

To my friends Almeno Fernandes, André Cunha, Bruno Morais, Daniel Magro, and João Godinho, thanks for putting up with my quirks and keeping me company through all these years.

I'm grateful to my father, Manuel, mother, Emília, and brother, Filipe, for the unconditional support, for sharing some of the burden and being patient in dealing with my tempers while always being ready to help on short notice.

Finally, I thank my partner, Catarina. Your willingness to sacrifice five years of comfort and time together for such an ambitious vision of our future is profoundly humbling, and proof of trust and love like there are few. You, and our future, have been my pillars of support, hope, and motivation to withstand all there was. I hope that soon these years will prove a well-worth sacrifice. Thank you.

Funding

Curriculum vitae

André Miguel Alves Farinha, M.Sc.

Nationality: Portuguese
Gender: Male

Academic

09.2017-04.2022   Doctoral Research Fellow
Max Planck Institute for Microstructure Physics, Halle (Saale), Germany

05.2015-08.2015   Research Fellow
INESC Institute for Microsystems and Nanotechnology, Lisbon, Portugal

Education

09.2017-2023   Doctoral Candidate
Martin-Luther-University Halle-Wittenberg, Halle (Saale), Germany

04.2012-05.2015   Master of Science in Physics
Instituto Superior Técnico, Lisbon, Portugal

09.2009-03.2012   Bachelor of Science in Physics
Instituto Superior Técnico, Lisbon, Portugal

Göttingen, May 2, 2024   André Miguel Alves Farinha